Impact of texture on resistivity of silver-based model low-emissive coatings

Francesca Corbella

THÈSE DE DOCTORAT
SORBONNE UNIVERSITÉ

Spécialité

Physico-Chimie des Matériaux

École doctorale « Physique et Chimie des Matériaux »

réalisée aux laboratoires

Surface du Verre et Interfaces, UMR 125 CNRS – Saint-Gobain
Institut des Nanosciences de Paris, UMR 7588 CNRS – Sorbonne Université

présentée par

Francesca CORBELLA

pour obtenir le grade de

DOCTEUR DE SORBONNE UNIVERSITÉ

Sujet de la thèse

Impact of texture on resistivity of silver-based model low-emissive coatings

soutenue publiquement le 12.05.2022

devant le jury composé de :

M. Philippe Lecoeur	Professeur, C2N	Rapporteur
M. David Babonneau	Directeur de Recherche, PPRIME	Rapporteur
M^{me} Emmanuelle Lacaze	Directrice de Recherche, INSP	Examinatrice
M. David Horwat	Professeur, EEIGM	Examinateur
M. Rémi Lazzari	Directeur de Recherche, INSP	Directeur de thèse
M. Denis Guimard	Chef de Groupe, SGRP-CM	Encadrant industriel, invité
M. Hervé Montigaud	Ingénieur de Recherche, SGRP-SVI	Encadrant industriel, invité

Acknowledgment

This thesis was a real challenge, both from a scientific and a personal point of view. An obstacle course that I managed to overcome thanks to the help of many people.

First of all, I would to express my deepest appreciation and gratitude my PhD director, Rémi, and my supervisors, Hervé and Denis. Thank you for always being there for me and supporting me through all the difficulties, despite the distance of this past year. I really admire your dedication and the passion you put into your work, it is a real inspiration. I would like to thank you for all the countless hours you have dedicated to this project, especially in the last few months, and all the lessons you have taught me. There are not enough words to describe my gratitude.

I sincerely thank Professor Matthias Wuttig, and all the members of the physics lab at RWTH University, for welcoming me and integrating me into the German life, despite the current pandemic.

Thanks to Yunlin Zheng and David Hrabovsky, for the scientific discussions and all the hours they dedicated to my work.

I must also mention all the members of the SVI group, and of the MISSTIC team, Jeff and Justine. It was a pleasure to join this wonderful group, where I was able to meet not only colleagues but friends.

I am also grateful to my family, for their unconditional support.

Finally, a special thanks to Jérémy, for putting up with me every day, which is certainly more difficult than tackling a PhD. Thank you for always being there.

Introduction

The industrial context of reinforced thermal insulation glazings

In the world-wide context of global warming due to the increasing emission of greenhouse gases, the best energy is the one that is not used ! Since heating/cooling of buildings represents a sizeable fraction of the energy consumption in our modern societies (40 % in the European Union), a direct way to follow the mandatory trajectory of CO_2 emission reduction is to improve the thermal insulation of housing. To address this issue, the glass industry has developed and improved over the years numerous products such as glass wool, insulating panels or specific multiple glazing windows. Due to the intrinsic properties of glass, windows are one of the main source of thermal losses in a building with a figure of about 40 l/m^2/year of equivalent fuel [1]. If heat transport via conduction/convection is strongly reduced by the presence of a cavity filled with a low conductivity gas between the two glasses panels, losses through windows via radiation remains an issue that is handled by specific low-emissive (low-E) or anti-solar coatings deposited on the inner surfaces (see Fig. (1)-a for the case of double glazing system). These coatings should be as reflective as possible in the far infra-red range to reduced the heat loss, without compromising the transparency in the visible range for indoor comfort, while maximizing passive heating by the free solar energy. In nearly all products, such a goal is achieved through complex stacks of layers among which the active element for the infra-red reflection is a (or several !) film of silver with a thickness in the range of about 10 nm (Fig. (1)-b). Accordingly to the Hagens-Rubens relation [2] $R \simeq 1 - \sqrt{2\varepsilon_0\omega/\sigma}$ (with ω the frequency and ε_0 the vacuum permittivity), the infra-red reflection R of a given metal is directly related to its conductivity σ leading to the choice of silver, an inert metal with one of the lowest bulk resistivities. Since the nanometric thickness is the result of the visible/infra-red trade-off, the minimization of the film resistivity is a key control lever of the coating performances. It can be considered as the compass of the industrialist.
Therefore, there is a fierce competition among glass manufacturers to improve this figure of merit. For instance, accordingly to European Union prospective, a pro-active replacement of windows by today advanced glazings at a modest rate of a few percent per year would save annually almost a third of the CO_2 emission in buildings in 2030. The market is huge and, since windows are long-lasting products, any gain of resistivity today has an exponential impact in the future in terms of greenhouse gas reduction.

In industrial glazings, low-emissive and anti-solar coatings are conventionally deposited by magnetron - sputtering on large glass panes (3.2×6.0 m^2) in dedicated factories. This technique is selected for its high deposition rate and versatility in terms of materials (metals and dielectrics) and deposition conditions. The active silver layers are encompassed in complex stacks of thin films which properties and thicknesses are finely tuned to achieve the required mechanical and optical properties. Tempering for glass toughening or glass shaping for windshield applications in the automotive industry require annealing of the product above the glass transition leading

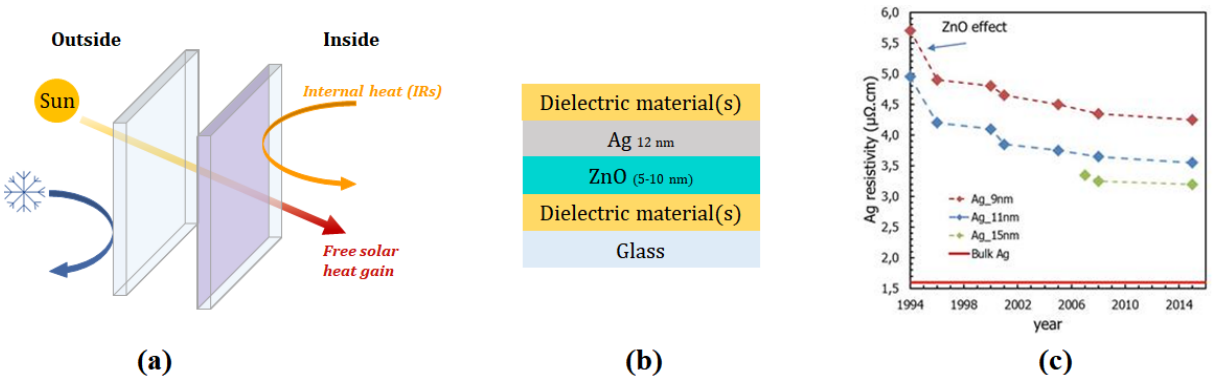

Figure 1 (a) Principle of a typical low-emissive insulating double glazing. (b) Typical stack of thin layers in a low-emissive glazing. (c) Evolution overs the years of the resistivity of a silver film of various thicknesses commonly used in coated glass products; the full line corresponds to silver bulk room-temperature resistivity.

to numerous troubles such as silver dewetting and mechanical failure due to internal stresses. To protect silver from diffusion of alkaline elements from glass or of oxygen from surrounding materials, barrier layers (such as silicon nitride) and sacrificial blocker layers of transition metals are included in the industrial stacks. Annealing, sometimes performed with a laser, favours also recrystallization of materials and improves silver resistivity. Silver is usually encapsulated in between thin layers (5-10 nm thick) of zinc oxide (ZnO), a material that was recognized as the best silver seed in terms of cost, manipulation and performances (silver wetting, crystallization and thermal stability). Indeed, the preferential columnar oxide growth exposes ZnO basal planes which favour the out-of-plane (111) texture growth of the metal (but randomly oriented in-plane) with enhanced electrical properties (Fig. (2)). Introduced in the mid-90's, the ZnO seed layer has allowed a significant decrease of silver film resistivity. Since then, performance improvement via the optimization of the ZnO/Ag/ZnO system and the surrounding dielectric materials has been only incremental and has reached a limit today (Fig. (1)-c). Nowadays, the resistivity of a polycrystalline Ag 10-11 nm thick film in a coating with blocker is of about 4.2 $\mu\Omega$.cm at room-temperature, and of 3.6 $\mu\Omega$.cm after thermal treatment, *i.e.* significantly higher than the bulk value of 1.6 $\mu\Omega$.cm (Fig. (1)-c). This room for improvement drives on a deep understanding of the various actual contributions to the film resistivity. In a metal single crystal, the electrical transport can be hindered by scattering mechanisms on phonons and point defects. In the case of a polycrystalline thin film, where one dimension is of the same size of the electron mean free path, two additional scattering phenomena have to be taken into account, that at the grain boundaries and that at the layer interfaces. These mechanisms depend on the grain size, their relative orientation and the interface roughnesses. Shortly, these latter are related to the microstructure of the film, that in turn depends on the seed layer and the deposition conditions.

The present approach

Recent studies [3,4] at Aachen University have demonstrated that an improvement of the metal grain orientation, in-plane and out-of-plane (Fig. (2)), induced by a proper choice or growth of the seed layer, can help enhancing the conductive properties of the silver film. In this context, this work aims at understanding the relative role of interfaces and grain boundaries on silver film resistivity by focusing mainly on the crystalline texture induced by the ZnO seed layer. The simplest way to reproduce the c-axis fibre texture of sputtered ZnO and to obtain an

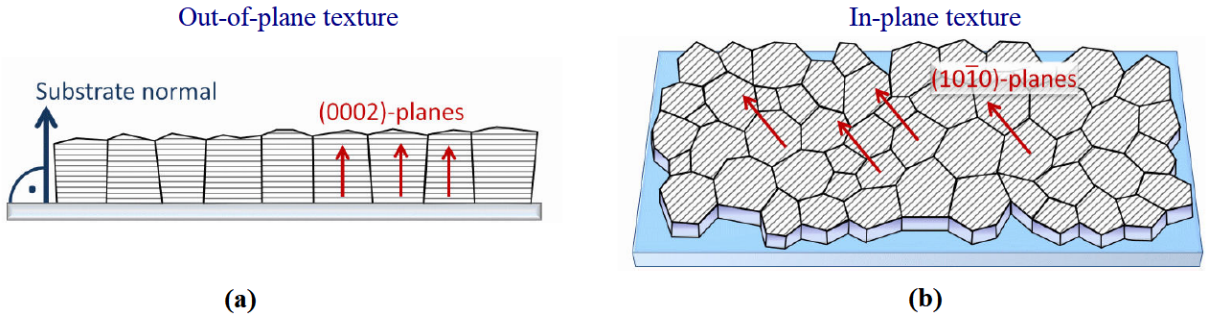

Figure 2 Sketch of oriented ZnO grains (a) along the perpendicular direction of the surface, the so-called out-of-plane texture, and (b) along the surface plane, the so-called in-plane texture [3])

.

in-plane textured silver film is to grow it on a ZnO single crystal of (0001) orientation. Due to its crystallinity, its very low surface defect density and its large terrace size compared to sputtered ZnO films, such a substrate can be considered as the ideal seed layer to favour an hetero-epitaxial growth. Therefore, prior to silver deposition by sputtering, an optimal surface preparation method of ZnO crystals has been developed in this work resulting in a highly biaxial textured silver layer. The emphasis was put on the role of the polar crystal termination (-Zn or -O) on the structural characteristics of the silver film. X-ray diffraction in various geometries combined with atomic force microscopy and transmission electron microscopy was intensively used to have a complete view of the microstructure of the metal (epitaxy, lateral/vertical grain size, intra-grain strain, mosaicity, degree of texture, film thickness, interface roughnesses etc. . .). These informations have served as a sound basis of the interpretation of the film resistivity. To disentangle the role of interface and grain boundary scattering mechanisms, the present work resorted to the analysis of the temperature dependence of film resistivity within 5 K and 300 K. A comparative study between the models of Fuchs-Sondheimer that considers only interface scattering and that of Mayadas-Shatzkes that also includes the role of grain boundary scattering was performed to pinpoint the major contribution to resistivity. Of course, the results obtained on model systems on single crystals were compared with those obtained for typical glass-based silver coatings that do not present an in-plane texture. The impact of a very thin additional ZnO buffer layer between the silver film and the single crystal substrate was also addressed.

The structure of the manuscript

This manuscript is divided into five chapters.
The first chapter gives an overview of all the theoretical background required to understand the present work. It starts with a reminder about the underlying concepts of thin film growth before describing the sputtering deposition method. After introducing the two materials of this thesis, namely Ag and ZnO, and in particular the question of polar termination of ZnO, the literature on the hetero-epitaxy in this system is then reviewed. The chapter ends up with a full description of the modellings of the electrical resistivity in metallic films, the Fuchs-Sondheimer, Mayadas-Shatzkes models and their variants. It is shown that their different temperature dependence allows for disentangling grain boundary and interface contributions in electron scattering.
The second chapter introduces all the experimental methods that have been used in the course of this thesis. It describes the employed substrates, the deposition chambers, the tools involved in the single crystal surface preparation (electron bombardment heating and Ar ion bombardment, low-energy electron diffraction and x-ray photoemission spectroscopy). Finally, the specificities

of all the used *ex situ* characterization techniques (X-ray diffraction, atomic force microscopy, transmission electron microscopy and 4-point resistivity measurements) are detailed.
The following chapter is dedicated to the industrial reference samples. The discussion starts with an investigation of the role and influence of the different layers in the stack on the structural and topographical properties of silver film. The chapter then focuses on the origin of the resistivity via fits of its temperature variation.
Chapter four deals with the growth of silver on ZnO single crystal substrates. It includes a section on the preparation methods applied to the substrate surface before the coating deposition. Then a full structural investigation of the biaxial textured silver film by x-ray diffraction based techniques is presented. Follows an analysis of the relative contribution of interface and grain boundary scattering mechanisms to resistivity with an emphasis on the possible correlations between structural characteristics and resistivity and a comparison with industrial references. The chapter ends up with the positive impact of annealing.
The next chapter follows closely the previous one as it deals with the tremendous improvement of the structural and electrical characteristics of the silver film induced by a thin ZnO buffer layer deposited at the surface of the crystal.
After an overall summary and conclusion, a prospective section is dedicated to some experimental results obtained by Ion Beam Assisted Sputtering (IBAS) technique, an innovative sputtering method used to grow textured films on an amorphous substrate.

Contents

Chapter 1

Concepts on thin film growth and resistivity

This first chapter gives an overview of all the background required to understand the experimental work performed during this thesis. After an introduction on the concepts of crystal growth involved in thin films, the sputtering deposition method and the underlying parameters that allow its control will be presented. Then the two main materials used in this work, namely ZnO and Ag, will be introduced. The emphasis will be put on the question of ZnO polarity and on the knowledge about their hetero-epitaxy. Finally, the chapter will conclude with a brief review of the various contributions to thin film resistivity and their modelling.

Chapter summary

1.1 Thin film growth concepts and mechanisms

A film is a bulk material which third dimension, the so-called thickness, can vary from a few atomic layers in the case of an ultra-thin film to several micrometres in the case of a coating. Although arbitrary, the distinction is somehow related to the additional properties that they confer to their substrate. These latter can differ from the bulk ones due to the reduced dimensionality or to the increased ratio of atoms at surfaces/interfaces. Because of their ease of manufacturing, thin films are used today in countless fields such as electronics, optics, protective coatings against corrosion or in harsh temperature and stress environment, medical applications and so on [5,6]. Their popularity is also due to the many advantages that accompany their use. These include their reduced manufacturing costs compared to bulk while maintaining attractive properties, the possibility of miniaturisation of systems, their reduced weight, and even the elaboration of new complex materials, not found in nature with new and specific properties. In the glass industry field which motivates the present study, thin films bring an added value to windows that can not be achieved by a change of glass composition ; thermal insulation or self-cleaning properties are two examples.

Given the paramount importance of thin films, models based on parameters related to the substrate and the methods of deposition have been developed over the past years to describe their processes of growth. The first approach that neglects transient phenomena relies on thermodynamic equilibrium of interfaces. But soon, it was recognized that the growth process is clearly an out-of-equilibrium and that kinetics plays a key role.

1.1.1 Thermodynamic point of view of thin film growth

To a large extend, the morphology of a thin film is determined by the initial conditions of nucleation, growth and coalescence of the first deposited layers.

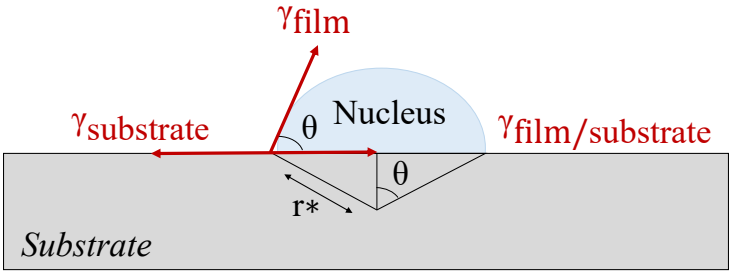

Figure 1.1 Scheme of the equilibrium shape of a supported particle as given by the surface/interface energies.

According to the classical theory of nucleation, the nucleation rate is defined from the supersaturation of the deposited element. Thermodynamically, this is translated through the balance between the surface energy of the film γ_{film}, that of the substrate $\gamma_{substrate}$ and that of the interface $\gamma_{film}/\gamma_{substrate}$, which characterize the film wettability and its nucleation mode [7]. For a nucleus at equilibrium, these quantities are linked by the Young-Dupré law defined as :

$$\gamma_{film/substrate} + \gamma_{film} \cos\theta = \gamma_{substrate}, \tag{1.1}$$

where θ is the contact angle formed between the nucleus of radius r and the substrate surface. Theoretically, the θ value ranges from 0 to 180°. The balance between bulk and surface/interface energies as a function of size r gives rise to a critical size r^* above which the nucleus becomes

stable and can grow. The condition gives a qualitative criterion, the so-called Bauer criterion, to predict the wettability and therefore the growth mode of the film [8] (Fig. (1.2)). If $\gamma_{film/substrate} + \gamma_{film} > \gamma_{substrate}$ or in other words $0 < \theta \leq \pi$ $(0 \leq \cos\theta < 1)$, the substrate is partially wetted and the film grows in a 3D mode, known as Völmer-Weber mode. This happens in particular if, for a weak $\gamma_{film/substrate}$, the film surface energy exceeds the substrate surface energy as in the case of a metal deposit on a semiconductor or dielectric (oxide or nitride) substrate. If $\gamma_{film/substrate} + \gamma_{film} \leq \gamma_{substrate}$, then the wetting is perfect ($\cos\theta \approx 1$ and $\theta \approx 0$). For a low $\gamma_{film/substrate}$, this case arises when materials have very close surface energies, such as metal-on-metal or semiconductor-on-semiconductor deposition. The growth mode is then layer by layer and is identified as the Franck-Van der Merwe type. A third growth mode, known as Stranski-Krastanov, is also distinguished by introducing in the energy balance the contribution of elastic distortions. At the first stages of growth, the stress build-up is not enough to overcome the favourable energy balance leading to a layer-by-layer growth as in the Franck-Van der Merwe case. However, after a given thickness, elastic distortions occurring in the layer lead to a change of growth regime with the formation of 3D islands that partially release the accumulated stress.

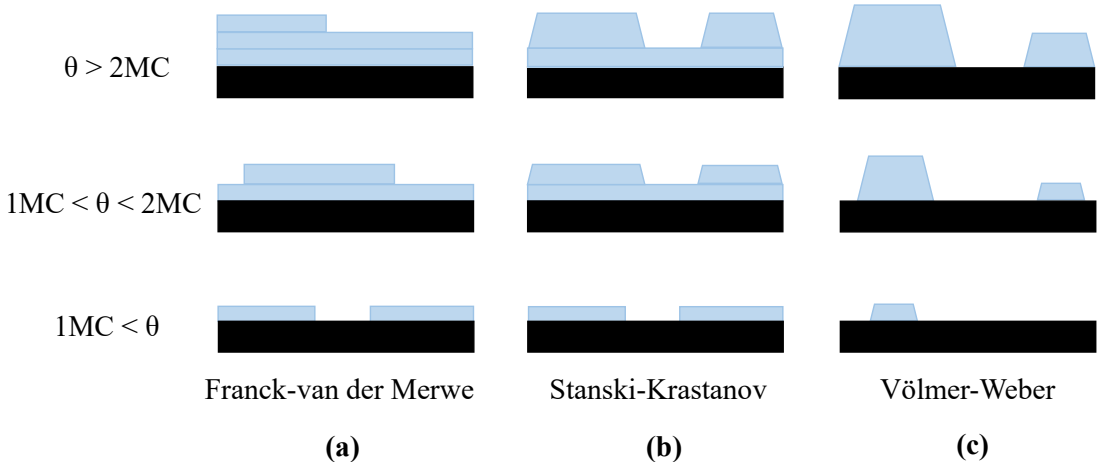

Figure 1.2 Schematic representation of the different growth modes according to the number of monolayers (ML) [8].

1.1.2 Kinetic approach of thin film growth

The thermodynamic approach is based on macroscopic considerations at equilibrium and it shows some limits in describing non-equilibrium, dynamic and energetic phenomena at the atomic scale. For this reason, kinetic models have been developed to account for the atomistic phenomena that happen during deposition. In particular, Venables [9] proposed to describe the nucleation/growth phases of a thin film in the Völmer-Weber case with a set of kinetic rate equations based on the following events (Fig. (1.3)) :

- the atoms adsorption at the substrate surface from an incident flux, becoming adatoms ;
- the diffusion of adatoms at the surface ;
- the adatom desorption ;
- the adatom aggregation to form nuclei.

According to their relative roles as given by characteristic energies at a given temperature and flux, these phenomena will impact the out-of-equilibrium growth process of the layer leading to a specific dependence of the surface density and of the size of clusters.

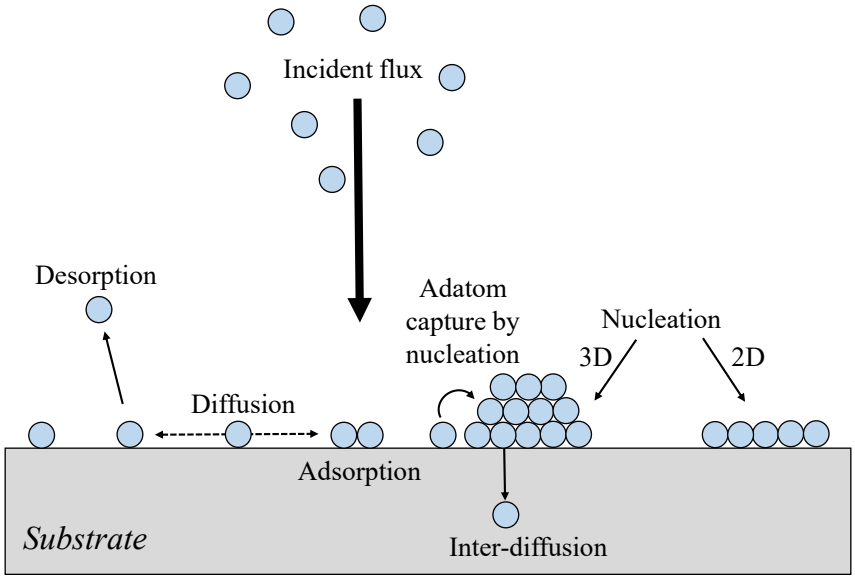

Figure 1.3 Scheme of the different atomistic surface phenomena occurring during layer growth and taken into account in the kinetic growth model.

Absorption and desorption

The formation of a layer starts with the arrival of a flux of atoms F at the surface of the substrate. The flux of incident atoms is characterised by the energy deposited per atom, expressed as :

$$E_{final} = E_{k_0} + E_p - E_{lost}, \tag{1.2}$$

where E_{k_0} is the atom kinetic energy at the source exit, E_p is the gained potential energy generated by the substrate attractive force and E_{lost} is the energy loss through the various collisions that atoms undergo on their way through the chamber. Depending on the E_{final} value, one can distinguish three types of bonds between the atom and the substrate. In the case of physisorption with a bond energy lower than ~ 1.0 eV, the atom is attracted by weak Van der Waals forces. Due to this weak interaction with the substrate, the particles can easily diffuse on the surface as potential barriers usually scale with the bond energy. At the opposite limit of chemisorption, the atom forms a strong ionic, covalent or metallic bond with the substrate (energy $\gtrsim 1.0$ eV). In this case, the atom is incorporated into the surface atomic structure. In the case of a large final kinetic energy greater than several tens of electronvolts, the atom can be implanted in out-of-equilibrium crystallographic position and lead to a cascade of atomic displacements. Therefore, E_{final} will drive to large extend the probability of sticking of the incoming atom (Fig. (1.4)). The type of bond of an adatom with the surface will also impact the probability of desorption. This phenomenon, which is concurrent to adsorption, is often neglected due to the high energy barrier to overcome once the adatom is accommodated on the surface [10]. It depends on the substrate temperature T_{sub}, on a characteristic desorption energy E_D and on an attempt frequency ν_0 (generally of $\sim 10^{-13}\text{s}^{-1}$) through an Arrhenius equation ;

$$F_{des} = n_1 \nu_0 \exp\left(-\frac{E_D}{k_b T_{sub}}\right), \tag{1.3}$$

with n_1 is the density of adatoms, k_b the Boltzmann constant and T_{sub} the substrate temperature.

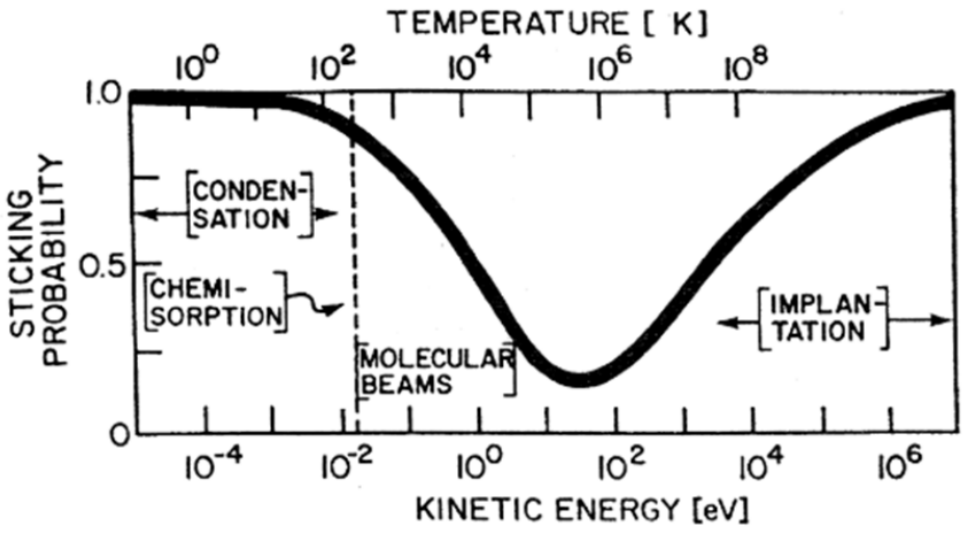

Figure 1.4 Sticking probability of an incident atom on the substrate surface as a function of its kinetic energy and the substrate temperature [7].

Diffusion

Again depending on the binding with the substrate, the adatoms (and even some clusters) absorbed on the surface can have enough energy to travel along the substrate thanks to their thermal agitation. The activation barrier for surface diffusion (Fig. (1.5)) is generally smaller than the atom/surface bond energy as some bonds with the surface are conserved when the particles diffuse from one position to another.

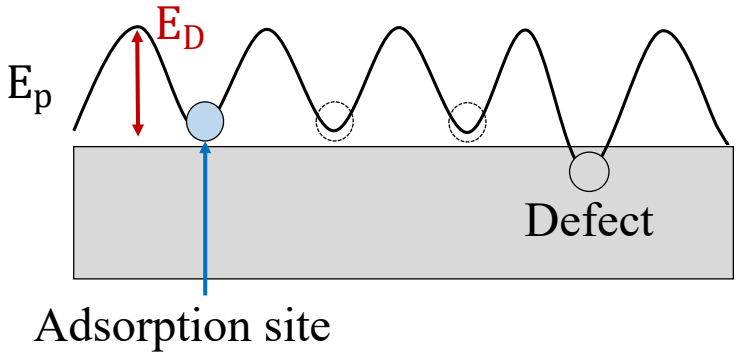

Figure 1.5 Schematic representation of an adatom diffusion and the involved energy barrier (red arrow). Defects as steps, corners, aggregates, adatoms, etc., are associated to higher coordination and therefore to a lower potential energy and more likely to bind with the diffusing adatoms.

The diffusion rate is given by :

$$D_s = D_0 \exp\left(-\frac{E_D}{k_b T_{sub}}\right), \tag{1.4}$$

with D_0 the diffusion coefficient at infinite temperature and E_D the activation energy to overcome from one equilibrium position to other. Based on Eq. 1.4, it is also possible to define a mean diffusion length with a $\sqrt{t}$ time dependence [11] :

$$\sqrt{\langle (L_{diff}(t) - L_{diff}(0))^2 \rangle} = 2\sqrt{D_S t}. \tag{1.5}$$

In case of a surface without defects, the adatom trajectory statistically follows a Brownian motion. In presence of defects (steps, corners, aggregates, other adatoms, etc.), the atoms are brought to bind to these energetically favourable sites where the atomic coordination of the adatom will be larger. Their diffusion can also be impacted by the kinetic energy of the incident species. If the atom keeps a part of its momentum after adsorption, the excess energy can be use to cross more easily the diffusion barriers [11]. A transfer of their momentum to the atoms or aggregates already present on the surface can even occur favouring the diffusion of the latter. These phenomena can notably lead to a redistribution of the sizes of the aggregates [12, 13]. At last, not only adatoms can diffuse but also large clusters.

Nucleation and growth : the rate equations

During the nucleation phase, the adatoms aggregate and form stable clusters thus increasing their density and consuming incoming atoms. Then, the formed stable clusters will grow by capturing diffusing species. Venables [9, 11, 14] developed a statistical description of these phenomena through a set of rate equations, the goal being to describe the time evolution of the density of stable clusters $n_x(t)$ containing x atoms (Fig. (1.6)). Thus $n_1(t)$ corresponds to the density of adatoms, $n_2(t)$ to the density of dimers, etc.... The evolution of $n_1(t)$ is given by :

$$\frac{dn_1}{dt} = F - 2\Gamma_1 - \sum_{x\geq 2} \Gamma_x, \tag{1.6}$$

where F is the incident flux, Γ_x is the frequency with which clusters of size x become of size $x+1$. By assumption, only the nuclei whose number of atoms is at least equal to i^* are stable. The smaller ones will decay. Hence, the time evolution of the density of the stable nuclei at the substrate surface is given by :

$$\frac{dN}{dt} = \Gamma_{i^*} = \xi_{i^*} D_S n_1 n_{i*}, \tag{1.7}$$

where D_S is the diffusion coefficient of adatoms and ξ_x the probability for a cluster of size x to grow by one atom. Furthermore, if only the stable islands are considered, Eq.1.6 can be rewritten as :

$$\frac{dn_1}{dt} = F - \xi_{i^*} D_S n_1 n_{i^*} - \overline{\xi} D_S n_1 N \tag{1.8}$$

where $\overline{\xi}$ is the average probability of a stable nuclei to capture an adatom.

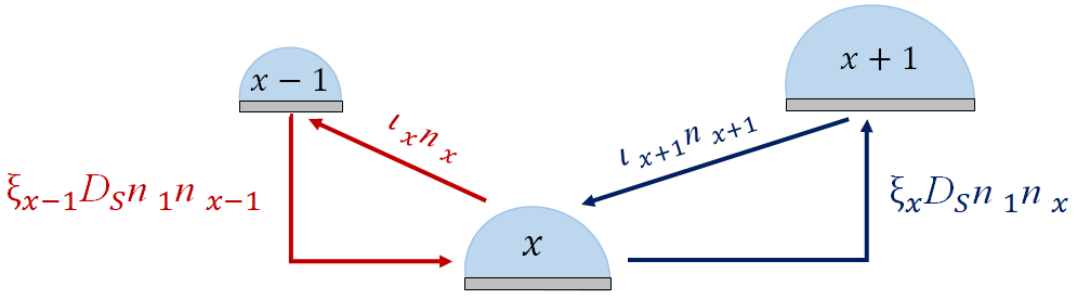

Figure 1.6 Evolution of the nuclei size during nucleation and growth. ι_x is the probability for a nucleus of size x to lose an atom. At the opposite, ξ_x is the probability to gain an atom.

The solution of Eq.1.7 and 1.8 allow to identify two regimes in the growth process. The first, known as the transient nucleation regime, is characterized by a high adatom density and an

increasing number of stable nuclei N. In this regime, an adatom is more likely to encounter another adatom than a nucleus. The second, identified as the steady state regime, is characterized by the growth of the stable nuclei only through adatom capture at constant cluster density, the so-called saturation density. As the flux of atoms is totally compensated by their capture, the concentration $n_1(t)$ is constant and becomes :

$$n_1 = \frac{F}{D_S \bar{\xi} N}, \tag{1.9}$$

which can be used to simplify Eq.1.7 to give the steady-state density of clusters :

$$N \approx \left(\frac{F}{D_S}\right)^{\chi} \quad \chi = \frac{i^*}{i^* + 2}. \tag{1.10}$$

The power law scaling of N with the ratio of flux F to the surface diffusion D_S shows that the density will increase with the flux and decrease with diffusion (and temperature). The critical size i^* (for homonucleation $i^* = 1$) depends on the geometry of the phenomena considered (adatoms diffusion, dimers diffusion, etc...). The rate equations of growth can be refined to include cluster diffusion and also heterogeneous nucleation on defects [15]. In the latter case, it was demonstrated that the saturation density is merely driven by the density of active defects for nucleation at the given growth temperature.

Coalescence and percolation

Following the steady state regime, the amount of stable nuclei decreases due to the joining of the islands, called coalescence [16–21]. Since the surface covered by the clusters increases, island growth by direct impact will compete with adatom diffusion. If the coalescence is fast enough to recover the equilibrium cluster shape as in the case of liquid droplets (Fig. (1.1)), the surface coverage will saturate and the growth will be self similar [16]. Sometimes secondary nucleation can happen in between particles. At the opposite limit of impeded coalescence, the surface coverage will increase and the particles will become worm-like with an increasing density of grain boundaries until percolation. Jeffers *et al.* [17] developed a capillary approach of coalescence, which however does not describe quantitatively the onset of percolation [22].

1.1.3 Structure zone model for polycrystalline films

In the case of 3D growth mode, typical of silver films growing on an oxide substrate as studied herein, when the density and the size of the islands are sufficiently large, interaction between particles can occur resulting in the previously described coalescence [16–21]. At the contact between two islands, a grain boundary (see Sec. (1.1.4)) forms since most of the time the crystal lattices of the two neighbours are not in registry.

In the case of low atomic diffusion at the surface of the islands, the grain boundary remains immobile through the growth process and the grain structure tends to become columnar. The structures will be characterized by a large out-of-plane size and, due to competing processes, an increasingly large in-plane diameter as further the grain grows from the substrate surface [21].

If the atomic diffusion is faster, several processes can alter the shape of the coalescing particles : (i) Ostwald ripening, (ii) sintering and (iii) cluster migration. The Ostwald ripening describes the decay of small islands in favour to larger ones via diffusion on the substrate surface. Driven by the minimization of surface free energy and the reduction of curvature, the phenomenon can occur even before the islands get into contact [7, 20]. The sintering process, on the other

hand, can occur when two islands are in direct contact and a neck is formed in between. As the chemical potential of the atom is related to the curvature, a mass transport will set up to reduce the surface area of the neck via bulk or surface diffusion, forming an intermediate shape between the islands [7]. Finally, the coalescence can happen through the random diffusion of the clusters themselves along the substrate surface [7, 20]

In addition to these mechanisms, grain boundary can have a limited mobility depending on the involved atom bonds. Grain growth can therefore occur by the continuous switching of bonds from one side of the gain boundary to the other. The mechanism is driven by the minimization of the grain boundary energy and it can take place also when the film is already continuous [19–21].

Based on these accounts, a structure zone model in polycrystalline films was developed [20, 23] to describe the evolution of the microstructure and the texture defined as the orientation distribution of the crystallites as a whole. A distinction is typically made between in-plane and out-of-plane orientation (see Fig. (2)) depending on the direction alignment of the crystallites. When a film grows with crystallites that are oriented in both directions, in-plane and out-of-plane, it said to be biaxial textured. The structure zone model is often drawn as a function of the homologous temperature T_{hom} expressed as $T_{hom} = \frac{T_{sub}}{T_m}$ where T_{sub} is the substrate temperature and T_m the melting temperature of the material. T_{hom} is a good descriptor of the activation energy of diffusion that scales with the material melting temperature [24]. As the film microstructure is mainly influenced by diffusion processes [19, 20], this qualitative classification is well suited for metals and not really for oxides for which mobility does not correlate with the melting temperature [24]. Furthermore, for sputtered films, diffusion is not only influenced by the substrate temperature but also by ion bombardment. Therefore, a quantitative link with T_{hom} will not be performed in the following discussion of the various zones.

Zone Ia

The zone Ia (Fig. (1.7)) corresponds to very low adparticles mobility *i.e.* very low surface diffusion or very fast deposition rate. Also known as the hit-and-stick growth scenario, the incident atoms that reach the substrate surface remain freezed at their arrival point. In the absence of diffusion, the films that grow in these conditions will show an amorphous-like structure. Vacancy defects are highly probable to occur. As a result, the density of the film is much lower than the bulk one.

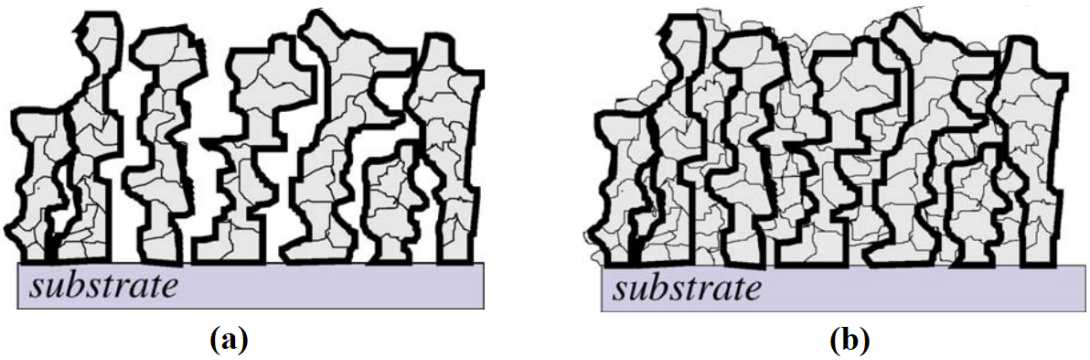

Figure 1.7 Sketch of the microstructure of a film grown under (a) *zone Ia* and (b) *zone Ib* [20].

Zone Ib

This zone (Fig. (1.7)) is characterized by an energetic particle bombardment filling the structural voids through knock-on events. The resulting films will show an enhanced density but still an amorphous structure.

Zone Ic

In this structure zone (Fig. (1.8)), adparticles have enough mobility to diffuse and nucleate on the substrate or film surface. Films grown under these conditions will therefore show a void-free compact crystalline structure. During the initial island phase, crystalline faceted particles are formed. The dominating facets correspond to the planes with the lowest perpendicular crystallographic growth rate. This is translated in a high lateral growth rate and therefore in the extinguished adjacent facets with high perpendicular growth rates (Fig. (1.8)).
For sputtered thin films, the perpendicular growth rates are determined by the sticking coefficient and the adparticle mobility of the facet. At low sticking coefficient, the probability for an adparticle to bond with the plane decreases, and with it, the growth rate. When the adparticle mobility on a facet is high, the diffusion length on the corresponding plane is very large. As a result, the adparticle can easily reach the edge of the facet and even overcome it, reaching an adjacent facet with a lower mobility. Less likely to return to the initial facet, the adparticle will contribute to the lateral growth, while keeping the perpendicular growth rate low.

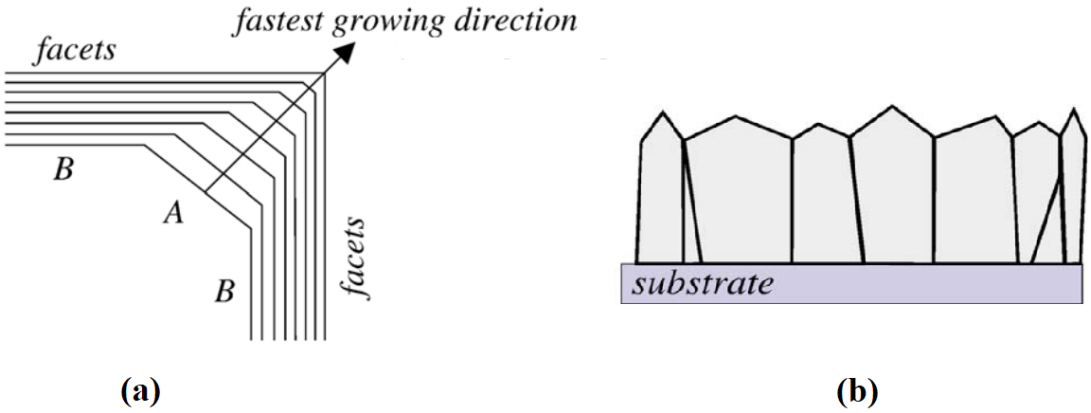

Figure 1.8 (a) Illustration of the facets evolution of a crystallite during its growth. In this example, plane A has a larger crystallographic growth rate than plane B, and thus disappears during the growth process. (b) Resulting microstructure for a zone Ic film [20].

The adparticle mobility and the sticking coefficient are influenced by the number of nearest neighbours that an adparticle will have on the corresponding facet. Higher is the number of nearest neighbours, lower will be the mobility. Therefore a higher sticking coefficient and perpendicular growth rate will be observed on dense planes.
In this zone, the diffusion length of the adparticles is limited to one grain. As no exchange of adparticles can occur between grains, the only competition in grain growth is through shadowing effects, independently of the crystal structure. Under these conditions, the resulting film will be characterized by a columnar structure but without a clear out-of-plane orientation of the grains.

Zone T

The zone T (Fig. (1.9)) is characterized by high mobility conditions, allowing the diffusion between grains of the adparticles. During nucleation, the randomly oriented crystallites are terminated by the planes with the lowest crystallographic growth rates. When two islands merge, an immobile grain boundary is created and as the film thickens, a competitive growth between the crystallites will take place, known as evolutionary selection or survival of the fastest [3]. Without limitations of the diffusion length, crystallites with the fastest growth rate perpendicular to the substrate will overgrow the slower ones (Fig. (1.9)-a). Generally, the highest perpendicular growth rate is associated to the crystallites with the most tilted facets with respect to the substrate surface. As a result, the final film will grow with a preferential out-of-plane orientation characterized by faceted V-shaped columns. At a certain critical layer thickness, represented by a dashed line in Fig. (1.9)-b, the overgrowth procedure ends and the out-of-plane texture quality does not improve with increasing layer thickness.
Nevertheless, in this zone, if the deposition is performed on an inclined substrate, an additional in-plane texture can also be induced. The mechanism is based on an anisotropic particle diffusion along the substrate surface and on an orientation dependence of the capture length of faceted crystallites. The higher growth rate is therefore associated to crystallites able to catch the largest ratio of the adparticle from the substrate, due to their favoured orientation. Following this process, biaxially textured films are obtained for large layer thicknesses [19, 20, 25, 26].

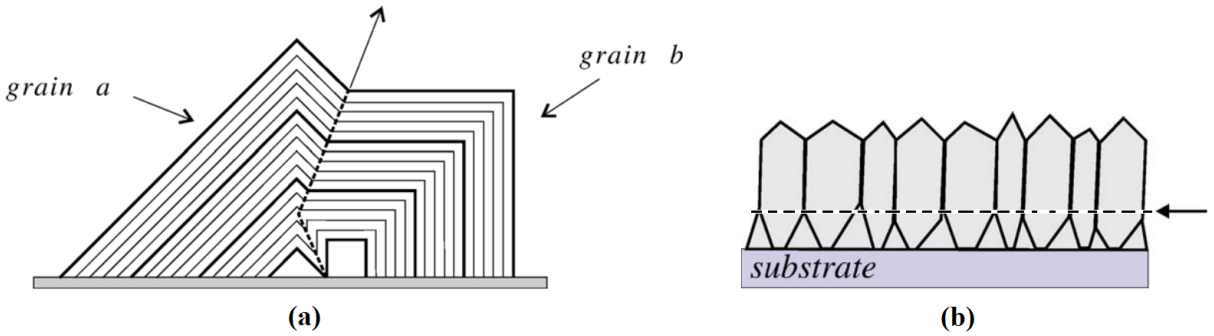

Figure 1.9 (a) Illustration of the overgrowth process of faceted grains. The grain with the most tilted facets (grain a) with respect to the substrate surface slowly covers the other grain (grain b). (b) Sketch of a zone T structure, characterized by V-shaped and faceted columns. The dash line indicates the film thickness at which the out-of-plane alignment is completed [20].

Zone II

This zone (Fig. (1.10)) is characterized by unlimited surface diffusion and additionally bulk diffusion. Here, ripening and grain boundary migration processes occur. The film microstructure will therefore be determined by energetics and consist of straight columns stretched along the whole film. From the initial stage of growth, the crystallites will grow facets corresponding to the lowest surface free energy and oriented parallel to the substrate surface. Thus the resulting film will present an out-of-plane texture already at small thickness.

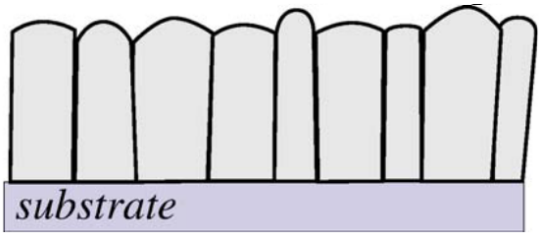

Figure 1.10 Sketch of the typical microstructure of a zone II film [20].

1.1.4 The notion of grain boundary

A grain boundary (GB) is planar defect that occurs where two crystallites of same crystallographic structure and composition but of different orientations meet. This type of defect appears during the growth phase of a film from the coalescence of two islands and leads to a narrow region of disorder limited to a few atomic planes on each side of the boundary. Depending on the misorientation angle that is formed between the two adjacent grains, it is possible to classify grain boundaries in two groups : (i) small angle and (ii) large angle GB (Fig. (1.11)).

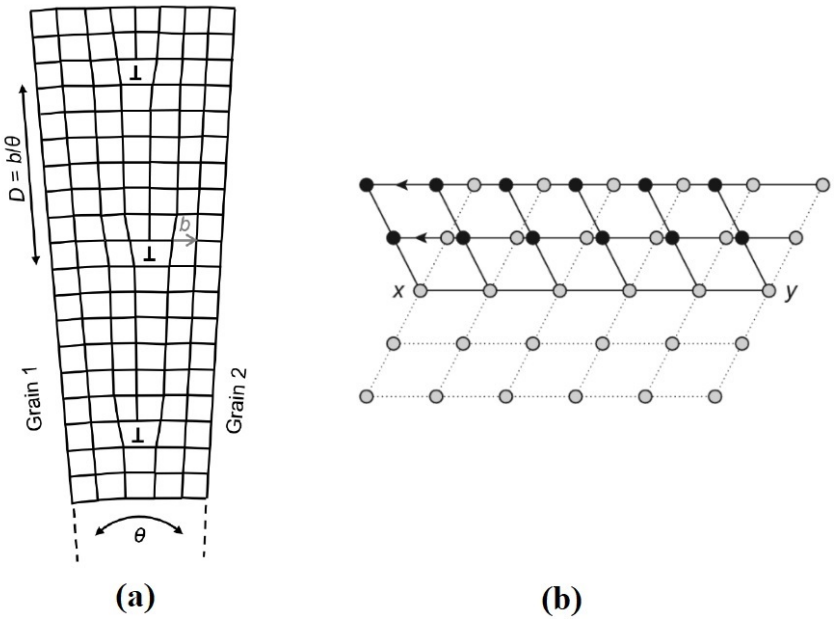

Figure 1.11 Examples of small angle grain boundaries : (a) a pure symmetrical tilt grain boundary can be described by an array of edge dislocations. $\theta \leq 10°$ corresponds to the tilt angle between the grains, while D is the distance between neighbouring dislocations [4] ; (b) arrangement of atoms in a twin related structure. x-y is the trace of the twin composition plane [27].

Small angle grain boundaries are simple defects usually consisting of tilt and twist orientation components giving rise to a mixture of different dislocations. For tilt angle lower than 10°, a grain boundary can be described as a stacking of step dislocations. Small twin boundary is associated to a cross grid of screw dislocations, resulting in grains separated by a rotation around the axis [4,27,28](Fig. (1.11)). In these configurations, the distance between two dislocation cores is

given by :

$$\frac{D}{b} = 2\sin\frac{\theta}{2} \approx \theta, \tag{1.11}$$

where b is the absolute value of the Burgers vector $\vec{b}$ of the dislocations inside the GB, perpendicular to the GB, and θ the tilt angle [29].

When θ is higher than 10°, the cores of the dislocations start to overlap, and the grain boundary cannot be considered as a small angle GB. Indeed, as the grain misorientation increases, the density of the dislocation increases linearly, resulting in a more complex structure. The interface between two grains is much more disordered and its description becomes more complicated. The coincidence site lattice (CSL) is a model used for the identification of large angle grain boundaries that form between two grains that have overlapping lattice points. Let us assume that two grains are misoriented by a chosen angle θ around an axis o. When superposing these crystals, some atomic sites coincide. Spread regularly, they create a superlattice called coincidence site lattice. Fig. (1.12) reports a simple 2D example while in a 3D cubic structure, CSL is generally tetragonal [28]. CSL are classified by the reciprocal value of the density of coincidence site $\sum$. $\sum$ is a number corresponding to the volume of the unit cell of the CSL divided by the volume of the unit cell of the crystal. The lower the number, the more coincidence points the grain boundary has (e.g. twin grain boundaries are characterized by $\sum$=3).

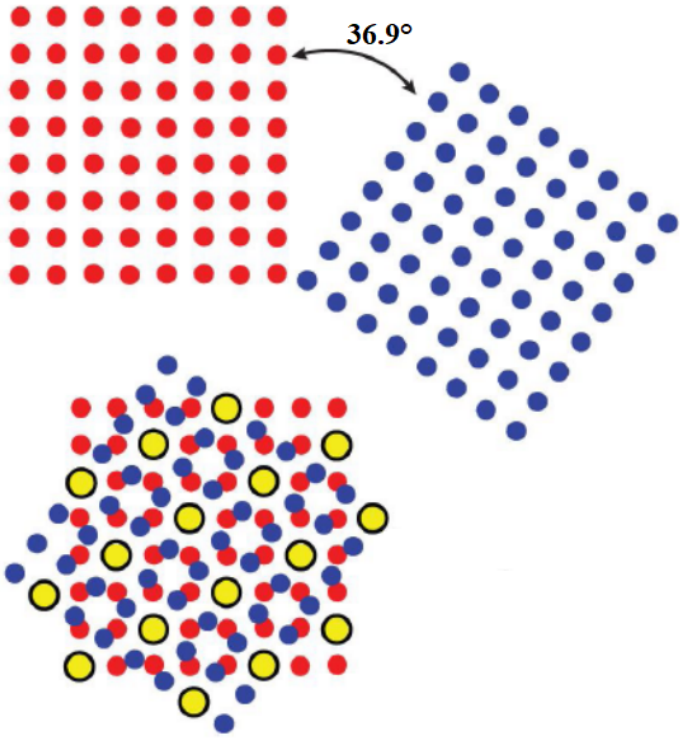

Figure 1.12 Model of a coincidence site lattice defect. The sketch represents the $\theta = 36.9°$ rotation around the [001] axis of two (001) cubic planes. The yellow points indicate the coincidence site lattice. The grain boundary is classified as a $\sum = 5$ [30].

The formation of small or large angle grain boundaries, although strongly dependent on kinetics, is based on energy minimization considerations. Usually, small angle grain boundary and those with low $\sum$ values have a lower energy and therefore are preferentially formed. The energy of a

small angle grain boundary is expressed as :

$$E = E_0\theta(A - \ln\theta) \tag{1.12}$$

where E_0 and A are parameters depending mainly on the grain boundary. On the other hand, the relation between the $\sum$ value and the grain boundary energy becomes non linear. [29].

As other defects, grain boundaries can hinder the electrical conductivity of a material ; their impact is more important for large misorientation [31]. This is in agreement with the increasing dislocation density which act as electron scattering centres. Smaller angle grain boundary will therefore result in lower resistivity, while larger angle grain boundary will be associated to higher values. Nevertheless, when large angle grain boundaries form CSL, the resistivity significantly drops to a value that can even be lower than that of small angle GB. This behaviour has been experimentally observed in aluminium bicrystals [31] and in copper nanowires [32, 33] as well as in the theoretical studies of Cesar *et al.* [34]. In silver, the resistivity associated to a low angle grain boundary is estimated to $0.7\,10^{-12}$ $\Omega.\text{cm}^2$, while for large grain boundary the value is almost five times higher [35]. As explained below, the Mayadas-Shatzkes model accounts for the role of GB on thin film resistivity through an effective reflection parameter R for electrons. Intuitively, R should scale with the misorientation angle of the GB.

1.2 The sputtering deposition

Thin film growth can be carried out by a wide variety of techniques that can be divided into two major categories depending on the way material is brought to the surface. In Chemical Vapour Deposition (CVD), precursors in gas phase are decomposed at the substrate surface thus providing matter for the growing film. In Physical Vapour Deposition (PVD), the vapour of the material is condensed at the substrate surface. It can be provided by evaporation from an heated crucible or by sputtering a target. Sputtering deposition, first carried out in 1852 by Grove, is today one of the most widely used techniques, in particular in the glass industry. The popularity of this technique is linked (i) to its versatility [7], which allows the deposition of a wide range of materials (conductors, dielectrics or insulators) on a variety of substrates [36, 37], and (ii) to its high performances, characterized by rapid ($\sim 10^{-1} - 10$ nm.s^{-1}) and homogeneous depositions over large-scale surfaces (up to 18 m^2).

1.2.1 The sputtering process

The magnetron sputtering deposition (Fig. (1.13)-a) is a process whereby a gas of atoms, ions or molecular clusters is emitted from a solid material, called target, due to the bombardment by a beam of energetic particles. To perform a deposition, a rare and chemically inert gas, usually argon, is introduced in a vacuum chamber. A negative electrical potential is then applied to the cathode, causing free electrons to accelerate away from the target. The collisions between the electrons and the gas provoke the ionization of the gas atoms so initiating a plasma composed of neutrals, ions and electrons. A magnetic field created by permanent magnets placed under the target confines the electrons of the initiated plasma close to the target and favour the plasma self-supply, its stability and therefore its efficiency (when a plasma is ionised it becomes denser and thus increases the removal of atoms from the target). In parallel, the cations are accelerated towards the target by an applied electric field. The accelerated ions collide with the atoms on the surface of the target transmitting their momentum and leading to the atom sputtering process. The collisions cascade (number of atoms involved and ejection angle) occurring at the

target, is defined by the incident energy of the cations, during the first collision, and the mass of the atoms involved. Several sputtering regimes can be identified as a function of the kinetic energy (Fig. (1.13)-b) : (i) the simple or direct collision, (ii) the linear cascade and (iii) the spike regime. Following the collision model formulated by Sigmund *et al.* [38], the sputtering yield can be expressed as :

$$Y = \frac{3}{4\pi^2}\alpha\frac{GE_{ion}}{U_{target}}, \tag{1.13}$$

where E_{ion} is the incident ion energy, G is the energy transfer factor during an elastic collision between two atoms, U_{target} is the binding energy of the target material and α is a dimensionless function depending on the ratio between the mass of the ions and the mass of the atoms of the target. For an efficient sputtering, the incident energy of the ions needs to be high. The atoms are then ejected from the cathode, with an angular distribution defined by the incident energy of the ions [20], and are guided towards the substrate surface by the potential difference established between the cathode and the substrate.

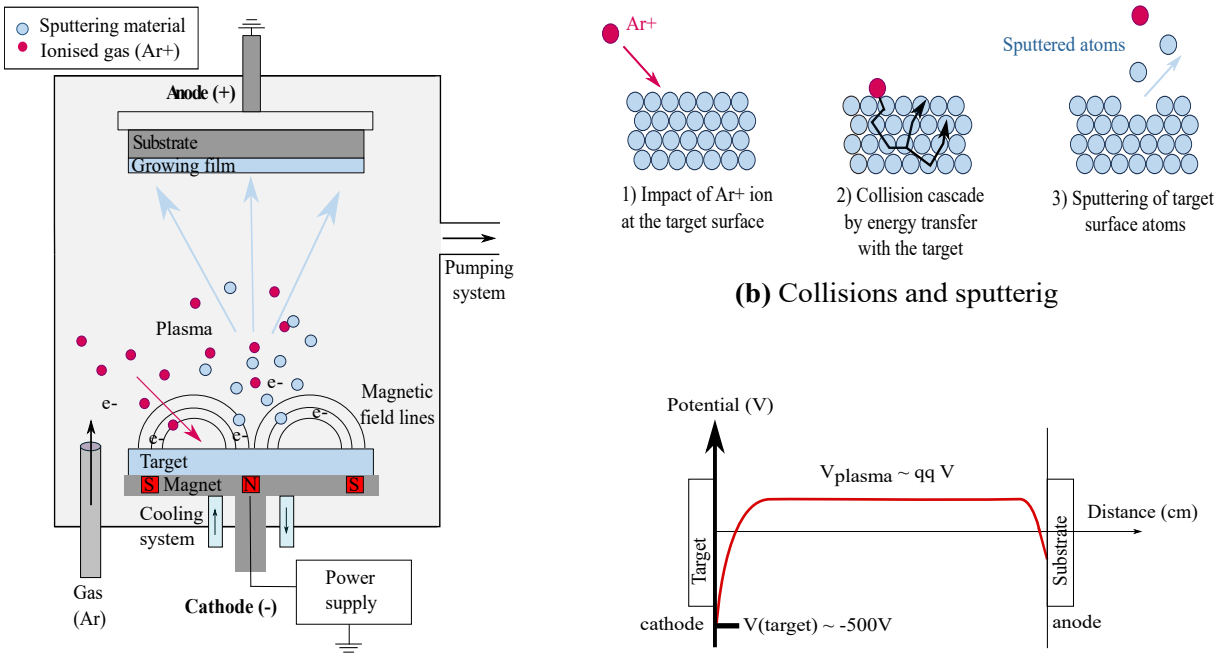

(a) Magnetron sputtering

(b) Collisions and sputterig

(c) Electronic potential evolution

Figure 1.13 (a) Schematic principle of the magnetron sputtering process. (b) Collision cascades during the impact of the incident ionized atoms on the target allowing the removal of the atoms to be deposited. (c) Anode-cathode potential difference helping to guide the sputtered atoms towards the substrate [39].

1.2.2 The deposition parameters

In the sputtering deposition, the chemical (nature and composition) and physical (microstructures) characteristics of a deposited layer is controlled by a series of tunable parameters which include : (i) the pressure, (ii) the nature of the gas, (iii) the target and the substrate, (iv) the type of source power, (v) the target/sample bias, (vi) the substrate temperature and (vii) the system geometry. These interconnected factors play an extremely important role in the growth of the film ; their impact will be briefly discussed in what follows.

The deposition pressure

The value of the deposition pressure is closely related to the density of the plasma. When the pressure is low, there is a sharp decrease in the number of plasma ions and in the current at the cathode. At constant power, this has the effect of increasing the cathode potential, the resulting electric field and so the energy of the sputtering ions [40]. On the other hand, however, due to the drop of the plasma density, it also leads to a reduction in the sputtering rate. When the pressure is increased, the number of ions increases, and with it the probability of collisions between species in the gas phase. This results in a shorter mean free path. A change is also observed in their angular distribution, varying from a ballistic regime of highly directional distribution to a intermediate regime of multi-directional distribution. At very high pressures (> 0.13 mbar), the number of collisions at the exit of the target becomes so large that it leads to a consequent decrease in the deposition rate [41]. Due to collisions with the gas and a reduced mean free path, sputtered species are more thermalized at high pressure. The choice of this parameter is therefore a compromise that should reconcile the deposition rate, the energy of the species and their angular distribution. Usually, the sputtering depositions are performed in a pressure regime of $10^{-3} - 10^{-2}$ mbar.

The deposition gas

Compounds can also be deposited via reactive sputtering. In this process, a reactive gas, typically oxygen or nitrogen, is introduced in the chamber and added to the neutral gas. The atoms from a metallic target chemically interact with the gas and form compounds such as oxides or nitrides. These conditions can also be used to enrich already oxidised (ZnO:Al) or nitrided (SiN_x) materials. The process can therefore be used to control the oxidation state of the film and thus to play with its microstructure. In reactive sputtering, the generation process of species and compounds is quite complex and depends on the inert/reactive gas ratio [42]. The transition from metal to compound deposition is described by an hysteresis curve on the evolution of the deposition rates, the chamber pressure or the discharge voltage (Fig. (1.14)) [43]. At low reactive gas flow, the gas (O_2, N_2) is completely consumed by adsorption throughout the chamber, before it can react with the metal target. The atoms are therefore deposited in a metallic phase under pure rare gas. As the reactive gas flow increases, a reaction with the target surface atoms is triggered. In this transition phase, the compound is only partially formed, and the reaction between atoms and gas continues at the substrate surface or during the transport between the target and the substrate. As a result, the monitored parameters remain almost constant. At the substrate surface, the combined kinetic effects will influence the energy of the arriving species, their adhesion and then their mobility. At sufficiently high gas flow, all surface target atoms can interact with the reactive gas to form the compound that is sputtered on the substrate. In this phase, known as target "poisoning", the compound covers the whole target surface, leading to a pressure increase and a significantly reduction of the discharge voltage and deposition rate.

The power supply

The type of power supply applied at the cathode can also have a strong influence on sputtering process with a direct impact on the growth rate and the deposited species energy. The power source is generally chosen as a function of the nature of the target. Conductive materials, such as metals (e.g. Ag) or doped insulating materials (e.g. ZnO:Al), are generally deposited using a direct current power supply. For dielectric insulators, on the other hand, the use of radio frequency or DC-pulsed power supplies is more appropriate. This limits the build-up of charges on the surface of the target, due to its insulating nature, and allows a constant deposition. The

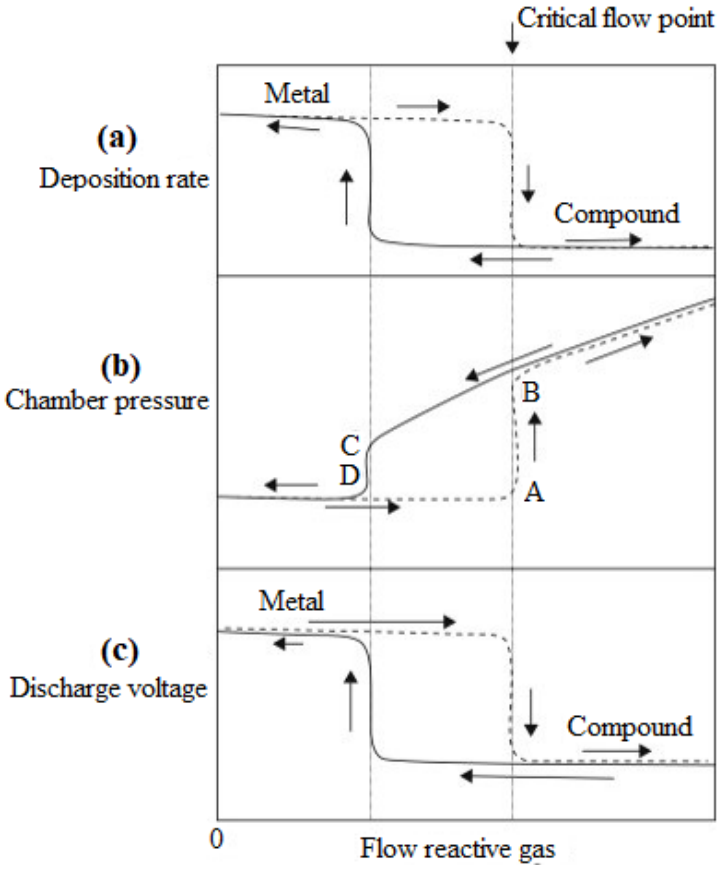

Figure 1.14 Hysteresis cycle observed during a reactive sputtering deposition process. The transition from metal to compound deposition is monitored as a function of (a) the deposition rate, (b) the chamber pressure and (c) the discharge voltage [44].

choice of the power supply affects the layer microstructure in terms of grain size, crystallinity and even composition [45]. For instance, the power applied to the cathode allows to increase the energy of the incident ions and thus enhances the sputtering efficiency and the energy of the sputtered species [40]. Hence, at higher power, the deposition rate increases.

The target atom kinetic energy

The energy at which the sputtered atoms leave the target determines their behaviour at the substrate surface. Three main processes can be identified : (i) the atom condensation, (ii) the atom implantation or (iii) the re-sputtering of the deposited layer leading to the backscattering of the impinging atoms. At low energy (< 0.1 eV), the atoms are absorbed on the surface at the position of their arrival. From there, they can self-diffuse on the surface to find a final adsorption site. For more energetic atoms ($0.1 - 1$ eV), part of the energy is used to directly diffuse at the substrate surface (so-called transient diffusion), part is dissipated in the substrate as thermal energy. At high energies ($1 - 100$ eV), the re-sputtering of the deposited layer can take place and thus a decrease of the deposition rate is observed. Finally, at very high energies (> 100 eV), atoms can implant themselves in the already deposited layer.
Nevertheless, the energy of the deposited species can be extrinsically modified by fixing the potential of the sample holder. By polarizing the substrate with a negative potential V_b, at an absolute value higher than the floating potential V_f, it is possible to increase the cation energy

by $-e(V_f - V_b)$ (Fig. (1.13)-c). If, at the opposite, the substrate is positively polarized, it will attract the electrons and anions. This results in the intensification of the substrate electronic heating, which favour surface diffusion. In DC mode, the species are not strongly ionised, and the effect remains weak.

The substrate

The substrate has a strong influence on the growing film. As shown at the beginning of the chapter, the layer wetting and therefore the observed growth mode is governed by the involved surface and interface energies. Substrate roughness impacts diffusion length like temperature [46, 47]. Deposition on a heated substrate favours recrystallization. Substrate crystallinity drives to a large extend the crystallographic orientation of the deposit, the so-called epitaxy. Finally, the motion of the substrate during sputtering deposition can modify the final crystallinity through shadowing effects [48].

1.3 The materials of this study : zinc oxide and silver

1.3.1 Zinc oxide (ZnO)

ZnO structure

Zinc oxide (ZnO) [49], known also as zincite in its mineral form, is an inorganic material with a wide range of applications. Classified as a II-VI-semiconductor, ZnO is characterised by a direct band gap of ~ 3.4 eV and good optoelectronic properties in the ultraviolet region and a volumic mass of 5.61 g/cm^3. ZnO has been observed in three different crystalline structures (Fig. (1.15)) : the predominant hexagonal wurtzite and the metastables zinc blende and cubic rocksalt structures [50]. Under ambient conditions, only the wurzite form is thermodynamically stable. The

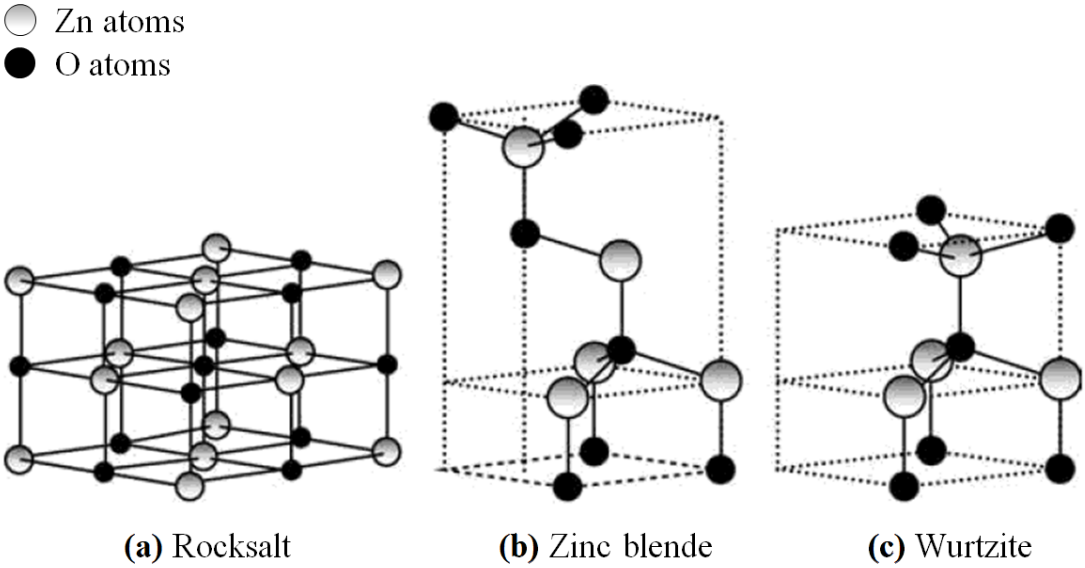

Figure 1.15 Stick-and-ball representation of the three main ZnO crystal structures : (a) rocksalt, (b) zinc blende and (c) wurtzite [51].

hexagonal wurtzite structure belongs to the P6$_3$mc space group, corresponding to a stacking sequence ABABAB of Zn and O layers along the $\vec{c}$ axis. The equilibrium lattice constants are

a = 3.25 Å and c = 5.21 Å [52]. In this configuration, each Zn^{2+} cation is tetrahedrally coordinated by sp^3 hybridization to four O^{2-} anions. However, due to the high electronegativity difference between the two ions, the Zn-O bond is partially (55 %) ionic. This ionic character, combined with the crystallographic anisotropy of the wurtzite, results in a natural electrical polarity along the $\vec{c}$ axis. The polarity confers to the material strong piezoelectric properties and a different (0001) plane termination. Zn- or O-terminated (0001) surfaces will therefore differ in their morphology, impurity incorporation, surface/interface electronic structures and reactivities [53] (see below).

Chemical symbol	ZnO
Crystal structure	Hexagonal (space group $P6_3mc$)
Lattice parameter	$a = 3.25$ Å ; $c = 5.21$ Å
Volumetric mass density	5.61 g.cm^{-3}
Surface energy	(0001) 1.59 J.m^2 $(11\bar{2}0)$ 1.97 J.m^2 $(10\bar{1}0)$ 3.35 J.m^2
Poisson ratio	0.36
Band gap	3.4 eV
Film out-of-plane orientation	generally (0001)

Table 1.1 Summary of the main ZnO material properties [3, 52, 54, 55].

ZnO applications

Transparent in the visible range but with a good electrical conductivity once doped, ZnO has received an increasingly interest as a transparent conductive oxide film (TCO) for solar cells, flat panel displays or other applications for electronic devices. Through stoichiometry intrinsic defects, ZnO develops a natural n-type semiconductor tendency [49, 54, 56]. The main defects correspond to zinc (V_{Zn}^{2-}) or oxygen vacancies, in a neutral or doubly positively charged form (V_O^0 and V_O^{2+}), but interstitial Zn atoms have also been reported [57–59]. Their associated energies of formation depend on the ZnO growth conditions, O-rich or Zn-rich. Although the origin of the intrinsic n-type behaviour of ZnO is still subject to debate, it is generally assigned to O vacancies and interstitial Zn as well as unintended hydrogen incorporation [60]. Extrinsic doping via an element belonging to the III group such as Al or Ga is also possible. The dopant with a formal charge 3+ replaces a Zn^{2+} cation enriching the system with a weakly bonded excess electron which can be easily excited into the conduction band. An other possibility to achieve n-type conductivity is to replace oxygen atoms by a group VII element like fluorine. Improved conductive films with a low resistivity but still a high transparency, such as Al-doped ZnO (ZnO:Al or AZO) become therefore valuable low cost candidates to replace the more common TCO indium tin oxide (ITO) [61]. ZnO:Al films are also presently used in the fabrication of silicon-based thin film solar cells as a transparent front electrode. There has been some attempts to fabricate p-type doped ZnO films [54, 56, 62]. However, due to its native defects that act as electron donors, the hole concentration achieved in the film is rapidly compensated [63]. Due to the piezoelectric properties of the material, ZnO is also used for sensors and surface acoustic wave devices [61], such as GHz frequency filters in the telecommunication industry. The large exciton binding energy of 60 meV allows the material to have bound excitons at RT (300 K - 26 meV), hence to be a suitable option for ultraviolet laser diodes since it promotes a significant population inversion. In this study, ZnO has been investigated due to its implication in low-emissive and solar control coatings as a seed layer for the growth and crystallisation of Ag thin films.

ZnO surface polarity

The wurtzite structure is characterized by two polar surfaces, the ZnO(0001)-Zn and the ZnO $(000\bar{1})$-O basal planes. The prism faces, e.g. $(10\bar{1}0)$ and $(11\bar{2}0)$, at the opposite, do not bear electrical charges since they contain an equivalent number of Zn and O atoms. The dipole moment along the $\vec{c}$ axis generates an electrostatic potential that scales with the thickness of the crystal and leads to an unstable (0001) surface with a diverging energy [64–66]. In an attempt to heal this polar electrostatic catastrophe, various charge compensation mechanisms via removal/addition of compensating changes can take place. The occurrence of a particular process will depend on the thermodynamic conditions *i.e.* the temperature and the environment but also on the surface termination of the sample. Healing processes include [64–67] :

- electron transfer from one face to the other ;
- atom removal and formation of vacancies, possibly leading to structure relaxation and reconstruction ;
- adsorption of foreign atoms or compounds, often corresponding to hydrogen via hydroxyl groups or even metallic films ;
- nano-faceting along the non-polar orientations ;
- change of atomic structures (graphitic or hexagonal boron-nitride (h-BN)) or uncompensated polarity as observed in ultra-thin oxide films.

Upon annealing under ultra-high vacuum conditions at moderate temperature (<1000 K), the ZnO(0001)-Zn surface has been proven to stabilize through the formation of nanoscopic triangular islands and pits (Fig. (1.16)) of half-unit cell height that are successively rotated by 180° [68, 69]. These features are due to Zn-vacancies required to compensate the charge of the polar surface. Their edges are oriented along the [100] directions and are therefore terminated only by anions or cations giving them a polar character [70]. At higher annealing temperature (>1300 K) under vacuum, the surface is stabilized by a complex interplay between triangular structures and faceting leading to highly ordered step arrays with edges exhibiting $\{10\bar{1}0\}$ nanofacets [71]. Surface reconstruction through hydrogen adsorption can also occur at the ZnO(0001)-Zn surface but this requires special wet chemical preparation methods with a hydroxide coverage that depends strongly on the chemical environment. After thermal treatment in dry and humid oxygen atmosphere, large scale terraces replace the triangular pits/islands typical of the ZnO(0001)-Zn surface [72, 73].

This triangular-like pit reconstruction has not been observed at ZnO(0001)-O terminated surfaces by near-field microscopy. First, ZnO(0001)-O surface has been proposed to stabilize through a (1×3) reconstruction via the adsorption of hydrogen, leading to an OH-covered surface [74, 75]. At the opposite, Lindsay *et al.* [76] claimed a possible (1×1) unreconstructed surface free of OH groups after high temperature annealing (1200-1370 K) under vacuum. More recently, combining high resolution scanning tunneling microscopy (STM) and non-contact AFM (Fig. (1.17)), Lauritsen *et al.* [77] revealed a (1×2)- H covered surface at room temperature, in agreement with polarity healing rule. With the increase of temperature, the surface transformed in a (5×5) honeycomb structure, in which the absence of 11 O atoms and 7 Zn atoms is compensated by 5 OH groups and a (2×2) termination constructed theoretically on the same principle of atom removal.

Despite numerous works [74], the atomic scale mechanisms of polarity healing of the basal ZnO surfaces are still today a source of debate. From the research carried out to date, it is clear that temperature, environment and hydrogen play an important role in it.

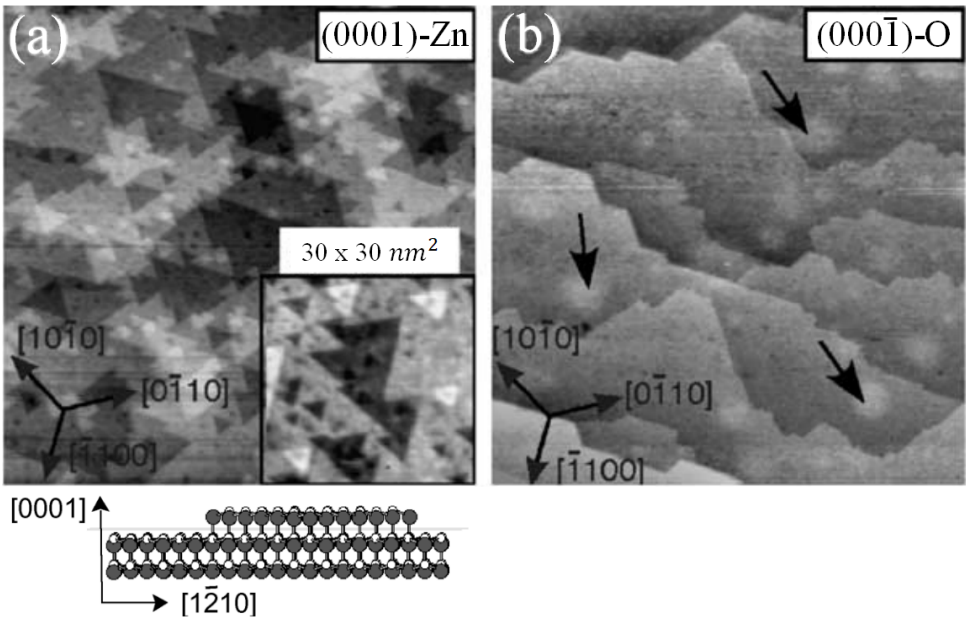

Figure 1.16 STM images ((200 × 200) nm) of the ZnO(0001) surfaces taken with tunnelling parameters $V_B = +2V$ and $I_t = 1.5$ nA. (a) The Zn-terminated ZnO(0001) surface is characterized by triangular islands with monoatomic step height. (b) The O-terminated (000$\bar{1}$) surface exhibits double-steps oriented at 120° [68].

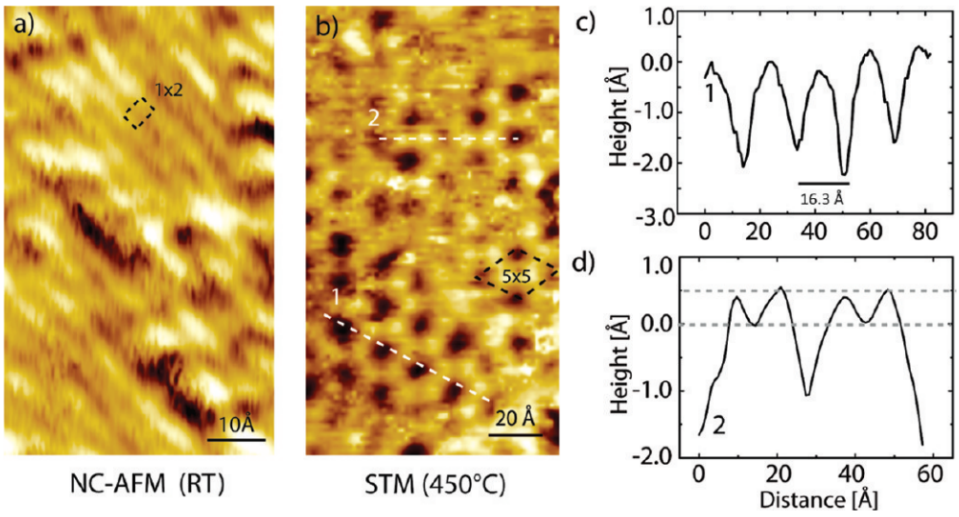

Figure 1.17 High-resolution images of the O-terminated ZnO(000$\bar{1}$) surface (a) acquired at room temperature via non contact-AFM showing the (1 × 2)-H reconstruction (b) via STM at 450°C showing the honeycomb (5 × 5) reconstructed structure. The dashed line corresponds to the line scans reported in (c), scan 1, and (d) scan 2. The first illustrates the 16.3 Å periodicity of the (5 × 5) unit cell and the 2.1 Å depth of the dark holes. The second represents the corrugation across a pair of protrusions [77].

ZnO thin film

As a thin film, ZnO can be grown using numerous techniques [49, 54, 56] including : sol-gel pro-

cesses, chemical bath deposition, atomic layer deposition, E-beam evaporation, metal-organic chemical vapour deposition, pulsed laser deposition, ion-beam sputtering and the industrial most relevant magnetron sputtering deposition [3].

During sputtering, the substrate is unintentionally heated by the plasma discharge. Consequently, zinc oxide films, deposited with this technique are already crystalline when deposited at room temperature. Due to a self-texturing mechanism, the film grows with a pronounced c-axis out-of-plane texture, so that the (0001) planes of the different crystallites are mostly aligned parallel to the substrate surface. The driving force behind the mechanism is linked to a preferred nucleation of this orientation in the initial growth stage of the film governed by the minimization of the surface energy. The self-texture is principally influenced by two deposition parameters : the energetic ion bombardment and the stoichiometry. It has been proven [3, 78], that simultaneous ion bombardment (xenon, argon or oxygen) during ZnO growth can significantly enhance the out-of-plane orientation quality of the film or even induce a biaxial texture. At the opposite, growing the film in an oxygen deficient environment will worsen the out-of-plane texture [79–81]. In addition to the growth parameters, the additional mobility induced by thermal treatment, during growth or post-deposition, has also an important impact on texture. By allowing to cure lattice defects and to favour a given orientation at the nucleation stage, temperature can also be used to support the formation of an out-of-plane textured film. It was also shown that the orientation of the film related to polarity, *i.e.* of the $\vec{c}$ axis (+c or -c), can be determined from the analysis of the valence band in photoemission [82, 83].

The sputtering process, reactive or not, can induce also a compressive stress in the ZnO film [4, 84–86]. Under energetic particle bombardment, ions and/or atoms can be incorporated within the film by knock-on implantation generating a compressive stress in the layer. The lattice freely expand along the $\vec{c}$ axis perpendicular to the substrate surface leading to a tetragonal-like distortion [87, 88]. The elastic response of the film to the stress is determined through Poisson ratio ν. In the case of an isotropic biaxial stress, the equation is given :

$$-\frac{2\nu}{1-\nu} = \frac{(c-c_0)a_0}{(a-a_0)c_0}, \tag{1.14}$$

where ν equal 0.36 for ZnO [89], a and c are the lattice parameters of the strained system and a_0 and c_0 are the equilibrium bulk lattice constants. For a textured film, the in-plane $\varepsilon_{11} = \varepsilon_{22} = \frac{a-a_0}{a_0}$ and the out-of-plane $\varepsilon_{33} = \frac{c-c_0}{c_0}$ strains can be determined via the variation of the lattice parameter constants that can be estimated through X-ray diffraction. For ZnO layers, the phenomenon has been attributed to the influence of negative oxygen ion bombardment during the sputtering process [4, 84, 86, 89, 90]. These ions are created at the target surface and accelerated towards the growing film, with energies of over 100 eV. Their impact can therefore be reduced by controlling the oxygen bombardment during deposition through the pressure and/or oxygen content, by increase the target to substrate distance, by using a shield on the trajectory of high energy oxygen ions or by using a new non-eroded planar target. The target age has a strong influence on the trajectories of the accelerated oxygen ions [91] as during the sputtering process, a pronounced erosion trace is created at its surface (Fig. (1.18)). This topographical modification induces a variation of the electrical equipotential planes orientations, which follow the wrinkled shape of the erosion trace. Since the oxygen atoms are accelerated perpendicular to these planes, their trajectories are altered with the age of the target. For an highly eroded target, the oxygen ions bombardment concentrates above the centre of the target. At the opposite, in the case of a new target, where the electric field lines are maintained perpendicular to the target surface, the area of maximum bombardment corresponds to the region above the race-track. In

a reactive deposition, the target age can therefore influence the quality and the microstructure properties of the growing film.

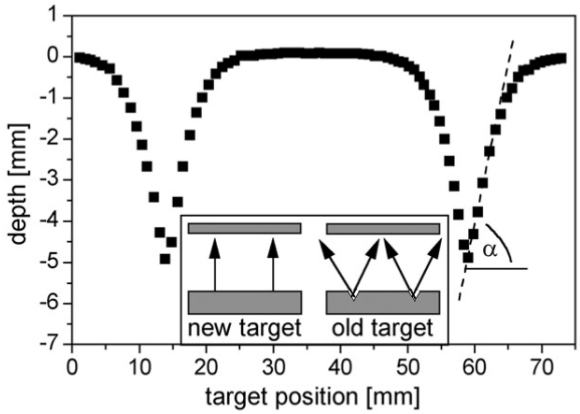

Figure 1.18 Profile of an old ZnO target with pronounced erosion zones. α corresponds to the angle between the original target surface and the erosion trace. In the insert, the trajectories of the accelerated oxygen ions are indicated by the arrows [91].

1.3.2 Silver (Ag)

Silver structure and properties

Silver (Ag) (Tab. (1.2)) is a metallic material that crystallises in a face centred cubic (FCC) structure with a lattice parameter of 4.085 Å (Fig. (1.19)). Its low index crystalline planes, (111), (100) and (110) can be ranked as a function of their surface energies [92] (1.12 J.m^{-2}, 1.20 J.m^{-2}, 1.29 J.m^{-2}) that follows their compacity in a broken bond picture. Silver is a ductile metal having, at room temperature, the lowest electrical resistivity (1.62 $\mu\Omega$.cm) and the highest thermal conductivity (428 W.m^{-1}.K^{-1}) of all elements in the periodic table [92, 93]. It also has a low melting point of 1235 K and a density of $\sim$ 10.49 g.cm^{-3}.

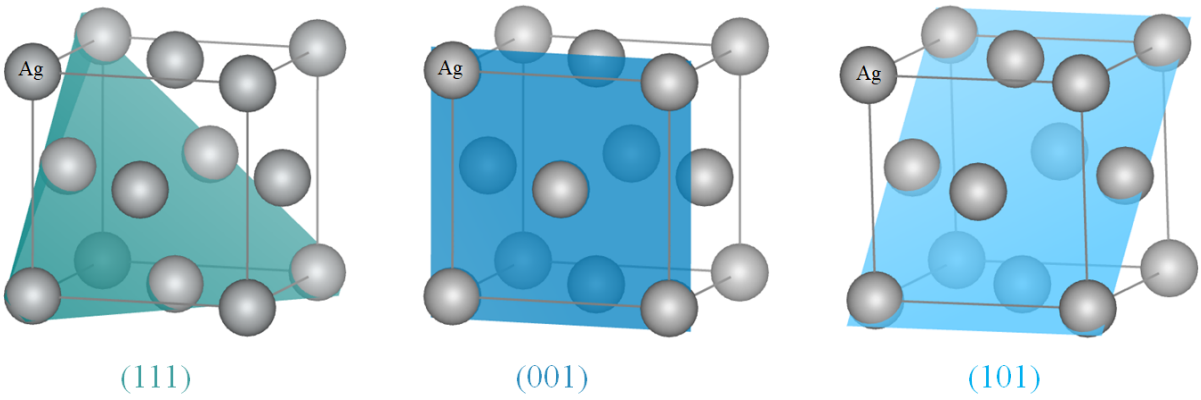

Figure 1.19 Sketch of the silver face centred cubic (FCC) structure and its low index lattice planes (111), (001) and (101).

Chemical symbol	Ag
Crystal structure	Face Centered Cubic (space group $Fm\bar{3}m$)
Lattice parameter	$a = 4.085$ Å $a = 2.89$ Å(111) in-plane hexagonal distance
Volumetric mass density	10.49 g.cm^{-3}
Surface energy	(111) : 1.04-1.25 J.m^{-2} (110) : 1.24-1.29 J.m^{-2} (100) : 1.20 J.m^{-2}
Melting temperature	1235 K
Poisson ratio	0.37
Bulk resistivity	1.62 $\mu\Omega$.cm
Charge carrier density	$6.93 \cdot 10^{22}$ cm^{-3}
Mobility	55.14 cm^{2}V^{-1}s^{-1}
Out-of-plane orientation	generally (111)

Table 1.2 Summary of the main Ag material properties [93–95].

Silver applications

Thanks to its specific properties, silver is widely used in industry, in jewellery, in electronics etc.. Due to its antibacterial properties, silver is also employed in water purification [96], or in the medical field, in creams for the treatment of burn wounds, as dental filling [97] or as coating for medical devices [98, 99]. Its specific optical properties [100] make it also suitable as coating for mirrors, as back reflector in solar cells, as transparent conductor in low-emissive and solar control coatings. In agreement with the Hagen-Rubens formula, low-emissive coatings require a metal with a very low bulk resistivity. Besides alkaline metals that are far too reactive, copper (Cu), gold (Au) and aluminium (Al) have interesting properties [100]. However, the potential use of Cu and Au is impeded by their optical behaviour in the visible range as they have intense interband transitions leading to their characteristic colours. Al has the disadvantage of being too chemical reactive and has an interband transition near the infrared region at 1.49 eV. At the opposite, interband transitions in Ag appears in the ultraviolet range below 320 nm (3.85 eV). Therefore, the dielectric function of this metal from the infrared to visible range is driven by s-conduction electrons with a nearly Drude free-electron behaviour [101]. At last being a coinage metal, silver is poorly reactive making it the best candidate for glazing applications. The drawback of this poor reactivity is its poor adhesion on oxides leading to a 3D growth mode.

1.4 Strain/stress in hetero-epitaxy and the case of Ag/ZnO

1.4.1 Strain/stress in hetero-epitaxy

When a film is grown on a single-crystal substrate of different nature, the crystal lattice of the deposit will tend to adopt a specific orientation relative the substrate, the so-called epitaxial orientation. It is driven by the minimization (i) of the interface energy for the epitaxial plane, thus favouring compact deposit planes in particular in the case of metals on oxide and (ii) of the strain induced by the film/substrate lattice mismatch $f = (a_f - a_s)/a_s$ [102] (a_f, a_s being the bulk lattice parameters of the film and the substrate along the in-plane direction of epitaxy). If the deposited film and the substrate have similar crystal structures (Fig. (1.20)), a limited number of coherent but strained layers is often grown to compensate the difference in the lattice constants. In those layers, as the film in-plane lattice constant matches the substrate one, the film material will expand or contract perpendicular to the contact plane to keep the atomic

volume almost constant ; this is the so-called tetragonal distortion induced by the epitaxial growth. In thicker films or when the mismatch is too large, the strain energy accumulated with the thickness of the film is released by the introduction of misfit dislocations at the interface. At the latest growth stages, the film lattice constant will fully relax towards the bulk value. The critical film thickness d_c, above which misfit dislocations are introduced, is determined by minimizing the sum of the strain energy E_c and the dislocation energy E_d with respect to the film strain ε_f [102, 103] :

$$E_c = \frac{2G(1+\nu)}{1-\nu}\varepsilon_f^2 d \tag{1.15}$$

and

$$E_d = \frac{Gb(f-\varepsilon_f)}{2\pi(1-\nu)} \ln\left(\frac{R_0}{b}+1\right), \tag{1.16}$$

where G is the shear modulus of the substrate and the film, ν is the film Poisson ratio, d is the film thickness and $b = |\vec{b}|$ is the absolute value of the Burgers vector of the dislocation. R_0 is the distance cutoff from the dislocation core where the strain field vanishes. While E_d presents only a weak dependence on film thickness, E_c increases linearly with it. Hence, the dislocation formation is energetically favoured above a certain critical thickness. At this point, $\varepsilon_f \approx f$ and $R_0 \approx d_c$. By minimizing $E_c + E_d$, one finds :

$$d_c = \frac{b}{8\pi(1+\nu)f} \ln\left(\frac{d_c}{b}+1\right). \tag{1.17}$$

This expression can be solved graphically. The distance between dislocations is typically given by the ratio of the substrate lattice to the misfit, the so-called Vernier rule.

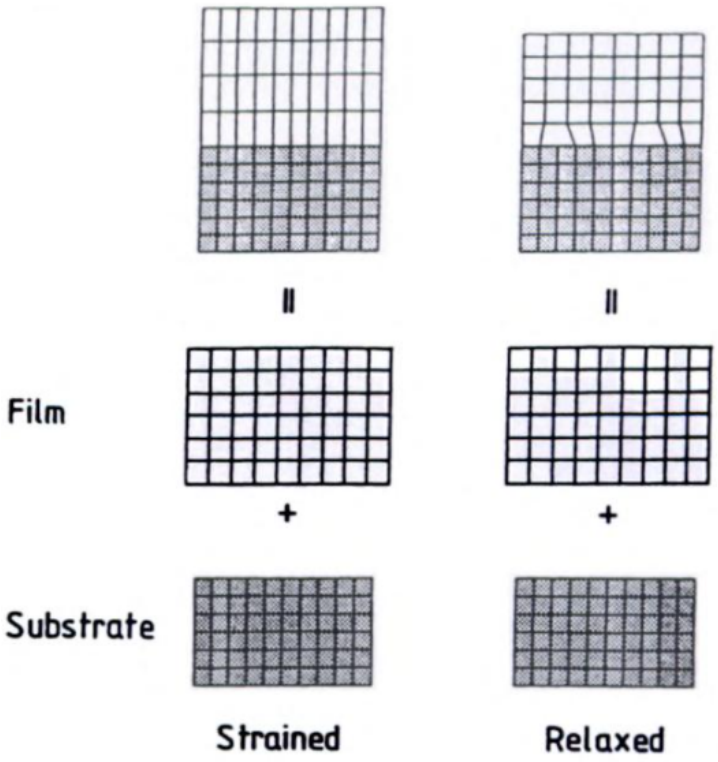

Figure 1.20 Lattice-mismatch of a strained and relaxed hetero-epitaxial structures. For large mismatch, misfit dislocations are introduced in the film [102].

1.4.2 Epitaxial relationship and growth mode in the case of Ag/ZnO

In low-emissive coatings, a silver layer of about 10 nm thick is deposited on a thin film of zinc oxide. The improvement observed in the silver film electrical conductivity provided by the ZnO seed layer is often justified by the c-axis textured growth of ZnO and the Ag(111)‖ZnO(0001) epitaxial relationship.

Based on the respective theoretical surface energies (1.0−3.0 J.m^{-2} for $(0001)_{ZnO}$ and 1.12 J.m^{-2} for $(111)_{Ag}$ [92, 104]), the Bauer thermodynamic criterion would predict a 2D growth mode. In the literature, a 2D layer-by-layer growth is reported for electron-beam evaporated films while 3D island growth was observed for evaporated and direct-current sputter deposited thin films [105–109]. But a strong uncertainty comes from the actual surface energies of the (0001) polar terminations of ZnO that depend on the actual stabilisation mechanism and therefore on the environment [95]. A very strong adhesion is theoretically [95] predicted at metal/polar orientation (several J.m^{-2}) as the metal, by providing charges, helps healing the polarity electrostatic divergence. Nevertheless, as deposit is done on a pre-existing stabilized surface, the growth mode and adhesion is expected not to differ so much from non-polar substrates. Indeed, *in situ* grazing incidence small-angle X-ray scattering experiments during evaporation [105, 106] clearly demonstrated a 3D growth but of flat-top high aspect ratio (111) oriented Ag nanoparticles both on Zn- and on O-terminated ZnO surfaces.

The Ag/ZnO epitaxial relationship has been the topics of many studies. If the Ag(111)‖ZnO(0001) orientation is obviously favoured by the hexagonal symmetry and by the low Ag(111) surface energy, the in-plane orientation is still debated [4, 95, 105, 106, 109]. On a symmetry point of view, two in-plane high symmetry epitaxial orientations can be identified : (i) the rotated (or $(2\sqrt{3}\times 2\sqrt{3})R30°$) and (ii) the non-rotated (or hexagon-hexagon or $(9\times 9)/(8\times 8)$) orientations as represented in Fig. (1.21). The substrate preparation method seems to have an influence on the resulting interface. For films evaporated on sputtered/annealed ZnO single crystal surfaces, silver predominantly grows with a non-rotated configuration [105, 106]. On the other hand, the theoretical work of Lin *et al.* demonstrated that a rotated orientation should be preferred for sputtered thin films or for poorly crystallised ZnO surfaces [95]. Similar conclusions were achieved in the work of Arbab [109].

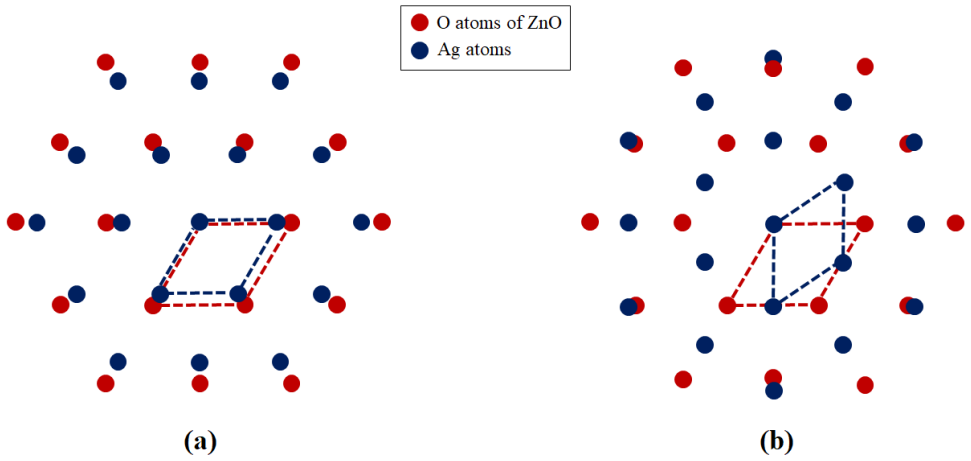

Figure 1.21 Representation of the in plane epitaxy of Ag(111)‖ZnO(000$\bar{1}$)-O : (a) hexagon/hexagon and (b) rotated orientations.

In the rotated orientation, the $[1\bar{1}0]_{Ag}$ dense row direction of Ag is rotated by 30° with respect to $[100]_{ZnO}$ [95,106]. In the other orientation, the hexagonal surface unit cell of the Ag(111) plane is aligned on the hexagonal unit cell of the ZnO substrate. The two epitaxies lead to drastically different lattice mismatch parameters f defined as the relative difference between the in-plane lattice constants [102] :

$$f = \frac{a_f - a_s}{a_s}. \tag{1.18}$$

In the rotated configuration, the interatomic distance within Ag(111) surface unit cell is equal to 5.76 Å, while within ZnO(0001) surface unit cell, it is given by $\sqrt{3}a_{ZnO} = 5.63$ Å resulting in a +2.5 % mismatch. For the hexagon/hexagon orientation, the interatomic distance within Ag(111) surface unit cells is given by $a/\sqrt{2} = 2.89$ Å. In the ZnO(0001) surface unit cell, it should be compared to the a-axis lattice constant of 3.25 Å leading to a much larger lattice mismatch of about -11 %. Based on strain/stress considerations, the rotated orientation should be clearly favoured. The critical thickness for dislocation introduction d_c has been calculated assuming the formation of dislocations with typical Burger vectors in fcc metals : $\vec{b} = 1/2 < 110 >$, $\vec{b} = 1/3 < 111 >$ and $\vec{b} = 1/6 < 111 >$. In each case, d_c results to be less than one monolayer suggesting the absence of strained Ag on a ZnO(0001). Instead, misfit dislocations should be formed from the very beginning of the growth leading to unfavourable scattering centres for the electrical transport. Nevertheless, the hexagon/hexagon orientation was systematically observed by grazing incidence X-ray diffraction in the case of evaporated films [105,106] while the rotated orientation could be found only on ill-crystallised substrates. This difference was assigned to the existence of a coincidence site lattice (CSL) (Sec. (1.1.4)) between (9×9) Ag surface unit cell and (8×8) ZnO ones thus generating a Moiré pattern. The resulting lattice mismatch for these coincidence points is very low -0.01 % [106]. But on the deposition point of view, in the early stage of growth for island sizes lower than the CSL parameter, the clusters do not benefit from this CSL matching. More recently, Benedetti *et al.* [70] proposed an alternative explanation for this hexagon/hexagon epitaxy that appears surprisingly quite common to many fcc metals (Cu [110,111], Pd [112], Pt [113]) despite different lattice mismatches. By studying with scanning tunnelling microscopy and low-energy electron diffraction the growth of Ag on the non-polar ZnO$(10\bar{1}0)$ face, they showed a preferential growth of the (111) oriented clusters at step edges with an alignment of the dense row $[1\bar{1}0]_{Ag}$ along the $[100]_{ZnO}$ direction (Fig. (1.22)). Steps on this surface of rectangular symmetry are (i) either non-polar and terminated by cations and anions ($[001]_{ZnO}$) or (ii) polar and terminated by Zn or O atoms ($[010]_{ZnO}$). Step polarity corresponds to a 1D stacking of lines of charges ; the divergence of the electrostatic potential is less dramatic than in two dimensions. Density functional calculations proved the favoured adsorption of Ag adatoms at O-polar terminated step edges compared to Zn-terminated or non-polar ones, leading to a charge transfer as measured by photoemission that stabilises the configuration. As seen in Fig. (1.16), polarity healing of the (0001) terminated surface gives rise to numerous polar steps oriented along the $[100]_{ZnO}$ direction on which a step-driven epitaxy similar to that on ZnO$(10\bar{1}0)$ could occur.

1.5 Resistivity in metallic thin films

1.5.1 Conductivity in metals

In first approach, the electron transport properties of a metal bulk can be explained by the Drude theory [114]. In this model, which is the adaptation of the kinetic theory of gases to charges in a solid, electrons are considered as classical point particles confined within the sample volume. Under the presence of an external electric field $\vec{E_{ext}}$, the electrons of density n, of charge $-e$

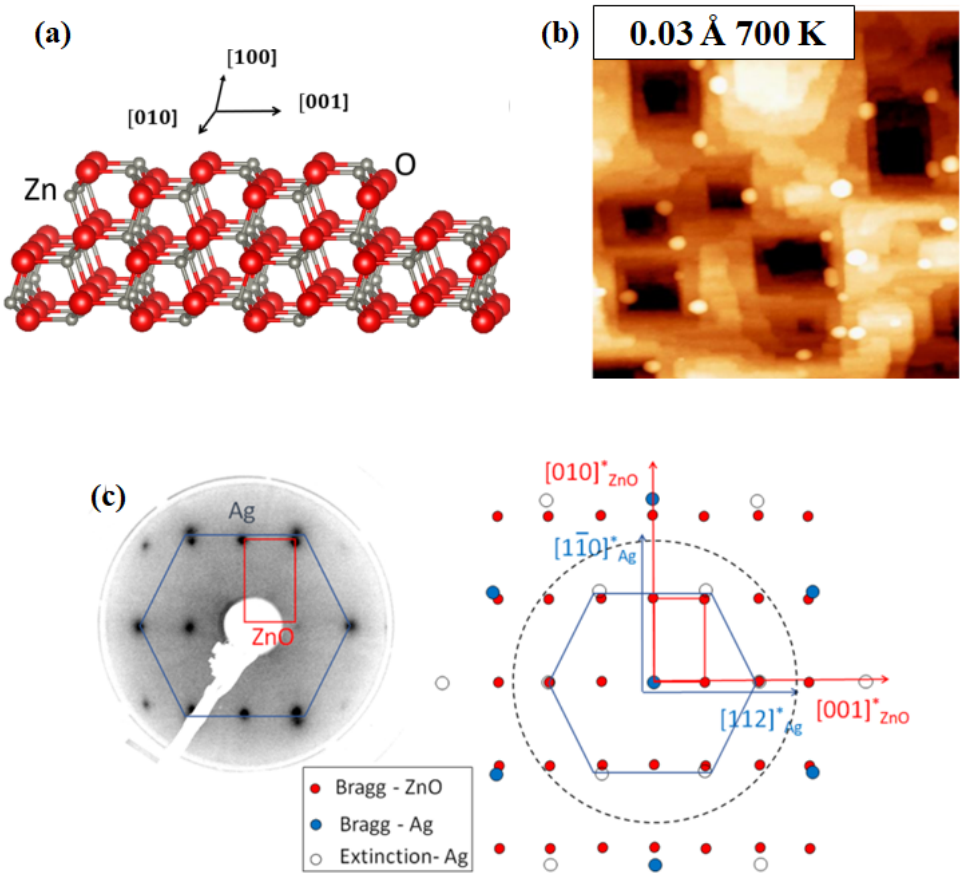

Figure 1.22 (a) Ball model of the ZnO(10$\bar{1}$0) surface with polar and non-polar steps. (b) STM image of a vapour deposited Ag film on ZnO(10$\bar{1}$0) kept at 700 K (thickness 0.03 nm). Nucleation and growth happen only at polar step edges. (c) Corresponding LEED pattern showing the epitaxial relationship with the alignment of dense Ag rows along $[010]_{ZnO}$.

and of mass m_e are accelerated by a driving force $\vec{F} = -e \cdot \vec{E_{ext}}$, and restrained in their motion by inelastic collisions with the lattice ions described by a viscous force. The probability for an electron to be scattered between t and $t + dt$ is given by $\frac{dt}{\tau}$, where τ is the average time between two consecutive collisions, also called the relaxation time. The equation of motion, in one dimension, can be written as :

$$m\frac{dv}{dt} + \frac{m_e}{\tau}v = -eE_{ext}, \tag{1.19}$$

where v is the electron velocity. In a stationary state ($\frac{dv}{dt} = 0$), the so-called drift velocity μ_D and electron mobility μ can be derived :

$$\mu_D = -\frac{\tau e E_{ext}}{m_e} = \mu E_{ext}, \tag{1.20}$$

which allows to define the current density j :

$$j = -ne\mu_D = \frac{e^2 n\tau}{m_e}E_{ext} = \frac{1}{\rho}E_{ext}, \tag{1.21}$$

and the resistivity $\rho = (ne\mu)^{-1}$. The Drude model remains naive as it erroneously ignores the band structure of the material and assumes collisions with lattice ions to describe the viscous force.

The Sommerfeld theory merges the Drude model with the Fermi-Dirac quantum statistics and the band structure due to lattice periodicity [94]. In this quantum mechanical approach of the problem, the so-called Boltzmann transport theory, the current density is defined as an integral of the electron velocity over all possible electron states in the first Brillouin zone of the reciprocal space :

$$\vec{j} = -\frac{e}{8\pi^3}\int_{BZ} \vec{v}(\vec{k}) f(\vec{k})\, d\vec{k}, \tag{1.22}$$

where $f(\vec{k})$ is the probability of a state $\vec{k}$ to be occupied and corresponds at equilibrium to the Fermi-Dirac distribution :

$$f_0(E(\vec{k})) = \frac{1}{e^{E(\vec{k})-E_F/k_BT}+1}, \tag{1.23}$$

with E_F the Fermi energy, k_B the Boltzmann constant and T the temperature. In a non-equilibrium condition, due to the presence of an external field $\vec{E_{ext}}$, $f(\vec{k})$ can be approximated in a steady state regime as :

$$f(\vec{k}) = f_0(\vec{k}) + \frac{e\tau(\vec{k})\vec{E_{ext}}}{\hbar}\nabla_{\vec{k}} f_0(\vec{k}). \tag{1.24}$$

where $\tau(\vec{k})$ is the relaxation time of state $\vec{k}$. The electrical conductivity along the field direction x is finally obtained by combining Eq. (1.24) with Eq. (1.22) :

$$\sigma = -\frac{e^2}{8\pi^3}\int v_x^2(\vec{k})\tau(\vec{k})\frac{\partial f_0}{\partial E}\, d\vec{k}. \tag{1.25}$$

Approximating the derivative of the Fermi-Dirac function to a Dirac delta distribution at E_F and transforming the integral into a surface integral above the Fermi surface, one obtains the expression :

$$\sigma \approx \frac{e^2}{8\pi^3\hbar}\int_{E=E_F} \frac{v_x(\vec{k})\tau(\vec{k})}{v(\vec{k})}\, df_E. \tag{1.26}$$

According to this equation, only charge carriers close to the Fermi energy can contribute to the transport. Furthermore, considering that the energy transfer during a collision is about $k_BT \ll E_F$ and according the exclusion principle, only electrons within an energy interval of k_BT close to the E_F Fermi level, can be scattered. These electrons will move with a speed equal to the Fermi velocity $v_F = \hbar k_F/m$ along a mean free path $l = v_F\tau$. l represents the average distance travelled by electrons of Fermi energy. The Drude model, implying a diffusive motion of the electrons due to collisions with the ions, considers that l is of the order of the interatomic distance. In the Sommerfield model, the mean free path depends on the Fermi velocity and is therefore an order of magnitude greater than the classical case. The mean free path is therefore not the result of collisions with ions, but instead is related to material imperfections, defects and thermal fluctuations of the ions, called phonons that come into play through the effective relaxation time $\tau(\vec{k})$ in the Boltzmann transport equation. For an ideal metal with perfectly parabolic conduction band, the resistivity is thus given by :

$$\rho = \sigma^{-1} \approx \frac{m^*}{e^2\tau(E_F)n} \tag{1.27}$$

where m^* is the effective mass of the electron that takes into account the influence of the band structure of the material. In the case of silver, the effective mass is only 1.03 times the actual electron mass [115], while the charge carrier density is $6.93\,10^{22}$ cm^{-3}. Its Fermi velocity $v_F = 1.39\,10^6$ m.s^{-1} and room-temperature resistivity $\rho_0 = 1.62\,\mu\Omega$.cm leads to an electron mean free path of $l = 38$ nm.

1.5.2 The various contributions to bulk electrical resistivity

In a metal, the conduction can be hindered by a variety of scattering phenomena that are hidden in the relaxation time $\tau(E_F)$. The main ones are : (i) the electron-phonon scattering, (ii) the electron-defect scattering (as impurities, grain boundaries, dislocations, interfaces etc.), and (iii) the electron-electron scattering (Fig. (1.23)), etc...

A phonon is a quasi-particle that describes a quantum of vibration in a rigid crystal lattice that is increasingly populated with temperature [116]. The electron-phonon scattering contribution to resistivity is therefore a temperature dependent mechanism $\rho_{phonon}(T)$. For a bulk material, it is given by the Bloch and Grüneisen expression [117, 118] :

$$\rho_{phonon}(T) = A\left(\frac{T}{\Theta_D}\right)^5 \int_0^{\Theta_D/T} \frac{x^n}{(e^x-1)\cdot(1-e^{-x})}\,\mathrm{d}x, \tag{1.28}$$

with Θ_D the Debye temperature of the material. A is specific to the material and describes the strength of the electron-phonon coupling. Its value is proportional to $\lambda_{tr}\omega_D/\omega_p^2$, where λ_{tr} is the electron-phonon coupling constant, ω_D is the Debye frequency and ω_p is the metal plasma frequency [119]. If only acoustic phonons are involved as in the case of a material with one element in the unit cell, A takes a value of 4.255 [119]. The value of the exponent n depends on the nature of the considered electron-phonon interaction. For a nonmagnetic elemental metal like Cu, Ag, or Au, $n = 5$ [119].

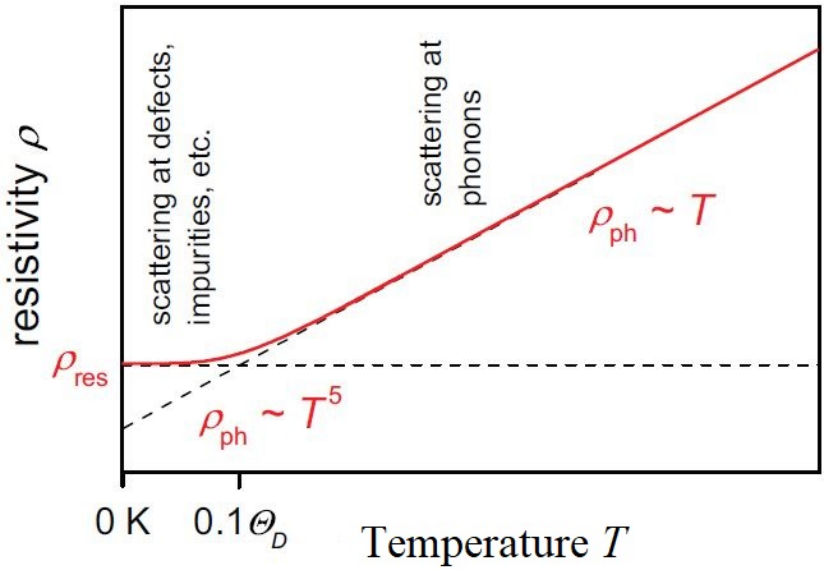

Figure 1.23 Typical temperature dependence of the electrical resistivity of a bulk metal. At high temperature, phonon scattering is the predominant contribution to resistivity. At low temperature, the scattering at defects and impurities dominates [120].

The electron-defect scattering contribution to resistivity varies with the type of lattice imperfections that can be classified depending on their dimensionality [121] :

— 3D defects, corresponding to bulk defects such as voids, cracks or precipitates ;
— 2D defects, corresponding to planar defects such as grain boundaries or interfaces ;
— 1D defects, corresponding to line defects such as dislocations ;
— 0D defects, corresponding to point defects such as impurities, vacancies or interstitial atoms.

The electron-defect scattering is to first order independent of temperature and it scales obviously with the defect concentration. At very low temperature, when the population of the phonon modes decreases, the electron-defect scattering becomes the main source of scattering in resistivity (Fig. (1.23)).

The electron-electron scattering is a temperature dependent mechanism, decreasing proportionally to T^2. Its contribution is often very small. According to the Pauli exclusion principle, below an electron density of $\sim 10^{16-}10^{17}$ cm^{-3} and an electric field value of 10^3 V.cm^{-1}, electrons can be considered as non-interacting, and the scattering mechanism can be neglected. However, significantly above these limits electron–electron scattering starts to dominate [122, 123].

According to the Matthiessen rule that considers the scattering mechanisms as independent, the total bulk metal resistivity $\rho(T)$ can be expressed as the sum of all individual contributions :

$$\rho(T) = \rho_{phonon}(T) + \rho_{defect} + \rho_{electrons}(T). \tag{1.29}$$

In the case of materials in which one or more dimensions are of the order of the mean free electron path, the contribution of an additional scattering phenomena, the scattering at the interfaces gains a non-negligible relevance [124]. In particular, for polycrystalline thin films, two scattering mechanisms can be identified (i) at grain boundaries and (ii) at interfaces. Fuchs and Sondheimer [125,126] were the first to tackle the question of interfaces in the electronic transport in a thin perfect film using the Boltzmann equation. Later on, Mayadas and Shatzkes [127, 128] treated the combined influence of scattering at interfaces and reflection of electrons at grain boundaries.

1.5.3 The Fuchs-Sondheimer and the Mayadas-Schatzkes models

The Fuchs-Sondheimer model

The Fuchs-Sondheimer theory (F-S) [125, 126] is based on the solution of the Boltzmann transport equation previously described under a series of simplifying assumptions [129] :

— the disorder in the film and the film thickness are independent quantities ;
— the film should have planar parallel and identical limiting surfaces ;
— the Fermi surface is spherical ;
— the scattering process should occur isotropically and can be characterized by an effective mean free path which implies the applicability of Matthiessen rule.

The scattering of electrons at interfaces is described by a phenomenological parameter $0 \leq p \leq 1$ (Fig. (1.24)) which describes the fraction of electrons that are specularly reflected at interfaces. The remaining fraction $1 - p$ is scattered isotropically over 2π. For $p = 0$, all charge carriers are diffusely scattered at the interface losing their parallel momentum along the transport direction. At the opposite for $p = 1$, all charge carriers are reflected specularly at the interfaces, conserving their momentum along the transport direction. One should keep in mind that only reflection occurs at interfaces because electrons face a potential barrier, the so-called Schottky barrier.

So p is somehow connected with the interface roughness but also the band alignment at the interfaces. Based on these assumption, the total film resistivity ρ_f reads :

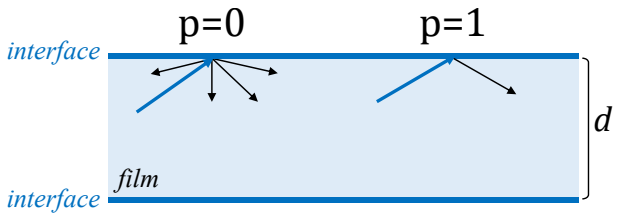

Figure 1.24 Schematic representation of the F-S electron scattering at interfaces. A fraction p of electrons is specularly reflected and $1-p$ scattered at interfaces. $p=1$ corresponds to a perfect mirror for electrons.

$$\frac{\rho_0}{\rho_f} = 1 - \frac{3}{2\kappa_0}\int_1^\infty \left(\frac{1}{t^3} - \frac{1}{t^5}\right)\frac{1-e^{-\kappa_0 t}}{1-pe^{-\kappa_0 t}}\,dt, \tag{1.30}$$

with ρ_0 the resistivity of a bulk material with the same density of lattice defects and impurities as the film, $\kappa_0 = d/l_0$ the ratio between the film thickness d and the mean free electronic path in the equivalent bulk material l_0. According to the Sommerfeld model, $l_0 = \frac{m_e v_F}{ne^2\rho_0}$, with m_e the electron mass, v_F the Fermi velocity, n the charge carrier density and e the elementary charge. The integral in Eq. 1.30, that can only be solved numerically, can be simplified for sufficiently thick films in the regime $d \gg l_0$ as :

$$\frac{\rho_f}{\rho_0} = 1 + \frac{3}{8}\frac{l_0}{d}(1-p), \tag{1.31}$$

leading to a $1/d$ thickness dependence and for very thin film when $d \ll l_0$ as :

$$\frac{\rho_f}{\rho_0} = \frac{4}{3}\frac{(1-p)}{(1+p)}\frac{l_0}{d\ln\frac{l_0}{d}}. \tag{1.32}$$

The Mayadas-Schatzkes model

The Mayadas-Schatzkes model (M-S) [127, 128] of thin film resistivity tries to account in the transport for the microstructure of the film, in particular the grain boundaries (Fig. (1.25)). These defects lead to a partial reflection of the electronic wave and therefore to an increase of the trajectory of electrons and thus of the resistivity. This phenomenon is described by a reflection coefficient $0 \leq R \leq 1$ at the grain boundary. $R=1$ corresponds to the fictitious case of perfectly reflecting grain boundaries ; in this theoretical case, the film is not even conductive. $R=0$ corresponds to transparent grain boundary and to a perfectly conductive layer if other scattering mechanisms are ignored. Zhu *et al.* [130] proposed a model to estimate R from the scaling of the potential barrier with the grain boundary interface energy. They found a linear dependence of R with the square-root of the metal melting temperature. The predicted value for silver ($R=0.34$) matches with the distribution of experimental values ($R=0.16-0.48$). In the M-S model [131, 132], grain boundaries are represented by an array of reflecting planes perpendicular to the external field, with a geometrical distribution that obeys a Gaussian law, so that the mean distance is equal to the average grain diameter D in the film. The effect of these planar defect is described by a Dirac potential related to the R-parameter. The resistivity

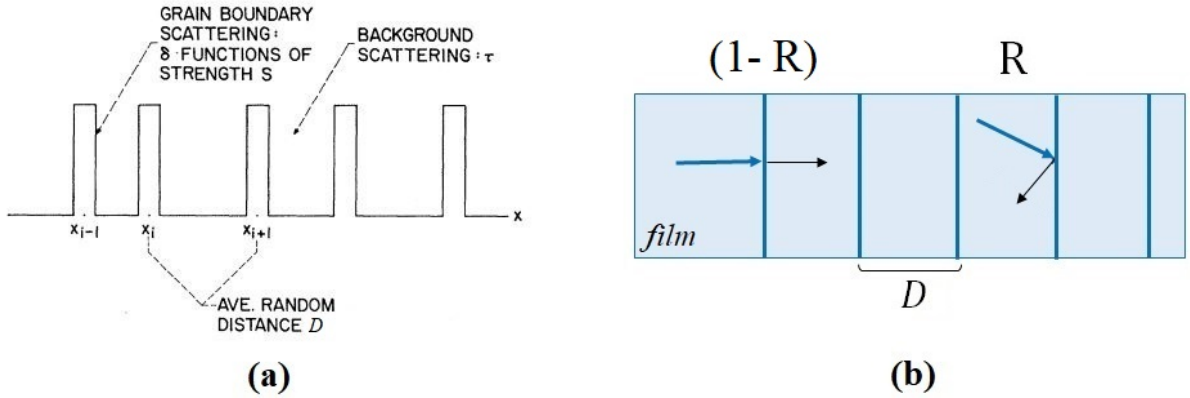

Figure 1.25 (a) Model of distributed Dirac potentials to account for the effect of grain boundary in resistivity ρ_{GB}. [128]. (b) Schematic representation of the reflection principle at grain boundary.

of the polycrystalline material is then obtained via the Boltzmann equation under a combined effect of electron scattering by intra-grain defects and phonons and by grain boundaries :

$$\rho_{GB} = \frac{\rho_0}{3} \cdot \left(3 - \frac{\alpha}{2} + \alpha^2 - \alpha^3 \ln\left(1 + \frac{1}{\alpha}\right)\right)^{-1} = \rho_0 \cdot f(\alpha)^{-1} \tag{1.33}$$

with

$$\alpha = \frac{R}{1-R} \cdot \frac{l_0}{D}, \tag{1.34}$$

where ρ_0 and l_0 have the same meaning as before. For large grain sizes ($D \gg l_0$), Eq. 1.33 can be simplified as :

$$\rho_{GB} = \rho_0 \left(1 - \frac{3}{2}\frac{R}{1-R}\frac{l_0}{D}\right) \tag{1.35}$$

which clearly shows how ρ_{GB} increases with grain boundary density ($\propto 1/D$) and with R.

To find the expression of the total resistivity of a thin film, which could include all occurring scattering mechanisms, Mayadas and Schatzkes combined their model with the framework of the Fuchs-Sondheimer theory to solve the Boltzmann transport equation [128]. The resulting calculations reveal a total resistivity ρ_f that depends in a complex way on the grain boundary reflection coefficient R and on the interface specular reflection parameter p :

$$\boldsymbol{\rho_f} = \left(\frac{1}{\boldsymbol{\rho_{GB}}} - \frac{6(1-p)}{\pi \boldsymbol{\kappa_0 \rho_0}} \int_0^{\pi/2} d\phi \int_1^{\infty} dt \frac{\cos^2\phi}{\boldsymbol{H^2(t,\phi)}} \left(\frac{1}{t^3} - \frac{1}{t^5}\right) \frac{1 - e^{-\kappa_0 t \boldsymbol{H(t,\phi)}}}{1 - p e^{-\kappa_0 t \boldsymbol{H(t,\phi)}}}\right)^{-1}, \tag{1.36}$$

where $\kappa_0 = d/l_0$ and $\boldsymbol{H(t,\phi)}$ is defined as :

$$\boldsymbol{H(t,\phi)} = 1 + \frac{\boldsymbol{\alpha}}{\cos\phi\sqrt{(1-t^{-2})}}. \tag{1.37}$$

The Mayadas-Shatzkes and Fuchs-Sondheimer models have been widely applied to analyse the dependence in thickness of metallic thin film resistivity [133–135]. However, for metals where the grains grow constantly with the film, and so that the grain size is proportional to the film thickness ($D \sim d$), it turns out to be hard to unfold the relative weights of the two contributions to film resistivity. As already suspected in limit $D \sim d \gg l_0$ (Eq. 1.31 and Eq. 1.35), the difference between the two models (Fig. (1.26)) is very weak. Consequently, by focusing only on the film thickness dependence of resistivity, it is not possible to clearly unfold the main contributions leaving room for free interpretation [135–138].

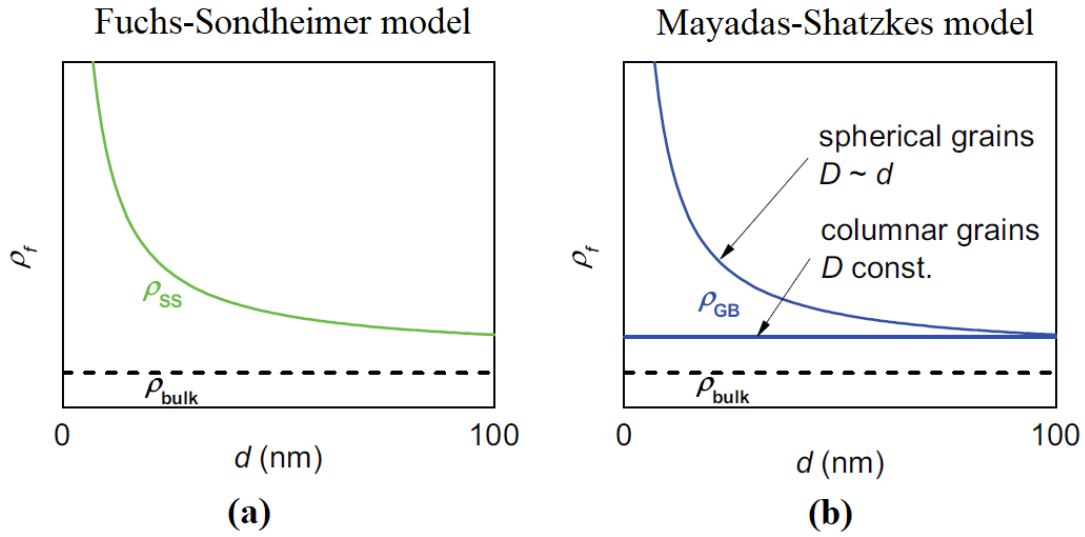

Figure 1.26 The resistivity versus the film thickness of a metallic film according to the Fuchs-Sondheimer model (a) and the Mayadas-Shatzkes model (b) [120].

One solution to overcome this ambiguity on the interpretation of experimental data is to use the temperature dependence of the resistivity [139], which in the M-S is contained in all the parameters reported in bold in Eq. 1.36. Contrary to the dependence in thickness, the F-S and M-S models have completely different behaviours when studied as a function of temperature. This is clearly demonstrated in Fig. (1.27) and discussed in previous publications [120, 140–142]. In Fig. (1.27), the temperature-dependent resistivity contribution ($\rho_{f,phonon}(T) = \rho_f(T) - \rho_f(T = 0K)$) of a 10 nm thick silver film has been calculated according to the two theories for different interface and grain boundary scattering parameter values. As a reminder, the implemented intra-grain temperature dependent resistivity is given by $\rho_{bulk}(T) = \rho_{res}^{bulk}(T = 0K) + \rho_{phonon}(T)$ with $\rho_{phonon}(T)$ given by Eq. 1.28. In the F-S model, interface scattering (*i.e.* lower p values) results in a strong enhancement of $\rho_{f,phonon}(T)$ with respect to the case of silver single crystal. At the same time, for sizeable interface scattering below $\sim$ 100 K, the resistivity curve looses its linear behaviour to show a more concave shape. This is particularly obvious when the bulk intra-grain resistivity $\rho_{res}^{bulk}(T = 0K)$ is equal to zero *i.e.* when no impurities or intra-grain defects are present. Similar behaviours were also reported in Ref. [139] for thicker gold films (see Fig. (1.28)). At the opposite, in the M-S model, despite the variation of R, the curves $\rho_{f,phonon}(T)$ still present a linear behaviour without showing strong deviation from the bulk. Nevertheless, the total resistivity $\rho_{f,phonon}(T)$ remains always larger than that of a silver single crystal. At last, the $\rho_f(T = K)$ offset also depend on (R,p) and ρ_{res}^{bulk} in an intricate way.

In conclusion, a clear distinction of the different scattering contributions to film resistivity can be achieved through the measurement of the temperature-dependent resistivity and the analysis of its shape and absolute value. In this work, the Mayadas-Shatzkes model simulation were therefore based on Eq. 1.36.

1.5.4 Refined modellings : the Soffer and Sambles approaches

The Fuchs-Sondheimer and the Mayadas-Shatkes models are limited by restrictive assumptions that many authors have tried to overcome over the years [124, 142].

Starting from the F-S model, few studies [143–145] focussed on the possibility of including dif-

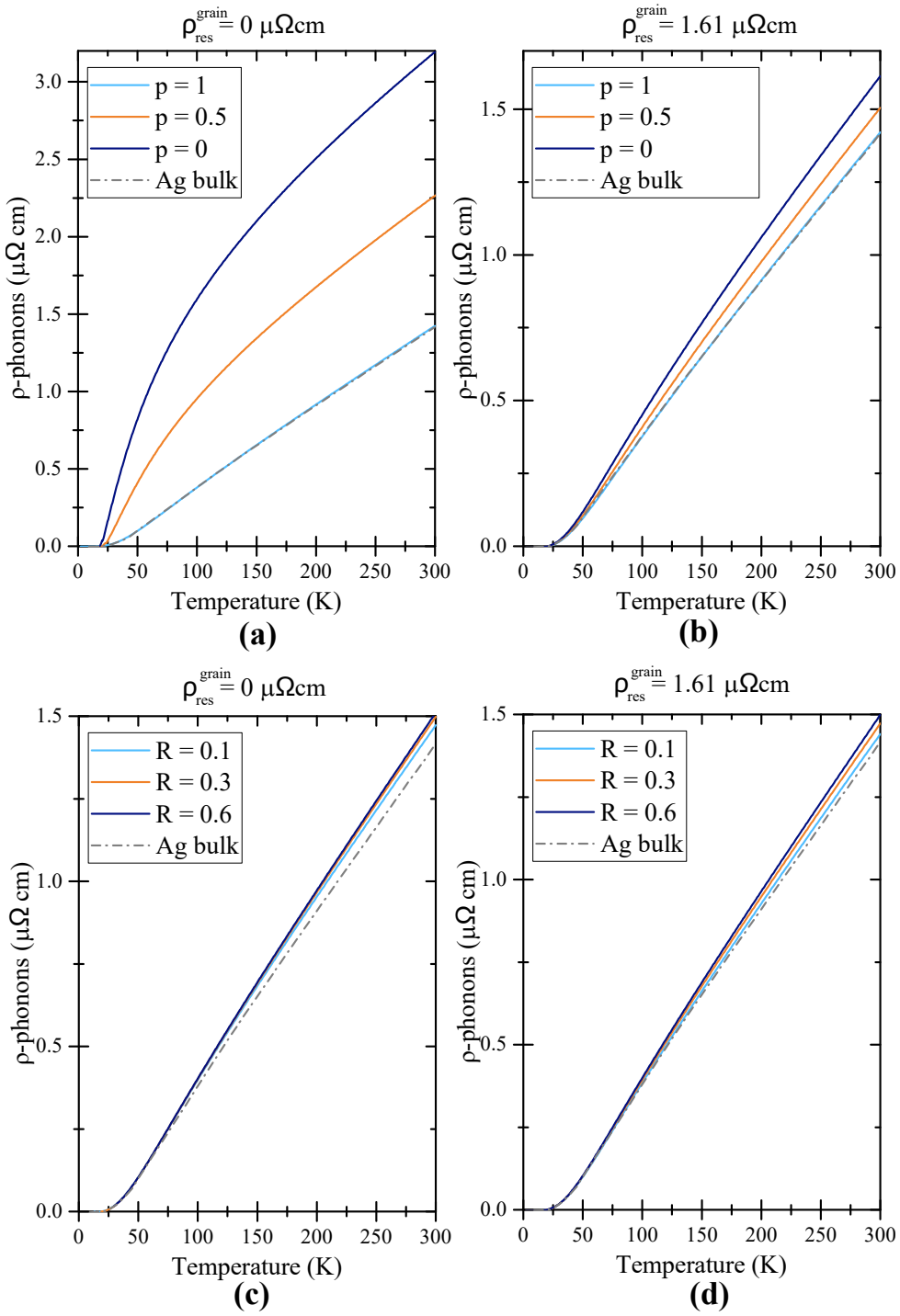

Figure 1.27 Temperature-dependent contribution to film resistivity (*i.e.* after subtraction of $\rho_f(T = 0K)$) as a function of temperature according to the (a-b) Fuchs-Sondheimer theory ($R = 0$, variable p) and to the (d-c) Mayadas-Shatzkes theory ($p = 1$, R variable), for a 10 nm thick silver film compared to the silver single crystal resistivity. The simulations were done by considering two values corresponding to the intra-grain resistivity at 0 K $\rho_{res}^{bulk}(T = 0K)$.

ferent scattering parameters, p_1 and p_2, at the upper and lower interfaces of the film. Others [146,

147] investigated the case of non-spherical Fermi surfaces or the question of anisotropic mean free path [148]. As the F-S model does not provide a direct link between the surface morphology and the parameter p, some authors tried to implement a dependence of p to the incidence angle of the electrons on the interface and on the roughness of film surface [121, 149–151]. Similarly, the M-S model on the role of grain boundaries has also been the topics of improvements. Warkusz *et al.* [152] proposed an approximate expression for metallic films resistivity, which takes into account the film thickness, the grain diameter, as well as the coefficients p and R. Further studies [153–155] focused on the development of a three-dimensional scattering model for polycrystalline films. In the following paragraphs, two relevant models, the Soffer and Sambles ones, will be discussed in more details.

In the Fuchs-Sonderheim theory, all the electrons, regardless of their angle of incidence on the interface have the same probability p of being reflected specularly at the surface and $1-p$ of being scattered isotropically (Fig. (1.24)). For a rough interface, these assumptions are generally violated. For small roughness correlation, the reflection coefficient will depend on the ratio between the wavelength of the incident field λ_e to the surface roughness h (the root mean square deviation from the average value) but also on the incident angle [142]. Based on this assumption, Soffer [149] developed a model of surface-scattering-based resistivity using an angular dependent specular reflection parameter in the limit of a small roughness lateral correlation length :

$$p(\theta) = \exp\left[-\left(\frac{4\pi h}{\lambda_e}\right)^2 \cos^2\theta\right] \tag{1.38}$$

where h is the interface roughness (assumed to be uncorrelated) and θ is the angle of incidence of the electron relative to the surface normal. Using this definition of $p(\theta)$ and substituting $\cos\theta = u$ and $\kappa = t_0/l_0$, the ratio of bulk to film resistivity becomes :

$$\frac{\rho_0}{\rho_f} = 1 - \frac{3}{2}\int_0^1 du \frac{(u-u^3)(1-p(u))(1-\exp(-\kappa/u))}{\kappa(1-p(u)\exp(-\kappa/u))}. \tag{1.39}$$

This model contains a temperature dependence similar to that of the Fuchs-Sondheimer model (Fig. (1.28)).

This expression has been used in the studies of Sambles *et al.* [141, 156, 157] for Au, Al and Ag films. Proven to be more close to reality than the Fuchs model especially for large-grained foils or wires, the model was further refined to improve the analysis of thin film resistivity. This included the dissymmetry between the two interfaces that often have entirely different roughnesses (metal-air vs metal-vacuum interfaces). In the case of a thin film with two different surface roughnesses h_1 and h_2, the expression becomes :

$$\frac{\rho_0}{\rho_f} = 1 - \frac{3}{2\kappa}\int_0^1 du(u-u^3)\left[(1-\exp\left(-\frac{\kappa}{u}\right)\right]\left[(1-\overline{p}+(\overline{p}-p_1p_2)\exp\left(-\frac{\kappa}{u}\right)\right] \tag{1.40}$$

with $\overline{p} = \frac{1}{2}(p_1+p_2)$ and a similar dependence as in Eq. 1.38 for p_1 and p_2. When one of the two interfaces is very smooth *i.e.* h tends to zero, $p_2 = 1$ and Eq.1.40 takes the forms of Eq. 1.39 with κ doubled.

The introduction of the grain boundary scattering in the Soffer equation was first made in the publication of Sambles *et al.* [141] in a similar spirit as for the classical Mayadas-Shatkes approach. The resulting film resistivity has a more complex expression :

$$\frac{\rho_0}{\rho_f} = f(\alpha) - \frac{4}{\pi}\int_0^{\pi/2} d\phi \int_0^1 du \frac{\cos^2\phi S(\kappa H(u,\phi), p_1(u), p_2(u), u)}{H(u,\phi)} \tag{1.41}$$

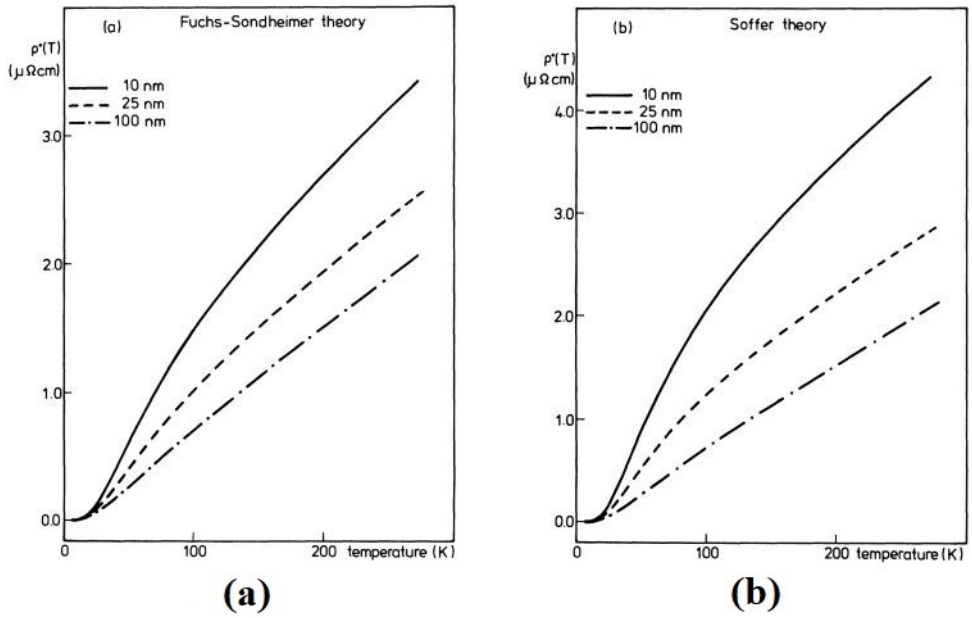

Figure 1.28 Temperature-dependent contribution to resistivity according to the (a) Fuchs-Sondheimer theory with $p = 0$ and to the (b) Soffer theory with surface roughness equal to 1.0 nm for gold thin films [139].

where :

$$S(\kappa H(u,\phi), p_1, p_2, u) = \frac{3(u-u^3)[1-\exp(-\kappa H/u)][1-\overline{p}+(\overline{p}-p_1p_2)\exp(-\kappa H/u)]}{2[1-p_1p_2\exp(-2\kappa H/u)]\kappa H}$$

Eq.1.41 is the basis of the resistivity models used for the simulations in this work in addition to the Mayadas-Shatzkes model.

To sum up, the model, that we will denote as *Samble model*, describes an asymmetric M-S model ($p_1 \neq p_2$) with flat interfaces. Here, the interface scattering parameters of Eq.1.41 are constants, $p_1(u) = p_1 = const$ and $p_2(u) = p_2 = const$, which value can vary between 0 and 1. The *Soffer model*, on the other hand, includes asymmetric interfaces with roughnesses h_1, h_2, leading to angular dependent parameters $p_1(u) = \exp[-(4\pi h_1 u/\lambda_e)^2]$ and $p_2(u) = \exp[-(4\pi h_2 u/\lambda_e)^2]$.

Chapter 2

Materials and methods

The present work was carried out at the joint CNRS/Saint-Gobain Recherche, Surface du Verre et Interfaces (SVI) laboratory in collaboration with the Institut des NanoSciences de Paris (INSP - CNRS/Sorbonne University) and the I. Physikalisches Institut (IA – RWTH Aachen University). This chapter provides an overview of the set of methods and of experimental setups used during the course of this thesis in all these laboratories. After introducing the type of substrates, the specificities of the used sputtering deposition chambers are presented. Follows a description of the sample preparations and their surface treatments. At last, the chapter ends up with a brief review of all the *in situ* and *ex situ* experimental techniques that were employed for topographical, structural and electrical characterizations of the stack of layers.

Chapter summary

2.1 Thin film deposition

In this study, stacks of films were synthesized by magnetron sputtering deposition with, in the case of some trials on ZnO seed layers, an ion beam assistance (Ion Beam Assisted Sputtering/IBAS), see conclusion. Depending on the final objectives, the stacks were grown on various substrates ranging from float glass to silicon wafer and ZnO single crystal (Tab. (2.1)). The elaborated stacks are fully described in the corresponding chapters and not discussed herein.

Substrate	**Orientation**	**Thickness**	**Size**	**Surface roughness (R_q)**	**Brand**
ZnO crystal	(0001)/(000$\bar{1}$)	0.5 mm	(1 × 1) cm^2	<0.5 nm	Neyco
Float glass	Amorphous	4 mm	(30 × 30) cm^2	0.3 ± 0.1 nm	Planiclear
Si [39, 108]	(100)	280 μm	2”	0.15 ± 0.01 nm	Neyco

Table 2.1 Characteristics of all susbtrates used during this study. The R_q values correspond to the surface roughness determined by probing a 1×1 μm^2 zone by AFM.

2.1.1 The substrates

2.1.1.1 ZnO single crystal

The main purpose of this work was to investigate the impact of in-plane texture on the structural and electrical properties of a simplified low-emissive coating. Thus, relevant model systems, that could be compared to industrial stacks, were prepared on ZnO single crystal surfaces. The ZnO substrates were chosen with a (0001) termination, to reproduce the typical (002) out-of-plane orientation commonly found in glazing coatings where the oxide grows on a Si_xN_y barrier layer deposited on glass [109]. As the wurtzite ZnO crystallographic structure is made of an alternate stacking of anions and cations along the [0001] direction, the (0001) bulk truncation is said to be polar ; it is either Zn-[or ZnO(0001)] or O-[or ZnO(000$\bar{1}$)] terminated (see Sec. (1.3.1)). The divergence of the electrostatic potential due to the infinite stacking of charged planes requires a mechanism of compensation, most of the time via a change of the surface charge (vacancies or hydroxyls groups). The exact mechanism for ZnO is still the subject of a vivid debate in the literature and strongly depends on the thermodynamic conditions and therefore the used surface preparation [65, 67, 158] (see Sec. (1.3.1)). The samples (purchased from Neyco) produced by hydrothermal growth were oriented and polished with a miscut of less than 0.5° ; they measured 10 × 10 × 0.5 mm^3, a typical size required for electrical transport measurements.

2.1.1.2 Float glass

Silver based low-emissive coatings are typically deposited on "float" glass, produced through the Pilkington process [159]. The technique consists in blending together the glass raw materials (sand, sodium carbonate, limestone, etc...) and melting them at about 1500°C. The mixture is then poured onto a bath of molten tin, where the glass spreads into a uniform smooth ribbon. As it floats along the bath, its temperature is gradually decreased to 600°C, and the sheet is transferred onto rollers. Here, the glass thickness and width are defined and regulated by controlling the speed at which the sheet is removed from the bath. Slowly cooled in order to avoid stress build-up or cracks formation, the ribbon is finally cut into smaller glass plates of 6 m long by 3.2 m wide. Typically characterized by a very flat surface, which does not require further polishing, and by a high structural flexibility, allowing, once heated, an easy control of

its shape and form, float glass finds various of applications, including insulated glazings, mirrors, automotive glasses, furnitures and so on [159,160].

The glass is composed mainly of amorphous silica, the so-called network former, mixed with other oxides, such as Na_2O (12.88 %mol), CaO (10.5 %mol), MgO (3.8 %mol), Al_2O_3 (0.35 %mol) and K_2O (0.11 %mol). Especially upon thermal treatment, the corresponding cations can easily diffuse inside the glass and through the deposited layers in contact with the substrate leading to detrimental effects for the coating functionality. For the same reason, the so-called atmosphere side that did not touch the tin bath is preferentially selected to receive any thin layer stack. Therefore a thick protective layer of silicon nitride is deposited on top of the glass surface to prevent this diffusion or at least slow it down [161]. Often additional very thin metal layers, such as nickel-chromium or titanium, the so-called blockers [46], are also inserted at the interface between silver layer and zinc oxide. These films play a number of roles within the coating by (i) protecting the silver from oxidation during reactive deposition of the ZnO layer, (ii) improving the chemical and mechanical durability of the stack and (iii) preserving the silver from oxygen diffusion occurring during the annealing step, that tends to favour the layer dewetting. However, for the purposes of the present study on silver texturization, the coating was simplified and the blocker layers were accounted only in some coatings.

2.1.1.3 Silicon substrate

For studies above the glass transition and to avoid diffusion of alkaline cations, the glass substrate was replaced by a similar but chemically less reactive substrate, namely a crystalline silicon wafer. In contact with the atmosphere, the silicon surface oxidizes creating a thin layer of amorphous SiO_2 with a thickness of around 2 nm. Having a RMS surface roughness lower than 0.15 nm, this substrate is a perfect model system of glass for film growth.

2.1.1.4 Silicon nitride membrane

In order to observe the microstructure of the deposited films by Transmission Electron Microscopy (TEM), without any specific preparation, using Focused Ion Beam technique (Sec. (2.3.6)), the layers were directly deposited onto a SiN_x membrane provided by Ted Pella Inc. These specific substrates, dedicated to the TEM analysis, are composed by 9 windows of $100 \times 100\,\mu m^2$ made of a Si_xN_y layer. Their thickness of 15 nm is small enough to be transparent to electron beam of 200 keV used during TEM acquisitions. The extreme surface of this Si_xN_y layer is partially oxidized leading to a surface similar to that of a silicon wafer.

2.1.2 The sputtering deposition chambers

The sample elaboration was shared between two main research centres : (i) the industrial pole of Saint-Gobain Research Paris (SGR Paris) and (ii) the academic Institute of Physics of RWTH Aachen University. The single crystal based model samples and the industrial reference stacks were produced at SGR Paris, while some IBAS samples were made at RWTH. In total, this work involved the use of four different sputtering deposition setups that are described below. All samples were deposited at room-temperature.

2.1.2.1 The sputtering machines MISSTIC and LINA at SGR Paris

The single crystal based samples were produced in the research sputtering machine of SVI CNRS/SGR Paris laboratory called MISSTIC (Multilayer and Interfaces Sputtered-deposition

on STructured substrates and In situ Characterization), a modified Vinci-Meca 2000 model (Fig. (2.1)).
Asides a sputtering deposition chamber, the vessel is composed of an analysis chamber and two load-locks, one between the two main chambers, allowing for the introduction of up to four samples of a 2" size, and one directly connected to the analysis chamber. The transfer between chambers is insured through a system of manually controlled arms. Thanks to this design, single crystal samples could undergo a specific surface treatment in the analysis chamber and be directly transferred to the deposition machine, without being exposed to air and therefore avoiding surface contamination. An average base pressure of the order of 10^{-8} mbar is reached in all chambers via turbomolecular pumps, combined with ion pump and titanium sublimator in the analysis chamber.

Name	**Target**	**Mode**	**Power** [W]	**Pressure** [μbar]	**Ar flow** [sccm]	**O_2 flow** [sccm]	**Deposition rate** [nm/s]
AZO	ZnO:Al-cer	DC	50	2.0	50	-	0.15
ZnO	Zn-met	DC	50	3.4	75	18	0.45
Ag	Ag	DC	50	2.0	50	-	0.63

Table 2.2 Deposition conditions of the different materials used in the MISSTIC sputtering chamber.

The deposition chamber can host three circular magnetron cathodes designed for 2" and 3 mm thick targets and equipped with a shutter. During deposition, the sample is positioned at a distance of 130 mm from the target. Gases (Ar for sputtering) are introduced into the chamber and monitored through MSK Instruments mass flow while the pumping speed is regulated through the opening of a throttle valve. In this work, the magnetron cathodes were powered by a direct-current (DC) source, while a magnetic field of about 0.3 T was generated by permanent magnets close to the target. Typical deposition conditions for all layers are reminded in Tab. (2.2). The analysis chamber is equipped with a photoemission spectrometer (Sec. (2.3.2)), a low-energy electron diffraction device (Sec. (2.3.1)) and specific tools for sample preparation (Sec. (2.2)).

The industrial reference stacks were made on a pilot line coater of SGR Paris (Alcatel LINA 350) (Fig. (2.2)). Compared to the other deposition chambers used in this study, the LINA 350 is designed for dynamic deposition with moving samples as in coaters of actual industrial plants. The substrates are placed on rectangular plates, which serve as sample holders, and uploaded in air on a stacker which can hold up to nine samples of 30×30 cm^2 size. Each plate is mechanically introduced in the load-lock and transported by a conveyor belt in the different chambers. Here, thanks to the presence of turbomolecular pumps, combined with liquid nitrogen trap, the average base pressure reaches the 10^{-7} mbar range. In the sputtering chambers, the cathodes are pointing downward, while the samples pass horizontally below them at a distance of ~70 millimetres. The sputtered layer thickness is controlled through the speed at which the sample passes under the target, and the power applied to the target. The machine can be equipped with up to nine magnetron cathodes able to hold rectangular targets isolated from each other. During the deposition, various gases and mixture of gases such Ar, O_2 or N_2 can be introduced depending on the deposition mode of the material, *i.e.* metallic or reactive sputtering. The following Tab. (2.3) describes the operating conditions selected for the different layers used in this work.

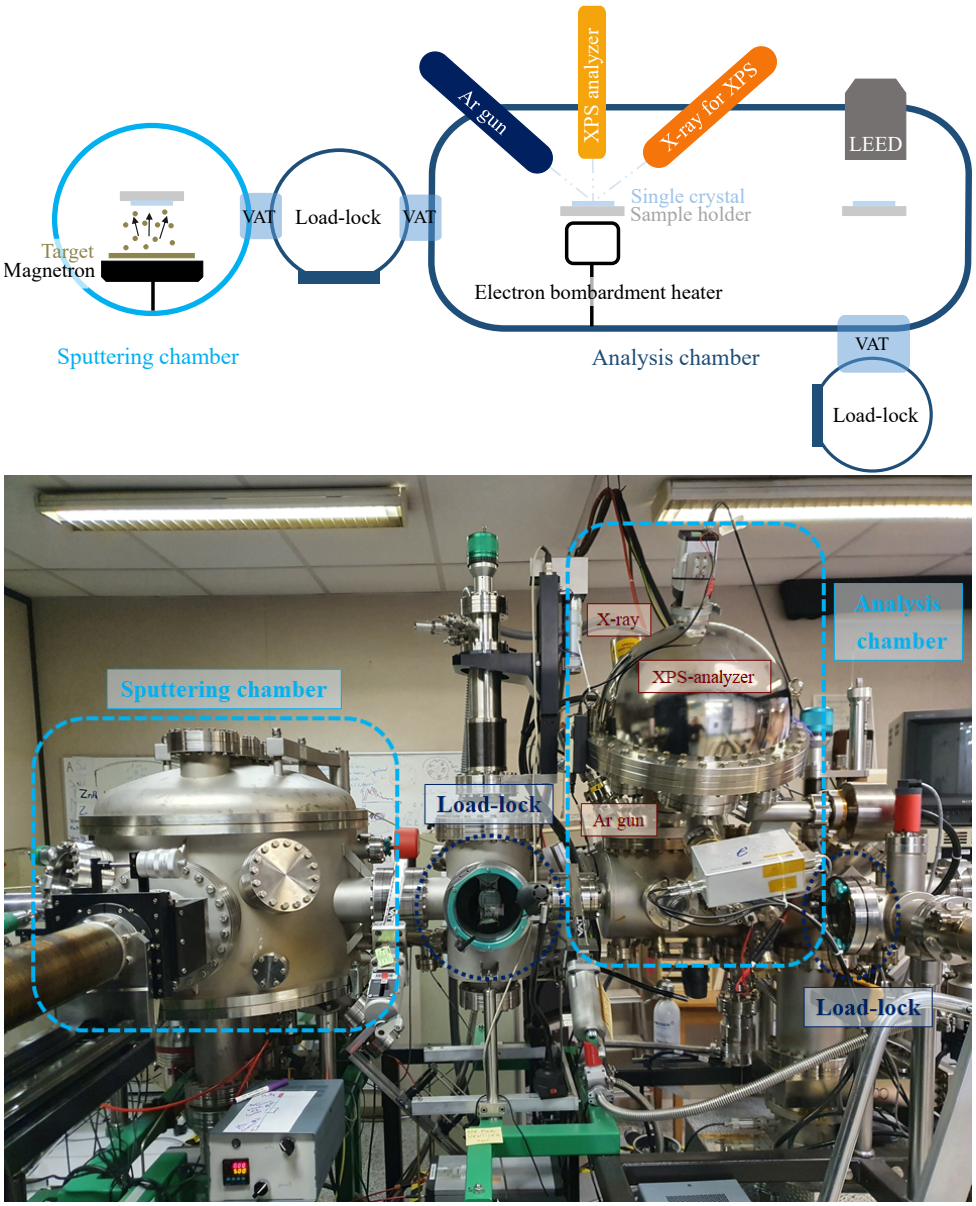

Figure 2.1 The schematic representation and picture of the MISSTIC machine, composed of a sputtering chamber which can host three different deposition targets, and an analysis chamber, equipped with a photoemission spectrometer, an argon gun, an electron bombardment heater and a LEED device. The different compartments are connected via load-locks.

Name	Target	Mode	Power [W]	Pressure [μbar]	Ar flow [sccm]	O_2 flow [sccm]	Plate speed [m/min]
AZO	ZnO:Al-cer	DC	500	2	40	-	1.50
ZnO	Zn :Al	DC	750	2	15	14	0.89
Ag	Ag	DC	210	8	80	-	0.82
Si_xN_y	Si :Al	DC	2000	2	18	20/24	0.46

Table 2.3 Deposition conditions of the different materials used in the LINA sputtering chamber.

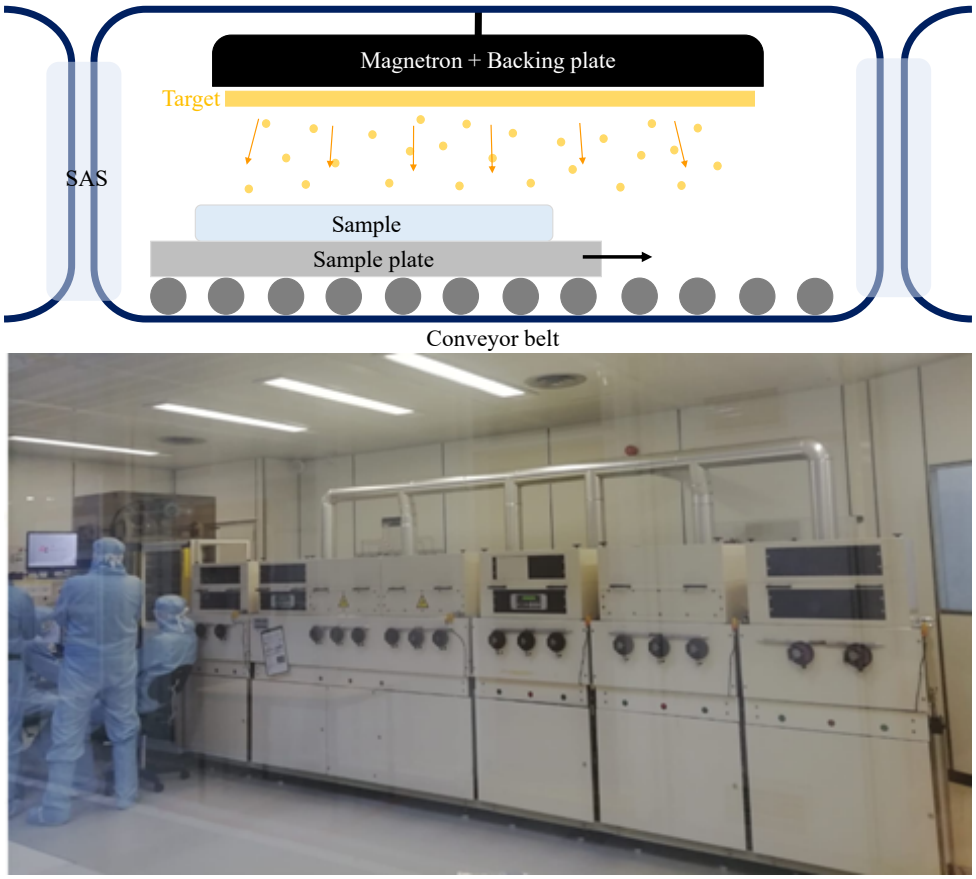

Figure 2.2 Schematics of a section of the LINA sputtering chamber. The setup is equipped with multiple chambers that can host one or more targets. During the deposition, the sample moves below the target at a speed defined by the material thickness that needs to be sputtered and the power applied to the target. On the bottom, a picture of the machine.

2.1.2.2 The sputtering machines MYTHIC and IBAS at RWTH Aachen Institute of Physics

At the RWTH Aachen Institute of Physics, a multiple-layer custom-built coater was mainly used for the fabrication of some reference stacks for comparison with IBAS results. The system, named MYTHIC (Multi-Layer Thin Film Coater) can contain up to six different magnetron cathodes that can be equipped with a 3" target, and allows the fabrication of 24 different samples of (2×2) cm^2 in size in one sputter run. Samples are positioned on a revolving substrate stage at 55 mm from the targets (Fig. (2.3)). To avoid the unintentional coating of targets and samples not in use, additional shields are installed between the target and the sample holder.

Prior to each deposition, a base pressure of about $2{\cdot}10^{-6}$ mbar is established in the sputtering chamber by a turbomolecular pump. During deposition, performed at fixed sample position, the pressure is controlled by reducing by half the pumping speed through the opening of a valve positioned in front of the pumping system. In addition to Ar, O_2 and N_2 can also be introduced in the system at a regulated flow (MSK Instruments mass flow controllers). For our samples, plasma was driven via a direct current power supply, with a maximum output of 20 kW, for metallic targets and ceramics targets. Deposition conditions are reminded in Tab. (2.4).

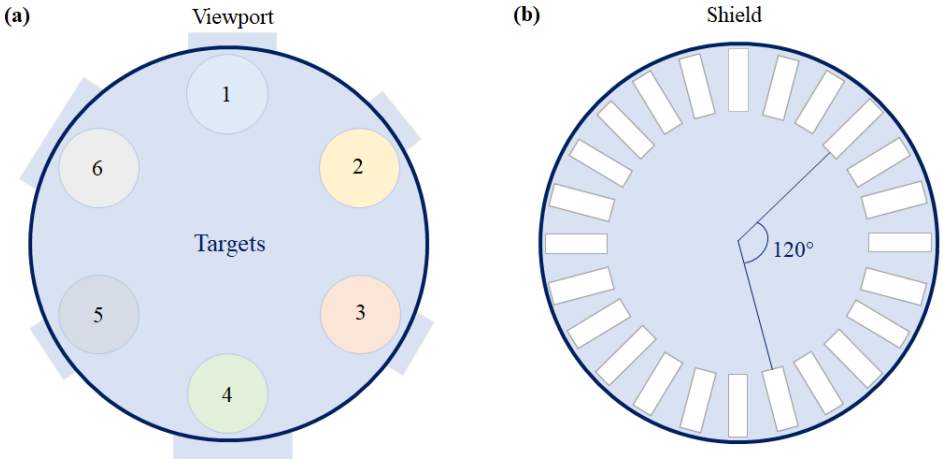

Figure 2.3 (a) Sketch of the MYTHIC deposition chamber view from the top equipped with six targets. (b) Schematic view of the sample holder.

Name	Target	Mode	Power [W]	Pressure [μbar]	Ar flow [sccm]	O_2 flow [sccm]	Deposition rate [nm/s]
AZO	ZnO:Al-cer	DC	30	5	35	-	0.33
Ag	Ag	DC	25	12	52	-	0.68
SiN	Si-met	DC	80	4	10	15	0.15

Table 2.4 Deposition conditions of the different materials used in the MYTHIC sputtering chamber.

Ion beam assisted sputtered layers were deposited on a specific custom-built coater named IBAS-chamber (Fig. (2.4)). The system, consisting of a cylindrical sputtering chamber, can be equipped with a maximum of two 3" magnetron targets. The sample-holder holds up to six samples of (2×2) cm^2 in size, and it is positioned at 55 to 80 mm from the target, a distance that can modified by adjusting the cathode position. A shutter is located just above each target and an additional shield can also be introduced to block the trajectory of high energy oxygen ions [86, 89, 90]. The system is designed for the deposition of thin films with the aid of an external ion bombardment gun. The ion source (Tectra Gen II) is installed next to one of the magnetron target, with an additional differential pumping stage. The gun is fixed at an angle of 45° with respect to the sample surface which is maintained at a distance of 80 mm to clear the gun ion trajectories to the substrate. The gas (Ar, O_2 or Xe) is fed directly into the plasma cup of the ion source, ensuring a high purity of the ion species. The ion current was calibrated on the surface of a flat copper substrate of (1×1) cm^2 size. The sputtering chamber base pressure is maintained by a turbomolecular pump at around $7{\cdot}10^{-7}$ mbar. Similarly to MYTHIC, the pump speed is reduced to half its value while Ar, O_2 and N_2 are introduced at controlled flow (MSK Instruments). The same power supply as for MYTHIC chamber is also available on the IBAS-machine. Deposition conditions are given in Tab. (2.5).

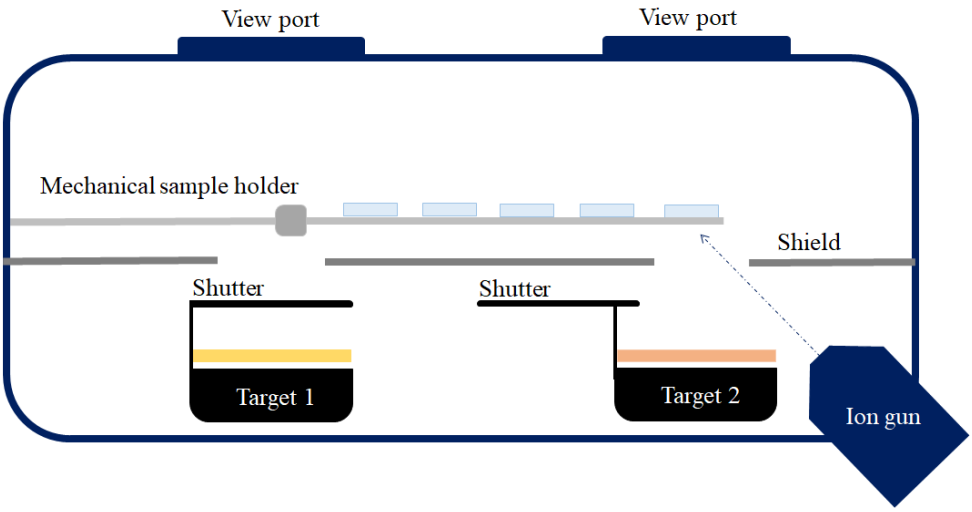

Figure 2.4 Schematic cross section of the IBAS setup. The chamber is equipped with two targets and an ion gun. For this study, the Ag cathode was positioned at Target 1 and Zn metallic cathode at Target 2.

Name	**Target**	**Mode**	**Power** [W]	**Pressure** [μbar]	**Ar flow** [sccm]	**O_2 flow** [sccm]	**Deposition rate** [nm/s]
ZnO	Zn-met	DC	85	2	15	13	0.36
Ag	Ag	DC	25	11	62	-	0.95

Table 2.5 Deposition conditions of the different materials used in the IBAS sputtering chamber.

2.1.3 Calibration of the deposition rate

Based on the sputtering time, the deposition rate of materials was mainly estimated through a profile analysis of a step in the film. Firstly before the introduction of the substrate in the chamber, a pencil marker line is made in its centre. To minimize the uncertainties, a thick layer of the order of hundred nanometres is then deposited on top of it. The sample is then transferred to an ethanol or acetone bath and sonicated to eliminate the marker trace and the material deposited on it. The resulting step height is measured via AFM or via a profilometer (Bruker Dektak XT) with a precision of ± 1 nm. This measurement is based on the assumption that the deposition rate is constant throughout all the sputtering process. As an alternative method, X-ray reflectivity (Sec. (2.3.5.5)) was used to determine the film thickness. In this case, thinner films of about 100 nm are preferred for a better accuracy.

2.2 Surface preparation of ZnO single crystal

Specific *in situ* surface treatments were applied to the ZnO single crystal substrates. They are intended not only to remove the surface contaminants, such as hydrocarbons or hydroxyl groups, but also to heal the damage of polishing by giving to the surface atoms enough mobility to recrystallize in a terrace-step structure. Treatments were performed in the analysis chamber of the MISSTIC sputtering system (Sec. (2.1.2.1)). They all involve a first low temperature surface heating, to outgas the surface and its holder, followed by cycles of argon bombardment and annealing at higher temperature. The details of the different treatments are reported in

Sec. (4.2). The treatments were performed under ultra-high vacuum ($8 \cdot 10^{-9}$ mbar average chamber pressure) just before the deposition of the Ag layer in the sputtering chamber without exposing the sample to air. At the opposite, all glass and Si substrates were used as provided without any specific surface treatments other than standard surface cleaning (for glass : washing, with surfactant and deionized water, and drying with nitrogen, for Si wafer : dusting with a flow of nitrogen).

2.2.1 Electron bombardment heating

Sample heating was achieved through electron bombardment produced by accelerating electrons by means of a high voltage (-1500 V) from a thermionic W-filament cathode placed at distance of 4.5 millimetres from the sample holder (Fig. (2.5)). In this configuration, the sample is held on a Mo backplate, which is positioned in front of the filament and transmits its heat to it. The calibration curve between temperature and dissipated power (product of emission current and accelerating voltage) was achieved via a thermocouple spot-welded onto the surface of the Mo sample backplate (Fig. (2.5)). Even if caution was taken to reach a stable temperature at each power ($\sim$ 30 min), an uncertainty of ± 50°C can be estimated on the temperature actually reached by the surface due to sample clamping and the poor thermal conductivity of the dielectric ZnO substrate. Nevertheless, this inaccuracy is irrelevant to the final conclusions.

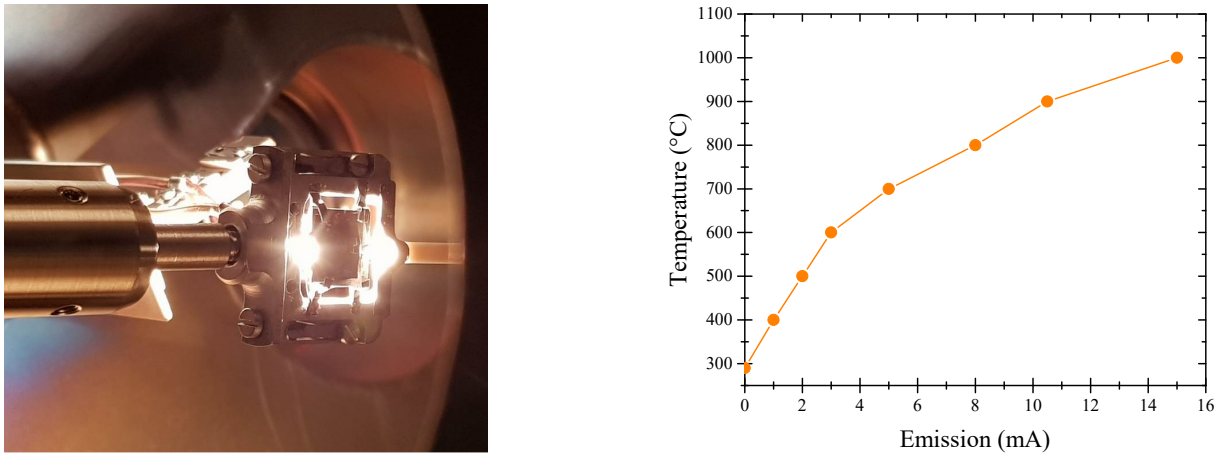

Figure 2.5 (Left) Picture of the *in situ* annealing process where the sample holder is positioned with a transfer rod in front of the filament. (Right) Temperature calibration curve as a function of the filament current emission at fixed voltage (-1500 V).

2.2.2 Argon ion bombardment

For the single crystal preparation, argon bombardment was used to remove the contamination layer from the surface by sputtering. The gun (IQE 12/38 from SPECS) is equipped with a small ionization chamber that is filled with argon gas at pressure higher by three order of magnitude than the measured pressure in the chamber (10^{-7} mbar). The Ar atoms are ionized by a flux of electrons produced by a 7 mm filament uniformly coated with thorium oxide to decrease its work function and improve its electron emission. Thanks to extraction plates suitably polarized, the positive ions are accelerated towards the sample (beam energy of 1000 eV) and collide with its surface, sputtering the atoms they encounter. The gun is set in unfocussed mode to homogeneously sputter the sample.

To calibrate the sputtering rate, a layer of zinc oxide was deposited on a glass substrate. At a fixed chamber pressure of 10^{-7} mbar and gun parameters, the film was bombarded until its disappearance as monitored through a camera and Zn 2p core level analysis in XPS. Knowing the initial thickness, a sputtering rate of ∼0.33 nm per minute was estimated for this material.

2.2.3 *Ex situ* annealing

After the stack deposition, which included a 30 nm layer of amorphous Si_xN_y protective capping layer, the samples were submitted to a thermal treatment to improve the structural and conductive properties of the Ag layer. This post-deposition annealing was performed in air following the conditions normally used in industry for glass tempering or shaping.

The larger samples on a glass substrate, with a surface wider than (5×5) cm^2, were annealed in a ceramic Naber oven at 650°C for 10 minutes. To avoid the deformation of the glass sheet and to ensure a uniform heating, the samples were placed on a vitro-ceramic plate with a high glass-transition temperature. Once annealed, the samples were allowed to cool down in air on this support which enables the slow release of heat avoiding the formation of cracks generated by thermal shock.

For smaller samples, with a surface area of about (1×1) cm^2, the annealing process was carried out in a smaller ceramic Nabertherm oven (model L9). To avoid the corrosion, especially occurring on the sample sides, degradation and dewetting of the Ag layers, the annealing temperature was lowered to 350°C while duration was maintained at 10 minutes. During processing, the samples were placed on a cylindrical refractory silimanite brick, an alumina-based composite, having the same role as the vitro-ceramic used with glass plates.

2.3 Characterization techniques

In this work, *in situ* X-ray photoelectrons spectroscopy (XPS) and Low-Energy Electron Diffraction (LEED) measurements were performed right after the single crystal surface treatment to check the surface chemistry and crystallography. These tools are located in the analysis chamber (base pressure $\sim 8 \cdot 10^{-9}$ mbar) of the MISSTIC sputtering system. This configuration allows to perform the analysis without air exposure before the growth of the stack in the connected sputtering chamber. At the opposite, the *ex situ* characterization techniques imply an exposure of the sample to the atmosphere which requires, in the case of silver layer, a protective coating (ZnO and Si_xN_y films) to avoid sample evolution and/or oxidation. These *ex situ* techniques encompass Atomic Force Microscopy (AFM), all the variants of X-Ray Diffraction (XRD), Transmission Electron Microscopy (TEM) and electric transport measurements.

2.3.1 Low Energy Electron Diffraction

Low-Energy Electron Diffraction (LEED) is a surface characterization technique used to analyse the crystallography of single crystal surfaces and deposit/adsorbate on top [162] (Fig. (2.6)-a). Basically, the surface sample is irradiated by a flux of monochromatic electrons generated by a cathode filament. Before reaching the sample surface, the electrons are accelerated to a kinetic energy in the range 10-200 eV and focused into a beam (typically $0.1 - 0.5$ mm wide) by a series of electrodes. Due to the dual particle-wave nature of electrons having a wavelength in the Angstrom range at these energies, the interaction with the crystalline lattice causes electrons to diffract. Thanks to a series of hemispherical concentric grids that act as a filter, only elastic backscattered electrons are then collected before being accelerated up to several thousands of

eV by the last grid onto a fluorescent screen creating the diffraction pattern. Due to the low energy of the electron beam, the penetration depth is limited to the very first layers, while the coherence length is restricted to the range of few nanometres due the beam divergence (few degrees) and energy spread (0.1 eV). Therefore, the resulting reciprocal space pattern of the sample consists of diffraction rods normal to the sample surface and only the in-plane periodicity is probed. Diffraction directions are given by the intersection of these rods and the Ewald sphere in the backward direction (Fig. (2.6)-b). It is from the analysis of the positions and of the broadening/intensity of diffractions spots that qualitative and quantitative information can be retrieved on the symmetry and quality of the reconstruction of the surface.

To digitalize the LEED patterns, a camera was installed behind the viewport in front of the fluorescent screen. The pictures were treated by a home-made *Python* code with the objective of quantifying the ratio of integrated diffracted peak intensity to background in between spots.

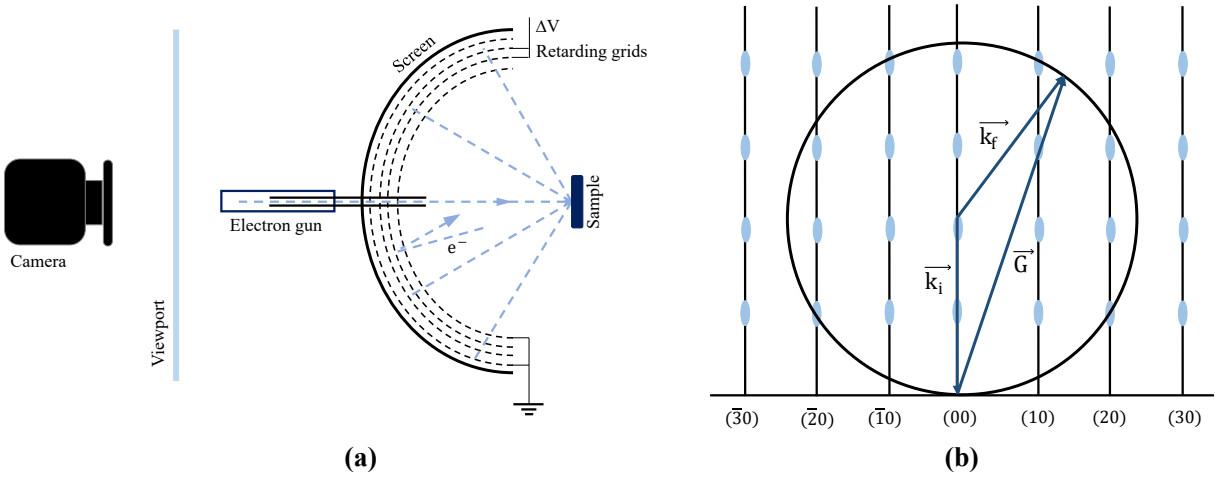

Figure 2.6 (a) Principle of a LEED acquisition. (b) The reciprocal lattice of the surface, represented by crystal truncation rods and the Ewald-construction for surface diffraction.

2.3.2 X-ray Photoelectron Spectroscopy

Principle

The X-ray photoelectron spectroscopy (XPS) is a surface-sensitive characterization technique used for the identification and quantitative analysis of the sample surface elements and their chemical states [163]. Its principle (Fig. (2.7)) is based on the photoelectric process. The sample is irradiated with an X-ray source (most common emission lines being Al Kα at 1486.6 eV or Mg Kα at 1253.6 eV). The absorption of a photon (energy $h\nu$) results in the emission of an electron with a characteristic kinetic energy (E_K) that is linked to the binding energy (E_B) of the corresponding core levels via the Einstein's photoelectric equation :

$$E_K = h\nu - E_B - e\phi_S, \tag{2.1}$$

where $e\phi_S$ is the work function of the sample. It is therefore through the measure of the kinetic energy of the emitted electrons that all the information are retrieved. Indeed due to the alignment of the Fermi levels of the sample and of the analyser, only the work function of the latter is really required. Starting from the Fermi level and the valence band of the material, the photoelectron

energy distribution is mainly characterized by a series of peaks corresponding to the core levels (s,p,d,f) from which electrons are ejected. The peak intensity is proportional to the element concentration on the sample surface. As each atom has its own characteristic energy spectra, it is possible to identify the different elements present on the surface. Due a change of screening of core levels upon binding, E_B is also sensitive to the chemical environment of the probed atom. In addition to the photo-peaks, a series of features associated to Auger transitions is also present in the spectrum. Upon photon absorption, a core hole is created at its initial energy state. To return to equilibrium, the system can release a photon via a transition of an electron from an upper orbital or fill the vacancy with a higher energy electron, which transfers its excess energy to an electron from an upper orbital that leaves the atom (Auger effect) (Fig. (2.7)). The kinetic energy of the Auger electron is therefore the difference of the three energy levels involved in the process.
At last, core level and Auger peaks are overlapped on a background of secondary electrons generated through the inelastic interactions of the photoelectrons along their path to the surface. The elastic electron signal is damped exponentially over a characteristic lenght, the so-called Inelastic Mean Free Path (IMFP) [164]. Its dependence with kinetic energy follows a U-shaped curve with a minimum of $\sim$ 1 nm reached around 100 eV. This makes XPS a technique of extreme surface sensitivity.

Equipment

The used XPS equipment consists of (i) a dual unmonochromated X-ray source (XR50 from SPECS) equipped with Mg Kα (working power 150 W) and Al Kα (working power 200 W) anodes and (ii) an hemispherical concentric analyser (Phoibos 100 from SPECS). The electrons emitted from the surface are collected by a series of electrostatic lenses that not only focus the beam onto the entrance slit of the analyser but also accelerate/decelerate them to the so-called pass energy (10 to 50 eV). The hemispherical analyser acts as a band pass filter for this energy. At the exit of the analyser, the electron signal is amplified by channeltron electron multipliers. For the analysis, the sample is positioned at the focal point of the analyser with the help of a circular diaphragm while being illuminated by the broad emission X-ray gun. The resolution of the order of 1 eV is fixed by the X-ray source line-width, the choice of entrance and exit slits as well as by the pass energy.

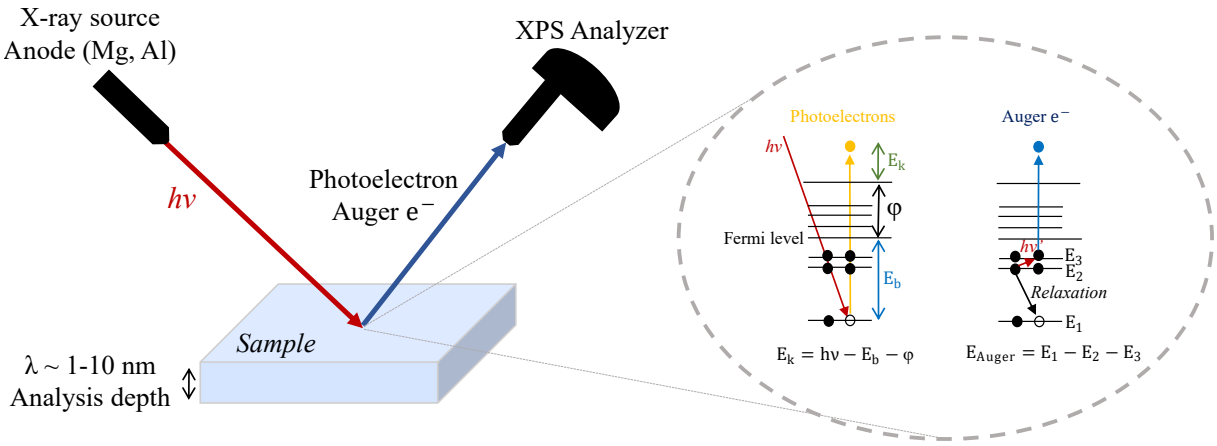

Figure 2.7 Principle of photoemission spectroscopy. Electrons emitted from a sample irradiated by X-rays are analysed in kinetic energy to retrieve their binding energy.

Data treatment

Photoemission was used during ZnO single crystal surface preparation to follow the evolution of surface contamination. Data were analysed by the *CasaXPS* software for the identification and quantification of the elements. If required, spectra were firstly corrected from charge effects due to the poor conductivity of the sample by realigning the binding energy scale on adventitious carbon (284.8 eV). Prior to calculating peak area, a Shirley background [165] over a common energy range for each core level of each sample was subtracted. To quantify sample composition, for the sake of simplicity, a model of homogeneous medium was used. This overestimates the impact of surface species. Peak area were corrected from the analyser transmission function and the relative sensitivity factors listed in the *CasaXPS* library. To analyse chemical environment of elements, peaks were fitted with a pseudo-Voigt function (mixture of Gaussian and Lorentzian). The analyses focused on C 1s, O 1s and Zn 2p 3/2 core levels. The Zn 2p core level is poorly influenced by the chemical environment shifting from 1021.5 to 1022.0 eV when going from metallic to oxide state. Regarding O 1s core level, several components can be distinguished : (i) 530.5 eV corresponding to bulk O^{2-}, (ii) a shoulder at 532.0 eV due to OH groups while adsorbed H_2O molecules appear at at 534.4 eV. Defective non-stoichiometric ZnO surface is characterized by a peak at 532.0 eV [166–168]. Finally, in the case of Al-doped ZnO films, oxygen bonded to Al appear at 531.0 eV. Therefore, it is not always possible to differentiate the various contributions of the different oxygen species. When a sample is exposed to the atmosphere, a thin contamination layer of carbon, usually between 1 and 2 nm thick, is adsorbed on the surface. The pollutant, called adventitious carbon (AdC), has a characteristic C 1s peak at 284.8 eV [169], corresponding to the C-C bond. Independent of the chemical composition of the substrate, AdC shift is often used, also in our case, as a binding energy reference for the spectra. In some cases, the carbon contamination peak includes C-O-C ($\sim$ 286 eV) and O-C=O ($\sim$ 288.5 eV) components.

2.3.3 Atomic Force Microscopy

Atomic Force Microscopy (AFM) belongs to the family of near-field scanning probe microscopies ; it is mainly used for the topographic characterization of surfaces at the nanoscale. It is based on the interaction of a nanoscopic sharp tip, whose curvature radius is typically around 10 nm, mounted at the front end of a cantilever (Fig. (2.8)). Upon approaching the surface, the attractive forces of Van der Waals type at large distances and the repulsive ones at contact provoke a deflection of the cantilever in agreement with Hook law. The deflection is measured through a laser, which is reflected on the back side of the cantilever to a photodiode array which records the laser intensity variations. The signal is then converted to a voltage directly related to the interaction forces. The cantilever is mounted on a piezo-electric ceramic that allows to scan the (x,y,z) space via controlled voltages. The range of scanning along (x,y) is of the order of the micrometre while along z it is of the order of nanometre. Measurements were performed in tapping mode. In this configuration, the cantilever is left oscillating close to the surface at its resonant frequency with a constant amplitude. The tip does not get in direct contact with the sample, avoiding friction and surface damage. However, as the tip scans the surface, the local topographic and chemical variations of the sample generate a change in the force applied to the tip and therefore in the phase and amplitude of the cantilever oscillation. These perturbations are compensated through a feedback mechanism which adjusts the tip-surface distance in order to keep the vibration amplitude constant. Recording the extension of the piezoelectric ceramic, the device allows to obtain a map of surface topography while the phase contains information on composition and density.

The present results were obtained at SVI laboratory on a Dimension Icon made by Bruker company using a monolithic silicon tip. The Bruker software *Nanoscope Analysis* was used for image treatment such as image flattening to correct from piezo curvature. Sample roughness was quantified through the root mean square average of height deviations taken from the mean image data plane :

$$R_q = \sqrt{\frac{1}{n}\sum_{i=1}^{n} \Delta z_i^2}. \tag{2.2}$$

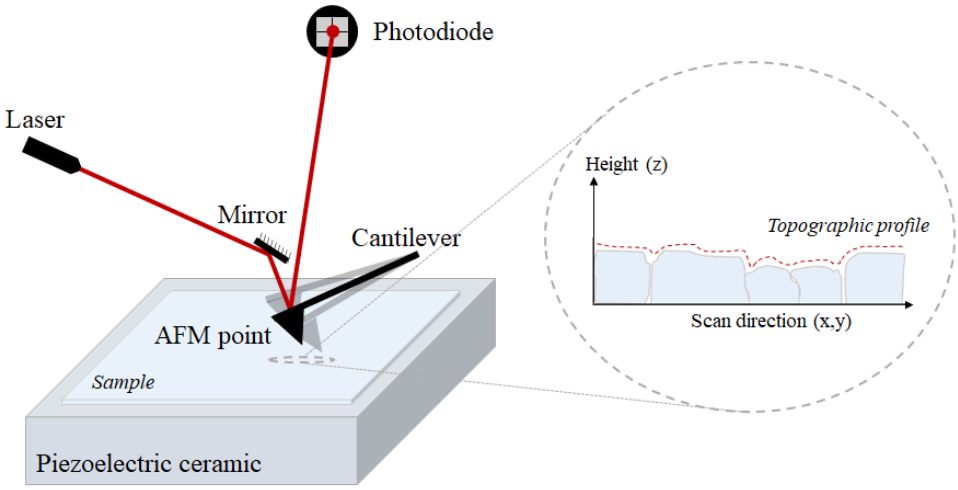

Figure 2.8 Schematic representation of the AFM principle : the forces of interaction between the surface and a nanoscopic tip is detected optically via the deflection of the cantilever ; a map of corrugation is obtained by scanning the tip over the surface via a piezoelectric device.

2.3.4 X-Ray Diffraction

X-Ray Diffraction (XRD) is a non-destructive technique used to determine the structural properties of matter. XRD was used herein to characterize the crystallinity of Ag and ZnO layers in the synthesised stacks. To extract (micro)structural information such as internal strain/stress, crystal size and orientation (texture), layer density, thickness and roughness, several measurement configurations have to be combined. They are described in the following sections.

2.3.4.1 General principle of X-ray diffraction

The XRD technique is based on the elastic interaction between a X-ray beam of a wavelength λ, and the electron cloud of atoms of the probed material. In a crystal, atoms are arranged in an highly ordered periodic way, the crystal lattice, that consists in the repetition of a unit cell, the smaller unit containing all the symmetries of the crystal structure [170]. When an incident X-ray of wave vector $\mathbf{k}_i$ hits the sample, it is elastically scattered by the atoms of the crystal planes of the solid. Due to the crystalline periodicity, the scattered wavefronts will interfere constructively along a given direction $\mathbf{k}_f$ if the optical path difference between scattering planes equals a whole number of wavelength (Fig. (2.9)-Fig. (2.10)). Consequently, a characteristic diffraction pattern will be created if the Bragg law is satisfied :

$$2d_{hkl}\sin\theta = n\lambda, \tag{2.3}$$

where n is an integer, referred to the order of diffraction, d_{hkl} is the distance between two adjacent crystalline planes belonging to the $\{hkl\}$ family where h, k and l are the Miller indexes, and θ is the angle between the incident/diffracted beams and the involved crystal plane. In the case of a powder where all crystal orientations are present, the diffraction pattern, called diffractogram, consists of a series of peaks at specific angles, each associated to a given crystal plane family. Therefore, from the position of the peaks, it is possible to determine the crystalline structure of the sample via d_{hkl}. For a cubic lattice of parameter a (such as in the case of silver) :

$$\frac{1}{d_{hkl}^2} = \frac{h^2 + k^2 + l^2}{a^2}, \tag{2.4}$$

while in the case of a hexagonal lattice (such as in the case of ZnO) of parameters a, c along $[100], [001]$ directions,

$$\frac{1}{d_{hkl}^2} = \frac{4}{3}\frac{h^2 + hk + k^2}{a^2} + \frac{l^2}{c^2}. \tag{2.5}$$

Beyond the Bragg description, the concept of reciprocal space is quite helpful in understanding and predicting the diffraction phenomena. It is the Fourier transform of the real space lattice ; the crystalline planes of the real space become spots, the shape of which is directly correlated to the microstructure of the material. Each point of the reciprocal space can be described by a vector via :

$$\vec{G_{hkl}} = h\vec{b_1} + k\vec{b_2} + l\vec{b_3}, \tag{2.6}$$

with h, k, l being integers, the Miller indexes of the corresponding diffracting crystal planes $\{hkl\}$, while $\vec{b_1}$, $\vec{b_2}$ and $\vec{b_3}$ are the basis vectors of the reciprocal lattice of size Å^{-1}. They are built from the basis vectors of the real space lattice $\vec{a_1}$, $\vec{a_2}$ and $\vec{a_3}$:

$$\vec{b_1} = 2\pi\frac{\vec{a_2} \times \vec{a_3}}{\vec{a_1} \cdot (\vec{a_2} \times \vec{a_3})}, \quad \vec{b_2} = 2\pi\frac{\vec{a_3} \times \vec{a_1}}{\vec{a_1} \cdot (\vec{a_2} \times \vec{a_3})}, \quad \vec{b_3} = 2\pi\frac{\vec{a_1} \times \vec{a_2}}{\vec{a_1} \cdot (\vec{a_2} \times \vec{a_3})}. \tag{2.7}$$

In the reciprocal space, the Bragg condition for a constructive interference is equivalent to the so-called Laue equation :

$$\vec{Q} = \vec{k_f} - \vec{k_i} = \vec{G_{hkl}}, \tag{2.8}$$

which implies that diffraction can only occur when the difference between the diffracted and incident wave vectors is equal to a reciprocal space vector. Since diffraction is an elastic phenomenon $\vec{k_f}$ and $\vec{k_i}$ have the same modulus. Therefore, one can define a sphere of radius $k_i = k_f = 2\pi/\lambda$, the Ewald sphere, on which lies the scattering vector $\vec{Q}$ when diffraction occurs (Fig. (2.9)).

At last, the total intensity I_{hkl} of a given diffraction node integrated over all the directions of reciprocal space is given by [171] :

$$I_{hkl} \propto c|F_{hkl}|^2 p f_{LP} A f_T, \tag{2.9}$$

where c is a proportionality constant, F_{hkl} is the structure factor, p the multiplicity of the reflection, f_{LP} the Lorentz-polarization factor, A the absorption term and f_T the Debye-Waller temperature factor. The structure factor describes the scattering by the content of an unit cell. Due to symmetries, F_{hkl} can be equal to zero meaning that the corresponding reflection is forbidden. Thus the description of the Ag structure by a face-centred cubic lattice leads to diffraction only when h, k and l indexes are of the same parity.

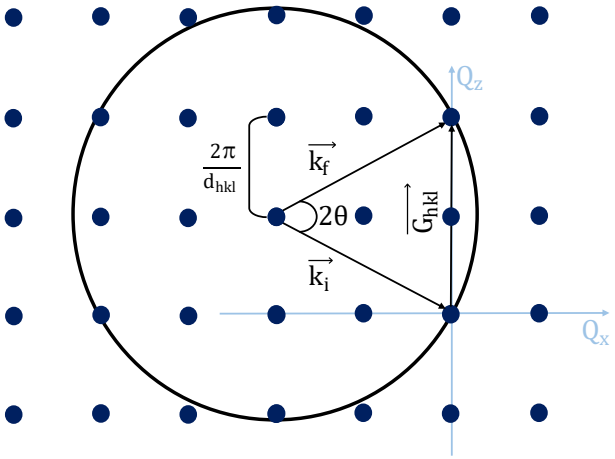

Figure 2.9 Ewald sphere construction of the diffraction process. The diffraction beam occurs along $\vec{k_f}$ only when $\vec{Q} = \vec{k_f} - \vec{k_i}$ is a vector of reciprocal space. All the points lying on the sphere will result in a diffracted beam.

For the purposes of the present study, different scattering geometries, that will be described in the next sections, were combined to analyse the coating (micro)structure :

— the usual $\theta - 2\theta$ or Bragg-Brentano configuration along the direction normal to the stack, the so-called out-of-plane direction ;
— the grazing incidence geometry for the analysis of in-plane grain size and orientation ;
— the pole figures for the overall texture analysis ;
— the X-ray reflectivity for film thickness and roughness determinations.

2.3.4.2 $\theta - 2\theta$ Bragg-Brentano scattering geometry and the rocking curve

In the $\theta - 2\theta$ configuration, also known as Bragg-Brentano, the incidence beam and the detector are positioned in a symmetrical specular configuration at the same angle θ with respect to the surface sample (Fig. (2.10)-a). During the measurement, the surface of the sample remains horizontal and the X-ray tube and the detector are moved simultaneously along the same circle at the same speed $d\theta/dt$, so that the bisector of the angle between the two directions is fixed and always parallel to the substrate normal. In this configuration, the wave vector transfer $\vec{Q}$ is always normal to the surface of the sample so that only crystallographic planes parallel to the surface contribute to the diffractogram.

From the analysis of the position and shape of the diffraction peaks, it is possible to retrieve microstructural information about the probed film. A change of the 2θ peak position compared to the bulk reference value indicates a change of lattice parameter induced by a macrostrain in the vertical direction. Also, beyond the instrumental resolution, the peak broadening as measured by its Full Width at Half Maximum (FWHM) is the result of different contributions :

— the microstrain inducing fluctuations of lattice parameters ; they are due to composition fluctuations, dislocations and other crystal imperfections such as grain boundaries or stacking faults ;
— the vertical finite crystallite size, limited at least by the thickness of the film.

In the case of a film containing only one crystallite in the vertical direction, the Bragg reflection can show additional oscillations on its side, the so-called Laue fringes ; they are an indication of an extremely well crystallized, textured and smooth film. The intensities of the oscillations I_{hkl}

are given by [172, 173] :

$$I_{hkl}(N_{hkl}, \vartheta) = N_{hkl}^2 u^2 \frac{(\sin \vartheta)^2}{\vartheta^2}, \tag{2.10}$$

with $\vartheta = 2\pi\ \mathrm{d}_{hkl} \Delta\theta \lambda \cos\theta$, $\Delta\theta$ the deviation from the Bragg angle θ, N_{hkl} the number of lattice planes in the film and u the scattering amplitude of one plane. For instance, in the case of (111) out-of-plane textured 10 nm thick Ag film, $N_{hkl} = 43$ atomic planes with a distance $d_{\{111\}} = 2.35$ Å. However, the constructive interferences which lead to Laue fringes are present only for a perfectly oriented film and vanish very quickly, as in the case of X-ray reflectivity, if the surface roughness is too high. A more detailed discussion on the analysis of peak FWHM is postponed to Sec. (2.3.5).

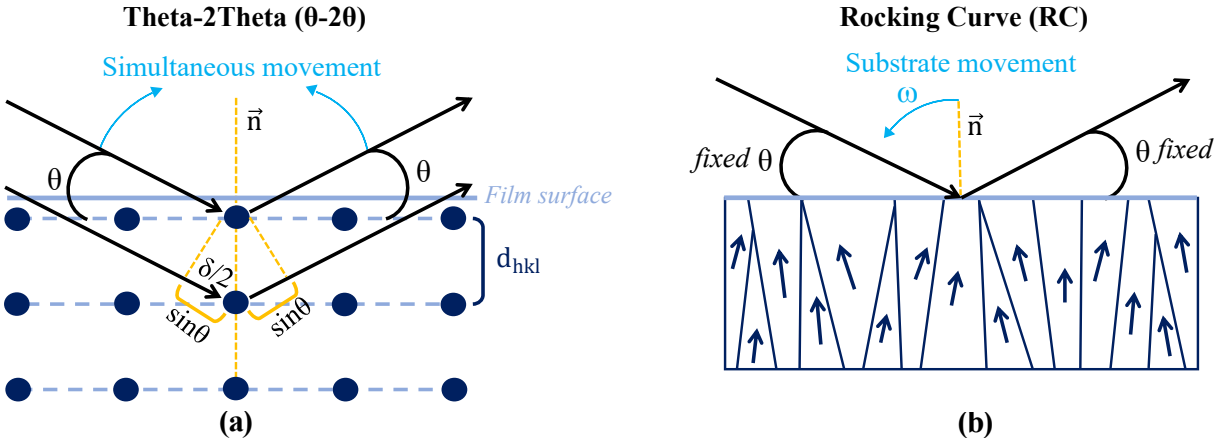

Figure 2.10 (a) In the $\theta - 2\theta$ or Bragg-Brentano scattering geometry, the X-ray source and the detector are moved simultaneously maintaining the same angle θ with respect to the surface; only the planes parallel to the surface are probed. (b) In the rocking scan geometry, the scattering 2θ angle associated to a given family of planes is kept fixed, while the sample is tilted by an angle ω. In this configuration, it is possible to collect information about the distribution of orientations of the probed plane (and therefore of crystallites) with respect to the sample surface.

The Rocking Curve (RC) measurements are used to determine the distribution of crystallite orientations around a given direction, the so-called mosaicity. In this geometry, the diffraction angle 2θ between the source and the detector corresponding to a specific family of planes is kept constant but the sample is tilted by an angle ω (Fig. (2.10)-b). During this scan, the scattering vector $\vec{Q}$ vector of constant length moves along an arc in the reciprocal space. All the planes belonging to the same family but tilted with respect to the direction normal to the surface will therefore be probed. In parallel, to first order in ω, a wave vector transfer Q_x is induced in the in-plane direction leading to a further broadening of the peak due to the in-plane grain size.

2.3.4.3 Grazing incidence X-ray diffraction and ϕ scans

Since the $\theta - 2\theta$ geometry only induces a scattering vector Q_z along the direction normal to the surface, all structural information in the plane of the film are out-of-grasp. This limitation is overcome by using a Grazing Incidence X-Ray Diffraction (GIXRD) geometry (Fig. (2.11)). In GIXRD, the incidence angle ω of the X-ray beam with respect to the sample surface is fixed at a value ω_c close to the critical angle of the sample (a fraction of degree). While inducing a large footprint on the sample, this configuration reduces the penetration depth of the beam by taking advantage of the total external reflection phenomenon; this increases the signal-to-noise

ratio for thin films. At the same time, the detector moves in the plane of the sample surface along the $2\theta_\chi$ angle at an exit angle close to the incident one ω. This type of configuration is called non-coplanar, as the normal to the surface is not in the plane of diffraction as given by the source and detector. So only lattice planes perpendicular to the surface can contribute to the diffraction diffractogram in this geometry. Similarly to $\theta - 2\theta$ Bragg-Brentano geometry, the peak position and broadening along a $2\theta_\chi$ scan will carry information about the in-plane macrostrain, microstrain and lateral grain size of the layer.

The ϕ-scan, equivalent to the rocking scan in Bragg-Brentano geometry, is used to estimate the quality of the lattice plane orientations but in the in-plane direction. For the analysis, the source and the detector are fixed at a diffraction angle $2\theta_\chi$ of a specific peak and the sample is rotated around its normal (ϕ angle). Hence, all the planes belonging to the same family but tilted in-plane with respect to the selected diffraction direction are detected and will contribute to the broadening of the peak. Larger the peak width, higher the misorientation of the planes.

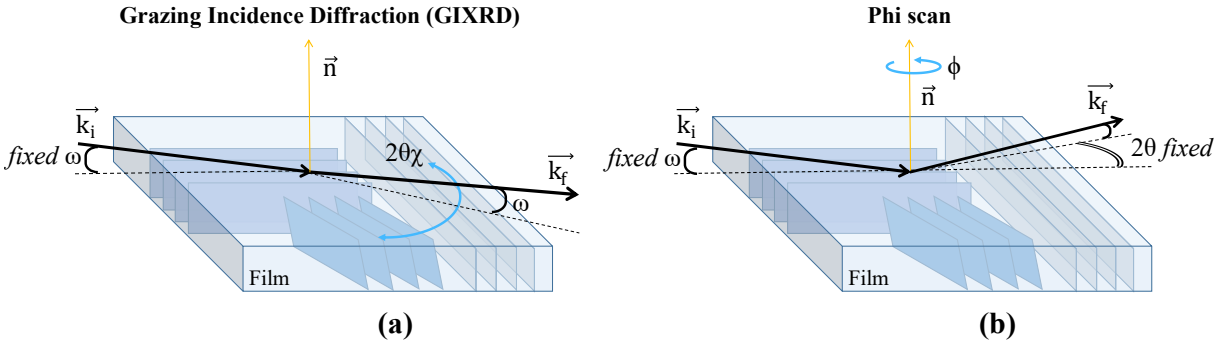

Figure 2.11 (a) In grazing incidence X-ray diffraction with non-coplanar configuration, the angle between the surface and the incident/diffracted beam is fixed at a very low value and only the detector is moved along the $2\theta\chi$ angle. In this case, only the lattice planes perpendicular to the surface will diffract. (b) During a ϕ-scan, the source and the detector are fixed at a diffraction angle of a specific Bragg peak while the sample is rotated around is normal. The scan is used to reveal the degree of in-plane orientation within a given family of planes.

2.3.4.4 Pole figures

A Pole Figure (PF) is a XRD measurement that allows a 3D visualization of a film texture (Fig. (2.12)). To start the analysis, the 2θ and ω angles are aligned on a specific interplanar distance *i.e.* a given reflection. During the measurement, the sample is rotated around its normal (ϕ) between 0° and 360° while the angle ψ between 0° and 90° is maintained fixed. Once a the ϕ scan is completed, the value of the angle ψ is increased and a new ϕ scan is performed until the whole range $0° \leqslant \psi \leqslant 90°$ is analysed. Hence, a PF measurement is basically a spherical cross section of the reciprocal space, the radius of which corresponds to a given vector of reciprocal space. All the collected diffractograms are plotted in a colour-coded 2D map following a stereographic projection as shown in Fig. (2.12). Each point of the plot corresponds to a projection of the reciprocal space points (such as P_1, P_2, P_3 and P_4 in Fig. (2.12)) on the in-plane reciprocal space points (in the figure P_1^*, P_2^*, P_3^* and P_4^*). During the projection, the azimuthal angle φ_{SC}, given in spherical coordinates (SC) is conserved while the radial distance r_{SC} and the polar angle θ_{SC} determine the distance between a projected point and the origin of the PF plane [174].

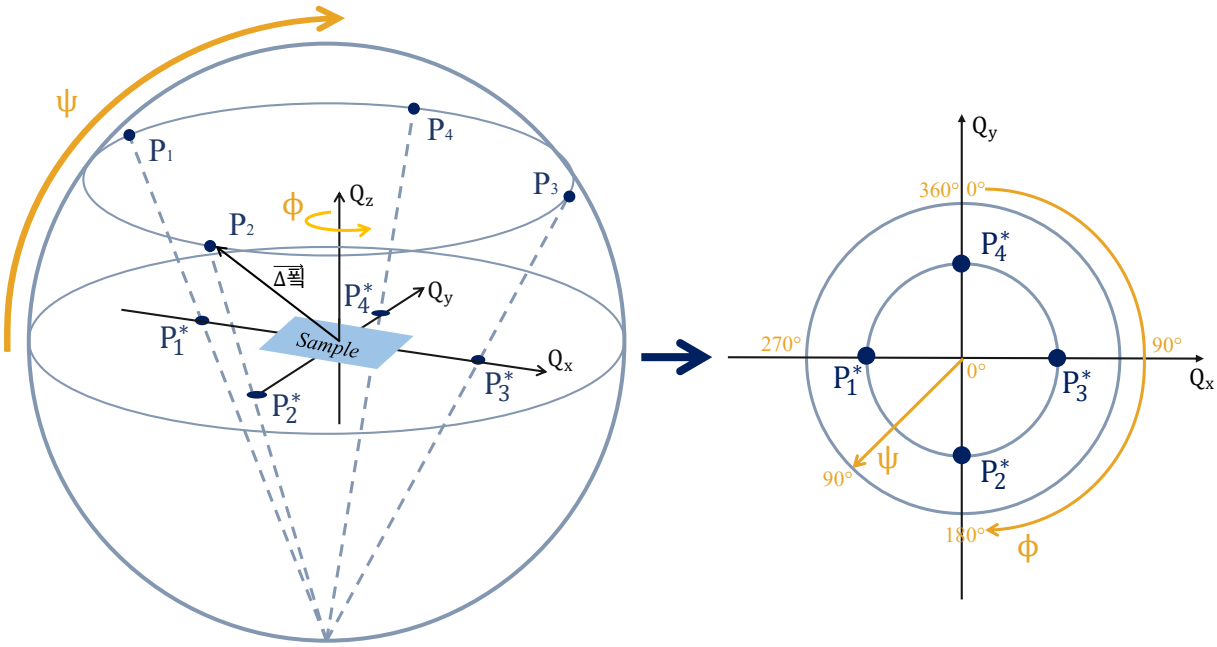

Figure 2.12 Principle of the stereographic construction of a pole figure map. During a measurement, the scattering vector moves along the ϕ and Ψ angles, defining a hemisphere of radius equivalent to the selected scattering vector length $|\vec{Q}|$. The detected reciprocal space points, here corresponding to the points P_1 to P_4, are then projected on the plane of the sample surface (P_1^* to P_4^*).

A PF is therefore a direct visualization of the texture of a film in the three directions of space (Fig. (2.13)). It can give information on the epitaxial relationship between the probed layer and the substrate. In a non-textured polycrystalline film where the diffracting plane orientation is fully isotropic, each point of reciprocal space has the same intensity and the PF map has a uniform intensity distribution. In the case of a fiber texture, the crystallites grow in a columnar mode with a specific out-of-plane direction but are randomly oriented in-plane. For this type of samples, the PF is characterized by a strong central peak, corresponding to the diffraction peak of the planes oriented parallel to the sample surface. The in-plane plane misorientation results in a ring-shape intensity pattern at a ψ tilt, related to the angle between the surface normal and the lattice plane probed in the PF measurement. In highly textured film as in the case of our single crystal based stacks, the crystallites have well defined in-plane and out-of-plane orientations. Due to the anisotropy of the sample, the rotational symmetry vanishes and the PF map exhibits peaks at specific ψ and ϕ values. The number of peaks depends on the symmetry of the unit cell, the probed lattice plane and the substrate. The appearance of additional reflections can be due to crystal twinning [171]. A crystal twinning occurs when two separated crystals are symmetry related by sharing some lattice points. To overlap the two lattices, a 180° rotation around an axis or a reflection across a plane has to be performed. This is quite common in the case of (111) stacking in face centred cubic material such as silver; during the growth process, ABC and BCA stacking should appear. Finally, peak broadening in PF can be influenced by edge and mixed dislocations or by substrate curvature [175].

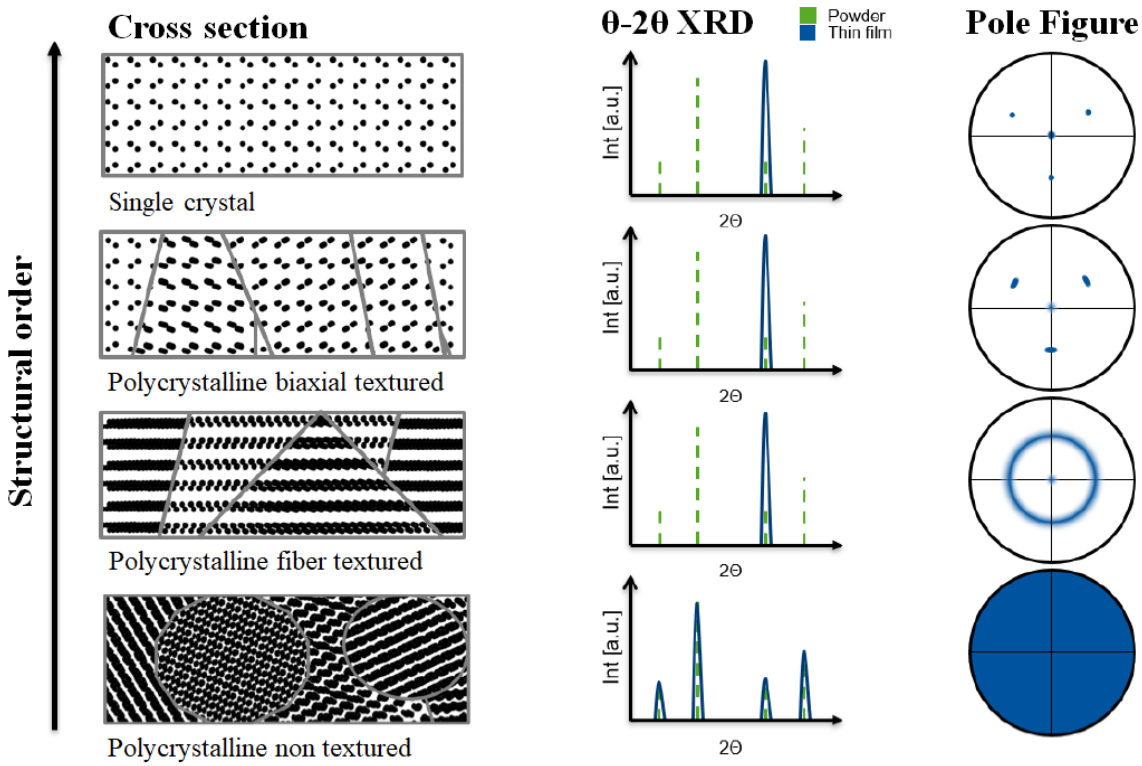

Figure 2.13 Different films microstructures and their associated θ-2θ diffractograms and PFs [4]. In a polycrystalline film, all the grains are randomly oriented. Therefore, as in a powder sample, its θ-2θ diffractogram will be characterized by multiple peaks and an homogeneous intensity will appear in its PF. In the case of a fiber texture, the film grows with a given out-of-plane orientation but with a random in-plane orientation. This will lead to a θ-2θ diffractogram with peaks associated only to the planes parallel to the surface. The PF will be characterized by a strong central peak, corresponding to the out-of-plane texture and a ring at a certain ψ value, corresponding to the in-plane anisotropy. When the polycrystalline film has a bi-axial texture, the PF diffraction ring will be replaced by peaks, while the $\theta - 2\theta$ diffractogram will not vary. In a highly orientated film, such as for an epitaxial layer on a single crystal, the same peaks as observed for a bi-axial texture polycrystalline film will be visible but much sharper.

2.3.5 X-ray data interpretation

The XRD data treatment was performed by a *Python* code dedicated to the diffraction analysis developed by J. Voronkoff [39] during her PhD at SVI. Diffraction peaks are fitted through a Pseudo Voigt (PS) function [176], defined as the linear combination of the Gauss (G) and the Lorentz (L) functions :

$$PS(2\theta, \beta_{exp}^{L,G}, \mu) = \mu \cdot G(2\theta, \beta_{exp}^{G}) + (1 - \mu) \cdot L(2\theta, \beta_{exp}^{L}), \tag{2.11}$$

with 2θ corresponding to the diffraction angle, β_{exp} to the peak full width at half maximum and μ to the Gauss-Lorentz weight factor ($0 \leq \mu \leq 1$).

2.3.5.1 Analysis of peak broadening in X-ray diffraction

The line shape of a diffracted peak, characterized to first order by its FWHM, brings important information on the structural property of the film. Each peak includes a broadening given by the instrument β_{instr}. A more detailed description of the used experimental setups can be found in Sec. (2.3.5.6). Being uncorrelated to the other sources of broadening, β_{instr} can be subtracted to that of the considered reflection β_{exp} though :

$$\beta_{hkl}^2 = \beta_{exp}^2 - \beta_{instr}^2, \tag{2.12}$$

to give the intrinsic contribution β_{hkl} [177]. This instrumental value was estimated by measuring the broadening of diffractions peaks of a perfect GaAs single crystal in the different diffraction configurations. In the Bragg-Brentano one, it is negligible compared to the measured width of our samples as it amounts to 0.001°. On the other hand, in the GIXRD configuration, $\beta_{instr} = 0.5°$ is much larger due to beam divergence and of the same order of the experimental peak width. Therefore, before processing data, the correction Eq. 2.12 was systematically applied.

2.3.5.2 Broadening along a radial scan : $\theta - 2\theta$ and GIXRD

Besides the instrumental factor β_{instr}, for the so-called radial scans for which the modulus of the scattering vector Q is varied such as in $\theta - 2\theta$ and GIXRD, the peak broadening results from the contributions of (i) the limited coherence length of the diffracting domains (β_D) and (ii) the microstrain (β_ε) due to fluctuations of lattice parameters around its average value [175] (Fig. (2.14)). The two contributions can be unfolded using their dependence with Q (Fig. (2.14)). Indeed, the broadening caused by the microstrain increases with the distance from the origin of the reciprocal space while the effect of the limited coherent length is constant over reciprocal space. Several methods have been put forward to quantify the two contributions : Williamson-Hall (W-H), Size-Strain Plot (SSP) and Halder-Wagner (H-W).

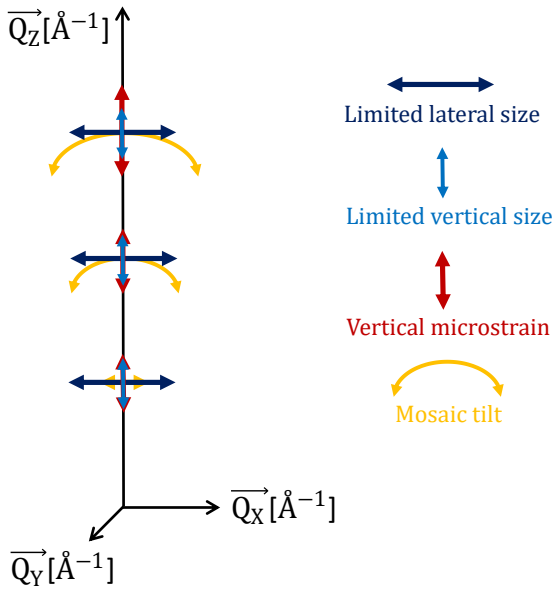

Figure 2.14 Contributions of different factors (limited size, microstrain and mosaicity) to the FWHM of the diffraction peaks along the $\vec{Q_z}$ direction. The same behaviour can be observed also in the other directions of the space such as $\vec{Q_x}$ or $\vec{Q_y}$.

Williamson-Hall method

In the Williamson-Hall (W-H) approach [178,179], the broadening of an X-ray diffraction peak can be expressed as the linear convolution of the two Lorentzian profiles :

$$\beta_{hkl} = \beta_D + \beta_\varepsilon, \tag{2.13}$$

β_D being linked to the limited coherent length of the diffracting domain assigned to the grain size (D) and defined by the Scherrer equation :

$$\beta_D = \frac{K\lambda}{D\cos\theta}, \tag{2.14}$$

where K is the shape factor with the value of 0.9 [180]. D corresponds to the vertical grain size in $\theta - 2\theta$ configuration or to the lateral grain size in GIXRD. The microstrain broadening

$$\beta_\varepsilon = 4\varepsilon\sin\theta \tag{2.15}$$

results from the local strains ε due to a lattice parameter distribution induced by a gradient of deformation between the crystallites or within the same crystallite. Rearranging the equations, the overall broadening reads :

$$\beta_{hkl}\cos\theta = \frac{K\lambda}{D} + 4\varepsilon\sin\theta\cos\theta, \tag{2.16}$$

from which the grain size D and the microstrain ε can be obtained if several reflections (*i.e.* θ values) can be measured.

Size-Strain Plot method

The Size-Strain Plot (SSP) method [181] assumes a peak profile as a combination of a Lorentzian and a Gaussian function. Here, the total broadening can be expressed as :

$$\beta_{hkl} = \beta_L + \beta_G, \tag{2.17}$$

where β_L is the Lorentzian peak broadening associated to the size effect, and β_G is the Gaussian peak broadening associated to the microstrain. Compared to the W-H method, the SSP model provides a better result for isotropic broadening, as it overweights low angle reflection peaks that are generally more defined than high angle peaks. The total peak broadening reads as [179] :

$$(d_{hkl}\beta_{hkl}\cos\theta)^2 = \frac{K\lambda}{D}(d_{hkl}^2\beta_{hkl}\cos\theta) + \frac{\varepsilon^2}{4} \tag{2.18}$$

where d_{hkl} is the interplanar distance.

Halder-Wagner method

The Halder-Wagner (H-W) method [182] is based on the assumption that the peak profile is described by a symmetric Voigt function, a convolution of a Lorentzian and a Gaussian function. The average coherent length and the microstrain can be estimated from the XRD peak broadening given by :

$$\beta_{hkl}^2 = \beta_{hkl}\beta_L + \beta_G^2, \tag{2.19}$$

with β_L and β_G are the FWHM of the Lorentzian and Gaussian contributions respectively. As for the SSP method, the H-W gives more weight to the peaks at low angles than those at higher angles which are often less reliable. The equation can be rewritten as :

$$\left(\frac{\beta_{hkl}^*}{d_{hkl}^*}\right)^2 = \frac{K}{D}\frac{\beta_{hkl}^*}{d_{hkl}^{*2}} + (2\varepsilon)^2 \tag{2.20}$$

which includes the integral width of reciprocal lattice points $\beta_{hkl}^* = \beta_{hkl}\cos\theta/\lambda$ and the interplanar spacing $d_{hkl}^* = 2d_{hkl}\beta_{hkl}\sin\theta/\lambda$.

In the present study, the Ag vertical grain size and the out-of-plane microstrain were determined from the (111) and (222) peaks in $\theta - 2\theta$ diffractogram. For the ZnO thin film, only one peak (002) was visible due to the limitation of the angular range. In this case, just the vertical grain size could be estimated through the Scherrer equation (Eq. (2.14)). For the same reason, in the GIXRD configuration, the (220) and (100) peak were used to determine the Ag and ZnO lateral grain size, respectively.

2.3.5.3 Broadening along rocking scans : RC and ϕ scan

In the so-called rocking scans (RC in $\theta - 2\theta$ configuration or ϕ scan in GIXRD), the reciprocal space is scanned along an arc at constant scattering vector modulus around a given direction. This scan is used to quantify the misalignment of the diffracting planes around the selected direction. This contribution is overlapped with the peak broadening given by the limited lateral coherent length (L) of the domains. Assuming both contributions as uncorrelated, the measured FWHM can therefore be expressed as :

$$\beta^2_{RC/Phi} = \beta^2_M + \beta^2_L, \tag{2.21}$$

where β_M is the mosaicity broadening and β_L the broadening due to the limited lateral coherence length. Similarly to the radial scans, β_M and β_L have different behaviours upon increasing the distance from the origin of the reciprocal space. Their values can be separated by applying the Williamson-Hall method [183], that reads :

$$2\sin\kappa\beta_{RC/Phi} = \frac{\lambda K}{L} + 2M\sin\kappa, \tag{2.22}$$

with $\kappa = \theta, \phi$ depending on the diffraction configuration. The equation can be solved graphically if at least two peaks of the same family of planes are available in the RC or ϕ scans.
In the present study, only the out-of-plane (111) and (222) silver peaks in the $\theta - 2\theta$ geometry could be really used.

2.3.5.4 Texture and the Lotgering Factor

Beyond the pole figure, the Lotgering Factor, also known as Texture Coefficient (TC), is an index of the crystalline texture widely used in literature [184–188]. Its value quantifies the level of texturization of a certain family of planes via a percentage. $TC = 0$ % corresponds to perfectly random orientation and $TC = 100$ % to single crystal. TC is calculated starting from the areas of the diffraction peaks through :

$$TC = 100\frac{P - P_0}{1 - P_0}, \tag{2.23}$$

where $P = P_{hkl} = \frac{\sum A_{hkl}}{\sum A}$ is the ratio between the sum of the areas (A_{hkl}) of the peaks of the same family along the analysed direction, and the sum of the areas of all the other material peaks that are present in the diffraction pattern. P_0 is P but calculated for a perfectly isotropic powder with a random grain orientation.

In the frame of this study, the TC factor was determined in the GIXRD configuration from the (100) and (110) ZnO peaks visible in silicon or glass based samples. For the Ag layers, it was evaluated from the (220) and, when visible, the (111), (200), (311) and (331) planes.

2.3.5.5 X-Ray Reflectivity

X-ray reflectivity (XRR) is used to retrieve information about the density, thickness and roughness of a film or a multilayer stack [189]. Basically, it is a $\theta - 2\theta$ Bragg-Brentano scan but over a smaller angular range (usually between $0 - 5°$) and therefore at a Q-value closer to the origin of reciprocal space (Fig. (2.15)). Thus the measurement is not any more sensitive to the atomic arrangement of the material but to variations of the electronic density around its average value due to the microstructure of the sample. The contrast comes mainly from jumps in density at interfaces.

The X-ray interaction with the matter is described by a complex refractive index $n = 1 - \delta - i\beta$ where δ corresponds to dispersion and β to absorption. They can be expressed by $\beta \approx \frac{\lambda}{4\pi}\mu$ with λ the X-ray wavelength and μ the linear absorption coefficient and :

$$\delta = \frac{r_0\lambda^2}{2\pi}n_e = \frac{r_0\lambda^2}{2\pi}N_A\sum_i x_i(Z_i + f_i')\frac{\rho}{A}, \tag{2.24}$$

where r_0 is the Bohr radius, n_e the electron density of the material, N_A the Avogadro number, x_i the molar fractions of element i, $(Z_i + f_i')$ the charge of an atom i with a dispersive correction factor, A is the molar mass and ρ the material density. Usually, in the hard X-ray range, δ is in the order of 10^{-6}, making the real part of the refractive index slightly smaller than one. In these conditions, a phenomenon of total external reflection can occur at the vacuum/material interface if the incident angle is below the critical angle defined as :

$$\omega_C \approx \sqrt{2\delta} = \lambda\sqrt{\frac{r_0\rho}{\pi}}. \tag{2.25}$$

ω_C related to the electronic density is in the range of $0.1 - 0.5°$

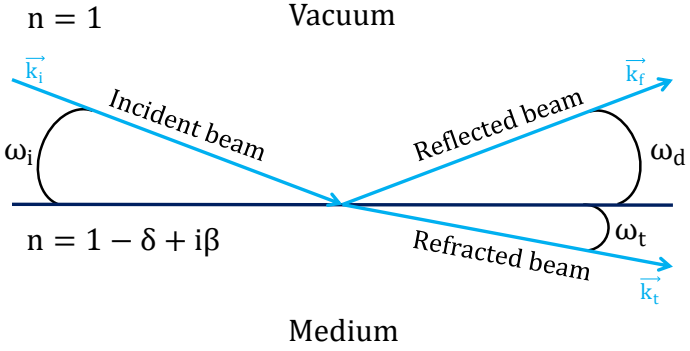

Figure 2.15 Refractive phenomenon occurring during a X-ray reflectivity measurement.

For incident angle larger than the critical angle ω_C, the beam penetrates the film and is reflected/refracted at lower interfaces (Fig. (2.15)). In a stack of N layers, the various reflected/refracted beams will overlap giving rise to an angle dependent interference pattern, called Kiessig fringes. From its modelling via transfer matrices or Parrat formalism [189], a very precise estimate of the thicknesses and roughnesses of the analysed layers can be obtained. More specifically, for a single layer (Fig. (2.16)), the layer thickness d can be determined from the distance between two successive fringes ($\Delta\omega_{m/m-1}$) :

$$d = \frac{\lambda}{2\Delta\omega_{m/m-1}}, \tag{2.26}$$

while the surface roughness leads to an increase of out-of-specular reflection and therefore a decrease of the fringe visibility with m and angle ω.

In the course of this work, the reflectometry data were modelled using the software *GenX 3.3.4* or the program *GlobalFit*, belonging to the *Rigaku-Smart Lab* package.

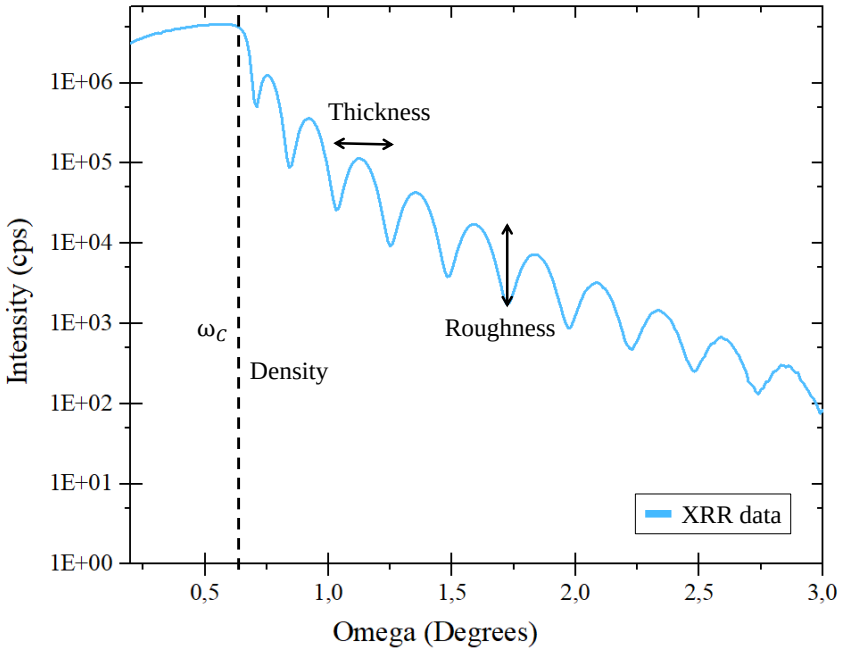

Figure 2.16 Typical X-ray reflectivity measurement of a single ZnO layer deposited on glass. From the fit of the fringes, the thickness, density and roughness of the layer can be determined.

2.3.5.6 X-ray diffraction equipment

The diffraction analyses were performed mainly at the INSP laboratory on a high resolution *Rigaku SmartLab* diffractometer. The X-rays are produced by the excitation of a copper rotating anode tube maintained under vacuum and bombarded by electrons emitted from a tungsten filament (200 mA, 45 kV, 9 kW). The generated CuK$\alpha_{1,2}$ radiations have a characteristic wavelength of about 1.5419 Å. Once diffracted, the X-rays are collected by a *HyPix-3000* high-energy-resolution 2D multidimensional semiconductor detector. Thanks to its geometry with five axes of rotation and one axis of translation, the sample can be analysed in a variety of diffraction configurations, including Bragg-Brentano, pole figures, non-coplanar GIXRD and XRR. In order to suppress the Kα_2 contribution of the copper radiation, the X-ray source was equipped with a Ge(220) monochromator for the $\theta - 2\theta$, rocking curves and reflectivity analyses. For Bragg-Brentano configuration, Soller slits were mounted in front of the source and the detector and a divergence slit of 2 mm was added to the setup. For GIXRD, the incident beam was fixed at $\omega = 0.5°$, equal to the exit angle. To maintain a constant resolution along the scanned range, the X-ray source and the detector were equipped with a collimator of 0.5°. In addition, a vertical slit of 5 mm was placed in front of the incident beam to maximize the detected area on the sample. Due to the lower intensities of the peaks, the monochromator was not employed in the GIXRD setting, and the Kα_2 contribution was subtracted *a posteriori* with the *Bruker*

software *DIFFRAC.EVA*. The same configuration was used also for the ϕ-scans. For pole figure measurements, the exit slit was close to 2 mm instead of 20 mm.

Few analyses were also performed at the Institute of Physics of RWTH Aachen on a *Bruker AXS D8 Discover* system. The diffractometer uses a X-ray copper source coupled with a *LynxEye* motorized detector. The setting was mainly used for analyses in the Bragg-Brentano geometry, using a Ge(220) monochromator, two Soller slits and a divergent slit of 0.6 mm.

For both diffractometers, the sample vertical alignment was achieved by cutting-off the direct beam at half its intensity, while the cradle alignment was obtained by performing a rocking scan on the total reflected beam from the sample surface. For the single crystal based samples in GIXRD, an additional step was included, namely the alignment of the ϕ azimuth of the sample on an intense in-plane (100) Bragg diffraction peak of ZnO substrate.

2.3.6 Transmission Electron Microscopy and its associated technique of Focused Ion Beam (FIB) for samples preparation

The different Ag/ZnO interfaces and the Ag and ZnO layers microstructures were investigated by Transmission Electron Microscopy (TEM) in two configurations of sample observation :

- the thin layer stack was observed along its cross section in order to control the layer thicknesses, to observe their interface and to obtain information concerning Ag and ZnO crystallites (independently of each other) such as their size, the presence of defects, their relative orientation ... ; the sample has then to be prepared by a dedicated Focused Ion Beam (FIB) protocol ;
- the whole stack was analysed in plane-view configuration to access to the lateral grain size and the relative orientation of the Ag crystallites. For this purpose, 15 nm thick TEM lamella were directly placed in the sputtering deposition chamber in order to receive the thin layer stack of interest. In the case of samples with Ag film on a ZnO single crystal with an additional ZnO thin layer, a thin lamella which surface is parallel to the ZnO crystal surface was extracted by the FIB technique. Otherwise, dedicated silicon nitride lamellae were used.

The TEM samples were prepared by FIB at SGR Paris with the *SCIOS* tool provided by *ThermoFischer*. This dual-beam device is equipped with a Field Emission Gun (FEG) electron column allowing to achieve high resolution pictures of Secondary Electron (SE) combined with a Ga^+ ion gun (Liquid Metal Ion Gun) for the milling operation in order to extracted the lamella from the sample. The protocol used for the cross section observation is a conventional lift-out but that applied for plane view lamella extracted from a stack on a ZnO single crystal was inspired from a recipe developed for atom probe tomography measurement [190]. A micro-manipulator controls the probe used for the transfer of the raw lamella from the "bulk" sample surface to a Cu grid. A Pt-Gas Injection System (Pt-GIS) was used to weld the lamella onto the Cu grid. Ga^+ gun is then used from 30 kV to 5 kV and different ranges of progressively lower ion currents for final thinning to generate a lamella about 50 nm thick.

The analyses were performed using different acquisition modes. In the case of conventional transmission electron microscopy, a parallel beam of high energy electrons (200 keV) is transmitted through the thin sample to form an image. Before reaching the sample, the electron beam is shaped by a series of magnetic lenses. Two condenser lenses define the beam size and the angle of convergence on the sample, while the objective lens and the diaphragm modify the angular opening. As the beam passes through the sample, it interacts with the atoms of the sample and the electrons are elastically or inelastically scattered. The transmitted electrons, containing

the information on the structure of the material, are then collected on a phosphorescent screen during the TEM adjustment or on a CCD camera for the final acquisition. The TEM resolution can reach the tenth of a nanometre thus allowing the visualization of atomic structures. Another configuration of analysis, namely Scanning Transmission Electron Microscopy (STEM) mode, was used for the structural and composition investigations at the atomic scale. In this configuration, the electron beam, emitted from a field emission gun, is focused to a fine spot which is scanned over the sample. Thanks to the development of aberration corrector, the spot size reaches a value small enough to achieve a lateral resolution down to 0.05 nm. Different detectors can be used to collect the transmitted electrons. High Angle Annular Dark Field (HAADF) detector collects the fore-scattered incident electrons in order to generate an atomic resolution image where the contrast is related to the atomic number of the atoms. Bright Field (BF) detectors located in the center of the cone of illumination are used to provide complementary pictures to HAADF ones, especially interesting for light elements. Furthermore, the X-rays emitted by the ionized atoms of the sample irradiated by the electron spot are collected in the case of X-ray Energy Dispersive Spectroscopy (EDS). The elements present in the sample can thus be identified while atomic resolution chemical mapping can be obtained.

The TEM and STEM acquisitions have been performed on the *TEM/STEM Titan THEMIS* from *ThermoFischer* of the *PANAM* platform based in C2N (Centre de NanoSciences et de Nanotechnologies) laboratory ; this equipment is also one of the 3 microscopes of the Equipex *TEMPOS*. It features a 80-200 keV high-brilliance XFEG gun, a Cs corrector on the condenser system allowing 80 pm of lateral resolution, a super-X detection system (EDX), several STEM detectors (BF, ABF and HAADF) and a CMOS ($4k \times 4k$) TEM camera. Further acquisitions were carried out at ICMPE, Institut de Chimie et des Matériaux Paris Est, (Thiais, coll Julie Bourgon) using a TEM TECNAI F20 provided by ThermoFischer, comprising an analysis module ASTAR which generate texture maps. This system uses the electron diffraction pattern obtained locally in point mode. A database of the theoretical diffraction patterns of the material is then compared to the measured one to determine the crystal orientation at each pixel. [191].

2.3.7 Electrical transport measurements

The goal of this work was to study the impact of the microstructure of the Ag layer in model low-emissive stacks on its electrical transport properties. The resistivity was measured by a four-points probe method [192] applied in a temperature range varying from 5 K to 300 K. To do so, four probes are positioned in line at the centre of the sample, usually corresponding to the more homogeneous area of the coating (Fig. (2.17)). The two outer electrodes are so used to inject the current (I^+ and I^-), while the inner two are used to measure the potential difference (V^+ and V^-) in the two current polarities ; thus the offset due to the electronics or thermoelectric voltages, as well as the contact resistance, can be removed. If the thickness d of the conductive layer is small compared to the probe spacing, the current can be assumed to spread cylindrically from the metal electrode [192]. Thus, the voltage drop can be expressed as :

$$V = V_2 - V_3 = \frac{I\rho}{2\pi d} \ln\left(\frac{s_2 s_3}{s_1 s_4}\right), \tag{2.27}$$

where ρ is the film resistivity and $s_{i=1,\dots,4}$ are the spacing between the probes (Fig. (2.17)). In the case of equally spaced in-line probe geometry, the resistivity is then given by :

$$\rho = \frac{\pi d V}{I \ln 2}. \tag{2.28}$$

In the case of thin film, resistivity is often replaced by the so-called sheet resistance $R_{\square} = \frac{\rho}{d}$ given in $\Omega.\text{sq}^{-1}$.

At room temperature, the measurements were made on a *Napson* 4-points probe (model RT-300/RG-80N.) For the analysis, the metallic tips are mechanically pressed into the layer surface with the help of a weight of 300 g, ensuring the contact with the Ag film below the capping layers (Fig. (2.17)-a). The electrodes are equally spaced at 1.5 mm from each others. The measurements are made with a current range varying between 1 nA and 100 mA. For each sample, the resistivity value represents the arithmetic mean of at least four acquisitions at different locations.

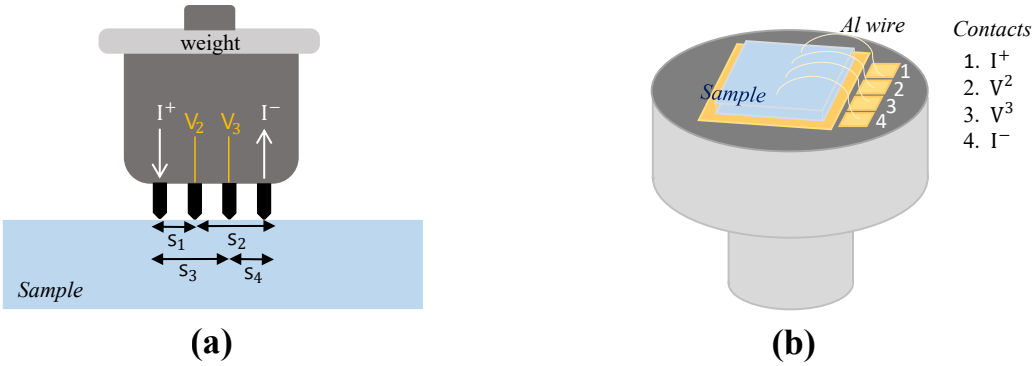

Figure 2.17 Four probes resistivity configuration for (a) room temperature and (b) variable temperature measurements.

The temperature dependent resistivity measurements were performed on a *Physical Property Measurement System* (PPMS) provided by *Quantum Design* at Sorbonne University. The sample was fixed on a holder, called resistivity puck, equipped with four contacts, two positives and two negatives (Fig. (2.17)-b). The sample was connected to the puck contacts using four 25 μm thick aluminium wires that were manually positioned along a line in the center of the surface. Applying an ultrasonic pulse, the aluminium diffuses into the sample forming a stable junction. The distance between the electrodes was determined with an optical microscope. The resistivity was measured in the temperature range from 5 to 300 K in a He cooled cryostat. The excitation current was set to 100 μA with a sampling frequency of 6.25 Hz, 4 periods of 50 Hz for each polarity. Each point was averaged on 16 measures.

To distinguish between the grain boundary and the interface scattering contributions to resistivity, the temperature dependent curves were fitted with three different models : (i) Mayadas-Shatzkes (M-S) [127], (ii) Sambles [142] and (iii) Soffer [149]. The three theories describe the scattering phenomena in slightly different ways. In the original M-S model, grain boundaries are treated as vertical scattering planes between two symmetric interfaces where only a fraction $1-p$ of electrons are scattered isotropically contributing to path length and resistivity increases. However, in this model, the phenomenological scattering parameter p has no clear connection with any physical characteristics of the interfaces. The Sambles model is a variant of the previous one where the possibility of asymmetric interfaces is included, based on flat interfaces but with different scattering probabilities ($p_1 \neq p_2$). Finally, in the Soffer model, the scattering probability p is not anymore isotropic but described by a Croce-Névot term as a function of the incident angle of the electron on the interface and of their roughnesses h_1, h_2. A comprehensive description of thin film resistivity, and the models used to describe it, can be found in Sec. (1.5).

To determine the R and p parameters, the temperature-dependent resistivity curves were modelled using a *Fortran 90* code developed at INSP. The fit was performed by Levenberg-Marquardt algorithm via the minimization of a χ^2 reliance factor as defined by :

$$\chi^2 = \frac{1}{N-f}\sum_{i=1}^{N}\left(\frac{\rho_{exp}^i - \rho_{th}^i}{\Delta\rho_{exp}^i}\right)^2, \tag{2.29}$$

where f is the number of fitted parameters, N the number of experimental/theoretical points $(\rho_{exp}^i, \rho_{th}^i)$ and $\Delta\rho_{exp}^i$ an estimate of the error bar on data. This latter was arbitrarily taken as 1 % of the ρ_{exp}^i value. The fitting parameters were Θ_D (Eq. (1.28)), $\rho_{res}^{bulk}(T = 0K) = \rho_{defect}$ (Eq. (1.29)), R, p, p_1, p_2, h_1, h_2 (Eq. (1.36)-Eq. (1.41)) while the lateral grain size D and the film thickness d were systematically fixed at their values measured by X-ray diffraction. If possible, $\rho_{res}^{bulk}(T = 0K)$ was fixed using the intercept of a linear fit of the room-temperature resistivity with thickness in the regime of large grain sizes and thicknesses ($D \gg l_0$ and $d \gg l_0$; Eq. (1.35)) and by subtracting it to the room-temperature resistivity of a perfect Ag crystal $\rho_{bulk}(T = 300K) = 1.62\ \mu\Omega$.cm. Most of the time, whatever the used model, the agreement between experiment and theory is very good with $\chi^2 < 1$. Error bars on parameters are obtained from the inverse of the χ^2 curvature matrix at minimum once renormalised by the final χ^2. Typical values are $\Delta\Theta_D = \pm 5$ K, $\Delta\rho_{res}^{bulk}(T = 0K) = \pm 0.2\ \mu\Omega$.cm if fitted, $\Delta R = \pm 0.05$, $\Delta p = \pm 0.02$. Nevertheless, some strong correlations between fitted parameters exist, in particular $\Theta_D - p$ and $\rho_{res}^{bulk}(T = 0K) - R$, thus encouraging to fix as much as possible $\rho_{res}^{bulk}(T = 0K)$ from the linear fit and Θ_D at a value close to the bulk one ($\Theta_{D,bulk} = 221$ K). Thus, the perfect correlation between R and D (Eq. (1.34)) requires an estimate of D for a reliable analysis. This justifies the exhaustive X-ray analysis performed in this work.

To conclude, a constant offset, between 10 and 20%, was found between the resistivity values determined at 300 K ($\rho_{300\ K}$) and the resistivity measured at room-temperature via *Napson*. The discrepancy is probably the result of a different calibration such as electrode spacings between the two techniques. This offset could influence the estimation of ρ_{res}^{grain} but does not have a significant impact on R and p since the parameters are driven by the concavity of the curve (see Sec. (1.5)).

Chapter 3

The prototype reference stacks

This chapter is dedicated to the silver-based coatings, identified as *prototype references*. Deposited on float glass, these stacks of layers were made based on a simplified version of actual industrial products and will be used as references throughout this work. After an investigation on the influence of the different components of the stacks (capping, substrate and seed layer) on the silver microstructure, the correlation between their room-temperature resistivity and their structural characteristics will be explored. At last, the temperature dependence of resistivity will be used to identify the main scattering phenomena hindering the conduction in the polycrystalline silver film.

Chapter summary

3.1 Structural analysis of the prototype reference stacks

The prototype reference stacks of layers on which this study is based are simplified versions of silver-based low-emissive industrial products. The stack (Fig. (3.1)) is composed of :

- a first layer of amorphous silicon nitride (Si_xN_y), 20 nm thick, having the role of barrier against diffusion of alkaline elements from glass and allowing to improve the optical properties of the whole stack ;
- an Al doped zinc oxide layer (AZO), 5 nm thick, having the role of a seed layer that promotes silver crystallinity while providing targeted optical, electrical and mechanical properties [109, 193] ;
- a metallic film of silver (Ag), 12 nm thick, giving the infra-red reflective properties required for thermal insulation ;
- a capping layer of AZO, 5 nm thick, which protects Ag from oxidation and contributes to the overall adjustment of optical properties ;
- a further amorphous capping film of 30 nm of silicon nitride, having the role of protection against oxidation, silver film degradation or dewetting especially during post-deposition thermal treatments, and contributing to the overall adjustment of the optical properties.

Each layer has its own influence on the structural, morphological or electrical properties of the silver film. Its investigation will be carried out in the following paragraphs.

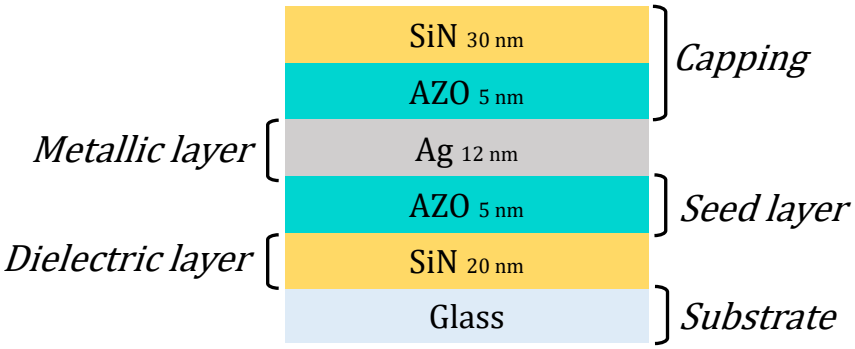

Figure 3.1 Schematics of the silver-based reference coating used all along this work.

Reference coatings were deposited using two sputtering machines (Sec. (2.1.2.1)) : (i) the line coater LINA, the semi-industrial research machine of SGR Paris and (ii) the academic research sputtering set up MISSTIC, involved also in the fabrication of single crystal based stacks (see Ch. (4)). The ZnO layers were deposited from an Al-doped ceramic target (AZO) in non-reactive mode while Si_xN_y (henceforth referred to as SiN) is deposited in reactive mode from a Si :Al target. All deposition parameters can be found in Sec. (2.1.2.2). As in the following sections, interest will also be given to ZnO seed layers sputtered from a metal Zn target in a reactive mode, layers will be designated in reference of the nature of their target : *AZO* or *ZnO-met*. The wording *ZnO* kept to designate the zinc oxide material in general (zincite).

All the samples were characterized through X-Ray techniques (XRD and XRR). Note that, due to a poor intensity and the absence of multiple peaks belonging to the same family of planes, it was not possible to deeply investigate the structural properties of the stacks (grain size, mosaicity, intra-grain strain etc...) at variance to single crystal substrates (Ch. (4)). In particular, only a simple Scherrer analysis could be performed to deduce the coherent domain size, in-plane $L_{S,IP}$ and out-of-plane $D_{S,OP}$. Nevertheless, all the data that could be retrieved are described in the following section. They can already give a general idea of the state of the

layers. Finally, as convention, the interface roughness determined by X-ray reflectivity is labelled hereafter according to the lower layer. The "ZnO surface roughness" corresponds to that of the interface between the ZnO seed layer and Ag. The "Ag surface roughness" corresponds to that of the interface between the Ag film and the AZO capping layer.

The evolution of structural properties was followed after post-deposition annealing, a treatment used to enhance the mechanical strength properties of the glass (tempering) or to shape it. This process, commonly used in the glazing industry, has also a beneficial impact on the structural quality and electrical performance of the stack, improving its infrared optical properties through the recrystallisation of the silver film. This latter is accompanied by a better texture, a reduced internal stress, a lateral grain growth and a decrease of the defects concentration. Following the optimized industrial annealing process, large (5×5) cm^2 samples, manufactured with the LINA, were annealed in air at 650°C for 10 min to achieve a conductivity gain between 20-30%, while the smaller (1×1) cm^2 MISSTIC samples were annealed only at 350°C for 10 min for reasons that are developed in Sec. (4.10). The resulting gain for this softer thermal treatment is around 10-20%.

3.1.1 The role of the capping layer

In a classical industrial stack, to prevent the oxidation of silver and the possible degradations that occur during annealing, a thick film, called the capping layer, is deposited to encapsulate and protect the metal. The capping layer is normally composed of a 30 nm layer of SiN, deposited on a thinner ~ 5 nm layer of AZO, which role, among others, is to avoid the direct exposure of the metal to the reactive atmosphere during the nitride deposition. In the present work, with the goal of studying the impact of annealing, a capping layer has to be used. Indeed, the uncapped silver grains tend to sinter and to form a discontinuous film with some separated islands; this dewetting is detrimental to the electrical transport. So an investigation about the type of target used to deposit the SiN film and its appropriate thickness is a prerequisite (Fig. (3.2)).

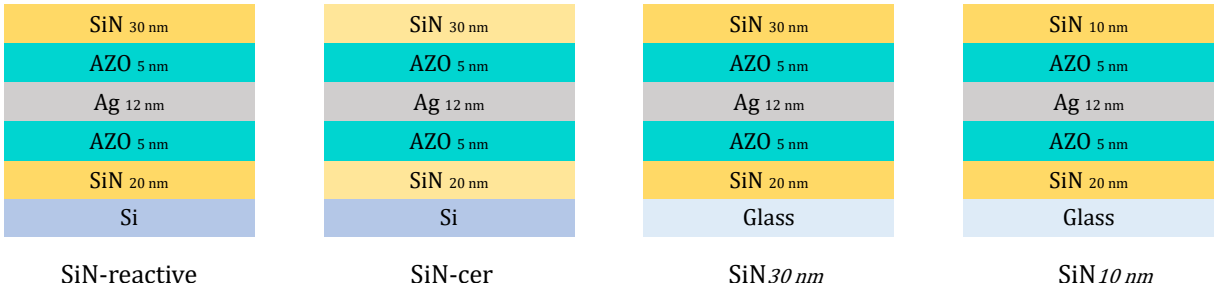

Figure 3.2 Schematics of the Ag-based stack with different SiN capping films deposited starting from a ceramic target or through reactive sputtering from a metallic target, and with different thicknesses.

Two identical stacks were capped by a SiN layer, one deposited through reactive sputtering using a Si metal target and the other using a Si_3N_4 ceramic target (Fig. (3.2)). The coatings were grown on a silicon wafer, a substrate commonly used in academic research and more practical for MISSTIC manipulations. Naturally covered by a nanometre thick SiO_2 layer with an additional amorphous sputtered SiN, the single crystal structure of the wafer does not play any role. Likewise, from the data that could be collected before annealing (Tab. (3.1)), it becomes obvious that the nature of the SiN layer does not have an influence on the structural or electrical characteristic of the lower layers. However, once the samples are thermally treated (650°C for 10 min)

(Tab. (3.2)), a strong increase of the resistivity is recorded for the coating capped with a ceramic SiN, from 7.08 $\mu\Omega$.cm to 20.38 $\mu\Omega$.cm. As no further analyses were performed on this sample to investigate the causes of this behaviour and as ceramic SiN is not used in silver-based coatings, only hypotheses can be formulated. The most common phenomena observed after annealing that induce a resistivity enhancement are silver corrosion and dewetting but diffusion of SiN within the silver layers is also not excluded. In response, SiN layers produced by ceramic targets have been completely discarded for the remaining of this study in favour of those produced in reactive mode deposition.

As-deposited samples				
			MISSTIC	
			Si wafer	
			SiN-reactive	**SiN-cer**
Ag	$\mathbf{D}_{S,OP}$	**[nm]**	9	7
	$\mathbf{RC}_{Ag(111)}$	[°]	6.52	7.20
	$\boldsymbol{\varepsilon_{33}}$	**($\cdot 10^3$)**	0.82	1.07
	$\boldsymbol{a}_{OP-Ag}$	**[Å]**	4.09	4.09
	$\mathbf{L}_{S,IP}$	**[nm]**	8	7
	$\boldsymbol{\varepsilon_{IP}}$		0.005	0.006
	$\mathbf{TC}_{Ag(220)}$	[%]	20	13
	$\boldsymbol{\varepsilon_{11} = \varepsilon_{22}}$	**($\cdot 10^3$)**	-0.69	-0.91
	$\boldsymbol{a}_{IP-Ag}$	**[Å]**	4.08	4.08
	$\mathbf{RMS}_{XRR}$	**[nm]**	0.59	0.64
ZnO	$\mathbf{D}_{S,OP}$	**[nm]**	5	3
	$\mathbf{RC}_{ZnO(002)}$	[°]	8.52	8.48
	$\boldsymbol{\varepsilon_{33}}$	**($\cdot 10^3$)**	7.27	5.54
	$\mathbf{c}_{OP-ZnO}$	**[Å]**	5.24	5.23
	$\mathbf{L}_{S,IP}$	**[nm]**	7	6
	$\mathbf{TC}_{ZnO(110)}$	[%]	40	39
	$\mathbf{TC}_{ZnO(100)}$	[%]	46	48
	$\boldsymbol{\varepsilon_{11} = \varepsilon_{22}}$	**($\cdot 10^3$)**	-8.33	-5.30
	$\boldsymbol{a}_{IP-ZnO}$	**[Å]**	3.22	3.23
	$\mathbf{RMS}_{XRR}$	**[nm]**	0.32	0.38
$\mathbf{R}_{\square-4P}$		**[Ω/sq]**	5.56	5.90
$\boldsymbol{\rho_{4P}}$		**[$\mu\Omega$.cm]**	6.67	7.08
Annealed samples				
		650°C		
$\boldsymbol{\rho_{4P}}$		**[$\mu\Omega$.cm]**	5.46	20.38

Table 3.1 Impact of the SiN capping layer on the microstructural characteristics of silver-based stacks. The samples were deposited in the MISSTIC sputtering machine from a Si_3N_4 ceramic target or in reactive mode from a Si metal target.

The second concern is the thickness of the SiN capping ; although amorphous, it needs to be thick enough to act as a diffusion barrier during annealing but not too thick to allow grazing incidence analysis. Hence, two identical stacks with a 10 nm and 30 nm thick SiN film were compared in terms of resistivity and crystallinity after annealing (Tab. (3.2)). After thermal treatment, the two samples present similar characteristics (vertical and lateral domain sizes, mosaicity, macrostrain, etc...) for the oxide and the silver layer while quite clear diffractograms

can be recorded for both of samples (Fig. (3.3)). In addition, their electrical properties are almost identical with a value of $\sim 4.16\,\mu\Omega$.cm. This means that both thicknesses are suitable for the present study. But to be on the safe side and to stick with a more traditional industrial stack, a thickness of 30 nm of SiN was systematically used for all the following samples.

Annealed samples 650°C				
			LINA	
			$\mathbf{SiN}_{30nm}$	$\mathbf{SiN}_{10nm}$
Ag	$\mathbf{D}_{S,OP}$	**[nm]**	11	11
	$\mathbf{RC}_{Ag(111)}$	[°]	7.25	6.56
	$\boldsymbol{\varepsilon_{33}}$	$(\cdot\mathbf{10}^3)$	-2.71	-2.46
	$\boldsymbol{a}_{OP-Ag}$	**[Å]**	4.07	4.08
	$\mathbf{L}_{S,IP}$	**[nm]**	14	14
	$\mathbf{TC}_{Ag(220)}$	[%]	40	69
	$\boldsymbol{\varepsilon_{11} = \varepsilon_{22}}$	$(\cdot\mathbf{10}^3)$	2.31	2.10
	$\boldsymbol{a}_{IP-Ag}$	**[Å]**	4.10	4.10
	$\mathbf{RMS}_{XRR}$	**[nm]**	0.53	0.59
ZnO	$\mathbf{D}_{S,OP}$	**[nm]**	5	6
	$\mathbf{RC}_{ZnO(002)}$	[°]	19.13	19.70
	$\boldsymbol{\varepsilon_{33}}$	$(\cdot\mathbf{10}^3)$	-1.82	-1.53
	$\mathbf{c}_{OP-ZnO}$	**[Å]**	5.20	5.20
	$\mathbf{L}_{S,IP}$	**[nm]**	9	10
	$\mathbf{TC}_{ZnO(110)}$	[%]	33	33
	$\mathbf{TC}_{ZnO(100)}$	[%]	54	54
	$\boldsymbol{\varepsilon_{11} = \varepsilon_{22}}$	$(\cdot\mathbf{10}^3)$	-4.09	-3.18
	$\boldsymbol{a}_{IP-ZnO}$	**[Å]**	3.24	3.24
	$\mathbf{RMS}_{XRR}$	**[nm]**	0.58	0.48
$\mathbf{R}_{\square-4P}$		$[\Omega/\mathbf{sq}]$	3.46	3.47
$\boldsymbol{\rho_{4P}}$		$[\mu\Omega\mathbf{.cm}]$	4.15	4.16

Table 3.2 Impact of the SiN capping layer thickness on the microstructural characteristics of silver-based stacks. The samples were deposited in the LINA pilot line coater in reactive mode and then annealed.

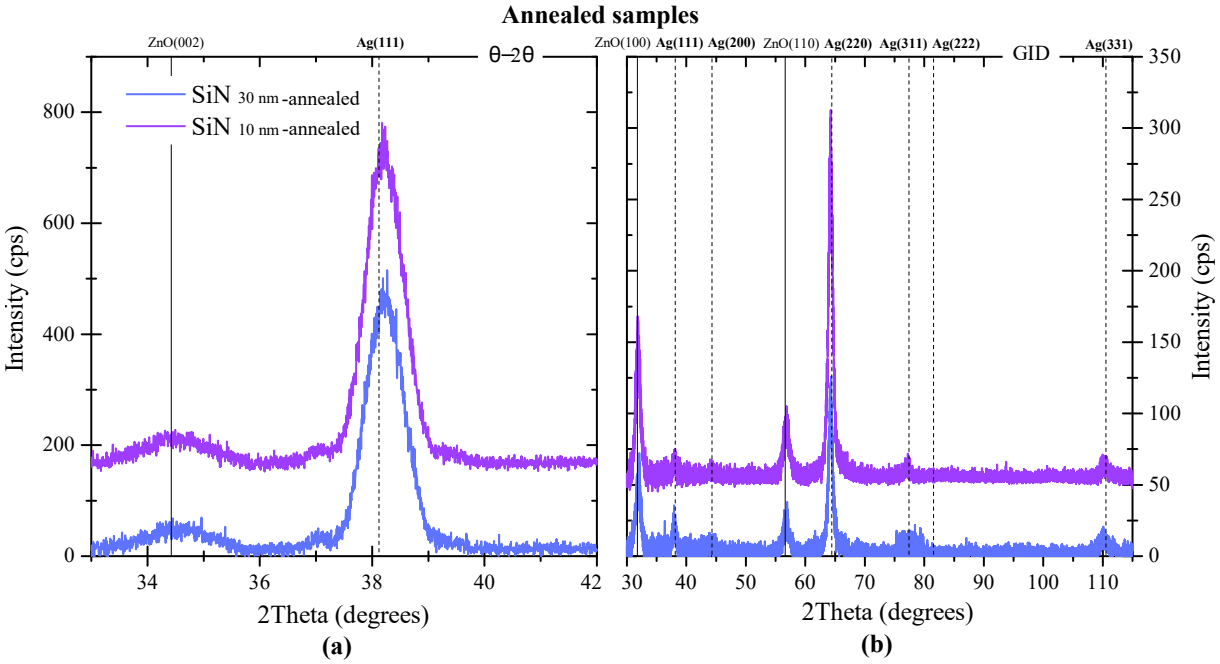

Figure 3.3 (a) $\theta - 2\theta$ and (b) GIXRD of Ag-based stacks with SiN capping layers of different thicknesses after annealing.

In summary

A SiN capping layer is needed in low-emissive coatings to prevent silver oxidation and degradation during air exposure or during post-deposition annealing. The optimal layer was found for a SiN film deposited in reactive sputtering mode from a Si-metallic target, 10 or 30 nm thick.

3.1.2 The impact of the sputtering machine and of the substrate

First of all, the same reference coating (Fig. (3.1)) was deposited with the two sputtering set ups, LINA and MISSTIC, on a float glass substrate. According to diffraction (Fig. (3.4)), both the AZO and Ag layers grow in a polycrystalline state while no peak related to SiN is observed.

Nevertheless, the grains of the zinc oxide and metallic layers grow with a clear out-of-plane orientation as seen in Fig. (3.4)-a where only diffraction peaks of the same family of planes are present. In AZO, this behaviour is linked to a self-texture mechanism (Sec. (1.3.1)) driven by the preferred nucleation of crystallites with a (0001) plane parallel to the substrate in the initial growth stage of the film. Similarly, the Ag (111) out-of-plane texture is induced by the lower surface energy of the (111) face and the hetero-epitaxial growth on the ZnO(0001) surface (Sec. (1.4.2)). Nevertheless, despite this same out-of-plane global orientation, the variation of the conditions of sputtering due to the use of different set ups results in different degrees of texture. Thus, before annealing, the MISSTIC samples present a more pronounced out-of-plane grain orientation compared to LINA samples (Tab. (3.3)), as testified by the peak intensities and their lower rocking curve widths of AZO $RC_{ZnO(002)}$ and Ag $RC_{Ag(111)}$ (16.80° and 6.64° compared to 22.12° and 17.79°, respectively). On the other hand, the grains are not clearly textured in-plane. Indeed, in the GIXRD diffractograms (Fig. (3.4)-b), all allowed peaks which one would expect for a randomly oriented powder are present. But given the preferential Ag (111) out-of-plane orientation, a prominent (220) peak is noted, while for the AZO layer only peaks associated to the family of planes perpendicular to (002) are observed, *i.e.* (100) and

(110). The degree of orientation appears also in the texture coefficient (TC) (Tab. (3.3)) which reveals a much higher value for the MISSTIC sample. The poorer texture of the LINA sample is also attested by the ASTAR images presented in Fig. (3.5)-a for the LINA sample and in Fig. (3.5)-b for MISSTIC glass-based sample. The out-of-plane grain orientation of the silver film and its random oriented in-plane organisation is further clearly confirmed by the pole figure images of the Ag (111) reflection reported in Fig. (3.6). Only a ring shaped intensity is observed.

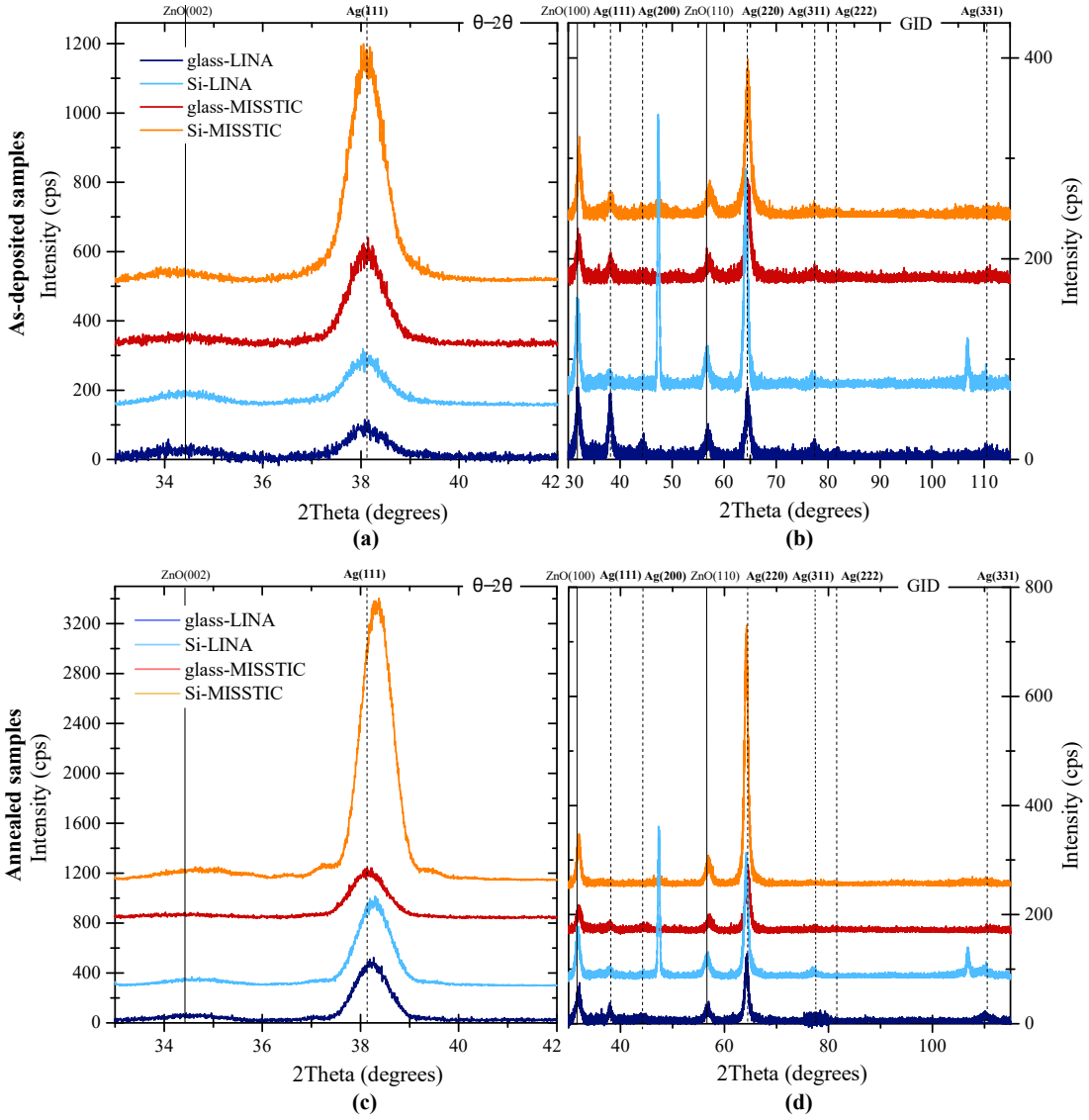

Figure 3.4 (a-c) $\theta - 2\theta$ and (b-d) GIXRD diffractograms, before and after annealing, of a reference silver stack based on glass or Si wafer substrates. The deposition was made in the LINA pilot line coater or in the MISSTIC research sputtering machine.

For both LINA and MISSTIC samples, the silver coherent domain size as determined from the Scherrer analysis of the most intense peak has very similar values of about $\sim 9 - 10$ nm in the vertical and parallel directions (Tab. (3.3)). The closeness with the film thickness (12 nm) shows that only one grain is expected to grow in the layer thickness. However, the ASTAR image ana-

lysis (Fig. (3.5) (a) and (b)) points at larger grains for the MISSTIC samples (∼14nm) compared to the LINA ones (∼10nm). The discrepancy may lie in the bias introduced by the Scherrer analysis of only one reflection, the absence of the 20 nm thick SiN under layer in ASTAR samples where the oxide seed layer is instead grown on a SiN_x membrane. On the other hand, the AZO domains have the same lateral length, $\sim 8-9$ nm, but a different vertical size (6 nm for MISSTIC compared to 9 nm for LINA). The LINA value is inconsistent with the AZO thickness of 5 nm. Even if the observed ZnO peak is the overlap of the contributions of the seed layer and the capping film that are impossible to unfold, one would expect a sharper global peak only if the diffraction from both layers are coherent. But owing to its poor intensity, an uncertainty does exist on the width determination of the ZnO (002) peak, thus contributing to an incorrect estimate of the Scherrer size.

			As-deposited samples				**Annealed samples**			
							650°C	650°C	350°C	650°C
			LINA		**MISSTIC**		**LINA**		**MISSTIC**	
			glass	**Si**	**glass**	**Si**	**glass**	**Si**	**glass**	**Si**
Ag	$\mathbf{D}_{S,OP}$	**[nm]**	9	9	10	10	11	11	10	12
	$\mathbf{RC}_{Ag(111)}$	[°]	17.79	14.20	6.64	5.85	7.25	6.27	5.74	3.62
	$\boldsymbol{\varepsilon_{33}}$	$(\cdot\mathbf{10}^3)$	0.31	0.56	0.31	0.31	-2.71	-3.71	-0.95	-5.22
	$\boldsymbol{a}_{OP-Ag}$	**[Å]**	4.09	4.09	4.09	4.09	4.07	4.07	4.08	4.06
	$\mathbf{L}_{S,IP}$	**[nm]**	9	9	9	8	14	13	9	14
	$\mathbf{TC}_{Ag(220)}$	[%]	29	27	64	74	40	57	53	90
	$\boldsymbol{\varepsilon_{11}=\varepsilon_{22}}$	$(\cdot\mathbf{10}^3)$	-1.28	3.99	-1.84	-1.42	2.88	3.99	-0.041	3.71
	$\boldsymbol{a}_{IP-Ag}$	**[Å]**	4.08	4.10	4.08	4.08	4.10	4.10	4.09	4.10
	$\mathbf{RMS}_{XRR}$	**[nm]**	0.61	-	0.55	0.40	0.53	0.46	0.48	0.41
ZnO	$\mathbf{D}_{S,OP}$	**[nm]**	9	6	6	7	5	6	5	6
	$\mathbf{RC}_{ZnO(002)}$	[°]	22.12	13.56	16.80	8.53	19.13	10.91	15.54	5.65
	$\boldsymbol{\varepsilon_{33}}$	$(\cdot\mathbf{10}^3)$	0.44	0.72	4.11	6.68	-1.82	-5.73	2.13	-9.33
	$\boldsymbol{c}_{OP-ZnO}$	**[Å]**	5.21	5.21	5.23	5.24	5.20	5.18	5.22	5.16
	$\mathbf{L}_{S,IP}$	**[nm]**	9	10	8	10	9	7	9	11
	$\mathbf{TC}_{ZnO(110)}$	[%]	32	42	36	23	33	39	29	27
	$\mathbf{TC}_{ZnO(100)}$	[%]	55	44	51	30	54	48	59	37
	$\boldsymbol{\varepsilon_{11}=\varepsilon_{22}}$	$(\cdot\mathbf{10}^3)$	-4.39	-1.04	-6.82	-10.43	-4.09	-1.34	-7.72	-5.61
	$\boldsymbol{a}_{IP-ZnO}$	**[Å]**	3.24	3.25	3.23	3.22	3.24	3.25	3.22	3.23
	$\mathbf{RMS}_{XRR}$	**[nm]**	0.57	-	0.76	0.59	0.58	0.46	0.59	0.39
$\mathbf{R}_{\square-4P}$		$[\Omega/\mathbf{sq}]$	4.62	4.64	4.45	5.77	3.46	3.32	4.07	3.98
$\boldsymbol{\rho_{4P}}$		$[\mu\Omega\mathbf{.cm}]$	5.54	5.57	5.34	6.92	4.15	3.98	4.88	4.78
Gain		[%]					25	28	9	31

Table 3.3 Microstructural characteristics of reference stacks, before and after annealing, deposited on glass and Si wafer, in LINA and MISSTIC machines.

Another difference between samples is observed for the out-of-plane macrostrain (ε_{33}) of the AZO lattice, determined through the (002) peak position in the θ-2θ diffractogram (Tab. (3.3)). Indeed, it appears that the AZO film sputtered in the MISSTIC machine grows more in a tensile stress state than the LINA film, resulting in a lattice vertical parameter of 5.23 Å instead of 5.21 Å [52] in the bulk. In the literature, the ZnO stress state is often associated to strong oxygen ion bombardment during deposition [84, 86, 89, 90] ; as the AZO film has been sputtered from a ceramic target without additional oxygen in the MISSTIC machine, it explains why a larger

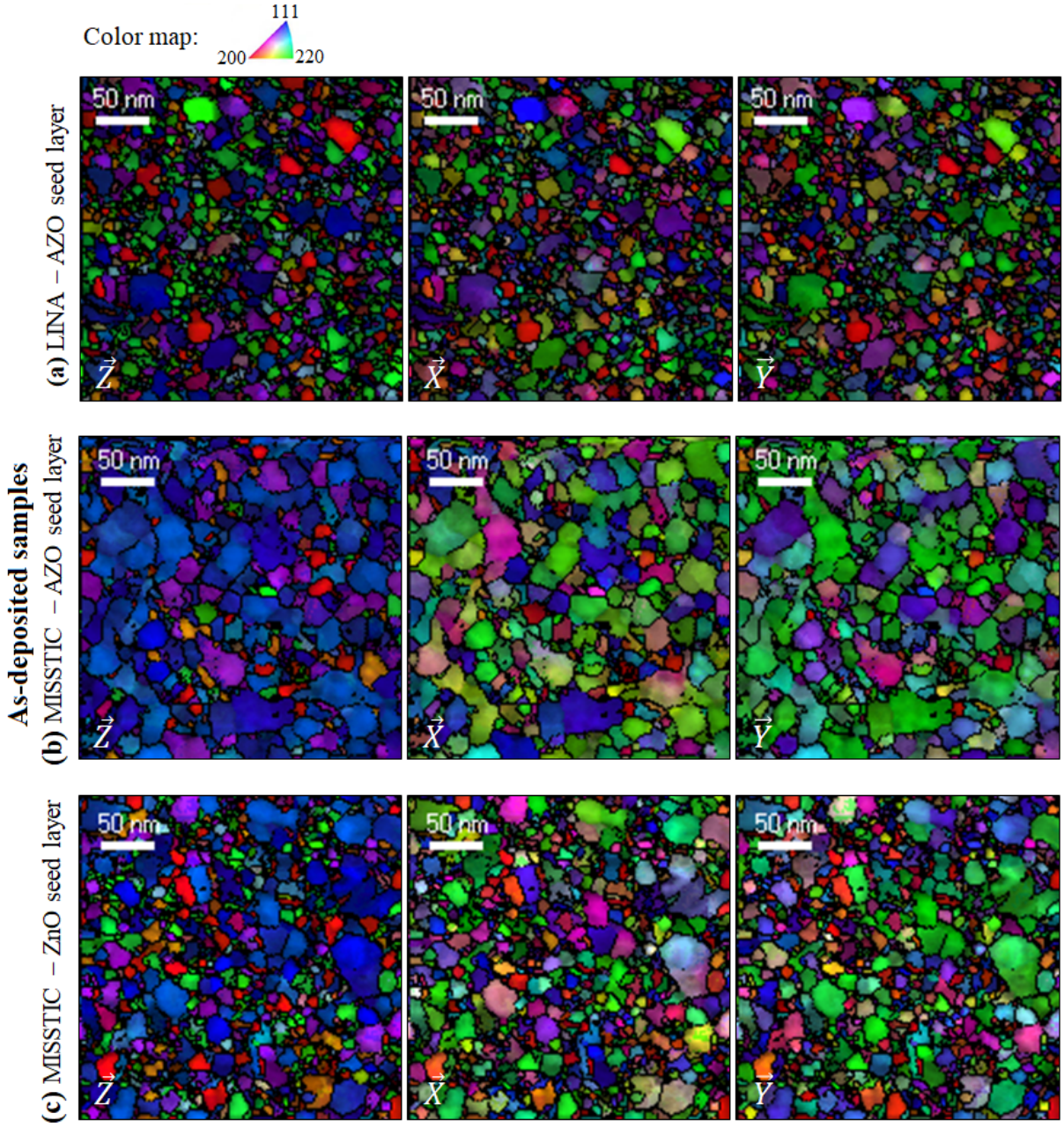

Figure 3.5 Plane view ASTAR texture maps, before annealing, along the three space directions of a Ag film obtained from a stack deposited onto SiN_x membrane via (a) the LINA pilot coater or via (b-c) MISSTIC. The silver was grown on AZO seed layer in (a) and (b), and on a ZnO-met film in (c). The colour maps code corresponds to the [111] (blue), the [220] (green) and the [200] (red) orientations.

macrostrain is observed. In response to this vertical tensile strain, a tetragonal Poisson distortion sets up leading to a slight compressive in-plane strain ($\varepsilon_{11} = \varepsilon_{22}$) with a lateral lattice parameter associated the LINA and MISSTIC of 3.236 Å and 3.228 Å (instead of 3.250 Å in the bulk [52]). Regarding the silver layer (Tab. (3.3)), its macrostrain is quite similar for the two sputtering set ups but very small. Vertically, both samples show a $\varepsilon_{33} = 0.31 \cdot 10^{-3}$, corresponding to a vertical lattice constant of 4.087 Å, and a $\varepsilon_{11} = \varepsilon_{22} = -1.28 \cdot 10^{-3}$ (LINA) and $-1.84 \cdot 10^{-3}$ (MISSTIC),

associated respectively to a lateral lattice constant of 4.080 Å, and 4.078 Å. The values are all very similar to the literature reference of 4.085 Å, underlining a small overall stress in the metal. At last, despite better structural characteristics of the MISSTIC sample, the electrical resistivity associated to the stack is surprisingly higher than the LINA sample.

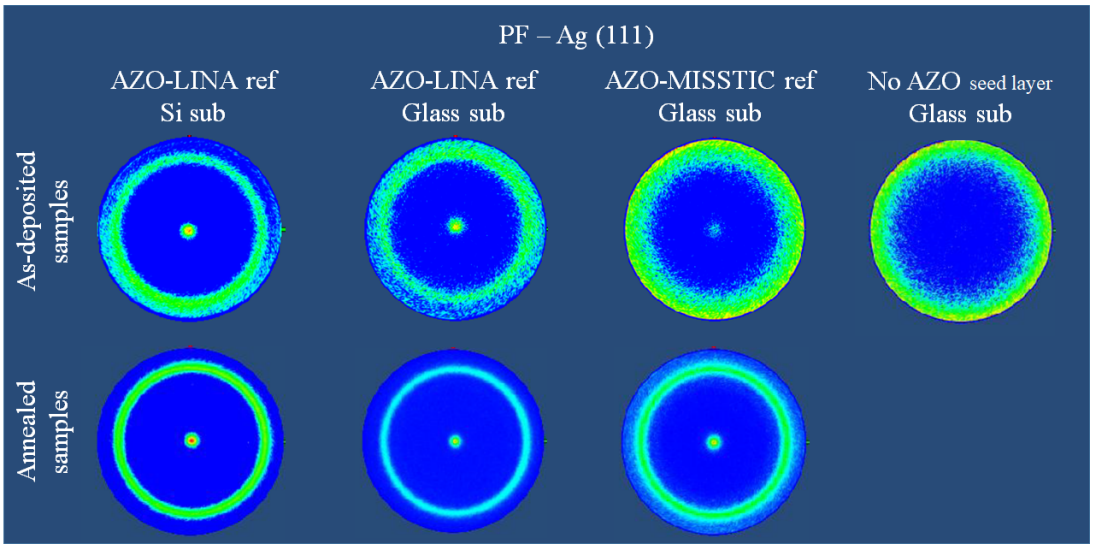

Figure 3.6 Pole figure before and after annealing of a reference silver stack, based on glass or Si wafer substrate. The deposition were made in the LINA coater or in the MISSTIC sputtering machine.

Glass-based stacks were then annealed, at 650°C for LINA samples and at 350°C for MISSTIC samples (Tab. (3.3)). Independently of the temperature applied, the AZO structural characteristics remains almost unchanged. Only a small improvement of the out-of-plane grain orientation as seen in the decrease of the $RC_{ZnO(002)}$ width of about ~ 10 %, and a relaxation of the stress are observed. In the direction perpendicular to the substrate surface, for the LINA samples, the AZO lattice goes from an unstressed to a compressive state (the 5.208 Å vertical lattice constant becomes 5.197 Å); the same change is observed in MISSTIC samples but with a lower impact (from 5.227 Å to 5.217 Å). In-plane, the lattice constant parameter variations are negligible. On the other hand, the variations induced in the Ag layer are much more pronounced, especially in the case of the LINA sample for which a higher annealing temperature has been used. For this latter, a strong improvement of the out-of-plane orientation is observed as the $RCAg(111)$ value drops from 17.8° to 7.25° while the (220) texture coefficient improved from 30 to 40 %. The lateral domain size exhibits a sizeable increase from 9 nm to 14 nm and a change from compressive to tensile state is observed in-plane. For the MISSTIC sample, the structural variations of the Ag layer is less pronounced. In agreement with the observed structural changes, a resistivity drop happens, corresponding to a conductivity gain of 25 % for the LINA sample but only 9 % for the MISSTIC sample.

To conclude the study, the same stacks were also sputtered in the same conditions with the two set ups but on a silicon wafer. The Si-based replicas present structural characteristics very similar to the glass-based samples (Tab. (3.3)). For the LINA sample, the difference is an improved out-of-plane texture, of both AZO ($RC_{ZnO(002)} = 13.56°$ vs 22.12°) and Ag layer ($RC_{Ag(002)}$ =14.20° vs 17.8°). A slight change is also observed in the values of the Ag macrostrain, particularly in-plane, where $\varepsilon_{11} = \varepsilon_{22} = 3.99 \cdot 10^{-3}$, compared to the glass reference $\varepsilon_{11} = \varepsilon_{22} = -1.28 \cdot 10^{-3}$. In

parallel, the stack resistivity does not vary at all exhibiting the value of $\sim 5.6\,\mu\Omega$.cm. Similarly, the MISSTIC Si-based replica shows characteristics very similar to the glass-based sample, with an improved out-of-plane orientation of the ZnO grains and a slightly higher silver out-of-plane texture.

To enhance the electrical and structural properties of the stacks, both Si-based samples were annealed at 650°C for 10 min (Tab. (3.3)). The annealed LINA Si-based sample has characteristics similar to the annealed glass-based stack. Nevertheless, the Si-based AZO layer has an enhanced out-of-plane texture after annealing ($RC_{ZnO(002)} = 10.91°$ vs 13.56°). The Ag layer shows also small improvement of its texture in both directions of space. But overall no strong changes are found; this is also reflected in the post-deposition resistivity value which is improved by only 4% ($3.98\,\mu\Omega$.cm) with respect to the annealed glass-based sample. Due to the higher treatment temperature, the annealed MISSTIC Si-based stack presents larger structural variations compared to the glass reference. Already showing a larger grain orientation before annealing, the AZO layer distinguishes itself by a very low rocking curve value of 5.65° after annealing. Along the out-of-plane direction, the lattice presents a macrostrain variation characterized by a vertical parameter change from 5.24 Å, before annealing to 5.16 Å after. In-plane, no clear improvement is observed. At the opposite, the Ag layer shows a significant in-plane structural improvement with a vertiginous rise of the texture coefficient ($TC_{Ag(220)}$=90 %). This improvement is also accompanied by an increase of the out-of-plane (111) orientation, from $RC_{Ag(111)} = 5.85°$ to $RC_{Ag(111)} = 3.62°$, as well as a strong increase of the lateral domain sizes, which almost double their length to 14 nm. The structural variations observed in the MISSTIC Si-sample are comparable to those of the annealed LINA samples. As a result of the enhance structural properties, the sample shows a strong conductivity gain of 31%, lowering its resistivity to $4.78\,\mu\Omega$.cm, comparable to the annealed MISSTIC glass-based sample resistivity ($4.88\,\mu\Omega$.cm).

In summary

A simplified Ag-based stack was deposited on glass using two sputtering set ups, namely the line coater LINA and the research sputtering machine MISSTIC. Before annealing, the different sputtering conditions between the two machines have a significant impact on the structural properties of the films, especially the out-of-plane grain orientation of the AZO seed layer and of Ag; the MISSTIC samples shows the best out-of-plane texture. Nevertheless, these structural differences do not reflect in the sample electrical properties as the resistivity values differ of only 4%. The annealing treatment was performed at different temperatures, 650°C for LINA samples and 350°C for MISSTIC ones. As a result, a higher conductivity gain was observed for the LINA samples in parallel to the film recrystallisation. To investigate the impact of the substrate, the same stacks were also deposited on a Si-wafer. Except for an enhanced out-of-plane (002) orientation of the AZO layer, the Si-replica showed only negligible structural differences compared to the glass substrate, both before and after annealing. Unchanged electrical properties were also observed for LINA samples, while a strong resistivity increase, of 23% before annealing and 11% after annealing, was observed between MISSTIC glass- and Si-based samples. Hardly correlated with structural changes or detrimental thermal process, the Si-based poor conductivity is supposed to originate from an increased but unexplained surface roughness and/or defect density.
Overall, the nature of the substrate has only a negligible impact on the structural properties of the film. Stronger changes are observed with the deposition environment due a different sputtering set up. With the machines used in this work, astonishingly, these changes does not clearly reflect in the electrical properties of the resulting stacks.

3.1.3 The role of zinc oxide as a seed or capping layer

In low-emissive coatings, zinc oxide is the most used industrial seed layer for silver. As previously stated (see *Introduction*), this material has been introduced to reduce the resistivity value of the stack by improving the crystallization of the metal film and promoting its out-of-plane (111) texture. Thus, in a stack where silver is deposited directly on the amorphous SiN film (Fig. (3.7)), only a poor quality metallic film is obtained as seen in the θ-2θ and grazing incidence diffractograms of Fig. (3.7)-(*no AZO-sub sample*). In the out-of-plane direction, Ag (111) signal is hardly visible. In-plane, all possible orientations within the measured angular range are visible. However, as compared to the grazing incidence diffraction of a classical industrial reference, the (220) peak does not show a pronounced intensity. At variance, this is the (111) peak that is the most intense reflection as in the case of a powder sample. In fact, all reflections present nearly the same relative intensity as in powder. A further proof of the lack of texture is given by the width of the Ag(111) peak rocking curve of about 26°, twice as large as a reference, and the Ag (220) texture coefficient value of 9 %, three time lower than the reference sample (Tab. (3.4)). Also, the in-plane coherent domain size is reduced to half of the layer thickness, indicating a larger number of grain boundaries. At the opposite, the out-of-plane (4.08 Å) and in-plane (4.07 Å) lattice parameters do not show a strong deviation from the industrial reference and the literature values. In conclusion, the silver film is not textured in none of the space directions. The observed structural changes are accompanied by a high electrical resistivity of 6.70 $\mu\Omega$.cm, 23% higher than a reference coating.

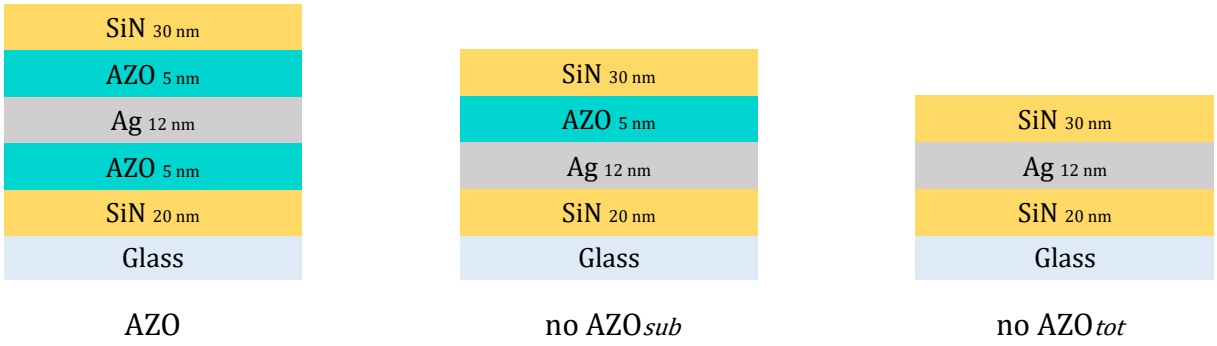

Figure 3.7 Schematic of Ag-based stack with and without the zinc oxide layers.

Despite the absence of the oxide seed layer, clear ZnO peaks associated to the capping layer are present. The corresponding structural characteristics are reported in bold in Tab. (3.4). The results, comparable to those including the seed layer (Tab. (3.3)), demonstrate that the observed oxide diffraction peaks are the combined response of the seed and capping AZO layers. Furthermore, as the upper AZO is grown on a crystalline metallic film with a (111) orientation, the layer is expected to be more crystallised than the lower film grown on an amorphous SiN layer.

Surprisingly, once the sample is annealed at 650°C for 10 min, the Ag layer undergoes a rapid improvement of its crystallinity (Tab. (3.4)) characterized by a noticeable out-of-plane texture with a Ag (111) rocking curve width drop to 6.15° and an increase of the partial in-plane orientation from nearly zero to $TC_{Ag(220)}$=49 %. In parallel, the lateral size of the coherent domain quadruples reaching a value of 20 nm. A consistent conductivity gain of 23% is recorded, which lowers the resistivity to 5.12 $\mu\Omega$.cm in the range of a reference stack before annealing. Nevertheless, this behaviour has not been proven fully repeatable resulting sometimes in the deterioration of the silver film after thermal treatment to such an extent that a reliable analysis of structural

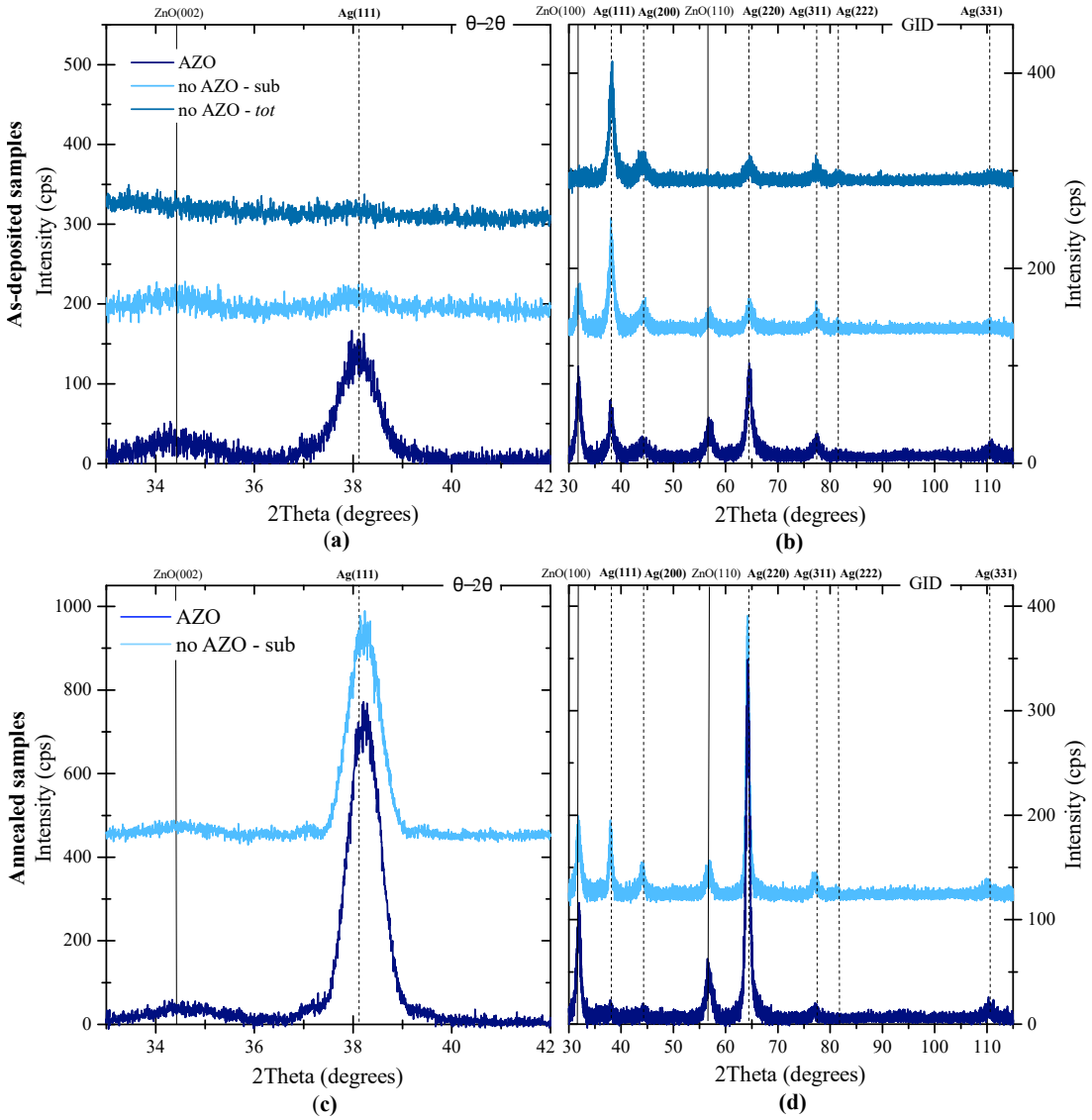

Figure 3.8 (a-c) $\theta - 2\theta$ and (b-d) GID scans of Ag-based stacks with and without the AZO layers before and after annealing. For sample labels, refer to Fig. (3.7).

and electrical properties was not possible. To remove any doubt about the possible influence of the capping layer, a sample with no AZO seed and capping layer was fabricated. The sample characteristics were compared to a stack without AZO seed layer produced in the same batch (Fig. (3.8)). Both samples present a silver layer of very poor quality. The lack of the (111) Ag peak in the two θ-2θ diffractograms attests the absence of a out-of-plane texture as well as a very low crystallization of the layer. Also in-plane, the two samples present the same diffraction patterns with peaks of similar intensities. On the other hand, the resistivities of the two samples differ ; in the absence of AZO layer, it worsens up to 9.38 $\mu\Omega$.cm (ρ_{4P}-AZO < ρ_{4P}-$no\ AZO$-sub < ρ_{4P}-$no\ AZO$-tot). These results mitigate the role played by the seed layer and points at a possible influence of the crystallized AZO capping layer in the metal recrystallisation. Annealing treatment of the *no AZO-tot* sample resulted in a strong degradation of the silver layer, with visible signs on the sample surface of the coating corrosion and metal dewetting, hindering reliable electrical or structural measurements.

			As-deposited samples			Annealed samples 650°C	
				LINA			LINA
			AZO	no AZO	no AZO	AZO	no AZO
				sub	*tot*		*sub*
Ag	$\mathbf{D}_{S,OP}$	[nm]	10	6	-	11	11
	$\mathbf{RC}_{Ag(111)}$	[°]	13.78	25.96	-	6.48	6.15
	$\boldsymbol{\varepsilon_{33}}$	$(\cdot\mathbf{10}^3)$	0.56	-1.71	-	-2.71	-2.46
	$\boldsymbol{a_{OP-Ag}}$	[Å]	4.09	4.08	4.08	4.07	4.08
	$\mathbf{L}_{S,IP}$	[nm]	7	5	4	14	20
	$\mathbf{TC}_{Ag(220)}$	[%]	31	9	6	78	49
	$\boldsymbol{\varepsilon_{11} = \varepsilon_{22}}$	$(\cdot\mathbf{10}^3)$	-0.48	1.45	1.03	2.31	2.10
	$\boldsymbol{a_{IP-Ag}}$	[Å]	4.08	4.07	4.08	4.10	4.10
	$\mathbf{RMS}_{XRR}$	[nm]	0.53	0.67	0.68	0.55	0.60
ZnO	$\mathbf{D}_{S,OP}$	[nm]	17	**6**	-	3	**11**
	$\mathbf{RC}_{ZnO(002)}$	[°]	21.39	**23.12**	-	18.18	**21.10**
	$\boldsymbol{\varepsilon_{33}}$	$(\cdot\mathbf{10}^3)$	1.85	**8.68**	-	-2.38	**0.44**
	$\boldsymbol{c_{OP-ZnO}}$	[Å]	5.22	**5.25**	-	5.19	**5.21**
	$\mathbf{L}_{S,IP}$	[nm]	9	**7**	-	10	**8**
	$\mathbf{TC}_{ZnO(110)}$	[%]	34	**36**	-	34	**33**
	$\mathbf{TC}_{ZnO(100)}$	[%]	52	**50**	-	53	**54**
	$\boldsymbol{\varepsilon_{11} = \varepsilon_{22}}$	$(\cdot\mathbf{10}^3)$	-3.79	**-4.70**	-	-3.18	**-3.48**
	$\boldsymbol{a_{IP-ZnO}}$	[Å]	3.24	**3.23**	-	3.24	**3.24**
	$\mathbf{RMS}_{XRR}$	[nm]	0.50	-	-	0.52	-
SiN	$\mathbf{RMS}_{XRR}$	[nm]	0.58	0.54	0.81	0.53	0.52
$\mathbf{R}_{\square-4P}$		$[\Omega/\mathbf{sq}]$	4.27	5.58	7.82	3.10	4.27
$\boldsymbol{\rho_{4P}}$		$[\mu\Omega\mathbf{.cm}]$	5.12	6.70	9.38	3.72	5.12
Gain		[%]				27	23

Table 3.4 Microstructural characteristics before and after annealing of Ag-based stacks on glass with or without AZO layers. The samples were deposited in the LINA pilot line coater. For sample labels, see Fig. (3.7).

In summary

The growth of Ag on AZO clearly favours a (111) out-of-plane Ag orientation and enhances the metal film crystallinity. As a result, the stack resistivity is strongly decreased. On the other hand, AZO as a capping layer, plays no clear role in the structural properties of silver. An annealed coating, where Ag was grown directly on SiN shows almost identical structural properties as a reference stack. The repeatability of this behaviour was however not ensured. Certainly, as seen directly through the stack resistivity, AZO capping protects the upper silver interface from environment during the growth of the SiN layer and from corrosion and dewetting of the coating during the high temperature thermal treatment.

3.1.4 Changing the seed layer

The zinc oxide nature

Crystallised zinc oxide thin films can easily be grown via a variety of methods (Sec. (1.3.1)). Already with magnetron sputtering, numerous deposition configurations can be selected : (i) ZnO ceramic targets, possibly Al-doped, with or without additional oxygen gas, or (ii) metallic Zn target, pure or Al-doped, with or without oxygen gas, all of them (iii) sputtered via RF or DC sources working at different conditions. All these parameters (deposition mode, power, gas mixture ratio, pressure, target, ...) can have a significant effect on the microstructure and compositions of the oxide layer, which can result in a rougher surface, a higher grain orientation or an enhanced columnar texture [39] (Sec. (1.2)). Up to now, the discussion has been based on zinc oxide seed layers produced from a ZnO:Al doped ceramic target (AZO) deposited in non-reactive mode with a DC source. In the first part of this section, these reference coatings will be compared to stacks where Ag has been grown on a ZnO layer deposited in a reactive mode starting from a metallic Zn target (ZnO-met) (Fig. (3.9)).

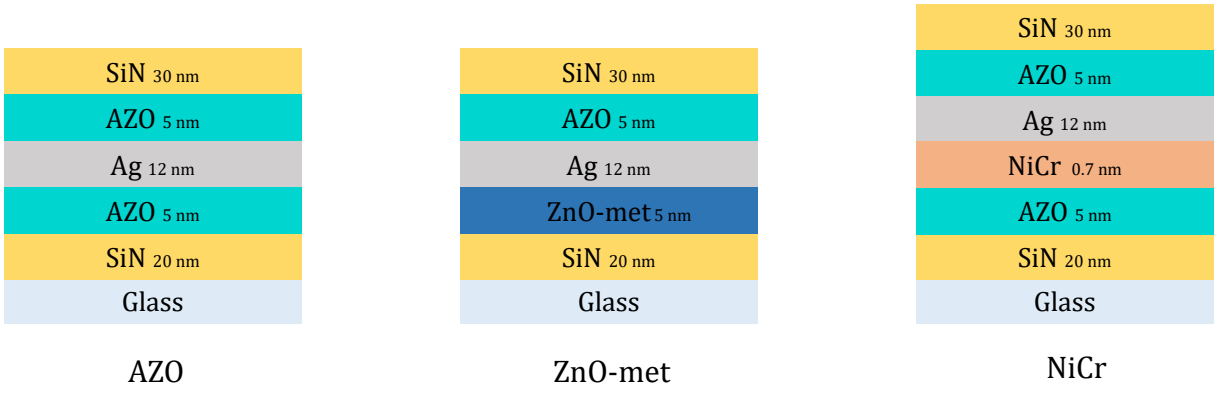

Figure 3.9 Schematic of the Ag-based stack with various seed layers. AZO corresponds to deposition from a ceramic target and ZnO-met to deposition from a metallic Zn target in reactive mode.

AZO- and ZnO-met-based coatings were grown in MISSTIC chamber and characterized by XRD analysis (Fig. (3.10) and Tab. (3.5)). In-plane, the oxide layers exhibit similar lateral coherent size (∼8 nm before annealing and 9 nm after annealing) and analogous stress states associated with lattice constant values of about 5.23 Å, slightly decreasing after annealing to 5.22 Å, and in-plane of 3.22 Å, that remains constant during thermal treatment. On the other hand, an inconsistency appears, before annealing, for the out-of-plane domain size of ZnO-met layer, which is larger than the film thickness, again because of the poor broad diffraction signal (Fig. (3.10)). Conversely, the same parameter for the AZO sample has a value of about ∼ 6 nm, and is in line with the sputtered layer thickness. Overall, the strongest differences of the samples structural properties are mainly related to the texture of the oxide and of the metal. Thus, before annealing, the ZnO-met layer presents a $RC_{ZnO(002)}$ of 24.19° and a $TC_{ZnO(100)}$ of 46 %, which indicates respectively an increase of misorientation of 30% in the out-of-plane direction and of 10% in-plane compared to AZO. The decrease in texture of the seed layer consequently induces the growth of a poorly oriented silver film, characterized by $RC_{Ag(111)}$ of 16.92° (against 6.64° for the AZO sample) and a $TC_{Ag(220)}$ of 21 % (compared to 64 % for the AZO sample). Nevertheless, in terms of domain size and micro- and macro-strain, the two metallic film present only negligible variations.
After annealing, performed at 350°C for 10 min due to the reduced size of the sample, the layers

show a slight improvement of their grain texture but the ZnO-met sample still presents a higher disorder than the AZO sample. Again, the poorer oriented ZnO-met sample has a lower conductivity, especially after annealing (5.58 $\mu\Omega$.cm against 4.88 $\mu\Omega$.cm). It should be noted that this behaviour is not representative for commercialized ZnO-met SGR products that commonly present equal conductivities to AZO stacks.

			As-deposited samples		**Annealed samples** 350°C	
			MISSTIC		**MISSTIC**	
			AZO	**ZnO-met**	**AZO**	**ZnO-met**
Ag	$\mathbf{D}_{S,OP}$	**[nm]**	10	9	10	10
	$\mathbf{RC}_{Ag(111)}$	[°]	6.64	16.92	5.74	14.60
	$\boldsymbol{\varepsilon_{33}}$	$(\cdot\mathbf{10}^3)$	0.31	0.82	-0.95	-1.46
	$\boldsymbol{a_{OP-Ag}}$	**[Å]**	4.09	4.09	4.08	4.08
	$\mathbf{L}_{S,IP}$	**[nm]**	9	8	9	9
	$\boldsymbol{\varepsilon_{IP}}$		0.001	0.002	0.012	0.006
	$\mathbf{TC}_{Ag(220)}$	[%]	64	21	53	47
	$\boldsymbol{\varepsilon_{11} = \varepsilon_{22}}$	$(\cdot\mathbf{10}^3)$	-0.26	-0.69	0.81	0.72
	$\boldsymbol{a_{IP-Ag}}$	**[Å]**	4.08	4.08	4.09	4.09
	$\mathbf{RMS}_{XRR}$	**[nm]**	0.55	0.74	0.48	0.67
ZnO	$\mathbf{D}_{S,OP}$	**[nm]**	6	10	5	6
	$\mathbf{RC}_{ZnO(002)}$	[°]	16.80	24.19	15.54	21.87
	$\boldsymbol{\varepsilon_{33}}$	$(\cdot\mathbf{10}^3)$	4.11	7.25	2.13	3.50
	$\boldsymbol{c_{OP-ZnO}}$	**[Å]**	5.23	5.24	5.22	5.22
	$\mathbf{L}_{S,IP}$	**[nm]**	8	7	9	9
	$\mathbf{TC}_{ZnO(110)}$	[%]	36	40	29	34
	$\mathbf{TC}_{ZnO(100)}$	[%]	51	46	59	50
	$\boldsymbol{\varepsilon_{11} = \varepsilon_{22}}$	$(\cdot\mathbf{10}^3)$	-6.82	-8.33	-7.72	-9.50
	$\boldsymbol{a_{IP-ZnO}}$	**[Å]**	3.23	3.22	3.22	3.22
	$\mathbf{RMS}_{XRR}$	**[nm]**	0.76	0.44	0.59	0.57
$\mathbf{R}_{\square-4P}$		$[\Omega/\mathbf{sq}]$	4.45	4.87	4.07	4.65
ρ_{4P}		$[\mu\Omega\mathbf{.cm}]$	5.34	5.84	4.88	5.58
Gain		[%]			8	5

Table 3.5 Microstructural characteristics of silver-based stacks, before and after annealing, deposited via MISSTIC. For these samples, the metal has been grown on ZnO sputtered in DC mode from a Al-doped ceramic target (AZO) and from a metallic target (ZnO-met) in oxygen atmosphere.

Electron-based microscopy investigations do confirm the X-ray diffraction conclusion of a better crystallised Ag film on AZO than on ZnO-met. STEM and HAADF imaging of a AZO MISSTIC sample reveals (generated like previously, by stack deposition directly on SiN_x TEM membranes) a poly-crystalline Ag film with clear grain boundaries, some Ag plane in zone axis and locally some "Moiré" patterns due to local interaction between Ag and zinc oxide crystal network (Fig. (3.11)). The grain mean lateral diameter is estimated at $\sim$ 14 nm, larger than the coherent domain size obtained through XRD. The imaging performed on ZnO-met MISSTIC sample leads to smaller grains ($\sim$ 10 nm) and less defined grain boundaries. Similar results were also observed in the PhD work on zinc oxide of J. Voronkoff [39]. From the focus in HR mode on a Ag domain, a distance of 0.240 nm could be obtained in close agreement with the $(11\overline{2})$

inter-reticular lattice spacing (0.236 nm).

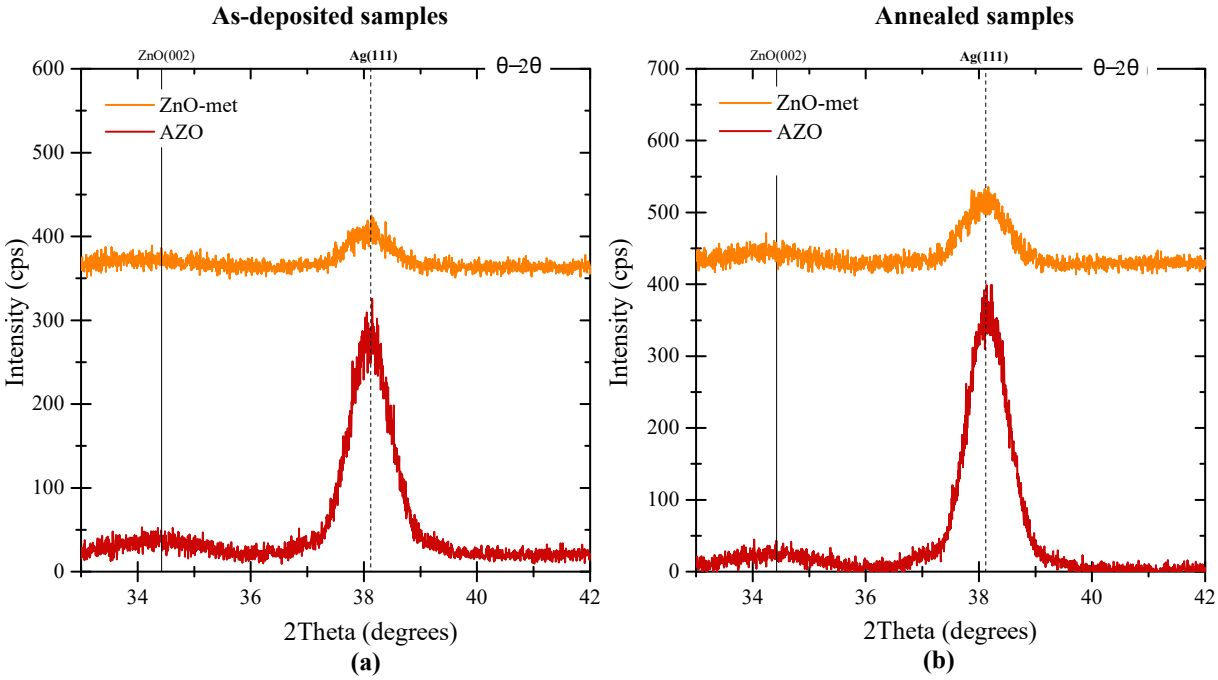

Figure 3.10 $\theta - 2\theta$ diffractograms of Ag-based stacks with zinc oxide layers sputtered in DC from an Al-doped ceramic target (AZO) or from a Zn metallic target in reactive mode (ZnO-met) before (a) and after annealing (b).

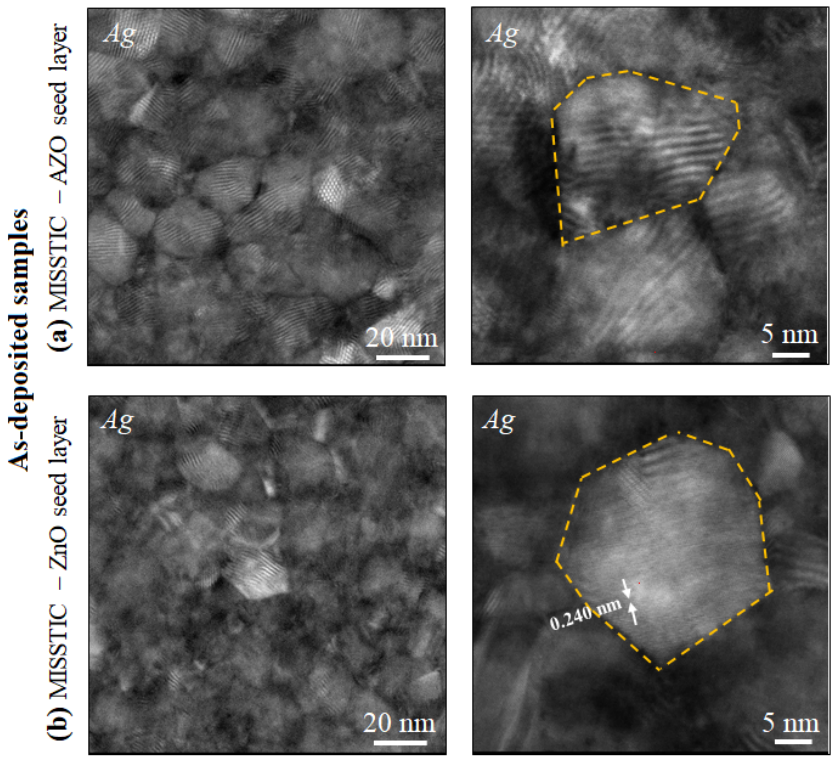

Figure 3.11 STEM-HAADF plane-view pictures of stack deposited with MISSTIC (without annealing) including (a) AZO and (b) ZnO-met seed layer.

The blocker layer

In industrial products, a very thin sacrificial metal layer (typically 0.3-1 nm thick), called the blocker layer, is often introduced at the interfaces between Ag and the zinc oxide. Placed below the Ag film, the blocker is used to improve the wettability and adhesion of the silver on the seed layer and in order to improve the brush resistance of the coating after tempering. Placed on top, its role is to protect silver from oxidation that may occur during the deposition of the capping zinc oxide [39,194]. In all cases, during annealing, it acts as a trap for oxygen diffusion that is known to favour silver dewetting [195]. Due to their affinity with oxygen, blocker layers are composed of Ti or NiCr alloy, this last one being deposited in the form of the binary alloy NiCr (80/20 %wt) [196,197]. Pure Nickel is also known to decrease the percolation threshold of silver required to achieve a conductive film [46]. Industrially, it has been observed, that stacks exhibit higher resistivity values with blocker layers than without. This trend has been mainly associated to a variation of the silver interface, as blocker layers introduce defects that act as scattering centres for electrons. To pinpoint this behaviour, a stack with an additional 0.7 nm NiCr under-layer (Fig. (3.9)) was analysed through XRD (Fig. (3.12) and Tab. (3.6)). In the following sections, the resistivity of coatings with an upper NiCr blocker and double (upper and under) NiCr films were also included in the study of resistivity as a function of temperature, unfortunately without advanced structural study like for NiCr under-blocker.

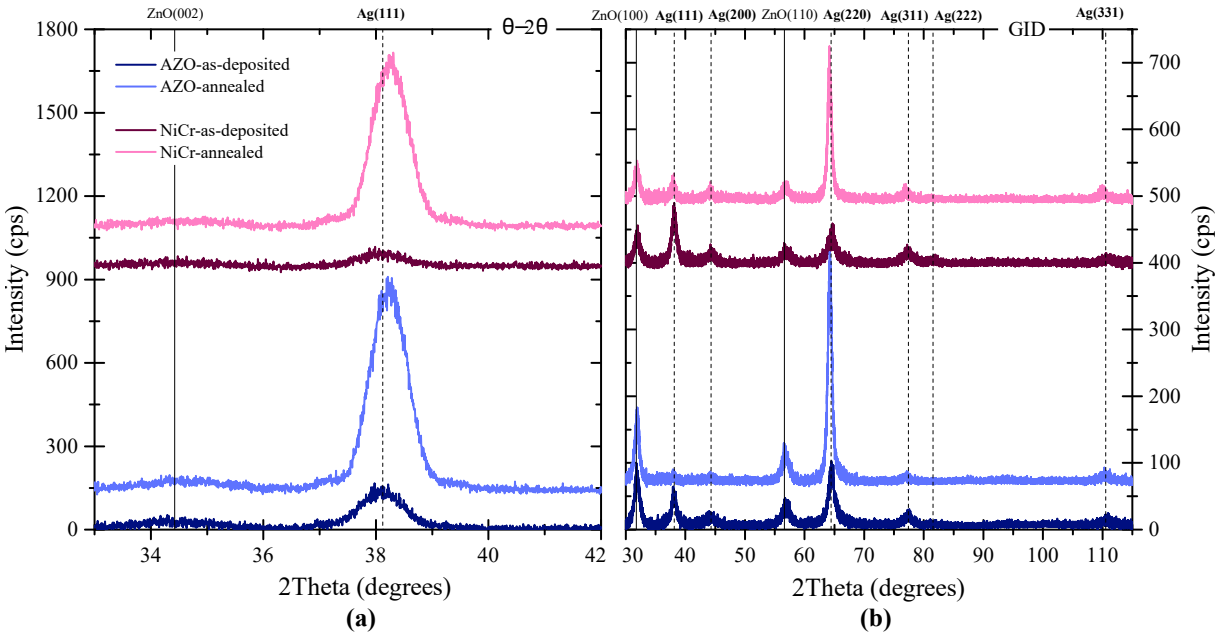

Figure 3.12 (a) $\theta - 2\theta$ and (b) GIXRD of Ag-based stacks with and without a NiCr under blocker. The diffractograms were acquired before and after annealing.

As expected, the introduction of the NiCr layer induces a clear increase of the coating resistivity of about 20 % compared to a stack without blocker (Tab. (3.6)). As the NiCr thin layer is positioned over the seed layer, the main changes would be expected in the AZO surface roughness and in the silver structure. But, structurally, the two samples present close characteristics, a proof that the presence of the under-blocker does not have a strong influence on the growth mode of the silver film. The silver grains exhibit a out-of-plane coherent domain size of $\sim$ 11 nm, equivalent to the film thickness, and lateral domain size of $\sim$ 6 nm. Still having a clear (111) out-of-plane texture, the Ag film shows a slightly lower degree of orientation with NiCr, associated to a $RC_{Ag(111)}$ of 15.11° compared to 13.78° and an in-plane $TC_{Ag(220)}$ of 18 % compared

to 31 %. As before, the overall Ag macrostrains remain small. After annealing, these small discrepancies observed between the two samples vanish, except the in-plane degree of orientation and the conductivity, both lower when the NiCr is present. The absence of strong structural variations with NiCr denotes that the increase in resistivity observed for these coatings is probably due to an increase of the silver interface roughness, especially after annealing ($\mathrm{RMS}_{XRR} \sim 1.1 - 1.2$ nm with NiCr vs 0.5 nm without). In addition, at the interface, the presence of the blocker metallic layer induces defects that act as scattering centres for electrons, as similar resistivity degradations are observed also when NiCr is positioned on top of silver, as it will be shown later.

			As-deposited samples		**Annealed samples** 650°	
			LINA		**LINA**	
			AZO	**NiCr**	**AZO**	**NiCr**
Ag	$\mathbf{D}_{S,OP}$	**[nm]**	10	11	11	11
	$\mathbf{RC}_{Ag(111)}$	[°]	13.78	15.11	6.48	6.81
	$\boldsymbol{\varepsilon_{33}}$	$\mathbf{(\cdot 10^3)}$	0.56	-0.06	-2.71	-3.22
	$\boldsymbol{a_{OP-Ag}}$	**[Å]**	4.09	4.09	4.07	4.07
	$\mathbf{L}_{S,IP}$	**[nm]**	7	6	14	14
	$\boldsymbol{\varepsilon_{IP}}$		-	-	0.001	0.009
	$\mathbf{TC}_{Ag(220)}$		31	18	78	50
	$\boldsymbol{\varepsilon_{11} = \varepsilon_{22}}$	$\mathbf{(\cdot 10^3)}$	-0.48	-0.05	2.31	2.74
	$\boldsymbol{a_{IP-Ag}}$	**[Å]**	4.08	4.08	4.10	4.10
	$\mathbf{RMS}_{XRR}$	**[nm]**	0.53	0.61	0.55	1.15
ZnO	$\mathbf{D}_{S,OP}$	**[nm]**	17	12	3	11
	$\mathbf{RC}_{ZnO(002)}$	[°]	21.39	23.75	18.18	21.15
	$\boldsymbol{\varepsilon_{33}}$	$\mathbf{(\cdot 10^3)}$	1.85	-0.97	-2.38	-3.50
	$\boldsymbol{c_{OP-ZnO}}$	**[Å]**	5.22	5.20	5.19	5.19
	$\mathbf{L}_{S,IP}$	**[nm]**	9	7	10	7
	$\mathbf{TC}_{ZnO(110)}$		34	36	34	33
	$\mathbf{TC}_{ZnO(100)}$		52	50	53	53
	$\boldsymbol{\varepsilon_{11} = \varepsilon_{22}}$	$\mathbf{(\cdot 10^3)}$	-3.79	-4.09	-3.18	-3.18
	$\boldsymbol{a_{IP-ZnO}}$	**[Å]**	3.24	3.24	3.24	3.24
	$\mathbf{RMS}_{XRR}$	**[nm]**	0.50	0.80	0.52	1.24
NiCr	$\mathbf{RMS}_{XRR}$	**[nm]**	-	0.79	-	1.12
$\mathbf{R}_{\square-4P}$		$\mathbf{[\Omega/sq]}$	4.27	5.29	3.10	3.70
ρ_{4P}		$\mathbf{[\mu\Omega.cm]}$	5.12	6.35	3.72	4.44
Gain		**[%]**			27	30

Table 3.6 Microstructural characteristics before and after annealing of silver-based stacks on glass deposited in the LINA machine. The table compares samples with and without a 0.7 nm thick NiCr under-blocker layer introduced between the AZO seed layer and the Ag layer.

In summary

The seed layer structure and morphology influence the silver structural characteristics. Depending on the deposition configuration, the zinc oxide layer can present some variations in its

structural properties. Changes in the target nature, from ceramic to metallic, and of the sputtering mode, from non-reactive to reactive, leads to the growth of less out-of-plane oriented zinc oxide grains. The worsened seed layer texture is then reflected in a poorer oriented silver layer with a higher resistivity, increasing by ∼9% before annealing and by ∼12% after thermal treatment in respect to the AZO sample. This behaviour is not commonly observed in marketed products, for which ZnO-met-based coatings have equivalent conductivities to AZO-based stacks, but are in agreement with the structural observations described in the PhD work of J. Voronkoff [39] on MISSTIC oxide layers. Often, to improve the silver wettability and adhesion on the oxide or to protect the metal from oxidation, a very thin layer (≤ 1 nm) of NiCr, called the blocker layer, is introduced at the interfaces of silver. Deposited on the oxide seed layer, this thin film only slightly worsens the out-of-plane texture of silver but modifies its interface via an increase in roughness leading to an increase of resistivity, particularly after annealing.

3.2 Correlations between resistivity and structural/morphological characteristics

As pointed before, changes in the stack composition and/or deposition conditions impact the conduction properties of the coating. As detailed in Sec. (1.5), beyond intra-grain defects, the resistivity of thin polycrystalline metallic films is driven mainly by scattering of electrons at interfaces and at grain boundaries, and thus should depend on the lateral grain size, the "quality" of the grain boundaries and the interface roughnesses. However, up to now, in the analysed samples, it has been difficult to clearly pinpoint the main reasons behind the observed electrical behaviour since the coatings presented very similar characteristics. Plotting the resistivity as a function of the different films properties as done in this section will help unravelling the key factors.

3.2.1 Before annealing

To highlight potential correlations between the structural/morphological characteristics of the ZnO seed layer and Ag layer, all parameters extracted from all samples analysed in XRD before annealing (Tab. (3.3), Tab. (3.5), Tab. (3.6)) are compared in Fig. (3.13). Somehow, such approach gets rid of the inherent statistical fluctuations from one sample to the other in the search of relevant parameters.

A clear linear correlation is established between the lateral coherent domain size of the oxide and of the metal (Fig. (3.13)-a) ; it means that larger seed layer domains induce larger silver domains. A linear trend is also observed between the rocking curve width of the main $\theta - 2\theta$ peaks of the two films (Fig. (3.13)-b). Already pointed in [3], an improvement in the out-of-plane oxide texture leads to a correlated enhancement of the metal texture. Both results are in line with an epitaxial relationship between both partners (Sec. (1.4.2)). The observed behaviour between the in-plane texture coefficients (Fig. (3.13)-c) appears very inconsistent. This odd behaviour could be partly due to the incertitude linked to the zinc oxide diffraction peak, from which the Lotgering factor (TC) is calculated ; it results from the contributions of the seed and capping layers. Within the error bars, a lack of correlation also appears between the roughnesses of all Ag interfaces (Fig. (3.13)-d), maybe because of the smallness of the measured values.

The herein analysed samples present small variations of the in-plane and out-of-plane lattice parameters of ZnO and Ag. Along the direction normal to the surface, a correlation does exist

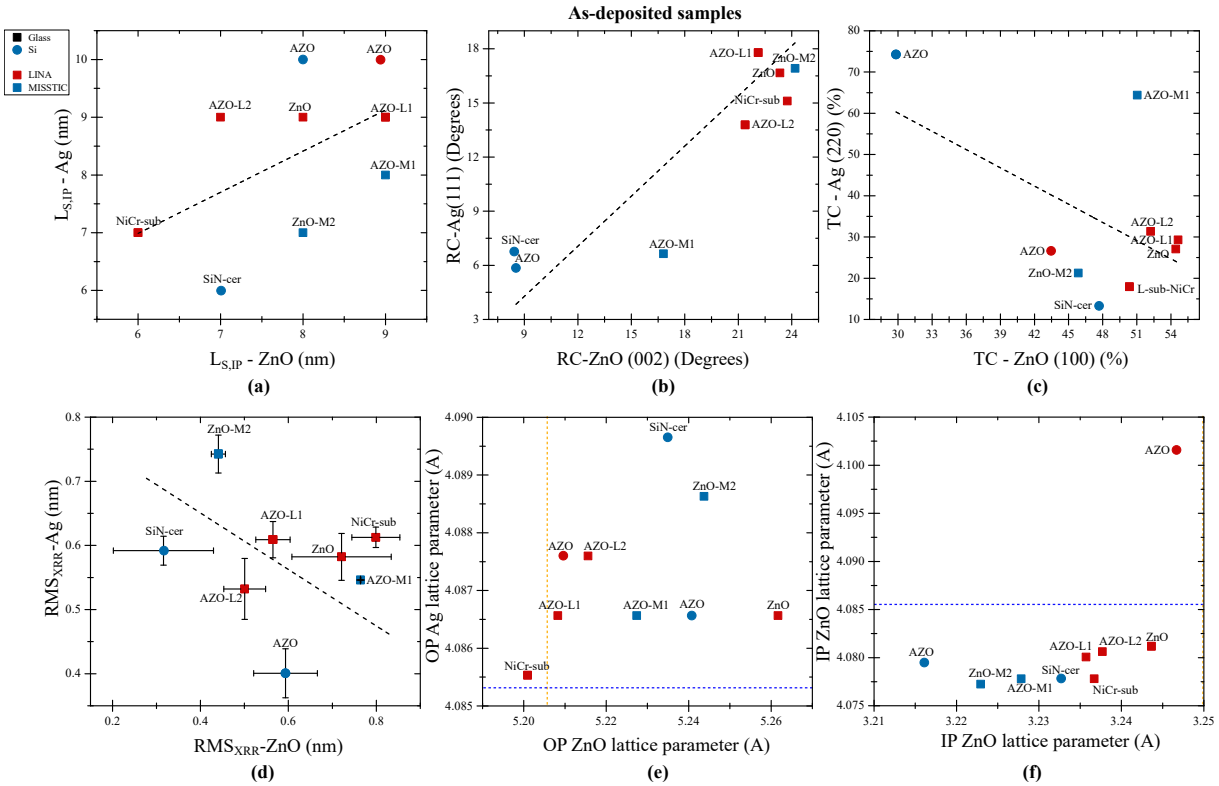

Figure 3.13 Correlations between the structural/morphological characteristics of the zinc oxide layer(s) and of the Ag film for as-deposited LINA/MISSTIC samples : (a) lateral domain size, (b) width of rocking curve, (c) texture coefficient, (d) interface roughness, (e-f) out-of-plane and in-plane lattice constants. Because of its preferred (0001) orientation, the in-plane and out-of-plane lattice parameters of ZnO do correspond to a_{IP-ZnO} and c_{OP-ZnO}. For Ag, they have been converted into the equivalent cubic lattice. The bulk lattice parameters are $a_{Ag}^{bulk} = 4.085$ Å (blue dashed line), $a_{ZnO}^{bulk} = 3.250$ Å and $c_{ZnO}^{bulk} = 5.206$ Å (orange dashed lines).

between both lattice parameters (Fig. (3.13)-e) ; but its does not reflect in the in-plane direction (Fig. (3.13)-f). In the case of hetero-epitaxy, the lattice parameter of the deposit can be strongly influenced by that of the substrate. In the case of the 30°-rotated Ag(111)/ZnO(0001) orientation (Sec. (1.4.2)), since the bulk mismatch is positive (+2.5 %), a ZnO tensile strain (*i.e.* larger a_{IP-ZnO}) would favour a better matching with the silver overlayer. But all grown ZnO layers are in compression in-plane (Fig. (3.13)-f; $a_{IP-ZnO} < a_{ZnO}^{bulk} = 3.250$ Å). For the Ag/ZnO(0001) hexagon/hexagon epitaxy, the reasoning is reversed since the bulk mismatch is negative. As it will be shown in Ch. (4) with single crystals and observed for evaporated films [106], this orientation is more likely. But, experimentally (Fig. (3.13)-f), it appears that the in-plane lattice parameter of silver is nearly independent of the underlying ZnO layer and very close to the bulk value ($a_{Ag}^{bulk} = 4.085$ Å) as if the film was not strained by its substrate. A more likely explanation for the observed variations of lattice constants and macrostrain (tensile or compressive) is the stress induced by the growth process of the layer itself or its encapsulation ; for instance, the stress state of the metal film during growth can be tensile upon zipping of grain boundaries at the coalescence/percolation stage and compressive upon bombardment or atom insertion at grain boundaries [108, 198, 199] before relaxing at the end of growth [200].

Since the seed layer has a clear influence on the silver film, its impact on the coating resistivity

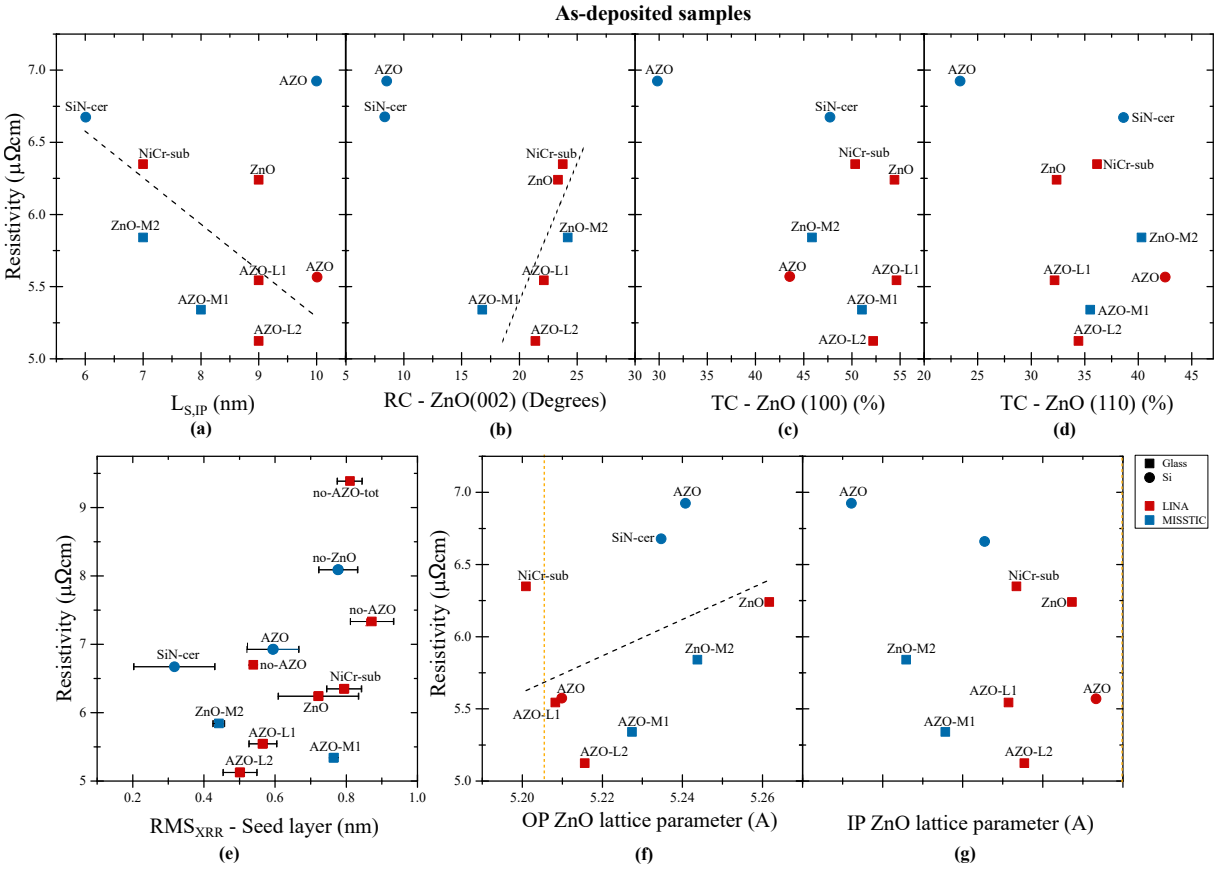

Figure 3.14 Room-temperature resistivity of the LINA and MISSTIC samples as a function of the structural and morphological properties of the ZnO layer(s). The different factors have been determined through X-ray analyses : (a) the lateral coherent domain size, (b) width of the (002) rocking curve, (c-d) the (100) and (110) texture coefficient, (e) the seed layer roughness (including NiCr layer and SiN layer), (f-g) the out of plane and in plane lattice parameters of ZnO. The bulk lattice constants are $a_{ZnO}^{bulk} = 3.250$ Å and $c_{ZnO}^{bulk} = 5.206$ Å (orange dashed lines).

has been directly investigated (Fig. (3.14)). Nevertheless, it is important to remember that the diffraction peaks associated with ZnO are the result of the contribution of the seed layer and the capping layer. Hence, the estimated values should be considered more as an average of the characteristics of the two films. Sharing a common vertical domain size close to the film thickness, the ZnO layers exhibit a more varied range of lateral domain sizes. Plotted as a function of this parameter, the resistivity shows a clear linear dependence (Fig. (3.14)-a). The conductivity is improved by the domain enlargement, which, as previously shown, helps to lower the grain boundary density in the Ag film. A linear trend also exists between the ZnO out-of-plane grain orientation associated to the (002) peak rocking curve and the electrical properties (Fig. (3.14)-b). Leading to an improved textured silver film, an enhanced seed layer orientation indirectly reduces the average Ag out-of-plane grain boundary angle, lowering its resistivity. On the other hand, along the in-plane direction, the improvement of the oxide texture represented by the increase in the (100)/(110) TC factors parallels a conductivity degradation (Fig. (3.14)-c,d). This behaviour is not completely surprising based to the fact that a negative (but poor) correlation was observed between the in-plane texture coefficient of ZnO and Ag (Fig. (3.13)-c). Consequently, an increase in the in-plane seed layer texture is associated with a decrease in the

in-plane metal orientation, which justifies the conductivity drop. However, in the picture of an epitaxial Ag/ZnO relationship, this findings remains puzzling.

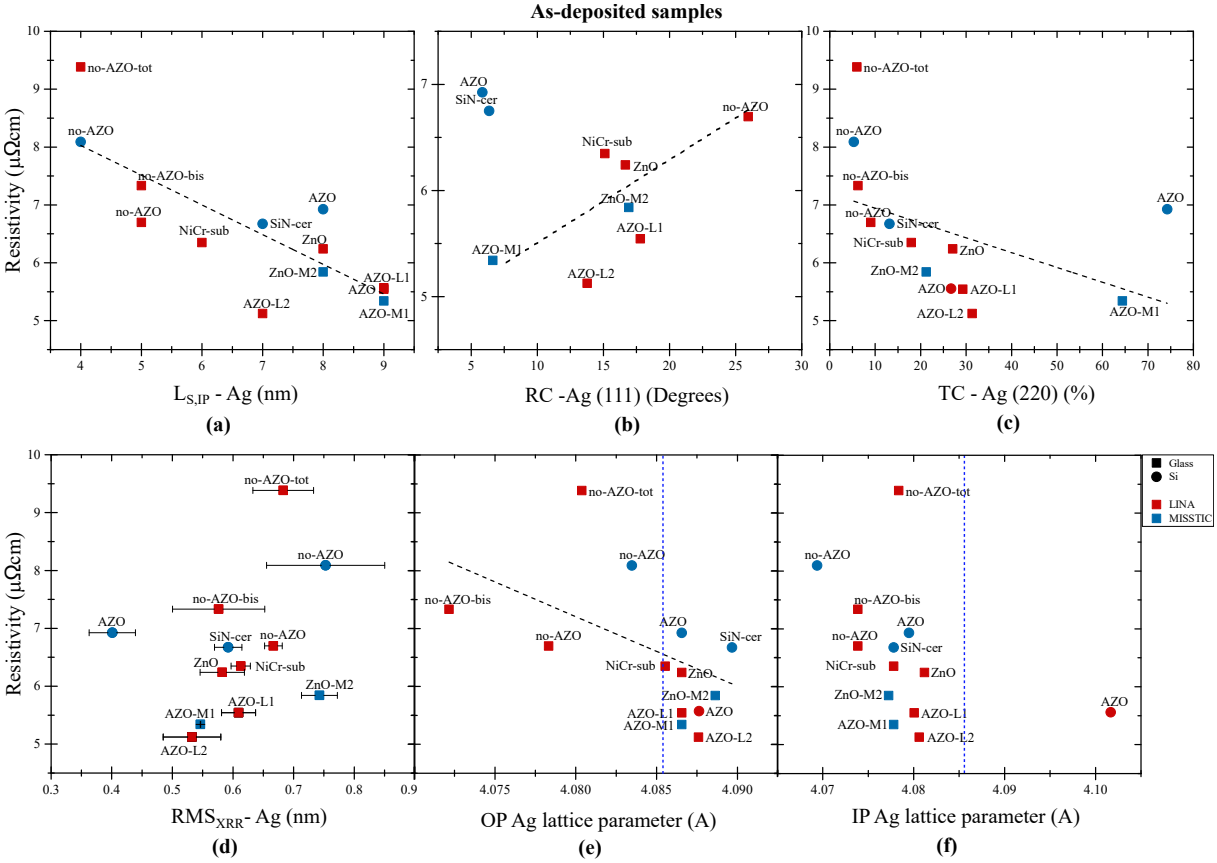

Figure 3.15 Room-temperature resistivity of the as-deposited LINA and MISSTIC samples as a function of the structural and morphological characteristics of the Ag layer determined through X-ray analysis : (a) lateral coherent domain size, (b) width of the Ag (111) rockig curve, (c) (220) texture coefficient, (d) roughness and (e-f) out-of-plane and in-plane lattice constants. The bulk lattice constant is $a_{Ag}^{bulk} = 4.085$ Å (blue dashed lines).

Previous works on similar simplified low-emissive silver-based coatings [3, 4, 85] have associated the improvement of resistivity with a reduction of the lattice mismatch between the oxide and the metal (and therefore interface defects such as dislocation density) obtained through the growth of strained ZnO seed layers. In the present results (Fig. (3.14)-f,g), an increase of conductivity is obtained for lower c_{OP-ZnO} and larger a_{IP-ZnO}. This trend disagrees with the conclusion of previous works, in which the improvement in electrical properties was linked to a lengthening of the ZnO vertical parameter and a narrowing of in-plane atomic distances due to the Poisson effect. But, it is consistent if silver grows in a 30°-rotated epitaxy. In this configuration, an elongation of the in-plane oxide parameter will result in a decrease of the lattice mismatch and the dislocation density. But to corroborate this hypothesis, a clear linear correlation between the in-plane oxide and metal lattice parameters would be needed which is not the case here (Fig. (3.13)-f).

The seed layer surface roughness constitutes one of the main source of the scattering of electrons. This point was already put forward as the main cause in the resistivity increase of coatings with

a blocker layer. Despite the large uncertainty that accompanies roughness determinations, the correlation outlined in Fig. (3.14)-e is a further proof of this contribution in the worsening of the coating conductivity.

At last, to corroborate the previous correlations, a deeper investigation has been pursued between resistivity and the silver film structural characteristics (Fig. (3.15)). In line with the decrease of the grain boundaries density, a visible lowering of the silver resistivity is observed for larger lateral coherent domain sizes (Fig. (3.15)-a). Similarly, the improvements of silver texture, out-of-plane (Fig. (3.15)-b) and in-plane (Fig. (3.15)-c) induce an enhancement of the metal conductivity in agreement with previous conclusions. A degradation of the silver electrical property is also observed with the increase of roughness (Fig. (3.15)-d) corresponding to the interface with the ZnO capping layer. The linear trend outlined proves the detrimental influence of interface roughening on electron scattering.

Plotting the electrical resistivity as a function of silver lattice parameters (Fig. (3.15)-e,f), one can notice an improvement of conductivity with increasing out-of-plane and in-plane lattice parameters. Assuming a 30°-rotated epitaxy with a 2.5 % lattice mismatch, the decrease of resistivity with the in-plane silver lattice parameter could be related to a decrease of interface dislocation density due to a reduced lattice mismatch; but this picture relies on a bulk ZnO lattice constant. At the opposite of the seed layer (Fig. (3.16)-a), the silver lattice does not follow a clear Poisson elastic behaviour (Fig. (3.16)-b) and its in-plane lattice parameter does not follow clearly that of the ZnO film (Fig. (3.13)-f). Further analysis are required to really clarify the situation about the actual role of epitaxy in the stress state of silver since other growth related reasons could be at work. Some clues about the actual epitaxial relationship will be given after annealing and with the single-crystal substrates (Ch. (4)); but still, one could argue that on poorly-crystallised ZnO layer, a switch between the rotated and hexagon/hexagon orientations is still possible [4].

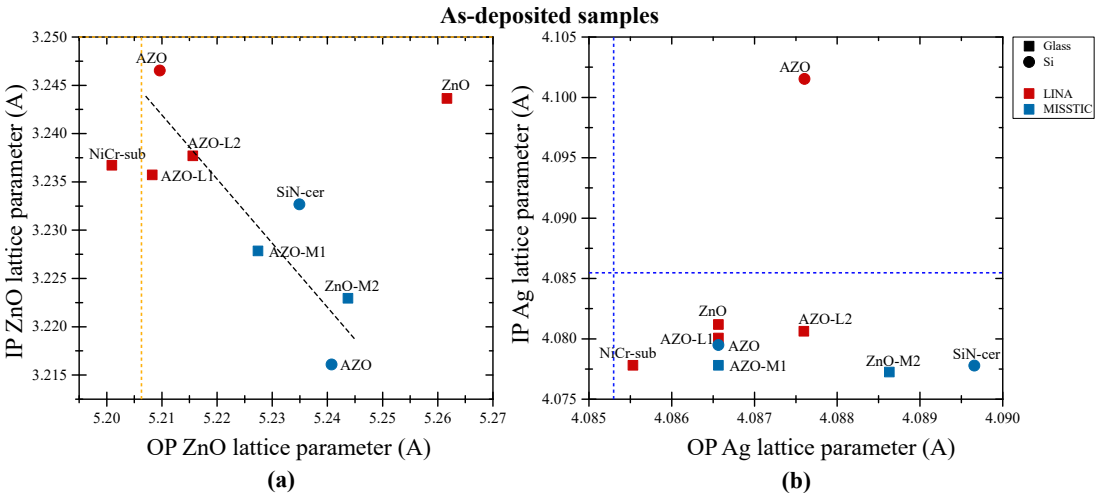

Figure 3.16 In-plane versus out-of-plane lattice parameters of (a) ZnO and (b) Ag in all the as-deposited LINA and MISSTIC samples. Because of its preferred (0001) orientation, they do correspond to a_{IP-ZnO} and c_{OP-ZnO} for ZnO. For Ag, they have been converted into the equivalent cubic lattice. The bulk lattice constants are $a_{Ag}^{bulk} = 4.085$ Å (blue dashed lines), $a_{ZnO}^{bulk} = 3.250$ Å and $c_{ZnO}^{bulk} = 5.206$ Å (orange dashed lines).

3.2.2 After annealing

In the same spirit, similar investigations on potential correlations were conducted on the samples after thermal treatment (Fig. (3.17)). Firstly, one can notice a loss of correlation between the lateral domain sizes of the two layers (Fig. (3.17)-a). This can be assigned to a better recrystallisation of silver than for zinc oxide at the used temperature. In the out-of-plane direction, the linear correlation between the seed layer texture and the (111) silver grain orientation is preserved (Fig. (3.17)-b). In-plane, the seed layer orientation does not seem to play a role on the metal texture (Fig. (3.17)-c). This finding does not differ much from the trend pointed out before annealing. At the opposite to as-deposited samples, a clear linear relationship is established between the in-plane and out-of-plane lattice parameters of both materials (Fig. (3.17)-e,f). Taking into account the error bar associated to the roughness determination with XRR, a linear correlation, essentially defined by the properties of *NiCr-sub sample*, is revealed between the roughnesses of the seed layer-metal interface and of the metal-capping interface.

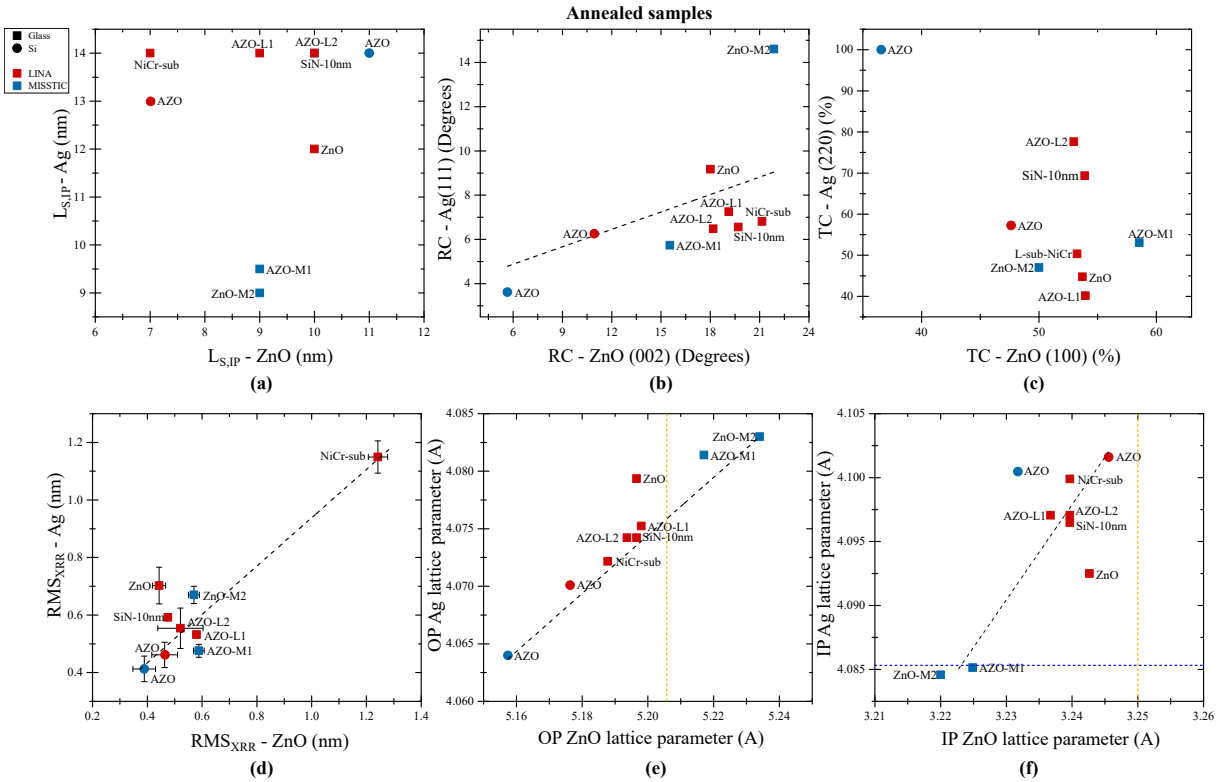

Figure 3.17 Correlations between the structural/morphological characteristics of the zinc oxide layer(s) and the Ag film for annealed LINA/MISSTIC samples : (a) lateral domain size, (b) width of rocking curve, (c) texture coefficient, (d) interface roughness, (e-f) out-of-plane and in-plane lattice constants. Because of its preferred (0001) orientation, the in-plane and out-of-plane lattice parameters of ZnO do correspond to a_{ZnO} and c_{ZnO}. For Ag, they have been converted into the equivalent cubic lattice. The bulk lattice parameters are $a_{Ag}^{bulk} = 4.09$ Å (blue dashed line), $a_{ZnO}^{bulk} = 3.25$ Å and $c_{ZnO}^{bulk} = 5.21$ Å (orange dashed lines).

The impact of the seed layer properties on the silver resistivity is reported in Fig. (3.18). Compared to as-deposited samples, a loss of a clear correlation is observed between the lateral domain size and the metal electrical properties (Fig. (3.18)-a) in line with the lack of correlation obser-

ved with the silver lateral domain size(Fig. (3.17)-a and Fig. (3.20)-a). Regarding the influence of the grain orientation, a weak correlation is preserved between the out-of-plane texture of the oxide and the metal conductivity (Fig. (3.18)-b). In-plane, as before thermal treatment, the silver resistivity follows the ZnO (100) texture coefficients (Fig. (3.18)-c) despite a clear relation between the in-plane orientation of the seed layer and of the metal. The absence of a clear correlation trend is also shared with the seed layer-silver interface roughness (Fig. (3.18)-e). However, given the incertitude of the measurement and the small size of the variation range, it is difficult to draw accurate conclusions.

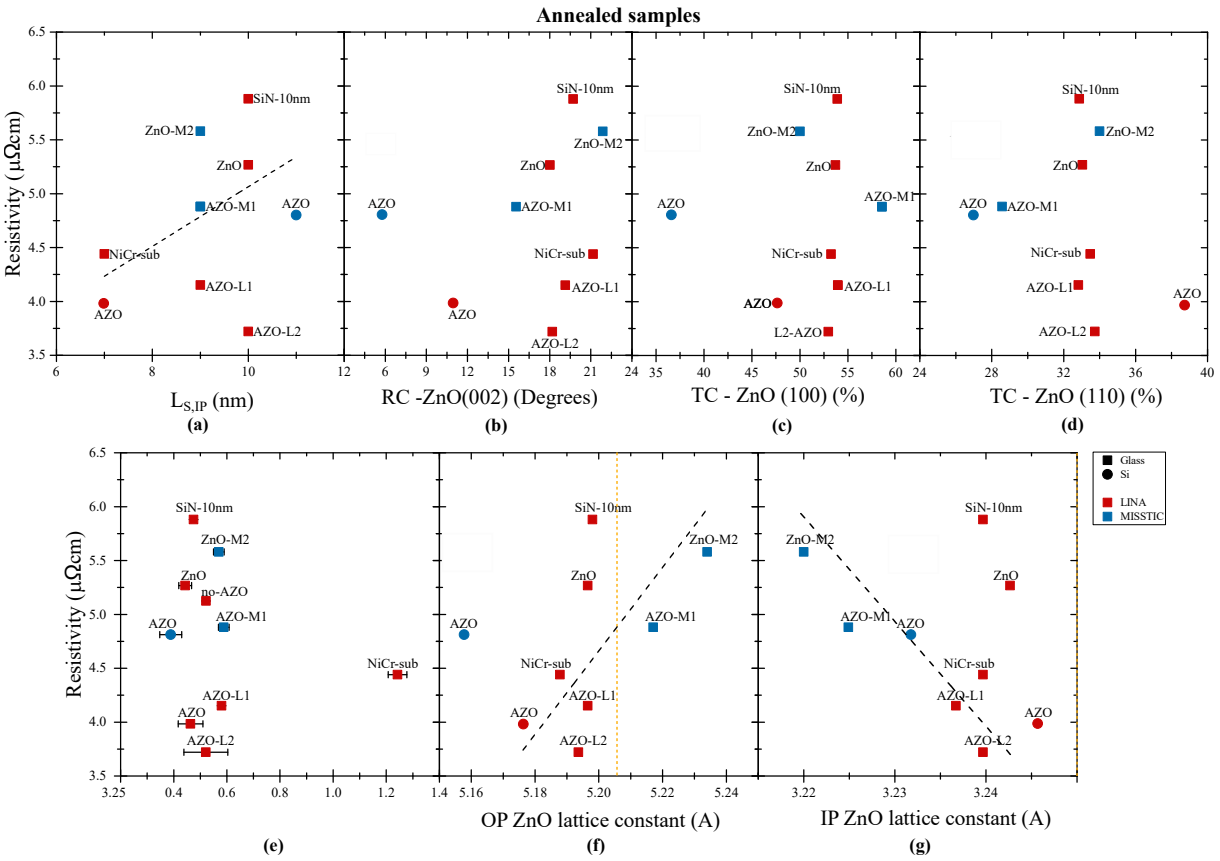

Figure 3.18 Room-temperature resistivity of the annealed LINA and MISSTIC samples as a function of the structural and morphological properties of the ZnO layer(s). The different factors have been determined through X-ray analyses : (a) the lateral coherent domain size, (b) width of the (002) rocking curve, (c-d) the (100) and (110) texture coefficient, (e) the seed layer roughness (including NiCr layer and SiN layer), (f-g) the out of plane and in plane lattice parameters of ZnO. The bulk lattice constants are $a_{ZnO}^{bulk} = 3.250$ Å and $c_{ZnO}^{bulk} = 5.206$ Å (orange dashed lines).

Regarding lattice parameters, the oxide confirms its elastic behaviour according to the Poisson effect (Fig. (3.19)-a). As before annealing, the conductivity is improved upon reducing the out-of-plane ZnO lattice parameter and upon increasing its in-plane value (Fig. (3.18)-f,g).

Presenting the strongest variations after annealing, the silver film also undergoes important variations in the correlations between its structural properties and its electrical conductivity. Already having a vertical grain size equal to the film thickness, most of the annealed samples show pretty similar lateral domain sizes. At the opposite of what previously observed before annealing, the correlation between lateral domain size and resistivity is lost (Fig. (3.20)-a).

Similarly, a loss of a clear correlation is also observed between the silver out-of-plane texture and the electrical properties (Fig. (3.20)-b). Both puzzling trends may be related to constant limit values reached in all samples at the end of annealing for both the in-plane domain size and the out-of-plane texture. It does not mean that the correlation does not exist but it is not any more easily evidenced with our results. At the opposite, a slight decrease in resistivity is observed for samples with a higher in-plane texture (*i.e.* larger $TC_{Ag(220)}$ value) (Fig. (3.20)-c). Again the in-plane texture seems to prevail over the contribution of interface roughness (Fig. (3.20)-d). Showing similar roughness values after annealing, independently of the stack structure (ZnO/AZO, w/wo NiCr...), the linear correlation with the resistivity (Fig. (3.15)-d) is indeed loss after annealing.

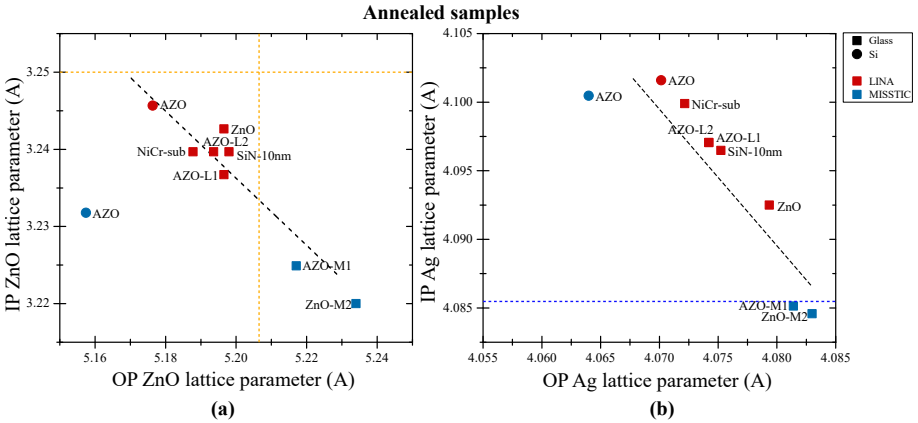

Figure 3.19 In-plane versus out-of-plane lattice parameters of (a) ZnO and (b) Ag in all the annealed LINA and MISSTIC samples. Because of its preferred (0001) orientation, they do correspond to a_{IP-ZnO} and c_{OP-ZnO} for ZnO. For Ag, they have been converted into the equivalent cubic lattice. The bulk lattice constants are $a_{Ag}^{bulk} = 4.085$ Å (blue dashed lines), $a_{ZnO}^{bulk} = 3.250$ Å and $c_{ZnO}^{bulk} = 5.206$ Å (orange dashed lines).

Induced by the additional mobility given by annealing, the silver film clearly undergoes atomic rearrangement during the thermal treatment. The recrystallisation results in a clear Poisson elastic relation between its in-plane and out-of-plane lattice constants (Fig. (3.19)-b). In parallel, the metal in-plane lattice parameter contracts with that of the ZnO (Fig. (3.17)-f) thus pointing an elastic deformation induced by an epitaxy. But the in-plane absolute value is always larger than the bulk one ($a_{Ag}^{bulk} = 4.085$ Å) in a tensile strain state. The 30°-rotated epitaxy with a positive mismatch would induce a silver film in compression. Further compression would be required, for an in-plane ZnO lattice constant smaller than the bulk one ($a_{ZnO}^{bulk} = 3.250$ Å) as experimentally observed for ZnO. This is not what is observed in Fig. (3.17)-f. At the opposite, the hexagon/hexagon epitaxy with its negative mismatch would imply a silver film in tensile strain as seen experimentally (Fig. (3.17)-f). If the conclusion was not clear for as-deposited samples, the results on the annealed samples favour an hexagon/hexagon epitaxy. Finally, when the silver resistivity is plotted as a function of the silver lattice constants (Fig. (3.20)-e,f), one notices a clearer trend with the resistivity which decreases with the increase of the Ag in-plane lattice parameter. This can be assigned to a reduction of interface dislocations, if any, with the better lattice matching with the substrate.

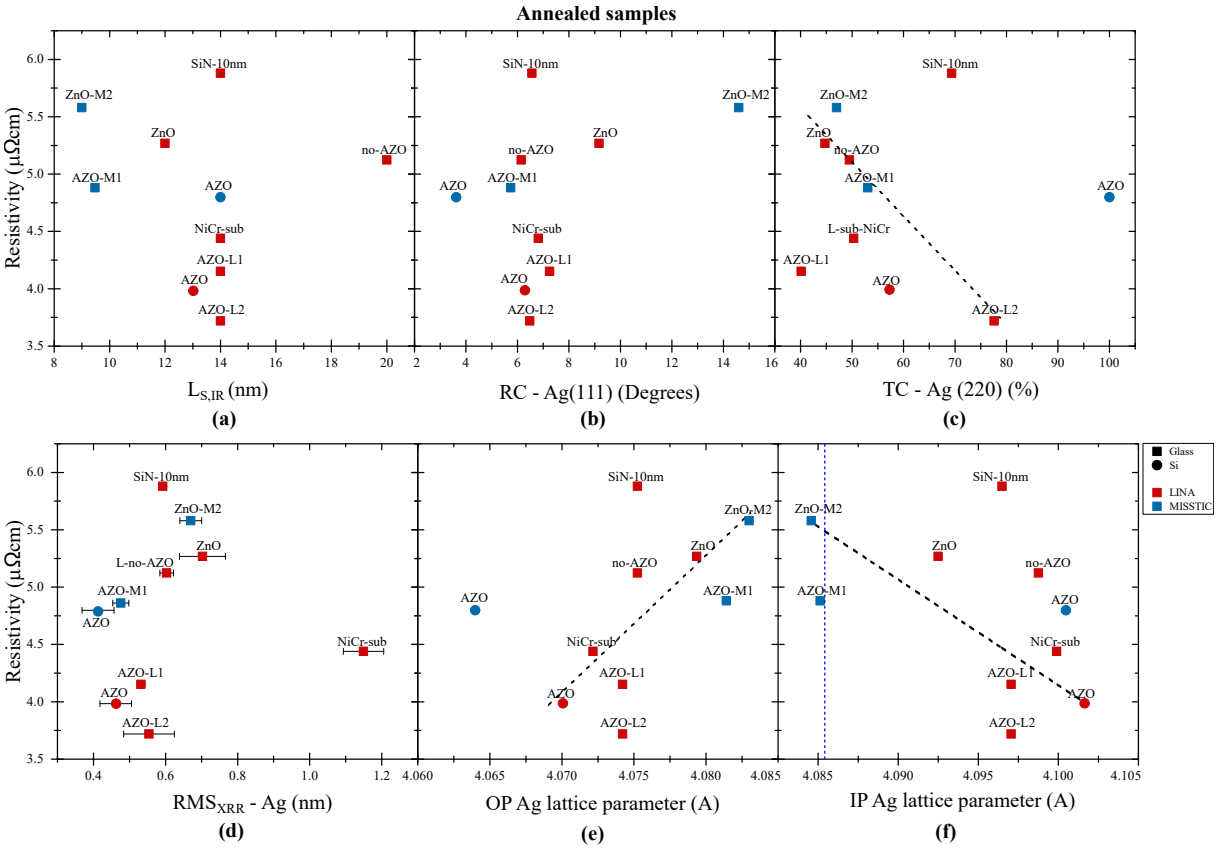

Figure 3.20 Room-temperature resistivity of the annealed LINA and MISSTIC samples as a function of the structural and morphological characteristics of the Ag layer determined through X-ray analysis : (a) lateral coherent domain size, (b) width of the Ag (111) rocking curve, (c) (220) texture coefficient, (d) roughness and (e-f) out-of-plane and in-plane lattice constants. The bulk lattice constant is $a_{Ag}^{bulk} = 4.09$ Å (blue dashed lines).

3.2.3 In summary

The systematic analysis of correlations between the structural and topographical properties of the metal and the oxide layers showed that the seed layer can strongly influence the quality of the silver film. An improvement in the structural quality of the ZnO seed layer induces the growth of a better metallic film. More specifically, for as-received samples, it has been shown that a smooth, highly out-of-plane oriented oxide film with large domain sizes will transmit the same characteristics to the growing film. These qualities, which make it possible to reduce the interface roughness, the density of grain boundaries and the average Ag grain boundary angle, have a direct impact on the conductivity of the material. This observation roots directly into an epitaxial relationship between Ag(111) and ZnO(0001) that will be further explored with the single crystal substrate (Ch. (4)). On the other hand, the seed layer in-plane texture appears to play a less important role in the development of the same silver structural characteristics. This is observed also after annealing, where, in addition, a correlation loss is also observed between the oxide and the metal lateral domain sizes.

Scrutinising the variations of silver resistivity as a function of oxide and metal structural properties, it appeared that the conductivity is driven by the contribution of several factors. Before annealing, within the silver layer, larger lateral domain sizes, higher in-plane and out-of-plane

texture and smoother interfaces have all revealed to effectively improve the metal conductivity. All these parameters control the scattering of electrons at interfaces and their reflectivity at grain boundaries. When the sample is annealed, the metal film is recrystallised with increased domain size and improved out-of-plane (111) texture up to similar limits for all samples. Thus, probably because of these (fortuitous ?) limits, their correlation with the resistivity found for as-deposited stacks is washed out after annealing.

At last, a clear dependence of resistivity with the in-plane lattice parameters of Ag and ZnO could be evidenced only after annealing. It is compatible with an hexagon/hexagon epitaxy although other factors related to stress build-up or relaxation during the growth and annealing processes can not be ruled out based only on the present measurements.

3.3 Electron scattering phenomena contributing to the coating resistivity

3.3.1 Application of the three temperature dependent resistivity models

Compared to a bulk, in a polycrystalline thin film, due to the finite thickness and to grain sizes of the order of the electron mean free path ($l = 38$ nm at $T = 300$ K for Ag), the conductivity is hindered by two additional coupled electron scattering contributions, that at the interfaces and that at the grain boundaries. Their individual contribution can be disentangled by analysing the resistivity variation of the film as a function of temperature through the fit of appropriated theoretical models (see Sec. (1.5)).

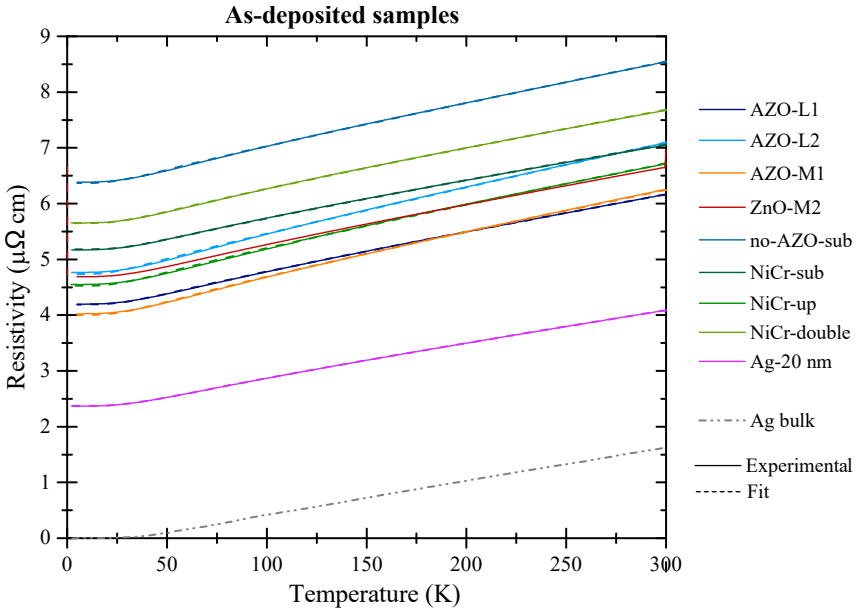

Figure 3.21 (a) Temperature dependent resistivity of as-deposited LINA/MISSTIC samples as a function of temperature compared to silver bulk [93]. The continuous curve correspond to the experimental data, while the dashed lines represent the simulations with three different resistivity models (Mayadas-Shatzkes, Sambles and Soffer). Fits parameters are reported in Tab. (3.7).

Temperature dependent resistivity measurements were performed in a range between 5 and 300 K (Sec. (2.3.7)) for a selected group of the previously presented samples. The resulting

curves were fitted using three resistivity models described in Sec. (1.5) : Mayadas-Shatzkes [127], Sambles [142] and Soffer [149]. The goal is to determine the relative contributions of the two scattering mechanisms, via p- and R-parameters as well as the interface roughnesses. The classical LINA and MISSTIC reference stacks are compared to coatings (i) with additional blocker layers (below, above or on both sides of the Ag layer), (ii) without the oxide seed layer, (iii) to a thicker silver-based sample and (iv) to bulk silver.

At a first sight, the resistivity curves of all samples (Fig. (3.21)) are mainly parallel to each others but present a clear variation in their residual resistivity values at $T = 0$ K. In the case of bulk silver, ρ_{res}^{bulk} is driven only by the density of point defects but for thin films, extra-contributions are present. The phonon contributions $\rho_{ph}(T) = \rho(T) - \rho_{res}(T = 0K)$ of the coatings (Fig. (3.22)-a) are significantly different and also differ from the resistivity of bulk silver. The smallest deviation from the bulk behaviour is trivially observed for the thicker Ag sample. Less affected by size effects due to its larger thickness, this sample also presents the lowest resistivity. Furthermore, emphasised by the normalised phonon contribution of the resistivity (Fig. (3.22)-b), all curves exhibit a similar weak concave shape over the entire measured temperature range. Described by the Fuchs-Sondheimer model [125], this behaviour is generally associated to an increased interface scattering occurring within the film.

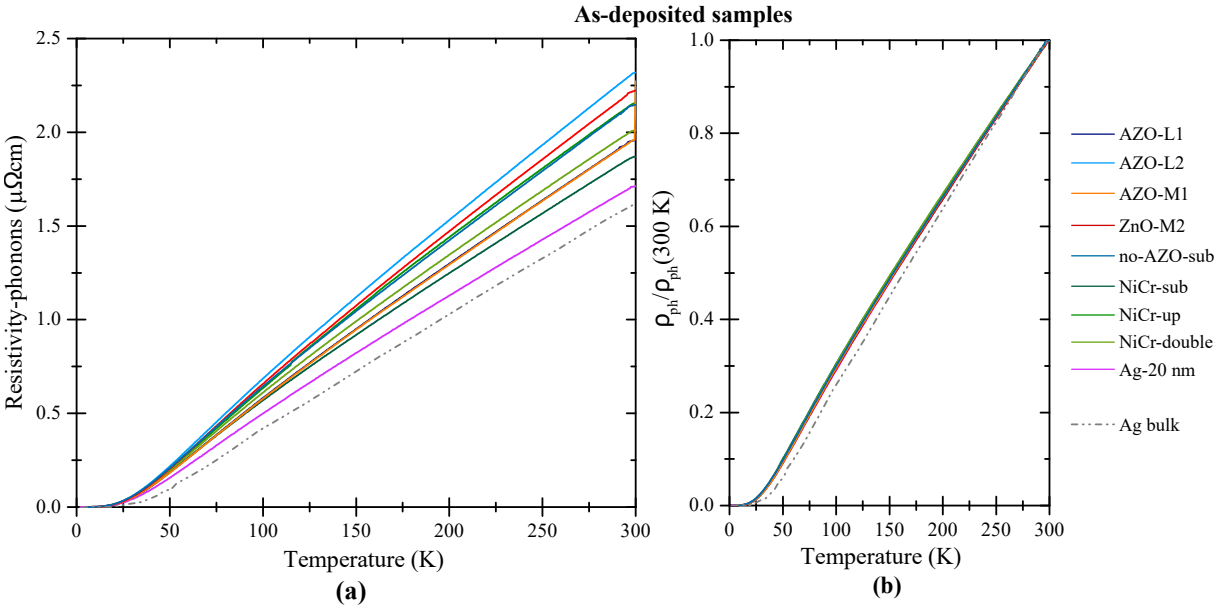

Figure 3.22 (a) Temperature dependent contribution $\rho_{ph}(T) = \rho(T) - \rho_{res}(T = 0K)$ and (b) normalized profile of the resistivity of as-deposited LINA/MISSTIC samples compared to silver bulk [93].

The Mayadas-Shatzkes model (see Sec. (1.5.3) and Sec. (1.5.4)), based on the expression

$$\boldsymbol{\rho_f} = \left(\frac{1}{\boldsymbol{\rho_{GB}}} - \frac{6(1-p)}{\pi \boldsymbol{\kappa_0 \rho_0}} \int_0^{\pi/2} d\phi \int_1^{\infty} dt \frac{\cos^2 \phi}{\boldsymbol{H^2(t,\phi)}} \left(\frac{1}{t^3} - \frac{1}{t^5} \right) \frac{1 - e^{-\kappa_0 t \boldsymbol{H(t,\phi)}}}{1 - p e^{-\kappa_0 t \boldsymbol{H(t,\phi)}}} \right)^{-1}, \tag{3.1}$$

was applied to estimate the main scattering contributions to resistivity, interface (p-term) or grain boundary (R-term), occurring in the Ag film. According to a previous study on low-emissive Ag-based coatings [120], the best agreement between the model and the experimental

data was found when all the interface scattering phenomena were assumed to be only specular ($p = 1$). Based on this result, the interface scattering factor p was fitted starting from one while the R-factor and Debye-temperature Θ_D were let free. For the simulation, the distance between the reflective planes of the resistivity models *i.e.* the lateral grain sizes D (Sec. (1.5)) was kept fixed at the in-plane coherent domain size $L_{S,IP}$ as derived through GIXRD. This underestimates the actual value. Similarly, the film thickness d was imposed at the value derived from X-ray reflectivity, while ρ_{res}^{grain} was fixed to 0.65 $\mu\Omega$.cm for LINA samples and to 0.69 $\mu\Omega$.cm for MISSTIC samples (see below). As a reminder, ρ_{res}^{grain} is the intra-grain resistivity at $T = 0$ K (Eq. (1.29)) that is driven by defects that are internal to the grain (point defect, impurities such as implanted Ar, stacking faults, dislocations etc...). In other words, it corresponds to the residual resistivity at $T = 0$ K of a bulk material with the same concentration of defects.

As shown in Fig. (3.23), ρ_{res}^{grain} can be estimated from the thickness dependence of the room-temperature resistivity using an approximation of the Fuchs-Sondheimer and Mayadas-Shatzkes models when the layer thickness d is larger than the bulk mean free path ($d \gg l_0$) :

$$\rho d = \rho_0 d + C_{SS} + C_{GB}. \tag{3.2}$$

C_{SS} and C_{GB} are the contributions of scattering at the interfaces and at the grain boundaries while ρ_0 is the room-temperature intra-grain resistivity. Provided that the Debye temperature is not strongly different from that of the bulk material, ρ_{res}^{grain} can be obtained by subtracting to ρ_0 the phonon contribution of bulk silver that amounts to 1.62 $\mu\Omega$.cm since ρ_{res}^{bulk} is close to zero [201, 202] (Fig. (3.21)). The range of validity of this approximation Eq. (3.2) is limited to film thicknesses higher than the average electron mean free path ($d \gg l_0$), which for silver is typically above 50 nm. When used on thinner films, the result is less accurate and, as shown in Fig. (3.23)-a, can result in a overestimation of the actual value of ρ_0. The similarities between the two values for the LINA (0.65 $\mu\Omega$.cm) and the MISSTIC (0.69 $\mu\Omega$.cm) samples proves that the intra-grain defect contribution are identical, maybe because they are intrinsic to silver and to the growth process (implantation, stacking faults, etc...).

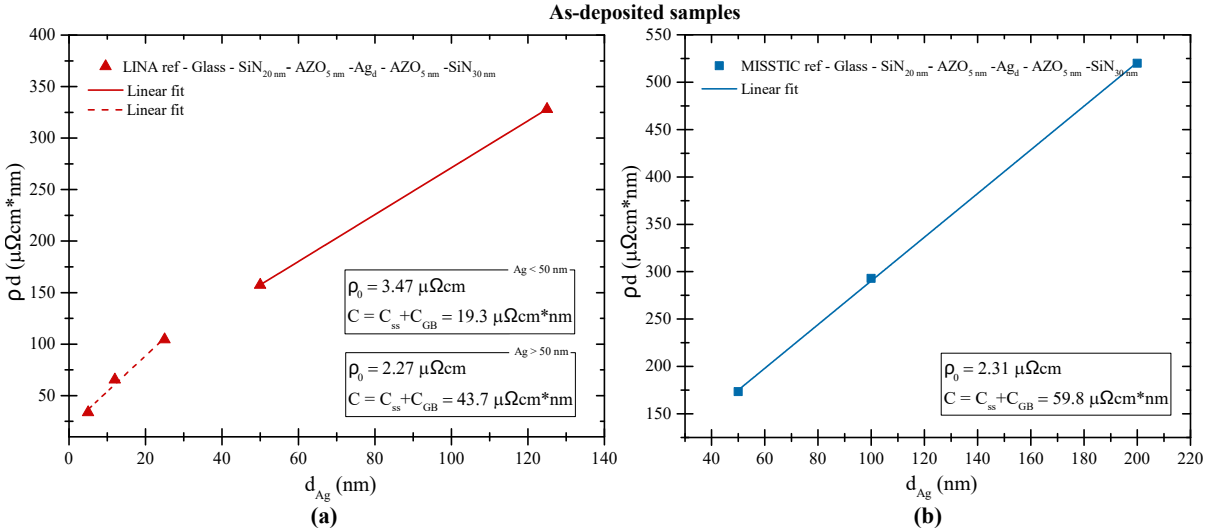

Figure 3.23 Room-temperature resistivity times film thickness as a function of the silver film thickness for (a) LINA and (b) MISSTIC samples. From a linear fit of approximated Fuchs-Sondheimer and Mayadas-Shatzkes models, it is possible to determine respectively the intra-grain "bulk" resistivity from the slope and the scattering contributions from the intercept.

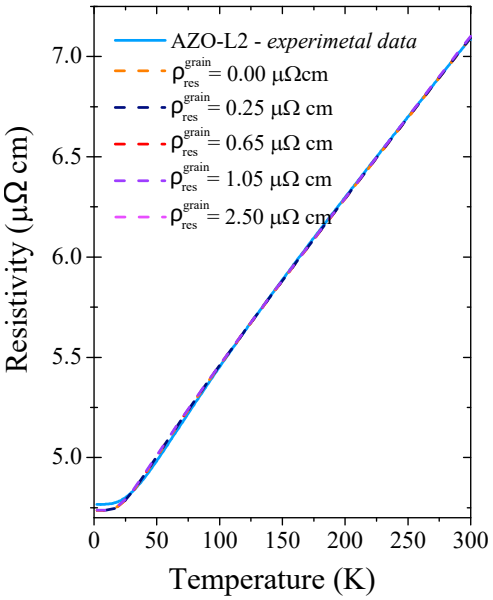

As-deposited **AZO·L2**			
$\boldsymbol{\rho_{res}^{grain}}$ $[\mu\Omega.cm]$	$\boldsymbol{R}$	$\boldsymbol{p}$	$\boldsymbol{\Theta_D}$ [K]
0.00	0.25	0.80	140
0.25	0.25	0.88	139
0.65	0.23	0.89	138
1.05	0.21	0.92	137
2.50	0.15	1.00	135

Figure 3.24 Scattering parameters R, p and Debye temperature Θ_D obtained by fitting resistivity versus temperature of the reference LINA sample *L2* with the Mayadas-Shatzkes model. The intra-grain resistivity value ρ_{res}^{grain} has been varied to observe its influence on the other fitted parameters.

Illustrated already in Sec. (1.5.3), the value of ρ_{res}^{grain} has a non-negligible impact on the resistivity line shape and the resulting fitted parameters. Moreover, the applicability of the Mayadas-Shatzkes model at large thicknesses can be questioned since several grains can be present in the thickness of the film. To estimate the ρ_{res}^{grain} influence, four different analyses (Fig. (3.24)) were performed on the LINA reference sample *AZO·L2* with variable ρ_{res}^{grain} values : (i) $\rho_{res}^{grain} = 0\mu\Omega$.cm, equivalent to the $\rho_{res}^{bulk}(T = 0K)$ of a pure defect-free silver crystal, (ii) $0.25\,\mu\Omega$.cm, (iii) $0.65\,\mu\Omega$.cm and (iv) $2.50\,\mu\Omega$.cm. As shown in Fig. (3.24), the variations in the residual resistivity induces small variations in the fitted values of the other parameters for a similar agreement with the data. For Θ_D, the changes are negligible. For p and R, the impact is more sizeable ; yet, except in very extreme and unlikely cases of $\rho_{res}^{grain} = 0$ and $2.5\,\mu\Omega$.cm, the variations on R and p remain in a range of ~ 0.05. Thus, as shown below, the uncertainty in the present choice of ρ_{res}^{grain} will not modify drastically the interpretation of the fits.

In addition to the uncertainty related to the fixed parameters, each fitted parameter (R, p and Θ_D) is also accompanied by an error that was estimated via a series of simulations by varying only one parameter at a time around the optimal set. The case of the *L2* sample is shown in Fig. (3.25) as an example. The most sensitive parameter is the reflection coefficient at grain boundaries R for which a noticeable curve change is already noticed for $\Delta R \sim 0.001$. Combined with the incertitude derived by ρ_{res}^{grain}, the reliability on R decreases to the second decimal place. Similarly, the error bar on p is of the order of 0.01 while for Θ_D, it is of the unit. Beyond systematic bias in the model or in the data acquisition, these results underline the sensitivity of the fit to small changes of the experimental profile.

In the Mayadas-Shatzkes model, grain boundaries are treated as vertical planes between two equivalent symmetric interfaces ; only a fraction p of the electrons are specularly reflected at the interfaces while the remaining ones are diffusely scattered over the half space. If, accordingly

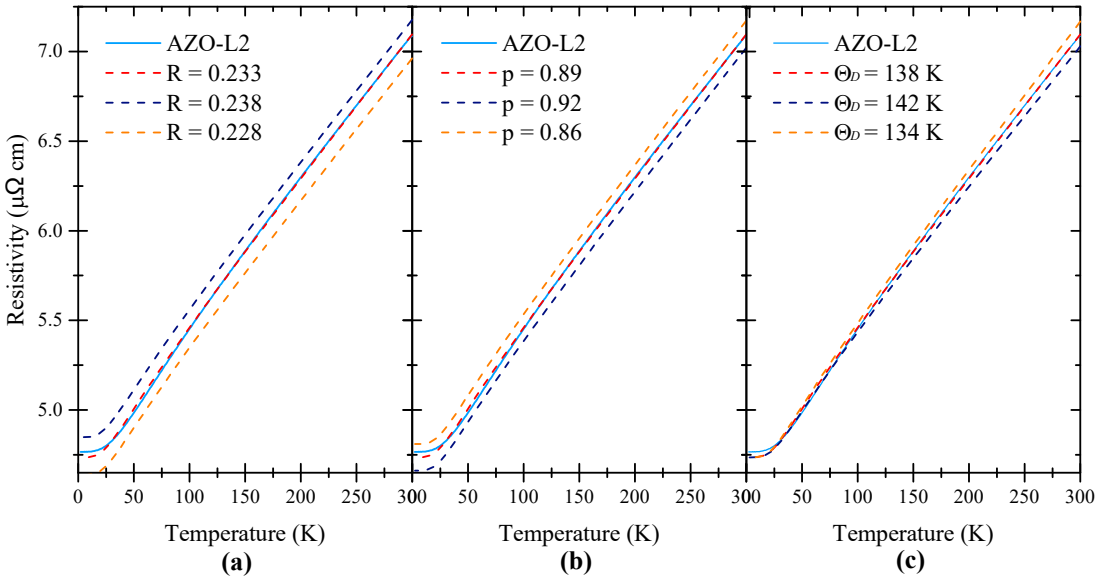

Figure 3.25 Influence of parameters (a) R, (b) p or (c) Θ_D of the Mayadas-Shatzkes model on the agreement with the temperature dependent resistivity of reference LINA sample *AZO·L2*. Only one parameter is changed at a time while the others are kept fixed at their best values ($R = 0.233$, $p = 0.89$ and $\Theta_D = 138K$).

to the diffraction analysis, the presence of only one metal grain in the thickness of the film agrees with the first assumption, the lack of relationship between the scattering parameter p and any physical characteristics of the interfaces prevents its direct interpretation. Moreover, in a glass-based stack, the upper (capping layer) and lower (seed layer) Ag-AZO interfaces, although of similar nature, could be different because of the sequence of deposition. Hence, not speaking about blocker layers, it is logical to think that they should have different scattering characteristics. To fill the gap, variants of the initial Mayadas-Shatzkes model [127] have been developed among which the Sambles [142] and Soffer [149] models. The Sambles model includes the possibility of an asymmetric system based on interfaces with different scattering probabilities ($p_1 \neq p_2$). On the other hand, in the Soffer model, the probability of interface scattering is assumed to depend on the angle of incidence of the electrons via Croce-Névot like factors that depend on interface roughnesses h_1 and h_2. Note that the parameters h_1 and h_2 are not associated to the specific upper and lower interface of silver. Both approaches were applied to the present data. The scattering parameters (R, p_1, p_2), the surface roughnesses (h_1, h_2) as well as the Debye temperature Θ_D were left free while ρ_{res}^{grain} and domain sizes were kept fixed.

As seen in Tab. (3.7), which gathers all fit results (fits are shown in Fig. (3.21) as dotted lines), the results obtained with the Sambles model are very similar to the Mayadas-Shatzkes one. For most samples, no difference is observed between the two interfaces ($p_1 = p_2$), in agreement with the symmetry presented by the h_1 and h_2 roughness values obtained through the fit with the Soffer model. Compared to other approaches, the Soffer R-parameter shows some deviations. The discrepancy lies in the fact that the diffuse scattering of electrons at interfaces is not any more isotropic but described by a more meaningful Croce-Névot factor based on roughness. Incidentally, the sensitivity of the R-parameter on the way the electrons are scattered at interfaces demonstrates the interplay between both phenomena.

Sample	ρ_{4P} [$\mu\Omega$**.cm**]	ρ_{300K} [$\mu\Omega$**.cm**]	ρ_{res}^{grain} [$\mu\Omega$**.cm**]	**R**	$\mathbf{p}_1$	$\mathbf{p}_2$	Θ_D [**K**]	$\mathbf{h}_1$ [**nm**]	$\mathbf{h}_2$ [**nm**]
As-deposited samples									
AZO·L1									
Mayadas-Shatzkes				0.12	0.35		170		
Sambles	5.54	6.15	0.65	0.12	0.35	0.35	170		
Soffer				0.17			178	0.08	0.06
AZO·M1									
Mayadas-Shatzkes				0.18	0.79		144		
Sambles	5.34	6.25	0.69	0.18	0.79	0.79	144		
Soffer				0.13			164	0.10	0.10
ZnO·M2									
Mayadas-Shatzkes				0.16	0.49		167		
Sambles	5.84	6.96	0.69	0.16	0.49	0.49	167		
Soffer				0.18			178	0.08	0.08
AZO·L2									
Mayadas-Shatzkes				0.23	0.89		138		
Sambles	5.12	7.08	0.65	0.23	0.89	0.89	138		
Soffer				0.18			153	0.09	0.09
No ZnO$_{sub}$									
Mayadas-Shatzkes				0.14	0.25		152		
Sambles	6.70	8.53	0.65	0.14	0.25	0.25	152		
Soffer				0.15			163	0.12	0.12
NiCr$_{sub}$									
Mayadas-Shatzkes				0.07	0.00		184		
Sambles	6.35	7.04	0.65	0.10	0.00	0.28	179		
Soffer				0.16			176	0.10	0.00
NiCr$_{up}$									
Mayadas-Shatzkes				0.11	0.29		153		
Sambles	5.62	6.71	0.65	0.11	0.29	0.29	153		
Soffer				0.11			171	0.13	0.13
NiCr$_{double}$									
Mayadas-Shatzkes				0.10	0.00		167		
Sambles	6.89	7.66	0.65	0.10	0.00	0.00	167		
Soffer				0.12			177	0.26	0.26
Ag-20nm									
Mayadas-Shatzkes				0.13	0.46		189		
Sambles	4.00	4.08	0.65	0.13	0.15	0.82	186		
Soffer				0.19			190	0.08	0.00

Table 3.7 Results of the fits of the resistivity in temperature of all the LINA/MISSTIC glass-based as deposited samples with three different models : Mayadas-Shatzkes, Sambles and Soffer. The estimated error bars are of the order of $\Delta p \simeq \pm 0.02$, $\Delta R \simeq \pm 0.05$, $\Delta\Theta_D \simeq \pm 5$ K and $\Delta h_1 = \Delta h_2 \simeq \pm 0.02$ nm. The first three samples will be used in the next chapters as references for single crytsal based samples. In the table, the resistivity at room-temperature of each sample, measured via *Napson* (ρ_{4P}) and via temperature-dependent set ups (ρ_{300K}) are reported.

For all samples, the grain boundary reflection parameter R stands below the value of 0.23 (Tab. (3.7)). In the range of literature R-parameter obtained for a single silver film (0.16 to 0.43 [93, 130, 138, 203]), it remains close to the theoretical predictions of Zhu *et al.* [130] (0.34). At the same time, the variation of the p-parameter is much wider ($0 \leq p \leq 0.89$), in line with the variety of interface configurations analysed. In literature, strong interface scattering mechanism, corresponding to p-factors ranging from 0 to 0.7, were already observed for single silver films grown on glass or mica substrate [204–206]. However, these values should be taken with caution since they were obtained only through the application of the Fuchs-Sondheimer model without taking grain boundary scattering into account. An agreement is also observed with the analysis performed by R. Sittner [4] as a function of film thickness with similar coatings. Nevertheless, M. Philipps [120] achieved contradictory results with similar temperature measurements on similar stacks but with some uncertainties on the actual grain size in his samples. In general, it is difficult to compare the parameters obtained by different studies or to identify a single reference value. This is because these parameters are highly sensitive to the microstructure of the sample and therefore to the type of substrate, to the deposition method, to the number of grains in the film thickness or to the neighbouring layers. Nevertheless, in a given study with a constant methodology of analysis as done herein, sound general trends can be drawn, as discussed below (Tab. (3.7)), on the "quality" of interfaces and grain boundaries in terms of electron scattering, beyond the obvious effect of density of grain boundaries that is included via the X-ray analysis.

The LINA reference *AZO·L1/L2*, as well as the MISSTIC sample *AZO·M1*, correspond to the classical coatings, where silver is grown on a AZO seed layer (Glass-SiN-AZO-Ag-AZO-SiN). As discussed in the previous paragraphs, the use of a different sputtering set-ups causes variations in the structural and morphological characteristics of the deposited films. These variations show up in the estimated values of the R, p-parameters. Showing the highest observed p and R values, the two samples present a strong contribution of grain boundaries, associated with minor, but not absent, scattering phenomena at the interfaces. In agreement with their similar interface behaviour, the two samples share also similar surface roughnesses as deduced by the Soffer model. Nevertheless, *AZO·L1* sample presents a resistivity characterized by a p value 60% lower than the *AZO·L2*. Compared to their structural characteristics (Fig. (3.15)), the lower p value, associated to *AZO·L1*, is in line with its higher interface roughnesses determined through XRR. On the other hand, the better in-plane and out-plane silver texture exhibited by *AZO·L2* does not lead to a lower R-parameter. Grown at several months of interval, it is plausible that although the two samples have the same composition, a variation in deposition conditions (pressure, age of the target, cleanliness of the chamber, glass quality, etc...) could have affected the quality of the final product. Furthermore, the *AZO·L2* sample presents also one of the strongest divergences between room-temperature resistivity determined via *Napson* and via temperature-dependent set up.

The *ZnO·M2* sample presents the case of Ag grown on a ZnO (undoped) polycrystalline film reactively sputtered from a pure Zn target and not on AZO (*AZO-M1*) (Glass-SiN-ZnO·met-Ag-AZO-SiN). For this sample, the different seed layer induces an increase of the electron interface scattering mechanism, characterized by a p-factor of ~ 0.50 instead of ~ 0.8 on AZO.

A strong decrease in the p-factor is also observed for the coatings without a seed layer (*No* ZnO_{sub} sample) (Glass-SiN-Ag-AZO-SiN) and with additional blocker layers. For these samples the $NiCr_{sub}$ corresponds to a stack of (Glass-SiN-AZO-NiCr-Ag-AZO-SiN), $NiCr_{up}$ to (Glass-SiN-AZO-Ag-NiCr-AZO-SiN) and $NiCr_{double}$ to (Glass-SiN-AZO-NiCr-Ag-NiCr-AZO-SiN). In the same way as for *ZnO·M2* sample, the lowering of the p-parameter is explained by less well-defined interfaces either in terms of interface defects and roughness or in terms of electronic properties (*i.e.* Schottky barrier). Astonishingly, the grain boundaries are more transparent to

electrons but slightly denser (*i.e.* lower grain size). Contrary to *(AZO·L1, AZO·L2, AZO·M1, ZnO·M2)*, this role of interface scattering reflects in the increase of the interface roughness deduced from the Soffer model, particularly enhanced when silver is encapsulated between two NiCr layers. In line with this results, the $NiCr_{double}$ sample presents also the strongest interface scattering contribution of all samples ($p = 0$). For the case of the $NiCr_{sub}$ sample, one can notice an asymmetry between the $p1$ and $p2$ parameters also visible in the estimated interface roughnesses h_1 and h_2. This is not the case for the *Upper-blocker* and *Double-blocker* samples. Although the interface labelling is not explicit in Sambles/Soffer models, this asymmetry can be assigned to more detrimental effect of the NiCr blocker when Ag is grown on it, than when it is positioned on top of Ag. A likely hypothesis is the reduction of the ZnO film by the NiCr that releases metallic zinc [67] ; as an upper layer, this phenomenon could be mitigated by the oxidative deposition of the capping ZnO.

The last sample is a classical silver-based stack, deposited with the LINA line coater, but with a thicker metallic film of 20 nm (*Ag-20nm*) that, consequently, exhibits a very low resistivity (Glass-SiN-AZO-Ag-AZO-SiN). The fits with the Sambles and Soffer model reveal an asymmetry between the two Ag interfaces that could be associated to an increase of roughness developed with silver thickness. Generally, this latter is assigned to larger grain size in the film [207], which, on average, is expected to be in the same range as the film thickness. The R-parameter does not change much compared to lower thickness as the larger grain size does not imply different grain boundary transport properties (*i.e.* different angles). Furthermore, as already previously seen [120] for such a thickness, the film starts to develop several grains in the film thickness, thus questioning the validity of the resistivity models (see Sec. (1.5.3)).

The modelling of the resistivity curves requires also fitting the Debye temperature Θ_D. It is the characteristic temperature of the density of normal modes of vibration [208] and in the bulk of silver, it amounts to 215 K [94]. In all cases, the effective Θ_D turned out to be lower than the bulk value. This behaviour, widely observed in thin films [119, 139, 209–211], is the result of a phonon softening phenomenon caused by the reduced/modified coordination of atoms at interfaces leading to changes of phonon mode density and vibration frequencies. Calculations of the surface phonons have proven that the surface Θ_D of a material will normally exhibit a smaller value than the bulk. For a silver (111) surface, it was found to drop to about 150 K (-30%) by LEED experiments [212], a value close to the present finding. In addition to the likely contribution of interfaces, the grain boundaries (*i.e.* the inner interfaces) are also a source of perturbations of phonon modes. An enhanced phonon softening was already observed upon decreasing the grain size [213, 214]. Likewise, it has been proven that defects and impurities provoked by ion irradiation involving Ar/Xe gas bombardment can also significantly reduce the Debye temperature [215, 216].

In summary

The present transport measurements in temperature helped to highlight the origin of the main electron scattering phenomena occurring in the metal film. At variance to silver single crystal, defects within the metals grains contribute to a non-zero residual resistivity. In addition in a metallic film, resistivity is driven by scattering of electrons at external and "internal" (grain boundaries) interfaces in a way that is dictated by the microstructure of the coating. For instance, when the interface is modified, either by removing the seed layer or by introducing a blocker film, the interface scattering is strongly modified. However, on the other hand, an increase in the lateral size of the grains within the herein explored range by changing growth conditions and by increasing the thickness of the silver film does not impact the reflection coefficient at

grain boundaries (parameter R). As it will shown in the next chapters (Ch. (4) and Ch. (5)), the reason lies in the in-plane texture of the film and the distribution of grain boundary angles, which both are quite similar for all the reference coatings.

3.3.2 Influence of annealing on electron scattering phenomena

The recrystallisation of the metallic film induced by thermal treatment results in a strong decrease of the stack resistivity. Accordingly, first of all, the residual resistivity ρ_{res}^{grain} drops to a lower value (from 0.65 to 0.21 $\mu\Omega$.cm for LINA and from 0.69 to 0.39 $\mu\Omega$.cm for MISSTIC samples) as the concentration of intra-grains defects and impurities is reduced. ρ_{res}^{grain} was deduced as explained above by considering the resistivity of the thicker silver films annealed at the same temperatures (Fig. (3.26)). As LINA and MISSTIC samples were annealed at different temperatures (650°C for LINA and 350°C for MISSTIC samples and *AZO·L1*), their gains on ρ_{res}^{grain} differ.

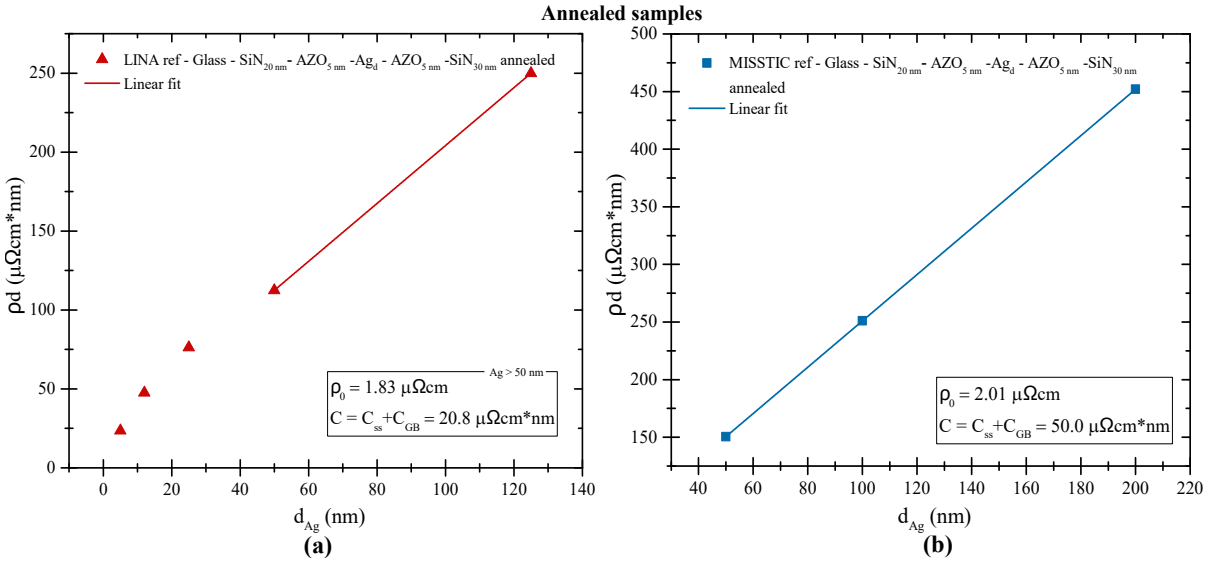

Figure 3.26 Room-temperature resistivity times the Ag film thickness as a function of the silver film thickness for the annealed LINA and MISSTIC samples. The linear fit at large thickness is used to deduce from the slope an estimate of ρ_{res}^{grain}.

Fig. (3.27) and Fig. (3.28) show the resistivity curves of the annealed samples and the corresponding temperature dependent contributions $\rho_{ph}(T) = \rho(T) - \rho_{res}(T = 0K)$. After annealing, the LINA samples have quite similar phonon contributions while their difference with the bulk of silver is increased (Fig. (3.27)-b versus Fig. (3.22)). The strongest evolution upon annealing is observed for the *Ag-20nm* sample with a room-temperature phonon contribution increase of 17% (Fig. (3.28)).

Using the same approach as for the as-deposited samples, the experimental data were fitted by the three resistivity models to obtain the p, R, Θ_D, and h parameters at fixed ρ_{res}^{grain}. All the results of the annealed samples are summarized in Tab. (3.8). As before, beyond the good fit agreement (Fig. (3.27)), the obtained parameters with the different models are quite consistent. A slight lower value is still found for the Soffer R-factors, a fact which however does not influence the interpretation of the data.

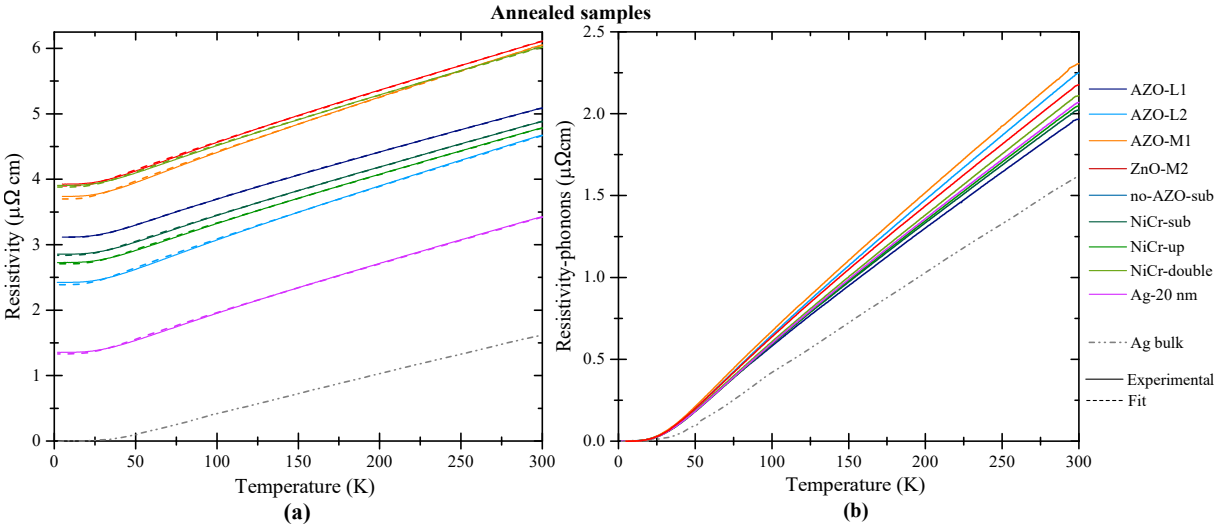

Figure 3.27 (a) Temperature dependent resistivity of the LINA/MISSTIC samples after annealing compared to silver bulk [93]. The continuous curves correspond to the experimental data while the dashed lines represent the simulations with three different resistivity models (Mayadas- Shatzkes, Sambles and Soffer). Fits parameters are reported in the Tab. (3.8). (b) Corresponding $\rho_{ph}(T) = \rho(T) - \rho_{res}(T = 0K)$ contribution.

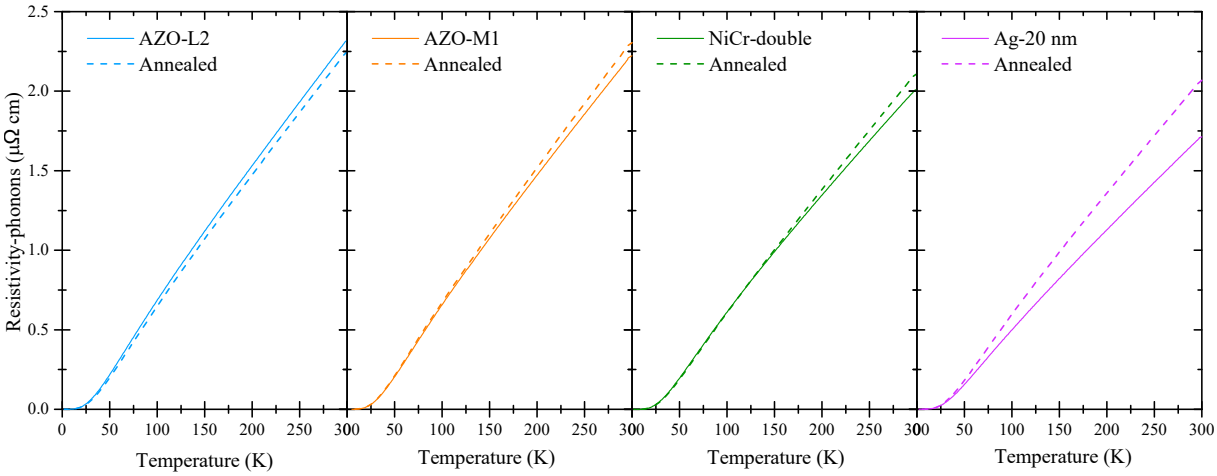

Figure 3.28 Phonon contribution ($\rho_{ph}(T) = \rho(T) - \rho_{res}(T = 0K)$) to resistivity for a few representative samples before (continuous line) and after annealing (dashed line).

In contrast to the as-deposited samples, a strong increase of the interface scattering parameter p is observed for all samples. In most cases, the p-parameter reaches even a value of close to one which corresponds to a complete absence of out-of-specular scattering. This improvement, also seen in the roughness parameters of the Soffer model, is not really due to a smoothing of interfaces according to X-ray reflectivity (Tab. (3.3), Tab. (3.4), Tab. (3.5)) but most probably to an healing of some interface defects upon annealing. Indeed even if the p-parameter accounts for the interface roughness, it is also an indirect descriptor of the quality of reflection of the electronic wave. In particular modulation of the Schottky barrier height or the existence of interface defect states can induced a loss of coherence upon reflection. In parallel to an increase

of p, counter-intuitively, the reflection coefficient at grain boundary systematically worsens from $R = 0.1 - 0.2$ to $R = 0.2 - 0.3$ for all samples. Of course, as seen before, the annealing induces an increase of the grain size, a phenomenon already taken into account in the resistivity analysis, and of the out-of-plane texture of the silver film (Tab. (3.3), Tab. (3.4), Tab. (3.5)). Therefore, the distribution of grain boundary angles is shifted by annealing towards larger values as the low angle ones are more prone to be disappear upon grain sintering. Consequently, the obtained R value is higher after annealing while the overall resistivity is improved as it accounts for larger angle grain boundaries that are the more temperature resistant and the more resistive (see Sec. (1.1.4)).

Among the ZnO seed layer based samples, *AZO·L1* and *ZnO·M2* samples are those showing a p-parameter lower than 1, most probably because of their lower annealing temperature (350°C instead of 650°C). As seen with the Sambles and Soffer models, no asymmetry between interfaces is introduced by the annealing. On the contrary, the asymmetry and the interface scattering worsening introduced by the blocker layers in the as-deposited samples is washed out by annealing although X-ray reflectivity points at a increase of roughness (Tab. (3.6)). In parallel, those samples see their $R-$parameters increase even more than for blocker-free samples passing from a value of ∼0.10 to ∼0.25-30, although lower variations are observed if considering Soffer results. Beyond the above described healing of low angle grain boundary, this behaviour is in fully in line with previous TEM findings on annealed ZnO-NiCr stacks [39]. Due to their reactivity, Ni atoms reacts with the ZnO and create $Zn_xNi_yO_z$ compounds that accumulate at the Ag grain boundaries. This oxide obviously is an obstacle to conductivity that worsens the transmission of electrons between adjacent grains. The diffusion of the other inclusions such as oxygen or argon is also not excluded. With a negligible contribution of the interface scattering (p=1), this could mean that a drastically improvement of the resistivity stack could simply be obtained by inhibiting the diffusion at the grain boundaries of the blocker species. Further and deeper investigation are however still needed to confirm this significant conclusion.

A strong smoothing of the interfaces is also observed for the $Ag-20nm$ sample, which also looses its interface asymmetry observed before annealing (Tab. (3.7)). But its R-factor remains of the same order of that of thinner layer which indicate a similar grain boundary angle distribution. At last, on average, the Debye temperature slightly decreases after annealing despite the film recrystallisation. The reasons of this behaviour are however not yet understood.

In summary

The thermal treatment induces a film recrystallisation and a strong decrease of the coating resistivity. In parallel to the increase of the lateral grain size and the decrease of grain boundary density which is the probably the main source of resistivity improvement, the contribution of out-of-specular scattering of electrons at interfaces nearly vanishes for all samples even for those with blocker layers.
According to X-ray reflectivity, interface smoothing is not the reason. Most probably, this behaviour is related to "interface defects" healing. In parallel, annealing increases the average R-parameter since it corresponds to grain boundaries with the largest angles that survived to thermal treatment. Regarding the samples involving blocker layers, the further worsening of R-parameter, compared to samples without, is compatible with the previously observed formation and diffusion of a $Zn_xNi_yO_z$ compound or of other species such as oxygen or argon at the grain boundaries. Consequently, by controlling the intra-layer diffusion of the blocker film, a strong conductivity enhancement should be obtained. Further analyses are, however, necessary to confirm this promising result.

Sample	ρ_{4P} [$\mu\Omega$**.cm**]	ρ_{300K} [$\mu\Omega$**.cm**]	ρ_{res}^{grain} [$\mu\Omega$**.cm**]	**R**	$\mathbf{p}_1$	$\mathbf{p}_2$	Θ_D [**K**]	$\mathbf{h}_1$ [**nm**]	$\mathbf{h}_2$ [**nm**]
Annealed samples 350°C									
AZO·L1									
Mayadas-Shatzkes				0.21	0.70		166		
Sambles	4.75	5.08	0.21	0.21	0.70	0.70	166		
Soffer				0.21			178	0.06	0.06
AZO·M1									
Mayadas-Shatzkes				0.21	1.00		138		
Sambles	5.58	6.04	0.39	0.21	1.00	1.00	138		
Soffer				0.16			151	0.07	0.07
ZnO·M2									
Mayadas-Shatzkes				0.20	0.88		147		
Sambles	4.88	6.10	0.39	0.20	0.87	0.87	147		
Soffer				0.13			167	0.09	0.09
Annealed samples 650°C									
AZO·L2									
Mayadas-Shatzkes				0.21	1.00		142		
Sambles	3.72	4.67	0.21	0.21	0.94	1.00	142		
Soffer				0.14			170	0.08	0.08
NiCr$_{sub}$									
Mayadas-Shatzkes				0.24	1.00		159		
Sambles	4.44	4.88	0.21	0.24	1.00	1.00	159		
Soffer				0.18			181	0.07	0.07
NiCr$_{up}$									
Mayadas-Shatzkes				0.24	1.00		156		
Sambles	4.27	4.77	0.21	0.24	1.00	1.00	156		
Soffer				0.16			182	0.08	0.08
NiCr$_{double}$									
Mayadas-Shatzkes				0.31	1.00		153		
Sambles	5.34	6.02	0.21	0.31	1.00	1.00	153		
Soffer				0.25			169	0.07	0.07
Ag-20nm									
Mayadas-Shatzkes				0.20	1.00		153		
Sambles	2.88	3.42	0.21	0.20	1.00	1.00	153		
Soffer				0.20			153	0.00	0.00

Table 3.8 Fit results of the temperature dependent resistivity of the annealed LINA/MISSTIC glass-based samples with three different models : Mayadas-Shatzkes, Sambles and Soffer. The estimated error bars are of the order of $\Delta p \simeq \pm 0.02$, $\Delta R \simeq \pm 0.05$, $\Delta\Theta_D \simeq \pm 5$ K and $\Delta h_1 = \Delta h_2 \simeq \pm 0.02$ nm. In the table, the resistivity at room-temperature of each sample, measured via *Napson* (ρ_{4P}) and via temperature-dependent set ups (ρ_{300K}) are reported. The first three samples will be used in the next chapters as references for single crytsal based samples.

3.4 In conclusion

This chapter dealt with simplified silver-based low-emissive coatings on glass substrate ; they consist of a 12 nm thick Ag layer encapsulated between two ZnO films and protected from the environment by Si_xN_y amorphous layers *i.e.* Glass-Si_xN_y-ZnO-Ag-ZnO-Si_xN_y.

Changes in the deposition environment, in the interface material or in the ZnO deposition mode can significantly impact the structural properties of the metal film. Compared to an amorphous substrate, the ZnO seed layer induces a strong (111) Ag out-of-plane texture while in-plane the grains are randomly oriented. The silver film characteristics are completely driven by those of the ZnO seed layer. In particular, the stronger correlation was observed for the out-of-plane grain orientation and the lateral domain sizes, especially before annealing. This findings was assigned to an epitaxial relationship between both materials, most probably hexagon/hexagon. A systematic search of correlation between the structural characteristics of the films in the stack as obtained by X-ray diffraction and the stack resistivity was performed. Reducing the density of the grain boundaries and improving the in-plane texture have a direct impact on the conductivity of the metal. Interface roughness also effectively influences the sample resistivity although the conclusion is not so clear-cut with the present X-ray reflectivity measurements.

The comparison between all samples has shown the relevance of the analysis of the temperature dependent resistivity in rationalising the main factors contributing to resistivity beyond the change of grain size. In as-deposited samples, both interface and grain boundaries contribute to the film resistivity. But when an interface is modified, either by removing the ZnO seed layer or by introducing a blocker film, the interface scattering rises. After annealing, interfaces do not contribute to resistivity beyond a simple specular reflection. As X-ray reflectivity does not evidence a clear smoothing, a mechanism of "interface defect" healing was put forward. In parallel, the worsening of the reflection of electrons at grain boundaries after annealing is interpreted by the survival of the larger angle ones and by the accumulation of $Zn_xNi_yO_z$ at grain boundaries when a blocker is present. Without a significant interface scattering contribution, this preliminary result sets a new objective for this type of coatings : to reduce intra-layer diffusion.

Chapter 4

Model systems : silver films on ZnO(0001) single crystals

This chapter is dedicated to the results obtained for a model system, for which a Ag thin film has been grown directly on a ZnO(0001) single crystal substrate, either Zn- or O-terminated. The idea is to favour the in-plane texture through epitaxy. In the first part, the efficiency of different preparation protocols of the substrate surface will be compared ; this is a fundamental step to ensure the best interface conditions for the silver growth. The evolution of the surface state has been followed with a combination of analyses (XPS, LEED, AFM). In the second part, the structural (XRD) and electrical properties of the films grown by sputtering deposition will be compared trying to understand the relationship between the epitaxy, the microstructure and the modelling of the temperature dependent transport measurements.

Chapter summary

4.1 The ZnO(0001) single crystal

As received, the ZnO single crystals, O- and Zn-terminated, were subjected to a series of analyses with the objective of checking their initial surface characteristics.

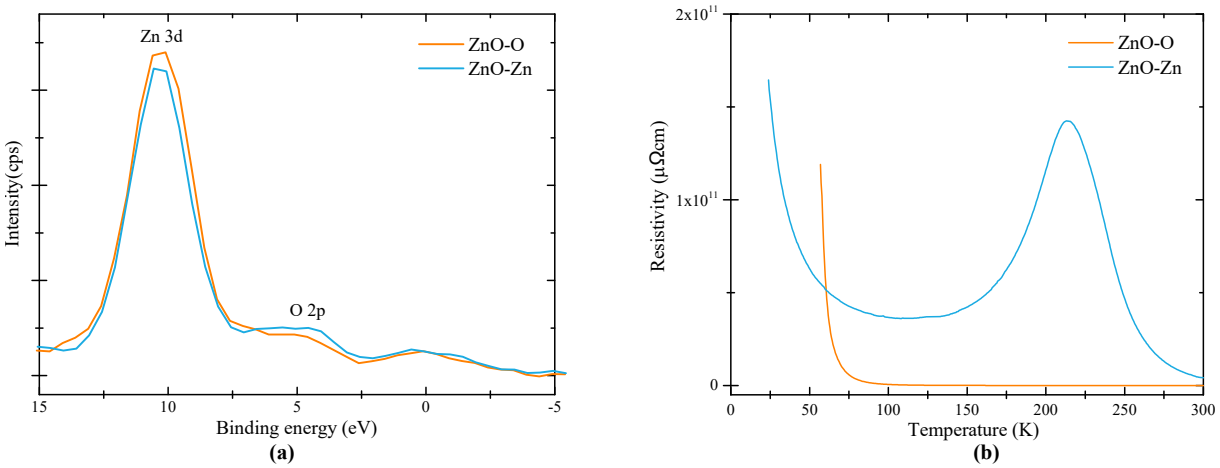

Figure 4.1 (a) Valence band photoemission spectra of as-received single crystals. The substrate termination can be determined by the intensity of the O 2p derived states. The intensity observed at negative binding energies is due to X-ray source satellites. (b) Resistivity variation of the single crystal as a function of temperature.

The substrate surfaces were firstly investigated through XPS. From the valence band photoemission spectra, the sample orientation was confirmed via the intensity variation of the valence band O 2p derived feature [217], as the Zn-termination exhibits a higher peak than the O-terminated face (Fig. (4.1)-a). At higher binding energies, the O 1s, Zn 2p 3/2 and C 1s core level signals (Fig. (4.3)) were used to quantitatively describe the surface atomic composition assuming an homogeneous material and following the methodology described in Sec. (2.3.2). As-received, the two surface terminations showed a similar composition : about 37 at.% of Zn and 21 at.% of O, considering only the contribution of O atoms in ZnO, in O-terminated sample (26 at.% for Zn-terminated). Regardless of their termination, also the types and the percentages of impurities were almost identical : 22 at.% of adventitious C (16 at.% corresponding to C-C bonds, 6 at.% of C-O-C bonds [218]), and between 13 and 21 at.% of O associated to weakly bonded compounds, as OH- group, or even non-stoichiometric substrate regions [168]. No traces of other contaminants were visible at the sensitivity of photoemission. These findings are not a surprise for an unprepared/contaminated surface leading to an overestimation of the actual Zn stoichiometry.

The strongest difference between both terminations was observed for the surface morphologies, most probably reflecting a fundamental difference of their surface reactivity [55]. The Zn termination revealed a smooth, flat surface with an average RMS_{AFM} roughness of 0.27 nm. At the opposite, the O-terminated sample exhibited a higher roughness, of about 0.78 nm, characterized by a pebble-like structures, only slightly visible for the Zn surface (Fig. (4.2)).

ZnO is known to be a semiconductor with a wide band gap, around 3.4 eV [219–221], and therefore with a high bulk resistivity in the undoped intrinsic state. At ambient temperature, the O-terminated samples showed a resistivity of $2 \cdot 10^7\ \mu\Omega$.cm and the Zn-terminated, a value two-orders of magnitude higher [$4 \cdot 10^9\ \mu\Omega$.cm]. Both measurements showed a good stability in

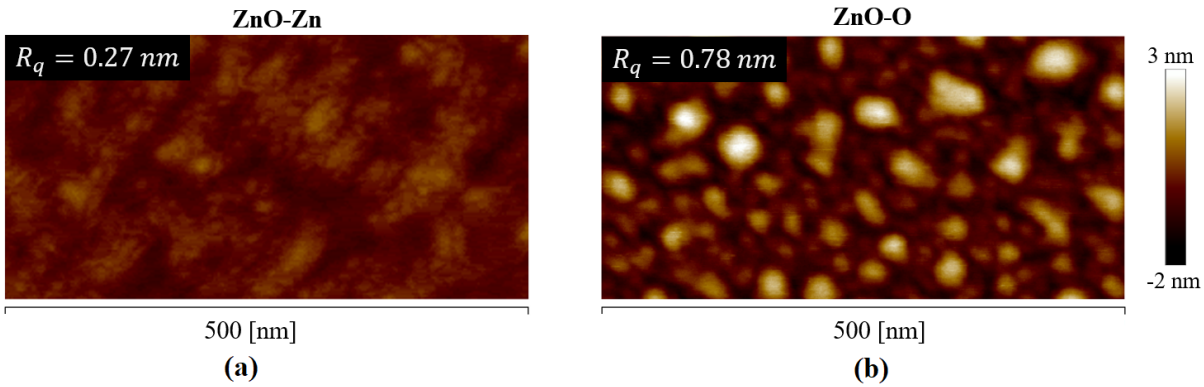

Figure 4.2 AFM images of the as-received ZnO(0001) Zn- (a) and O-terminated single crystals (b). The samples show a RMS_{AFM} surface roughness (R_q) of 0.27 nm for Zn- and of 0.78 nm for O-termination.

time and a good linearity of the I(V) characteristic thus demonstrating the independence of the resistivity to the applied current (Fig. (4.1)-b). The discrepancy between the two values could be due to different unintentional bulk doping during crystal growth of crystal batches. Both crystals showed the typical semiconductor behaviour ; as the temperature is reduced, the carrier density decreases and the resistivity increases [222]. On the Zn-terminated face curve, an anomalous maximum appears around $\sim$ 210 K that is most probably related to an experimental error artefact due to a high contact resistance. At last the resistivity of ZnO is large enough to neglect the contribution of the substrate in a four points probe measurements. Indeed, the corresponding 3D resistance $R_{ZnO} = \rho_{ZnO}/2\pi s$ is put in parallel to the 2D one of the silver sheet $R_{\square} = \ln(2)\rho_{Ag}/\pi d$ where ρ_{ZnO} and ρ_{Ag} are the respective material resistivities, d the silver film thickness and s the electrode spacing [192]. With $d = 12$ nm, $s = 1.5$ mm and $\rho_{Ag} \simeq 5\,\mu\Omega$.cm, $R_{\square}/R_{ZnO} \simeq < 10^2 - 10^3$.

4.2 Single crystal surface preparation

The polar surfaces of ZnO are highly hydrophilic and easily absorb ambient contaminants such as water in the form of OH species or carbon-based molecules [223]. As the Ag growth processes, in particular film nucleation and epitaxial orientation, are strongly influenced by the surface state of the substrate, it is important to prepare it to provide the best surface quality (i) by removing all the adsorbed pollutants and (ii) by increasing the terrace size to favour epitaxial growth and (iii) by decreasing the density of defects and therefore nucleation density.

A wide range of surface preparation methods can be found in the literature but an *in situ* one is highly preferred regarding carbonaceous contamination. The surface preparation protocols tested in the present study all involve (i) a first low temperature surface outgassing, to remove most of the adsorbed species, followed by (ii) a cycles of Ar^+ ion bombardment and high temperature annealing, to eliminate polishing/bombardment damages, carbon compounds, the remaining OH-groups and implanted Ar, and to give to the surface atoms enough mobility to favour surface recrystallization. Ar-ions sputter off atoms from the surface in a similar way as on the target during sputtering deposition.

To check the efficiency of the preparation protocol, the substrate surface was analysed *in situ* by LEED and XPS, two techniques that allow to check the crystallinity and the composition of the sample surface. For some samples, AFM analyses were performed *ex situ* in air at selected

stages of the preparation.

4.2.1 First preparation protocol

The single crystals with both orientations were introduced in the chamber without any prior treatment and then heated at 300°C for 30 min under ultra-high vacuum (10^{-8} mbar). Subsequently, the surface was bombarded with Ar^+ ions at 1 keV for 30 min in defocused mode to achieve a uniform etching speed and heated at 600°C for 30 min under the same conditions of vacuum. The single crystal surface has been controlled just after each annealing step by XPS ; the resulting spectra of the elements of interest (O, C, Zn) are given in Fig. (4.3).

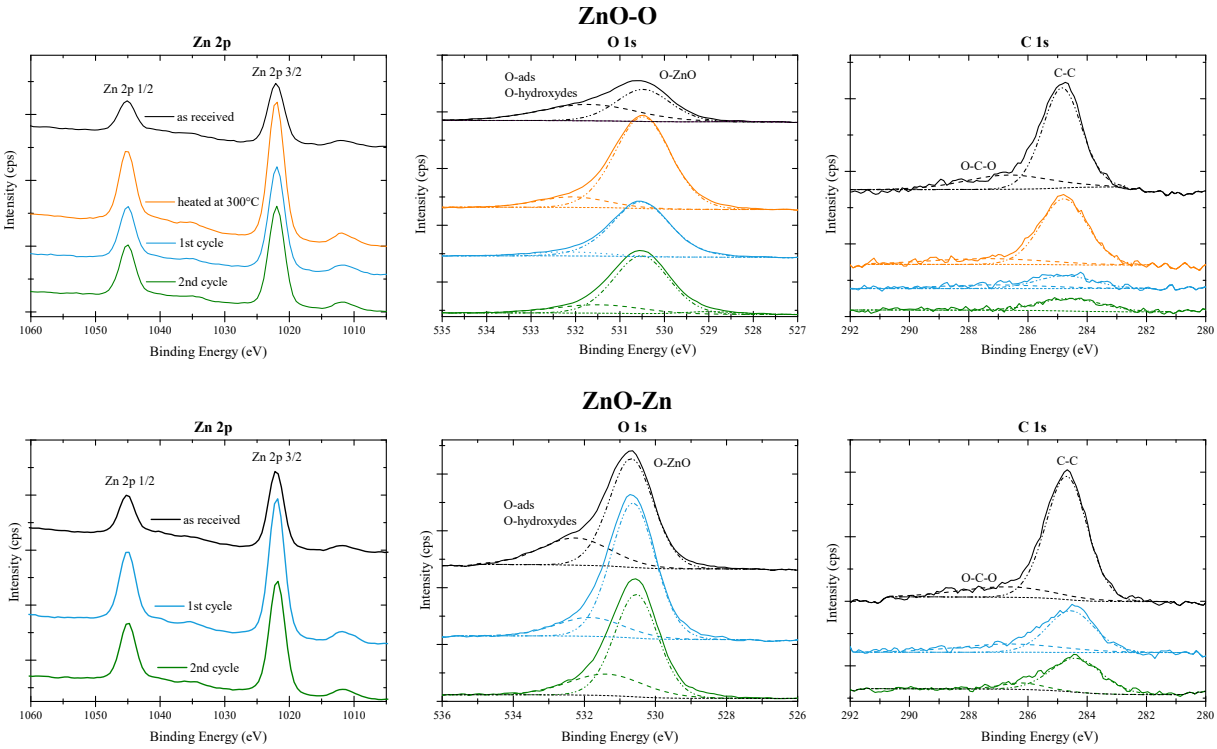

Figure 4.3 XPS core level evolution throughout the preparation steps of the first protocol of surface treatment for O- and Zn-terminated single crystals.

			As received	Heated at 300°C	1st cycle	2nd cycle
ZnO-O	**Zn 2p**		36%	44%	51%	50%
	O 1s	*O-ZnO*	21%	41%	41%	38%
		O-H	21%	6%	3%	9%
	C 1s	*C-C*	16%	7%	3%	3%
		C-O-C	6%	2%	2%	0%
ZnO-Zn	**Zn 2p**		38%		54%	54%
	O 1s	*O-ZnO*	26%		30%	29%
		O-H	13%		9%	10%
	C 1s	*C-C*	16%		4%	4%
		C-O-C	7%		3%	3%

Table 4.1 Quantitative XPS analysis of the ZnO single crystal surface after the first protocol of surface preparation. The %at. are calculated from peak area corrected from their relative sensitivity factors.

After the first low-temperature annealing, the O 1s core level shifted towards 530.5 eV, a value corresponding to O atoms in ZnO while the C 1s component (∼ 285 eV), associated to the adventitious carbon dropped rapidly (Tab. (4.1)). This partial removal of surface contamination is reflected also in the decrease of the damping of the ZnO (Zn 2p and O 1s) core level intensities. As the sample was subjected to the first cycle of ion bombardment and high temperature annealing, a further removal of the adsorbed carbon compounds was observed. The surface composition achieved at this point remained almost unaltered throughout the second cycle of sputtering/annealing, which appears to be less efficient than the first one in the contamination removal. A possible explanation lies in the recontamination and ageing of the surface due to the limited base vacuum pressure. Likewise, after the second cycle, the improvements in the surface crystallinity were less important, as shown by the only slight sharpening of the peaks in the LEED patterns and their unchanged intensities (Fig. (4.4)).
Overall, due to their different terminations, which give different surface energies and chemistry [224], the response to the surface preparation was slightly face dependent. It was more effective for the O-terminated samples, which, at the end, exhibited a lower carbon contamination and a higher surface crystallinity than Zn-terminated samples.

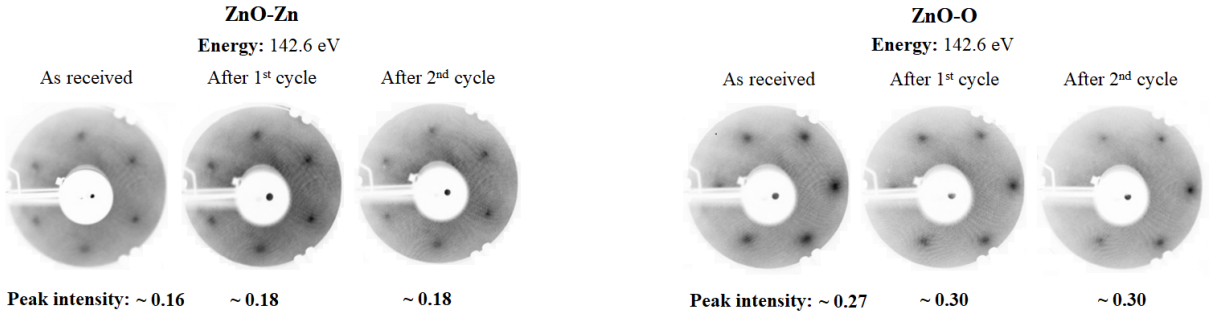

Figure 4.4 Evolution of the LEED patterns for O- and Zn-terminated single crystals after the first protocol of surface treatment : (i) as-received, (ii) after 1^{st} and (iii) 2^{nd} cycle of sputtering/annealing. The figure below is indicative of the signal/noise ratio of diffraction peak. The six-fold symmetry corresponds to the hexagonal surface unit cell of ZnO(0001) surface.

4.2.2 Second preparation protocol

At the end of the first process, a significant amount of contamination was still present on the single crystal surface. Hence, trying to further improve the preparation recipe, a second protocol was tested, which included one hour of Ar bombardment and two additional annealings, one at 600°C for one hour and the other at 750°C for 30 min. Like previously, XPS acquisitions (Fig. (4.5)) and AFM measurements (Fig. (4.6)) were performed after selected steps.

Longer Ar^+ sputtering degraded the surface roughness rapidly increasing its value from 0.06 nm to 0.27 nm (Fig. (4.6)) and turned out to be poorly efficient for the contamination removal (Tab. (4.2)). The roughness did not vary also after one hour of *in situ* annealing at 600°C. At the opposite, when the annealing temperature was increased to 750°C, all the contamination was practically removed (Tab. (4.2)). Indeed, XPS revealed the presence of only 1 at.% of carbon. Nevertheless, time and temperature of the annealing process did not seem to positively impact the surface smoothness, as the AFM scan showed an increase in the surface roughness to 0.34 nm. To avoid a further roughening as already reported in the literature [225, 226], no further temperature rise was tested.

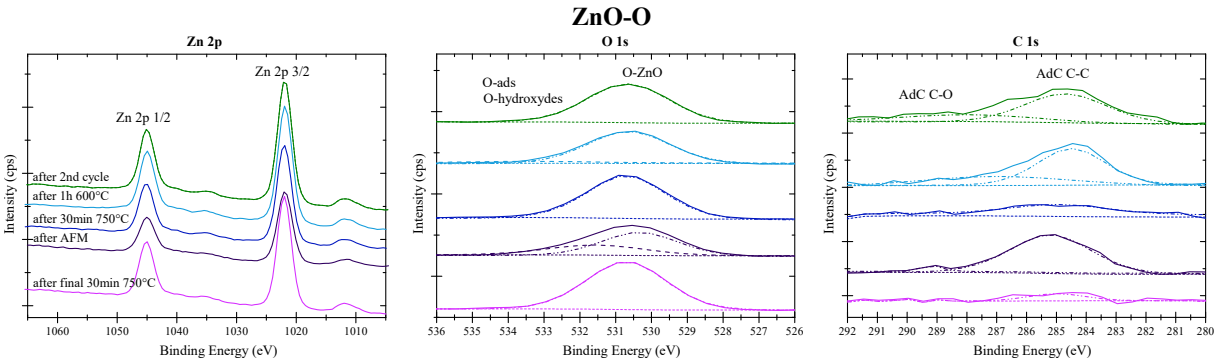

Figure 4.5 XPS spectra evolution throughout the preparation steps of the second protocol of surface treatment for an O-terminated single crystals.

			2^{nd} cycle	1h - 600°C	30min - 750°C	AFM	30min - 750°C
ZnO-O	**Zn 2p**		38%	38%	35%	30%	36%
	O 1s	*O-ZnO*	48%	44%	61%	28%	62%
		O-H	0%	4%	0%	26%	1%
	C 1s	*C-C*	10%	6%	4%	15%	1%
		C-O-C	4%	7%	0%	0%	0%
		C-O=C	0%	1%	0%	1%	0%

Table 4.2 Quantitative XPS analysis of the ZnO single crystal surface after the second protocol of surface preparation. The %at. are calculated from peak area corrected from their relative sensitivity factors.

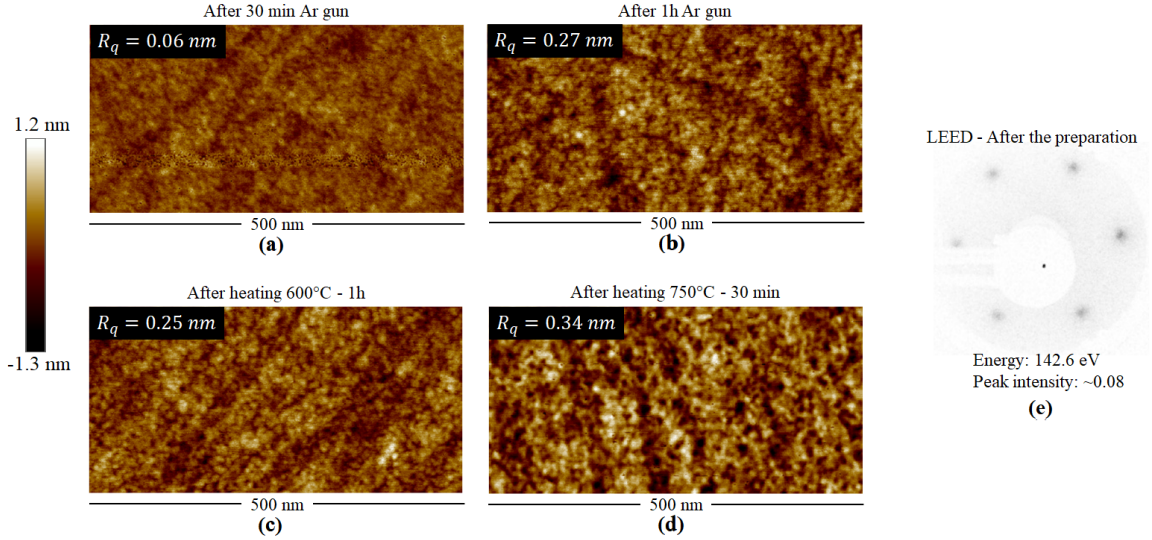

Figure 4.6 (a)-(d) AFM imaging after different surface treatment steps of the second protocol of preparation. Notice that the preparation reveals polishing scratches that are not directly visible on the as-received surface. (e) LEED pattern of the crystal at the end of all preparations.

Before depositing the stack, a third cycle of Ar^+ sputtering, followed by a high 750°C annealing was performed in order to restore the surface state obtained before the *ex situ* AFM analysis.

In fact, the exposure to the atmosphere provoked a recontamination of the single crystal surface while the LEED pattern had a poor contrast (Fig. (4.6)-f). This surface preparation, with an intermediate exposure to atmosphere, led to a worse surface quality but better than as-received single crystal (Fig. (4.6)). This "in between" surface was only used in order to compare the results obtained for the Ag layer with as-received samples and the optimum preparation surface.

4.2.3 Third preparation protocol

The high temperature annealing of the second preparation protocol was found to be very efficient in the removal of surface contaminants. Hence, in the third protocol, the 750°C annealing was systematically introduced in the preparation cycles. After 30 min of annealing at 300°C, the sample was bombarded for 30 min and subsequently annealed at high temperature for the same duration. The surface preparation was checked only on a Zn-terminated single crystal and compared the results of the second protocol. As previously observed, just after the first cycle (Fig. (4.7) and Tab. (4.3)), the sample presents only 2% of C and a RMS_{AFM} roughness of about 0.32 nm. To improve this figure, two more cycles were performed on the sample. Before pursuing the preparation, the sample was stored for a few weeks under vacuum (10^{-8} mbar) that led to surface recontamination by a thick adventitious carbon layer which could not be fully removed with the additional cycles.

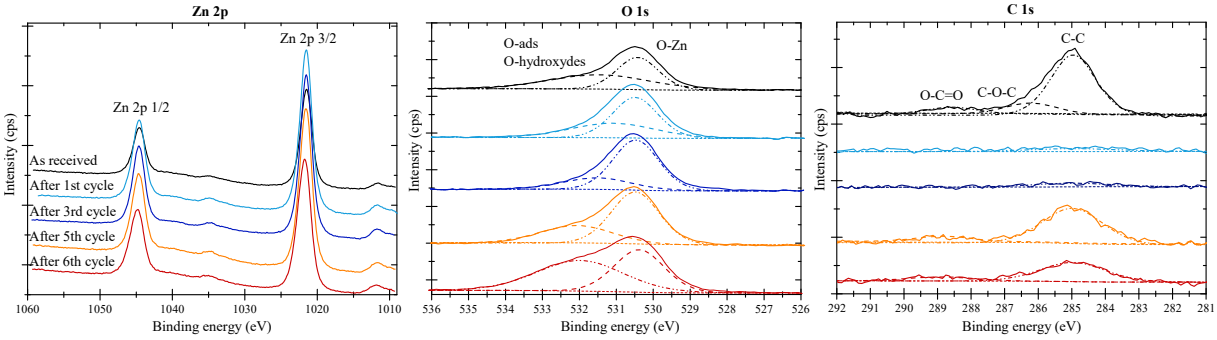

Figure 4.7 XPS core level evolution throughout the different steps of the third preparation protocol

			As received	1^{st} cycle	3^{rd} cycle	5^{th} cycle	6^{th} cycle
ZnO-Zn	**Zn 2p**		40%	61%	58%	50%	44%
	O 1s	*O-ZnO*	20%	25%	22%	28%	26%
		O-H	18%	13%	19%	12%	24%
	C 1s	*C-C*	17%	1%	1%	8%	5%
		C-O-C	3%	0%	0%	0%	0%
		C-O=C	2%	0%	0%	2%	1%

Table 4.3 Quantitative XPS analysis of the ZnO single crystal surface after the third protocol of surface preparation. The surface composition (%at.) is calculated from peak area corrected from their relative sensitivity factors.

At the end of the preparation, the surface roughness increased from 0.17 to 1.42 nm with the appearance of nanometric features on the surface (Fig. (4.8)), characterized by a peak-to-valley topography that reached 10 nm, a value definitely problematic for the deposition of a 12 nm thick Ag layer. The morphological changes reflected in the LEED diffraction pattern, showing a broadening of the peaks at each step until the diffraction completely vanished (Fig. (4.8)). Owing to the poor coherence length of a classical LEED tool, the final terrace domain size should be

lower than a few nanometers. This loss of surface crystallinity is also unsuitable for our final goal, *i.e.* obtaining a good epitaxial silver layer.

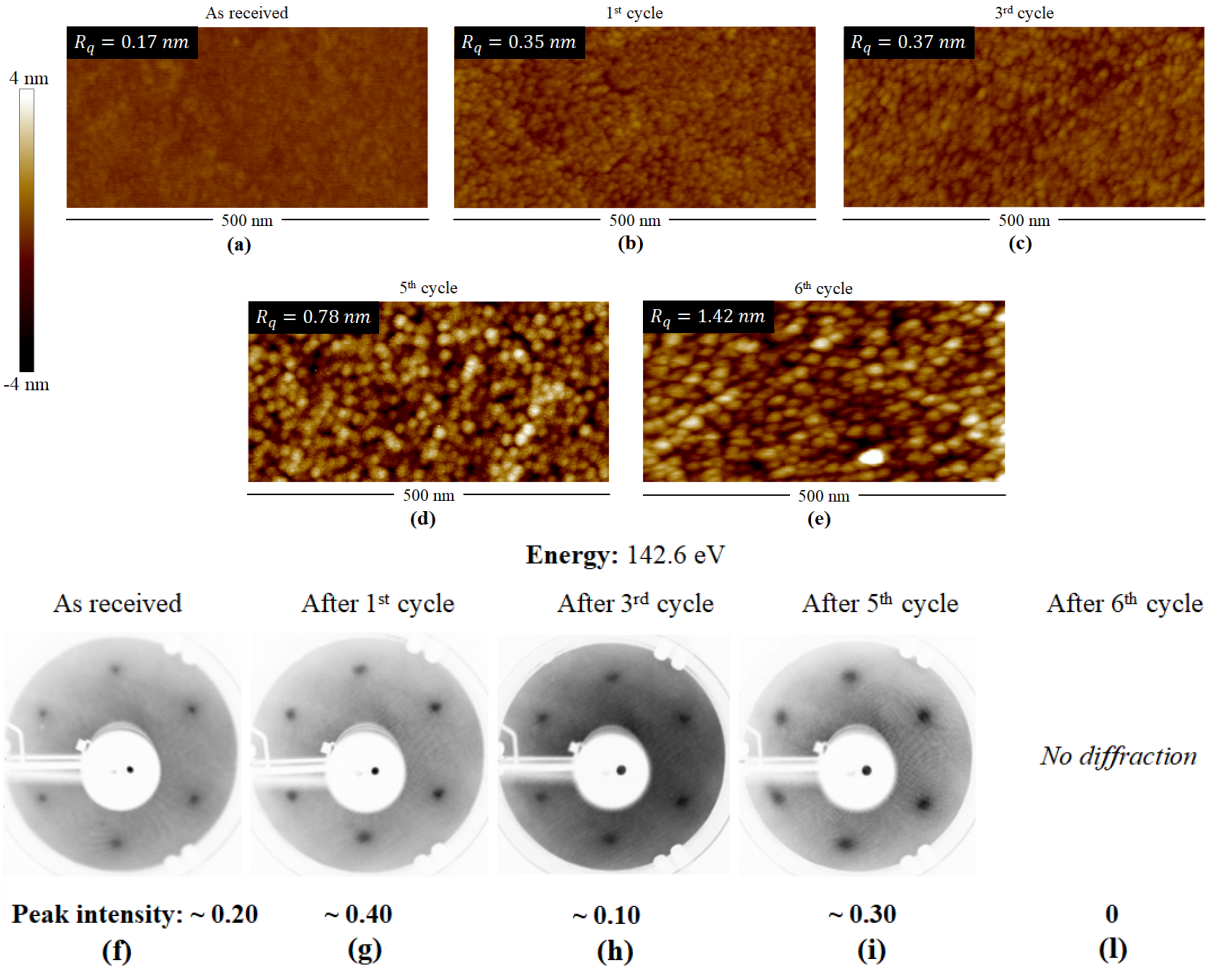

Figure 4.8 (a-e) AFM images and (f-l) LEED patterns of the ZnO-Zn surface sample along the third protocol of treatment.

4.2.4 In summary

Three surface preparation protocols were tested on ZnO single crystals, either O- or Zn-terminated faces. All the preparations included a first low temperature annealing (300°C) to outgas the sample, followed by cycles of Ar^+ bombardment and annealing at higher temperature which, depending on the treatment, varied from 600°C to 750°C. The results demonstrated that the use of higher temperatures easily removed the contamination adsorbed on the ZnO surface. Annealing seems to be more efficient than Ar^+ bombardment to remove impurities; a likely explanation is the high reactivity of the sputtered and poorly crystallized surface towards the residual vacuum (10^{-8} mbar). Sequential cycles of preparation reduced the contamination level after the first treatment but at the expense of an increase of roughness, which is unsuitable for the silver growth. Therefore, comparing the three protocols on the basis of surface composition, roughness and crystallinity, the first one (300°C - 30 min + cycle of [Ar^+ 1keV - 30 min + 600°C - 30 min] (×2)) appears to be the most suitable for the growth of a 12 nm thick silver.

4.3 Stack deposition by sputtering and its protective layer

To confirm if the single crystal substrate and its surface preparation indeed improved the crystalline quality and resistivity of Ag films, a stack similar to that of the reference samples was deposited by sputtering on each treated single crystal surfaces and analysed through XRD and 4-point resistivity measurements. As a matter of comparison, two stacks were deposited in similar conditions on as-received single crystal substrates, O- and Zn-terminated.

In more details, without taking out the sample from vacuum, each substrate was transferred from the treatment to the sputtering chamber of MISSTIC vessel. As previously observed, storing the sample for more than a night in vacuum leads to a surface recontamination with carbonaceous species ; therefore, the layers were deposited as soon as the surface preparation was completed. A 12 nm thick Ag films was deposited by magnetron sputtering directly on the single crystal surface, followed by a thin layer, around 5 nm, of polycrystalline aluminium doped ZnO (AZO). To finalize the stack, the sample was transferred to the LINA machine, shortly exposing it to the atmosphere, to cover it with a final protective SiN capping layer of 30 nm. This procedure was imposed by the limited number of available targets in MISSTIC machine.

The impact of the atmosphere exposure on the structural and electrical properties of the Ag-based stack, was firstly tested on typical reference coatings (Fig. (4.9)). The prototype samples, deposited in one go on the LINA/MISSTIC sputtering machines, were therefore compared to a stack exposed to air just after the deposition of the AZO capping layer ($SiN_{20\ nm}$ – $AZO_{5\ nm}$ – $Ag_{12\ nm}$ – $AZO_{5\ nm}$ -|*air*|- $SiN_{30\ nm}$). The coatings were deposited on silicon wafer substrates, used for their chemical stability, and analysed before and after annealing performed in air at 650°C for 10 min.

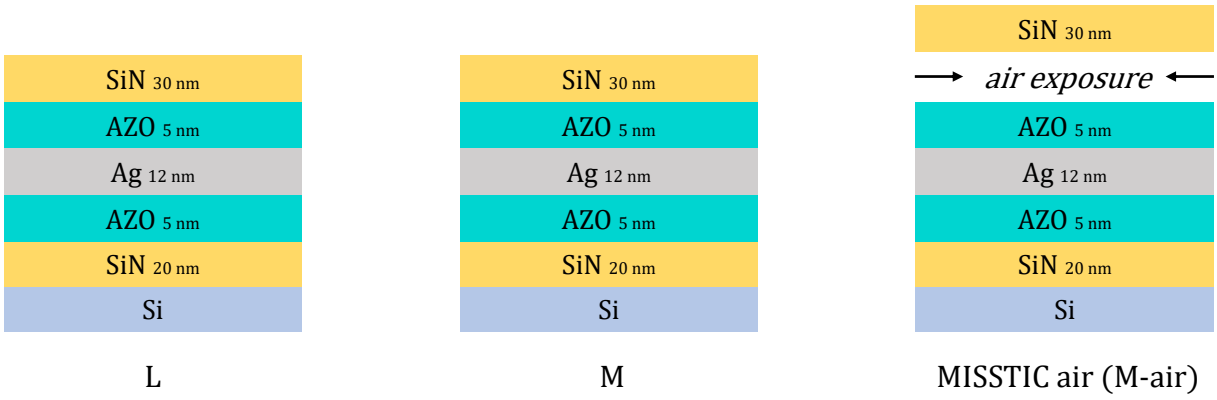

Figure 4.9 Schematic representation of the LINA (L), MISSTIC (M) references and the MISSTIC stack exposed to air (M-air).

As expected, the air transfer had a non-negligible impact on the resistivity before annealing (Tab. (4.4)). Compared to a classical stack made in one run, the sample after deposition had a sheet resistance of 1-2 Ω/sq higher. Nevertheless, the gap was closed once the sample was annealed, confirming that the capping layer is thick enough to preserve silver from oxidation upon annealing. From a structural point of view (Fig. (4.10) and Tab. (4.4)), evaluated through XRD analyses, all three samples showed similar grain sizes and mosaicities before and after annealing. In-plane, the Texture Coefficient (TC), revealed an even better texturization of the air-exposed-sample with respect to the LINA reference. A newer target and a cleaner sputtering chamber or wafer surface could have all contributed to such a better layer quality as already pointed

out in Ch. (3). Likewise, no meaningful structural variations are observed when comparing the air-exposed sample to the MISSTIC reference.

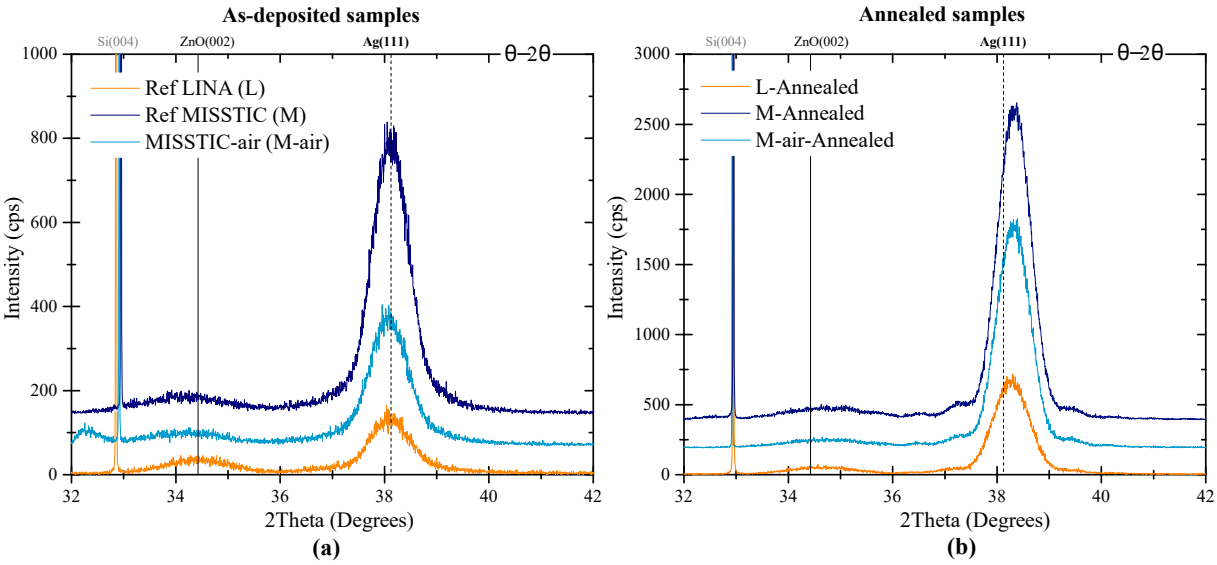

Figure 4.10 θ-2θ diffractograms of a MISSTIC sample exposed to air after the deposition of the AZO capping layer (a) before and (b) after annealing. The *M-air* sample is compared to the reference, made in one run, with LINA and MISSTIC machines. The sample characteristics as deduced from diffraction are given in Tab. (4.4).

			As-deposited samples			Annealed samples		
		unit	**L**	**M**	**M-air**	**L**	**M**	**M-air**
Ag	$\mathbf{D}_{S,OP}$	[nm]	9	10	11	11	12	13
	$\mathbf{RC}_{Ag(111)}$	[°]	8	6	6	6	4	4
	$\mathbf{L}_{S,IP}$	[nm]	10	10	10	13	14	12
	$\mathbf{TC}_{Ag(220)}$	[%]	56	70	70	80	90	90
ZnO	$\mathbf{D}_{S,OP}$	[nm]	5	5	2	5	6	4
	$\mathbf{RC}_{ZnO(002)}$	[°]	8	8	9	6	6	7
	$\mathbf{L}_{S,IP}$	[nm]	8	8	9	9	11	10
	$\mathbf{TC}_{ZnO(110)}$	[%]	42	23	25	39	27	28
	$\mathbf{TC}_{ZnO(100)}$	[%]	44	30	32	48	37	37
$\mathbf{R}_{\square-4P}$		[Ω/sq]	4.64	5.77	6.51	3.32	3.98	3.91
$\boldsymbol{\rho_{4P}}$		[Ω/sq]	5.57	6.92	7.82	3.98	4.78	4.70
Gain		[%]				28	31	40

Table 4.4 Structural and electrical properties, before and after annealing, (i) of a MISSTIC sample exposed to air before the deposition of the SiN capping layer and (ii) of two references, made in one run, one with LINA (L) and the other with MISSTIC sputtering machine (M). The $D_{S,OP}$ and $L_{S,IP}$ correspond to the vertical and lateral domain size respectively.

To conclude, exposing a stack not protected by SiN to air can cause variation in its structural and electrical properties. Nevertheless, the impact due to this exposure is in the same range of the changes provoked by a deposition parameter or a sputtering set up variations and is irrelevant for the following discussion. Hence, single crystal based stacks were all deposited following a protocol that involved an air exposure step before capping. The list of the samples

included Ag coatings ($Ag_{12\ nm}$ – $AZO_{5\ nm}$ -|air|- $SiN_{30\ nm}$) on ZnO single crystal substrates, Zn- and O-terminated, as-received or treated with the first and second surface process. Elemental maps obtained by STEM-EDS acquisition confirms the layer assignment and the lack of intense interdiffusion (Fig. (4.11)). In order to explore the structural characteristics and the growth orientation of the Ag layers, each sample was more deeply analysed by X-ray diffraction.

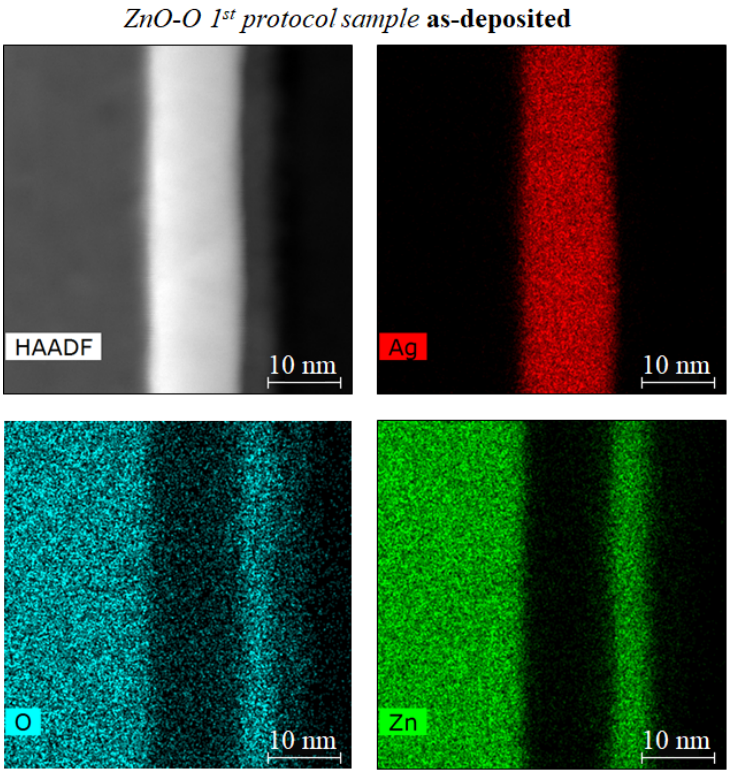

Figure 4.11 STEM-EDS elementary map of a cross section of a ZnO-O single crystal Ag-based sample prepared following the 1^{st} protocol of surface treatment.

4.4 X-ray analysis of the texture

Out-of-plane orientation

The θ-2θ diffractogram presents a unique silver peak corresponding to the {111} family of Ag planes oriented perpendicular to the $\vec{c}$ axis of the ZnO substrate (Fig. (4.12)). As previously observed for the prototype reference stacks (Ch. (3)), this is the direct consequence of the low Ag(111) surface energy and the good epitaxial match between ZnO(0001) and Ag (111) crystal faces [3]. Also, one can notice that the ZnO single crystal substrate has a poor influence on the residual stress state of the film as only a small shift of peak position from the expected bulk value is observed.

In addition to having the same out-of-plane orientation, all Ag layers exhibit similar vertical domain size ($D_{S,OP}$) as estimated from the classical Scherrer analysis (Tab. (4.5)). Including the microstrain contribution via the Size-Strain, the Halder-Wagner and the Williamson-Hall methods (Sec. (2.3.5)) does not change drastically the conclusion all the more than such analyses are performed only on the two available (111) and (222) peaks. Even if the simple Scherrer approach underestimates the actual size, the obtained microstrain in grains is also quite low in

agreement with the fact that the Scherrer vertical coherent domain sizes derived from the (222) peak, equals within ±1 nm, to the sizes obtained with the (111) peak.
In fact, all the vertical domain size values are equal within the error bar to the deposited layer thickness. This value can be further estimated by X-ray reflectivity or, when observed, through the Laue fringes analysis around the layer diffraction peaks (Eq. (2.10)). The agreement between the film thickness and the $D_{S,OP}$ value shows that one grain is present along the direction perpendicular to the film. Therefore, as all layers have about the same thickness, the peak intensity provides a direct way to compare the crystallinity and texture of the metallic layer.
According to this criterion, the first protocol of sample preparation, in particular for O-terminated samples provides the best silver crystallinity (Fig. (4.12)). This finding agrees with the best conditions previously obtained for a smoother sample surface and a lower contamination. For both terminations, the presence of Laue oscillations (*i.e.* side maxima around the $2\theta = 38°$ Ag(111) peak generated by the finite thickness form factor) confirms the presence of a very well texturized film in the perpendicular direction with smooth interfaces (Fig. (4.12)). On the other hand, despite expectations, the second protocol of sample preparation does not show the same improvements of out-of-plane texture. At the end of the preparation, the single crystal exhibited low roughness and contamination level. These characteristics seem, however, not to have a drastic impact on the Ag film out-of-plane texture quality, as confirmed by the rocking scans (Fig. (4.16)-a). Surface features, at the nanoscopic scale, that escape to the previous XPS/AFM analysis could explain the riddle. Nevertheless, the second protocol of preparation shows anyway a clear out-of-plane texture improvement compared to the as-received samples and to the glass references (Fig. (4.12) and Fig. (4.16)).

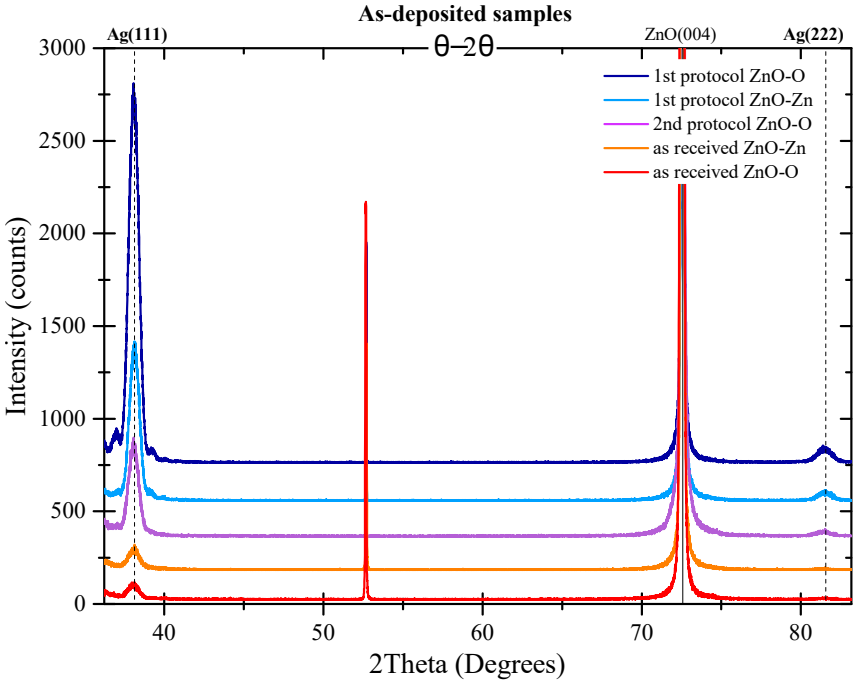

Figure 4.12 θ-2θ diffractograms of the single crystal based samples. The coating is composed of 12 nm of Ag, 5 nm of AZO and 30 nm of SiN. Before the layer deposition, the single crystal surfaces were treated following the previously described protocols (Sec. (4.2)). Before annealing, all treated samples show a good quality (111) silver out-of-plane orientation. Peak assignment is given on the top.

In-plane orientation

Regarding film resistivity and reflection of electrons at grain boundaries, the in-plane texture is a key parameter. The in-plane film orientation was analysed through Grazing Incidence X-ray Diffraction (GIXRD) (Fig. (4.13)). The ZnO reciprocal space was scanned along three azimuths : (i) azimuth 0°, corresponding to the $[100]_{ZnO^*}$ direction, and (ii) the azimuths at 15° and 30°, corresponding to $[210]_{ZnO^*}$ and $[110]_{ZnO^*}$ directions, respectively. Observing the variation of the peak intensities and positions, these three scans give important information about the in-plane orientation of the film as well as the percentage of texturization. As previously seen, the Ag thin film shows a very clear Ag (111) out-plane orientation when grown on ZnO(0001). In the cubic crystallographic structure of Ag, this family of planes is perpendicular to the Ag $\{2\bar{2}0\}$ family. Therefore, in an ideal 100% out-of-plane texturized layer, when observing the diffraction at grazing incidence, one would expect an in-plane diffractogram with a very intense $(2\bar{2}0)$ peak and the absence of the (111) peak along any azimuth. Now, if the sample is also in-plane texturized, when the azimuth is rotated by an angle lower than 60°, the very intense peak of $(2\bar{2}0)$ should disappear. At the opposite, the observation of a constant intensity peak would mean an isotropic distribution of the in-plane grain orientations. In our case, unlike the prototype reference samples that are randomly oriented in-plane (see Sec. (3.1.2)), all the single crystal based stacks show a clear biaxial texture. Yet, differences are found depending if their surface had or not been previously prepared.

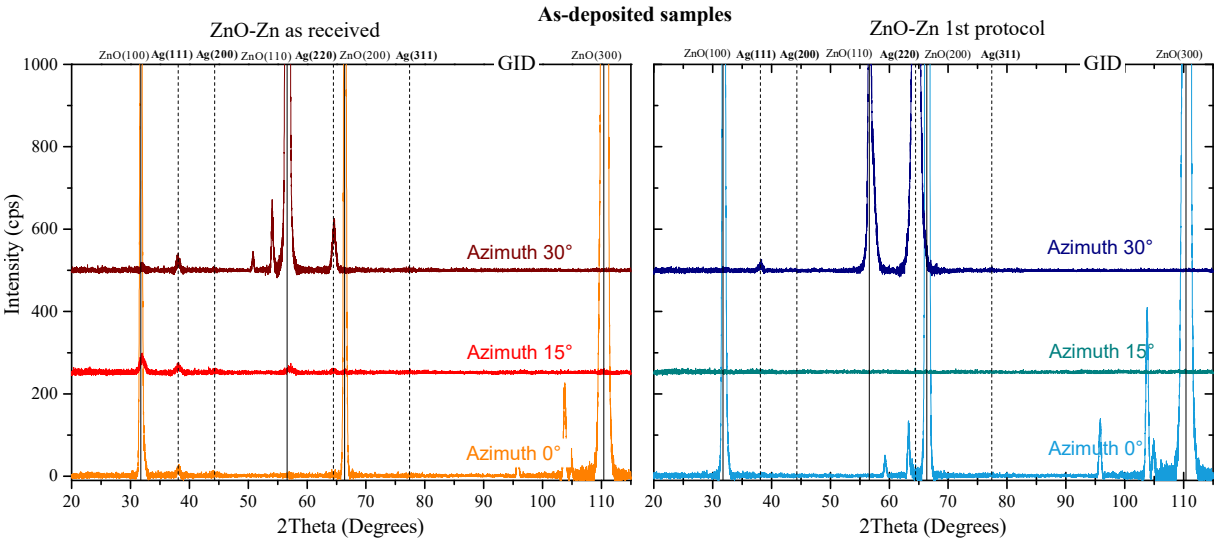

Figure 4.13 Grazing incidence X-ray diffraction of the stacks based on Zn-terminated ZnO single crystals (a) as-received and (b) treated with the first protocol. Each diffractogram corresponds to a different crystal orientation. Starting from the azimuth 0°, which corresponds to the $[100]_{ZnO^*}$ direction of the ZnO substrate, the sample is rotated by +15° and +30° for the following analyses. Peak assignment is given on the top.

The as-received substrate diffractogram shows only a partial texturization (Fig. (4.13)-a) ; a distinct $(2\bar{2}0)$ Ag peak at azimuth 30° is present. Its intensity drastically reduces as the sample is rotated, a sign of texturization. Nevertheless, in each diffractogram, a (111) Ag peak is also always clearly visible. Its intensity, which decreases depending on the sample rotation, suggests, as well, the presence of a preferential in-plane orientation for the corresponding crystallites ; however, as the peak does not extinguish, the texturization can be only be partial. Thus some

grains do not follow the (111) out-of-plane orientation, in agreement with the intensity of the rocking scans that will be discussed later on.
On the other hand, the treated samples, independently of the used protocol, show a better texturized silver layer. An intense $(2\bar{2}0)$ peak is clearly visible only at azimuth 30°. At the same orientation, a small (111) peak is also present at lower angle. The intensity ratio of the two peaks is, for these samples, much higher as compared to as-received samples, underlying the improved texturization of the film. As the sample is rotated, the two peaks disappear. All the coatings based on first protocol of single crystal substrate preparation, regardless of the polar face involved, Zn or O, exhibit a highly biaxial oriented silver film. For the sample prepared with the second protocol, silver presents a slightly lower degree of texture.

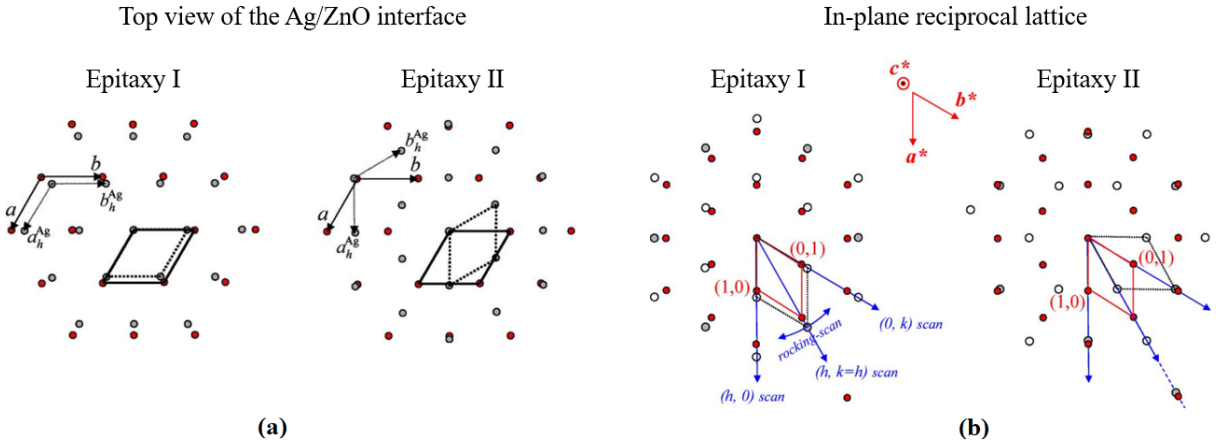

Figure 4.14 (a) Top view of the Ag (111)/ZnO(0001) interface in real space, according to the two most probable azimuthal orientations of the two lattices. The O/Zn atoms are in red and the Ag atoms are in grey. (b) Schematic representations of the two Ag/ZnO epitaxies in the reciprocal space. ZnO Bragg reflections are represented in red, while those of Ag are in light grey. The white points correspond to the Ag anti-Bragg peaks. The epitaxy I describes the hexagon/hexagon orientation with a mismatch of −11 % observed on single crystal based sample. In epitaxy II, Ag grows rotated by 30° with respect to the ZnO substrate leading to a lower mismatch of 2.5 %. From [105, 106].

Based on the orientation of the Ag $(2\bar{2}0)$ Bragg reflection, relative to the $[110]_{ZnO^*}$ substrate direction, one can conclude that the silver thin film grows preferentially with the so-called hexagon/hexagon epitaxy (Epitaxy I in Fig. (4.14)) in agreement with previous findings for evaporated films [105, 106]. In this configuration, the Ag and ZnO lattices are perfectly aligned, resulting in a large mismatch of $f = -11$ %, but with interface coincidence sites expected every $a_{Ag(111)}/|f| \simeq 2.6$ nm. On the contrary, based on the minimization of the epitaxial mismatch, a 30°-rotated orientation would appear more likely because of its lower mismatch of only 2.5 %. This orientation is often assumed in atomistic calculations for the sake of simplicity [95]. But beyond this accidental long-range coincidence lattice [105, 106], the observed hexagon/hexagon epitaxy is more likely due to the tendency of the metallic clusters to nucleate and grow with an alignment of their dense $[1\bar{1}0]$ direction along the polar [100]-oriented step edges of the reconstructed ZnO surface [70]. Governed by the competition between the energy gain, resulting from satisfying the charge compensation rule of polar surfaces (through the creation of surface vacancies or adsorption of foreign adatoms such as H) and the energy loss by breaking Zn-O bonds [69], the ZnO surface annealed in vacuum is indeed characterized by nano-sized triangular and striped shaped features aligned along the [100] direction, which heal the overall polarity of

the surface but exhibit polar step edges terminated by cations or anions [227–229]. This specific surface topography makes the adsorption of silver atoms on step edges thermodynamically more favourable than on flat terrace sites, with a preference for O-terminated ones [70]. Here, a charge is transferred between the metal and the terminal oxygen atoms, giving rise to slightly cationic silver and a partial healing of the step polarity. The binding to Zn-terminated step is, on the other hand, more metallic.

Beside the in-plane orientation, the GIXRD can give information also about the Ag lateral domain size and the microstrain state. Unfortunately, since only peaks of different families are present in the diffractogram, the SSP, HW and WH analysis (Sec. (2.3.5)) performed on the (220) and (111) peaks should be really taken with caution as they assume similar characteristics for grains of different epitaxial orientations which is most likely not the case. Nevertheless, values are reported in Tab. (4.5). All samples, whatever the preparation, give rise to similar values for the lateral domain size (Tab. (4.5)), ranging from 12 to 16 nm, larger than for the reference stacks (6-10 nm ; Tab. (3.3)). Contrary to a polycrystalline seed layer that already involved defective grain boundary zones, a film on a single crystal is expected naively to have a much lower density of grain boundaries and therefore much larger domain sizes. But this picture does not account for the three dimensional growth process. As clusters nucleate in registry with the step edge and grow along them, their respective lattices are initially aligned, but are not in registry due to the mismatch with the substrate. As the clusters touch and coalesce, defective zones, the so-called grain boundaries, should form. At last, it seems that, comparing the various crystal preparations, their density is more controlled by the parameters of the sputtering process than by the state of the substrate (*i.e* the nucleation sites), as the larger domain sizes are observed for as-received samples which present the lower surface quality.

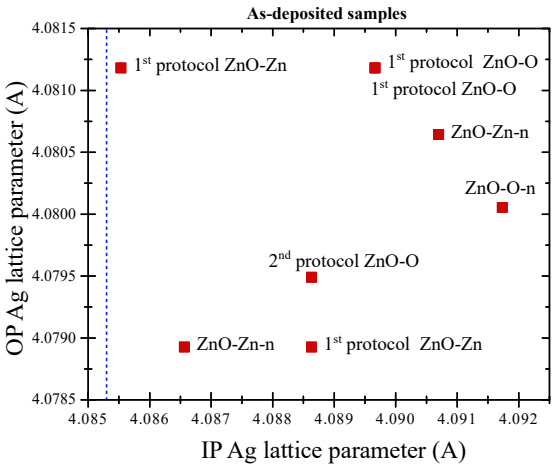

Figure 4.15 Relation between the in-plane and out-of-plane lattice constants (reported in cubic lattice) of the Ag thin films in the different single crystal based samples. The bulk value is $a_{Ag}^{bulk} = 4.085$ Å (blue dashed line).

At the opposite of the out-of-plane direction, which shows a slight decrease of the metal lattice constant, the in-plane lattice parameter is increased following a tetragonal distortion (Fig. (4.15) and Tab. (4.6)). But, even if the sign of the in-plane strain follows the mismatch with the substrate (-11 %), the strain remains very small in both directions (< 0.1 %) as well as the microstrain value (Tab. (4.5)). This agrees with previous X-ray diffraction findings on evaporated films [105] that showed nearly fully relaxed films since the early stage of the island growth despite the large lattice mismatch of the hexagon/hexagon epitaxy. To counterbalance these

conclusions, one should keep in mind that the stress state of the layer could be also influenced by the growth process itself or by the capping layer [108, 198–200].

As-deposited samples							
Out-of-plane							
	Vertical domain size				**Microstrain**		
	D -Scherrer	**SSP**	**H-W**	**W-H**	**SSP**	**H-W**	**W-H**
	nm				-		
ZnO-Zn-n	10	45	45	82	0.006	0.009	0.009
ZnO-O-n	10	10	10	10	0.001	0.001	0.001
ZnO-Zn $1^{st}protocol$	12	13	13	14	0.001	0.002	0.002
ZnO-O $1^{st}protocol$	12	14	14	18	0.002	0.004	0.003
ZnO-O $2^{nd}protocol$	11	12	12	13	0.001	0.002	0.002
AZO·L1	9						
ZnO·M2	9	9	10	7	0.002	0.002	0.003
In-plane							
	Lateral domain size				**Microstrain**		
	D -Scherrer	**SSP**	**H-W**	**W-H**	**SSP**	**H-W**	**W-H**
	nm				-		
ZnO-Zn-n	14	11	9	11	0.002	0.003	0.003
ZnO-O-n	16	10	10	7	0.000	0.005	0.004
ZnO-Zn $1^{st}protocol$	12	12	12	12	0.001	0.001	0.000
ZnO-O $1^{st}protocol$	12	9	9	8	0.002	0.003	0.002
ZnO-O $2^{nd}protocol$	13	12	12	12	0.001	0.001	0.000
AZO·L1	9	9	8	37	0.003	0.002	0.007
ZnO·M2	8	8	5	6	0.002	0.005	0.006

Table 4.5 Vertical and lateral domain sizes as well as the out-of-plane and in-plane microstrain of the different samples based on single crystal substrates. The values were estimated through the Scherrer equation, the Size-Strain, the Halder-Wagner and the Williamson-Hall plot. For the out-of-plane direction, the calculations were based on Ag(111) and Ag(222) diffraction peaks, while for the in-plane orientation Ag(111) and Ag(220) were used. Due to the absence of several peaks of the same family, the in-plane data calculated by S-S, W-H and H-W should be considered with caution. ZnO-n means as received and L1/M1 correspond to LINA/MISSTIC prototype references.

4.5 Quantification of the texture from transverse scans

Although all samples show a clear biaxial texture, the degree of texturization is not the same for all of them. The poorer crystallinity as judged from peak intensity in the diffraction scan was achieved for the as-received substrates (Fig. (4.12) and Fig. (4.13)) ; in parallel, they indeed present the highest width in transverse scans *i.e.* rocking and ϕ-scans (Fig. (4.16) and Tab. (4.6)).

Unfortunately not all the diffraction peaks of Ag were recorded in rocking curve or ϕ-scan; so it is not always possible to distinguish between the finite grain size and mosaicity broadening. Nevertheless, considering that all single crystal samples have similar in-plane domain sizes, the observed width is still indicative of the mosaicity but with an offset. From the reduced value of the FWHM$_\Phi$, 5° lower than for the as-received samples not speaking about reference stacks (Tab. (3.3)), it is clear that the use of a single crystal and its surface treatment has a strong positive impact on the in-plane mosaicity. In addition to the ϕ-scan, the in-plane texture was also evaluated through the texture coefficient of the Ag (220) peak, an additional proof of the lower mosaicity of the treated samples (see Tab. (4.6)). In line with the previous results obtained for the different surface preparation protocols, the first one shows the best texture and mosaicity in both directions among the single crystal based samples, with the best results obtained for ZnO-O terminated based sample. This result highlights once again the importance that the quality of the substrate surface can have on the structural properties of Ag film.
Along the out-of-plane direction, all single crystal based samples present well better textured silver films than the LINA and MISSTIC glass-based references, where a silver film of equal thickness was grown on a polycrystalline AZO and ZnO seed layer (Tab. (4.6)). In addition, in each case, the reference samples do not have in-plane texture at all.

As-deposited samples								
		Ref		**As-received**		**Treated single crystals**		
						1^{st} protocol		2^{nd} protocol
		L1	**M2**	**ZnO-Zn**	**ZnO-O**	**ZnO-Zn**	**ZnO-O**	**ZnO-O**
RC$_{Ag(111)}$	[°]	17.79	16.92	5.03	5.81	2.39	1.81	3.31
Mosaicity	[°]	-	-	-	-	2.29	1.15	2.43
$\boldsymbol{\varepsilon_{33}}$	$(\cdot\mathbf{10}^3)$	0.31	0.82	0.31	1.57	0.82	1.07	0.82
$\boldsymbol{a_{OP-Ag}}$	[Å]	4.09	4.09	4.09	4.09	4.09	4.09	4.09
L$_{RC,IP}$	[nm]	-	-	-	-	21	9	6
$\boldsymbol{\phi_{Ag(220)}}$	[°]	*non textured*		9.63	9.21	3.66	3.24	4.51
TC$_{Ag(220)}$	[%]	29	21	69	80	99	99	95
$\boldsymbol{\varepsilon_{11} = \varepsilon_{22}}$	$(\cdot\mathbf{10}^3)$	-1.28	- 0.69	-1.56	-1.28	-1.56	-1.01	-1.42
$\boldsymbol{a_{IP-Ag}}$	[Å]	4.08	4.08	4.08	4.08	4.08	4.08	4.08

Table 4.6 Structural data of the single crystal based samples and references (L1/M1) corresponding to the LINA AZO·L1 and MISSTIC ZnO·M2 samples. Lateral domain size as well as the mosaicity were derived from the corresponding rocking curve peak broadening. The texture coefficient (TC) was determined from the GIXRD peaks.

4.6 Texture and epitaxy as seen from pole figures

The pole figures of the single crystal based samples clearly demonstrate the biaxial texture of the Ag film (Fig. (4.17) and Fig. (4.18)). Compared to the prototype reference stacks which show a typical fibre texture (Fig. (3.6)), the pole figure of the Ag (111) diffraction peak is characterized by a central feature, which corresponds to the (111) out-of-plane orientation, and three peaks observed in the stereographic projection corresponding to $(\bar{1}11)$, $(1\bar{1}1)$ and $(11\bar{1})$ planes. Considering the hexagonal symmetry of the substrate, and the silver ABC or BCA stacking sequence along the [111] direction [230], an equivalent set of peaks is observed upon a rotation of 180° leading to the 6-fold symmetry of the pattern of Fig. (4.17). The intensity of the features is also correlated to the crystallinity and texture degree of each sample. For the

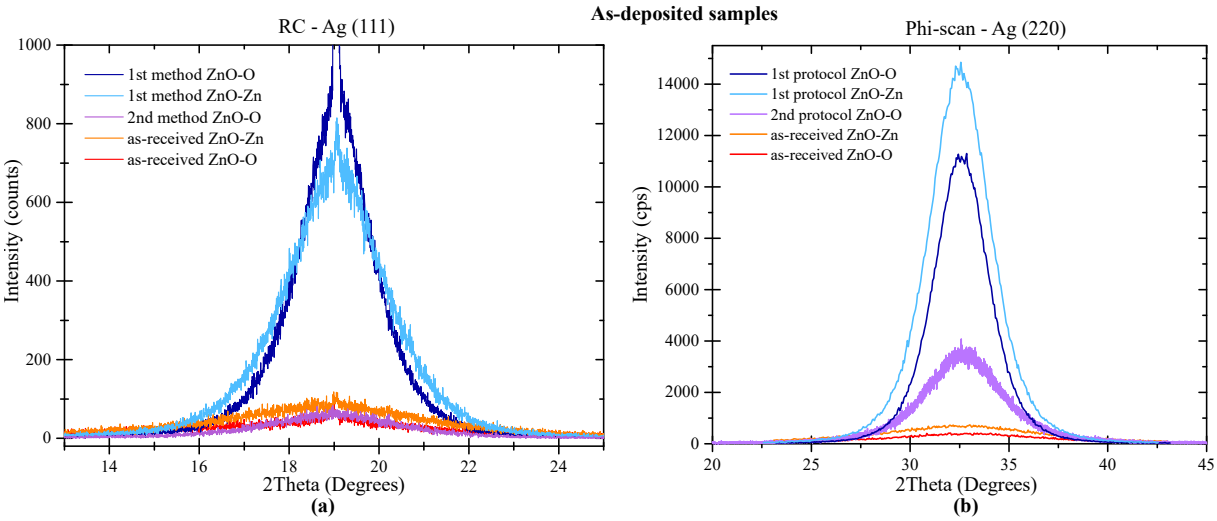

Figure 4.16 (a) Ag (111) rocking curves of different single-crystal based samples. (b) The same for Ag (220) ϕ-scan.

as-received single crystal based sample, which showed only a partial in-plane orientation of the grains, peaks are less intense, broader and accompanied by a ring-shaped feature, typical of the in-plane random orientation as previously pointed out by grazing incidence diffraction. On the contrary, treated samples show a 6-fold pattern in agreement with their outstanding crystalline quality. The comparison with the pole figure of ZnO(101) (Fig. (4.18)) confirm the previous finding of a hexagon/hexagon epitaxy, *i.e.* Ag(111)[1$\bar{1}$0]//ZnO(0001[100] (Fig. (4.14)).

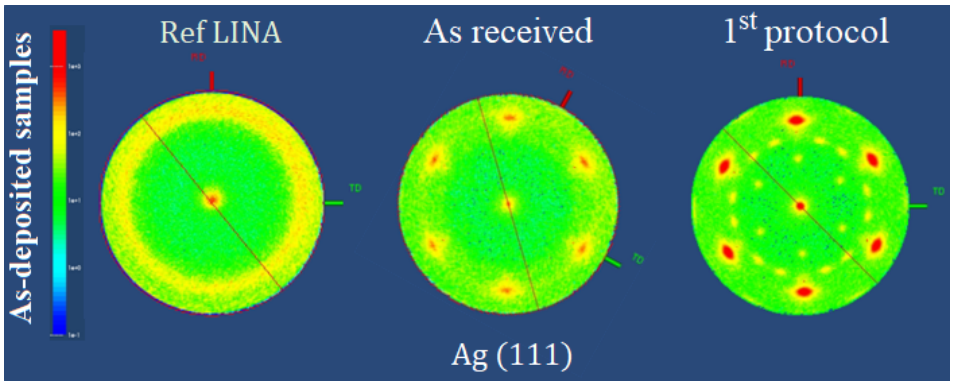

Figure 4.17 Ag(111) pole figures of the LINA reference and of ZnO-O as received and treated via 1st protocol samples.

In addition to the silver diffraction peaks, few "ghost" spots (marked in yellow in Fig. (4.18)) are present ; some correspond to flanks peaks of the substrate. Indeed, due to the low 2θ resolution used in the PF ($\pm 0.25°$), the peaks of the substrate and silver can overlap on the same pattern, as in the case of the Ag(111) central peak in the ZnO(101) PF pattern. The substrate peaks can be even more persistent, even if their diffraction angle is several degrees from the detector. With the low angular resolution used, these very narrow peaks manifest themselves as a Dirac, characterized by a strongly lit pixels.
Nevertheless, in some cases, the origin of the additional features remains unknown. Observed in the Ag(111) and Ag(200) PF patterns, they did not present a characteristic Dirac profile and their angle (φ,χ,2θ) positions could not be traced back to any known substrate peak. No

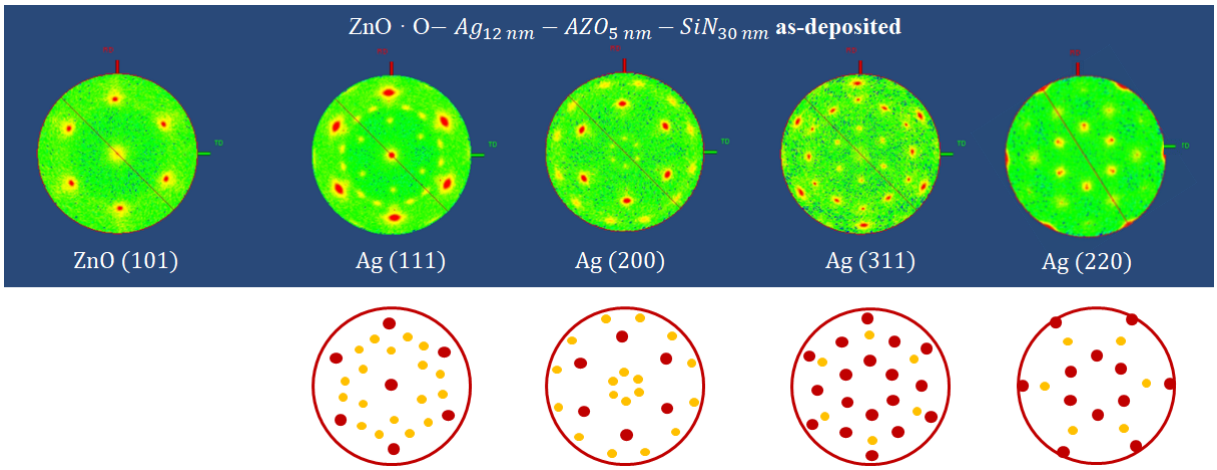

Figure 4.18 Pole figures (PF) of the Ag thin films grown on a ZnO substrate treated via 2^{nd} protocol. (Top) measured PF. (Bottom) corresponding simulated PF for an hexagon/hexagon epitaxy. The red dots correspond to the simulated Ag diffraction peaks, while the yellow dots added *a posteriori* to guide the eye and to highlight the peaks that are not predicted by the hexagon/hexagon epitaxy. They correspond to ZnO-single crystal flanks peaks with close diffraction angles or a minor Ag orientation that has not yet been identified.

solution could even be found for a variant of Ag texture, able to modify only the Ag(111) and Ag(200) pattern, leaving the Ag(220) and Ag(311) invariant. Moreover, the differences of inclination between the spots in the same figure do not correspond to the canonical angles of a cubic lattice. The last remark is also valid if considering the existence of another cubic compound, such as Ag_2O. One can certainly find spots which have a proximity in 2θ with those used, but the arrangement of the spots does not fit with that of a cubic lattice in particular with $Ag_2O(111)$. An hexagonal or trigonal structure is more likely, since the observed spots with azimuths ± 19 and $14°$ respectively are characteristic of the reciprocal rows $[210]^*$ and $[310]^*$ in hexagonal lattice, that possibly could be associated to more complex Ag_xO structures.

4.7 Room-temperature resistivity of single crystal based stacks

As explained in the previous chapters (Sec. (1.5)), the electrical properties of a film are directly related to its microstructure. The two main phenomena that contribute to resistivity through an increase of the path length of electrons are the scattering at the interfaces and at the grain boundaries. This means that a variation in surface roughness, grain size, mosaicity, intra-grain impurity/defect content etc. can cause an important variation in the resistivity of a metal film.

The sheet resistance of each single crystal-based coating was determined through a 4-points probe method at room temperature, the same equipment used for samples of Ch. (3), and compared to the reference glass-based samples (Tab. (4.7)). The use of a single crystal as a substrate has a clear impact on the sample resistivity. For all the samples, as-received and treated, an increase of conductivity is observed, with a gain with respect to the glass references ranging from 10% to 35%. In agreement with the structural characterizations (see Tab. (4.6)), the samples showing the lowest resistivities are the ones with the best silver texturization. The ZnO-O treated with the first protocol, with a mosaicity of $1.15°$ and a $\phi_{Ag(220)}$ width of $3.24°$, exhibits a resistivity of 3.92 $\mu\Omega$.cm, while the ZnO-O treated with the second protocol, with a mosaicity

of 2.43° and a $\phi_{Ag(220)}$ width of 4.51°, shows a resistivity of 4.39 $\mu\Omega$.cm. Nevertheless, despite their poorer silver quality with respect to O-terminated samples, Zn-terminated samples correspond to the lower resistivity values, with the ZnO-Zn sample, prepared via the first protocol, exhibiting the highest conductivity. Its resistance is one of the best ever measured for a full stack before annealing during this study. Regarding the second protocol of sample preparation, the improvement in conductivity is less obvious as it was for the structural properties. The high value of the substrate surface roughness as well as the poor out-of-plane texturization of the silver film could be the main reason of the worsening of its electrical properties. Nevertheless, the global comparison between the sheet resistance values of the as-received samples and of the treated samples clearly prove the interest of the surface treatment.

As-deposited samples								
		Ref		**As-received**		**Treated single crystals**		
						1^{st} protocol		2^{nd} protocol
		L1	**M2**	**ZnO-Zn**	**ZnO-O**	**ZnO-Zn**	**ZnO-O**	**ZnO-O**
$\mathbf{R}_{\square-4P}$	**[Ω/sq]**	4.62	4.87	4.08	4.13	3.15	3.27	3.66
ρ_{4P}	**[$\mu\Omega$.cm]**	5.54	5.84	4.90	4.96	3.78	3.92	4.39

Table 4.7 Sheet resistance and resistivity measured through a 4-points method at room temperature, of samples on single crystals compared to those of reference coatings on glass. L1/M2 correspond to LINA AZO·L1 and MISSTIC ZnO·M2 prototype references.

4.8 Correlation between resistivity and structural characteristics : the role of grain boundary angle

As done for reference samples (Sec. (3.2)), to unravel the most relevant structural parameters, potential correlations between room-temperature resistivity and film characteristics derived from X-ray analyses have been sought for (Fig. (4.19)). The similar film thickness and domain size in all samples offer an interesting opportunity to check the role of other structural parameters beyond the expected obvious dependence of resistivity on thickness and on grain boundary area density that scales only with the inverse of the square of the grain size. The apparent correlation seen in (Fig. (4.19)-d) is within the error bars of the lateral domain size determination and therefore not significant. However, a correlation does exist between resistivity and the FWHM of the silver (111) rocking curve and peak area in θ-2θ (Fig. (4.19)-a,e). The reason lies in the role of the vertical mosaicity that scales with the rocking curve width. A similar correlation appears with the FWHM of ϕ-scan of the in-plane (220) silver peak and its area (Fig. (4.19)-b,f). This roots into to a reduced in-plane mosaicity and misalignment of grains, or in other words a better in-plane texture. This correlation is also revealed via the texture coefficient of the (220) peak (Fig. (4.19)-c)). Not clearly evidenced in the case of reference samples (Fig. (3.15)-b), these findings highlight the importance that the mosaicity has on the electrical properties of a film.

In general, grain boundaries can be classified in two categories depending on the misorientation between the adjacent grains : (i) small angle up to 15° for which a description with a stack of dislocations is valid and (ii) large angle, the latter being more complex and disordered. As one would expect, the reflection coefficient R and therefore the sample resistivity scales with this grain boundary tilt angle. Indeed, Fig. (4.20) reports the theoretical variation of a silver film resistivity as a function of the tilt grain boundary angle θ [35, 231]. The calculation is based

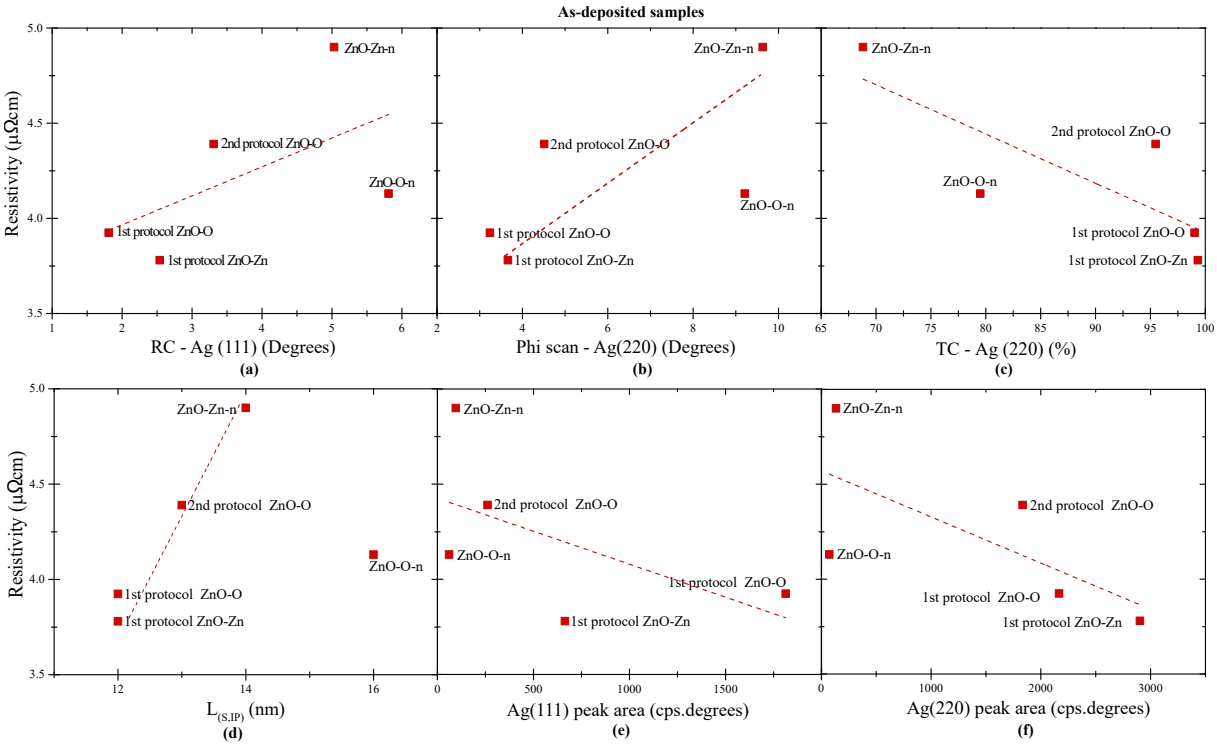

Figure 4.19 Room-temperature resistivity of the single crystal based samples as a function of the metal film characteristics : (a) the (111) rocking curve width, (b) the (220) ϕ-scan width, (c) the (220) texture coefficient, (d) the lateral domain size, (e) the Ag(111) peak area and (f) the Ag (220) peak area. Lines are only guides for the eyes.

on simple geometric considerations, starting by defining the specific grain boundary resistivity as [231] :

$$\gamma = \frac{\rho_{GB}}{S_v}, \tag{4.1}$$

where ρ_{GB} is the resistivity created by grain boundaries and $S_v = \frac{2}{D_L}$ is the total grain boundary angle per unit of volume, if the film is composed of consequential cylindrical grains of a diameter D_L corresponding to the lateral grain size. When the electrical transport is perpendicular to the grain boundary, ρ_{GB} can be expressed as :

$$\rho_{GB} = \frac{4\hbar\Omega_0}{e^2 n} S_v \frac{1}{D}, \tag{4.2}$$

where $\hbar$ is the Planck constant divided by 2π, Ω_0 the primitive unit cell volume (16.9 Å^3 for Ag), e the elementary charge, n the number of charge carriers per primitive unit cell (1 for Ag) and D the spacing between dislocations. For small tilt angle, D is determined by the product of the burger vector $\vec{b} = \frac{a}{2}\langle 110\rangle$ and the grain boundary tilt angle θ. Based on this model, the resistivity of silver film indeed increases linearly θ (Fig. (4.20)) up to values in the range of 1.5 $\mu\Omega$.cm for the typical grain sizes encountered up to now in our study (∼12 nm). On the other hand, calculations for large angle grain boundaries estimate the resistivity of a thin film of about 10 nm to about 6.6 $\mu\Omega$.cm [35], a value close to the more resistive samples of this study. According to these calculations, the hierarchy of resistivity between samples and of R-factor could be justified by a different concentration of large angle grain boundaries.

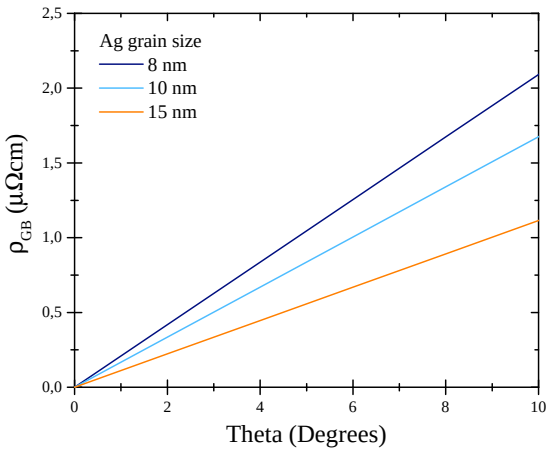

Figure 4.20 Theoretical resistivity of silver thin films as a function of the tilt angle between grains based on the Eq. (4.2) [35, 231]. For large angle grain boundaries, the resistivity increases up to 6 $\mu\Omega$.cm.

The measured resistivity were also plotted in Fig. (4.21) versus the roughness of the single crystal determined by AFM, that of the Ag film obtained by XRR and the corresponding values extracted from the Soffer model (see below Sec. (4.9)). Unfortunately, it is difficult to observe a clear trend.

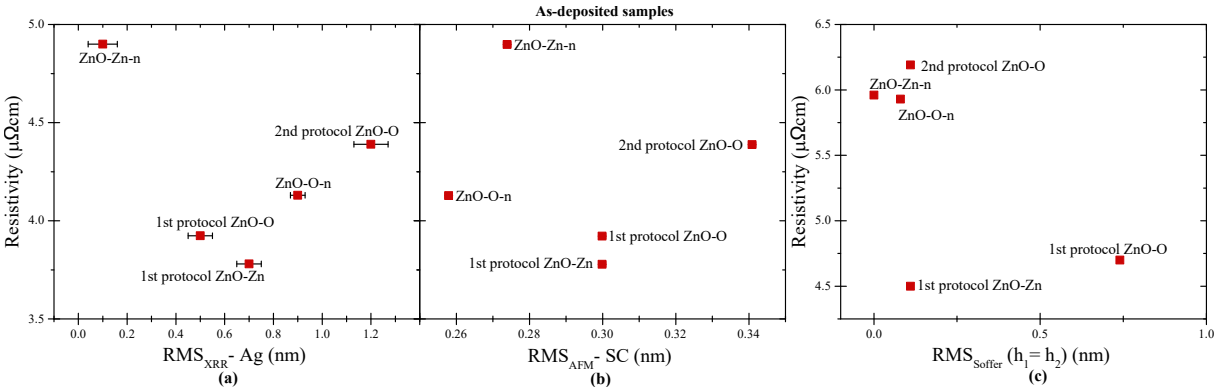

Figure 4.21 Influence of roughness on room-temperature film resistivity determined through the 4-points method, (a) and (b), and by temperature dependent measurements (c). The roughnesses were determined through (a) XRR for Ag film (b), by AFM for ZnO single crystal (SC) or through the resistivity fit with the Soffer model.

4.9 Resistivity versus temperature : R and p coefficients

To further explore the transport behaviour of all samples, the resistivity of each stack was measured as function of temperature (Fig. (4.22)). The fit values of these measurements, based on the three resistivity models, the Mayadas-Shatzkes [127], the Sambles [142] and the Soffer [149], are summarized in Tab. (4.9).

The resistivity curves, reported in Fig. (4.22), follow the classical linear behaviour with temperature for a metal due to phonon scattering [232]. This phonon contribution to resistivity shown in Fig. (4.22)-b presents clear differences among the individual samples, all of them exhibiting a higher value than the bulk of silver [93], with the strongest deviations observed for treated samples. Beyond this contribution, samples can be classified accordingly to their residual resistivity at 0 K ($\rho_{res}(T = 0K)$), the lowest values being achieved for ZnO samples treated with the first protocol. Focusing on the line shape of resistivity, the curve for the ZnO-O sample prepared following the first protocol presents an obvious concavity, typically associated with a resistivity dominated by interface scattering, and described by the Fuchs-Sondheimer model [125]. Therefore, a more pronounced interface scattering contribution is expected with this sample than in any other ones. This could indicate a rougher ZnO-O/Ag interface. The other single-crystal samples present only a weak concavity, comparable to the line shape of the glass references (Fig. (4.23)).

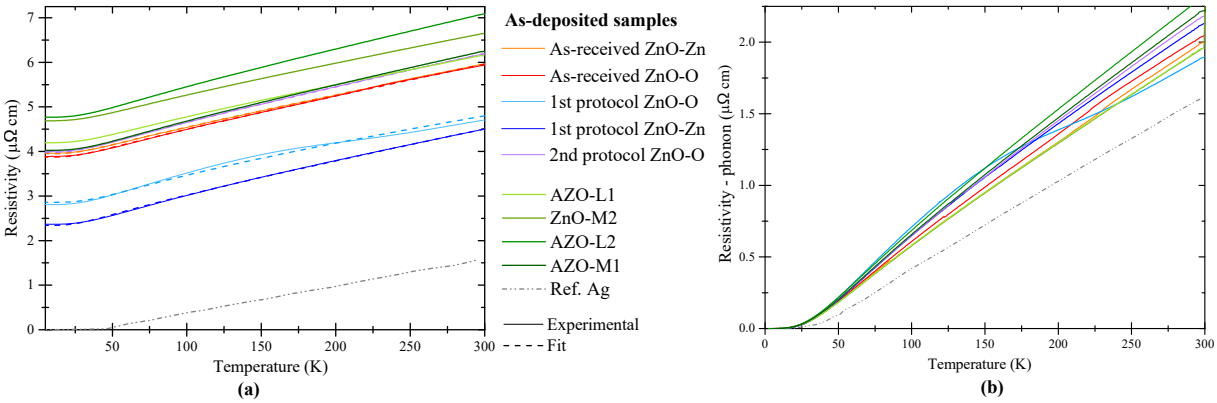

Figure 4.22 (a) Resistivity of single crystal based samples as a function of temperature compared to LINA/MISSTIC glass-based references and to bulk silver [93]. The experimental data are represented by continuous curves and the simulations with the three different resistivity models (Mayadas- Shatzkes, Sambles and Soffer) by dashed lines. Fits parameters are reported in the Tab. (4.9). (b) Corresponding temperature dependent contribution $\rho_{ph}(T) = \rho(T) - \rho_{res}(T = 0K)$.

Following the same procedure as in Sec. (3.3.1), the modelling of the data was carried out by fixing (i) the grain size (distance D between grain boundaries in the resistivity models) to lateral domain size $D = L_{GB}$ as obtained by grazing diffraction and (ii) the film thickness d to that determined by reflectivity analyses (Tab. (4.5)). The remaining parameters (p, R, Θ_D, h) were left free to vary. Typical fits are shown as dotted lines in Fig. (4.22). Regarding ρ_{res}^{grain}, *i.e.* the intra-grain resistivity at $T = 0$ K, the value was estimated through the linear room-temperature thickness dependence (Fig. (4.24)) of the Fuchs-Sondheimer and Mayadas-Shatzkes models (Eq. (1.31) and Eq. (1.35); see Sec. (3.3.1)). ρ_{res}^{grain} is obtained by subtracting to the slope the room-temperature resistivity of a perfect crystal ($\rho_{bulk}(T = 300K) = 1.62\,\mu\Omega$.cm). It is worth reminding that, for an accurate result, the application of the linear fit is limited to thick Ag films ($d \geqslant l_0$) and assumes $D \propto d$ for the grain boundary scattering contribution (Eq. (1.31) and Eq. (1.35)). When used on thinner films, the value can lead to a overestimation of the actual value. Nevertheless, in the case of single crystal based stacks for which the explored thickness range is small (Fig. (4.22)-b), the obtained value of $\rho_{res}^{grain} = 0.52\,\mu\Omega$.cm is in line with the estimation obtained for thicker LINA and MISSTIC samples (0.65 and $0.69\,\mu\Omega$.cm; Fig. (3.23)). Considering that the same sputtering conditions were used for the deposition of

single crystal coatings and of the reference MISSTIC, the estimated value is considered reliable.

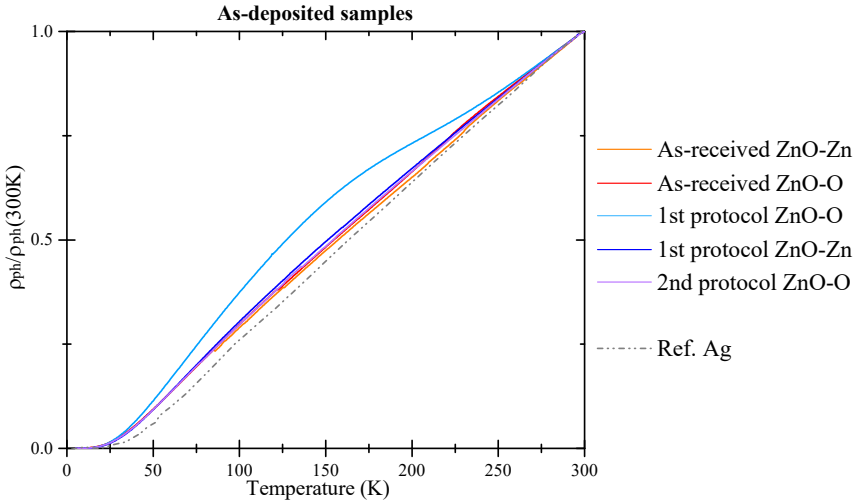

Figure 4.23 Normalized phonon contribution of the resistivity $\rho_{ph}(T)/\rho_{ph}(T = 295K)$ as a function of temperature for the single crystal based samples. The same curves for glass-based stacks L1 and M2 and for silver bulk [93] are added for comparison.

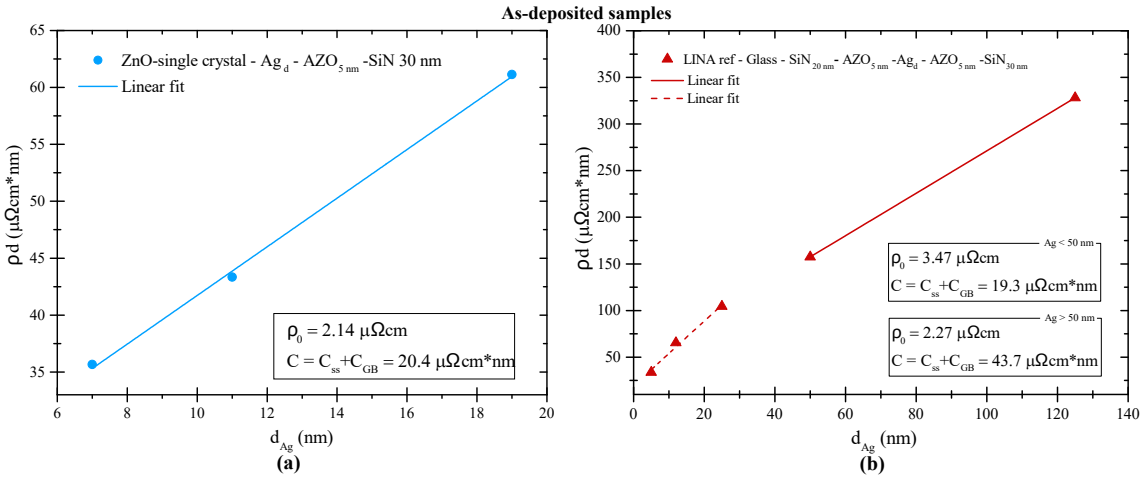

Figure 4.24 Room-temperature resistivity times the film thickness as a function of the silver film thickness for (a) single crystal based ZnO-Zn samples and (b) the LINA references.

To corroborate the hypothesis and estimate the potential error due to the ρ_{res}^{grain} choice, the fit based on the three resistivity models was repeated considering different values : 0.00 $\mu\Omega$.cm (the residual resistivity of silver bulk), 0.25 $\mu\Omega$.cm, 0.52 $\mu\Omega$.cm (the residual resistivity calculated for single crystal samples), 0.65 $\mu\Omega$.cm (the residual resistivity associated to the LINA samples) and 1.05 $\mu\Omega$.cm. The sample *ZnO-Zn* 1^{st} *protocol* was used as example (Tab. (4.8)). Slight variations in the estimated parameters are observed for the tested models ; the R-parameter is the most affected in a range of 0.1 while the impact on the p-parameter, the Debye temperature and the interface roughnesses is negligible. Thus the uncertainty on the estimate of ρ_{res}^{grain} from the linear fit will not drastically affect the interpretation of the data.

All fit results are gathered in Tab. (4.9). For all the analysed single crystal samples, a good agreement is observed between the parameters obtained with the different resistivity models. Negligible variations are observed for the R, p-coefficients and more significant ones for Θ_D determined through the Soffer theory, which is considered to be the most physically reliable model because of its relation with surface roughness. The case of the *ZnO-O* 1^{st} *protocol* sample is special. A direct demonstration is provided by the fit of its resistivity curve (Fig. (4.25)). Probably due to the strong concave shape of the curve, the fit quality turned out to be very poor. Since the concavity of a resistivity curve in temperature is strongly related to the residual resistivity value (Fig. (1.27)), in an attempt to improve the fit, the Mayadas-Shatkes and the Soffer models were run with various ρ_{res}^{grain} values as reported in Fig. (4.25). Although an accurate result could not be obtained, the best fit was found for the Soffer model with $\rho_{res}^{grain} = 0.52\,\mu\Omega$.cm.

As-deposited
ZnO-Zn 1^{st} protocol

ρ_{res}^{grain} [$\mu\Omega$.cm]	*Mayadas-Shatzkes model*			*Soffer model*			
	R	p	Θ_D [K]	R	h_1	h_2	Θ_D [K]
0.00	0.10	0.48	161	0.12	0.10	0.10	193
0.25	0.08	0.47	161	0.10	0.11	0.11	193
0.52	0.05	0.45	160	0.06	0.11	0.11	192
0.65	0.03	0.44	160	0.05	0.11	0.11	192
1.05	0.00	0.48	156	0.05	0.11	0.11	192

Table 4.8 Scattering parameters R, p and Debye temperature Θ_D obtained by fitting the resisitivity curve of the *ZnO-Zn* 1^{st} *protocol* sample through the Mayadas-Shatzkes and the Samble models. The intra-grain resistivity value ρ_{res}^{grain} has been changed to observe its influence on the other fitted parameters.

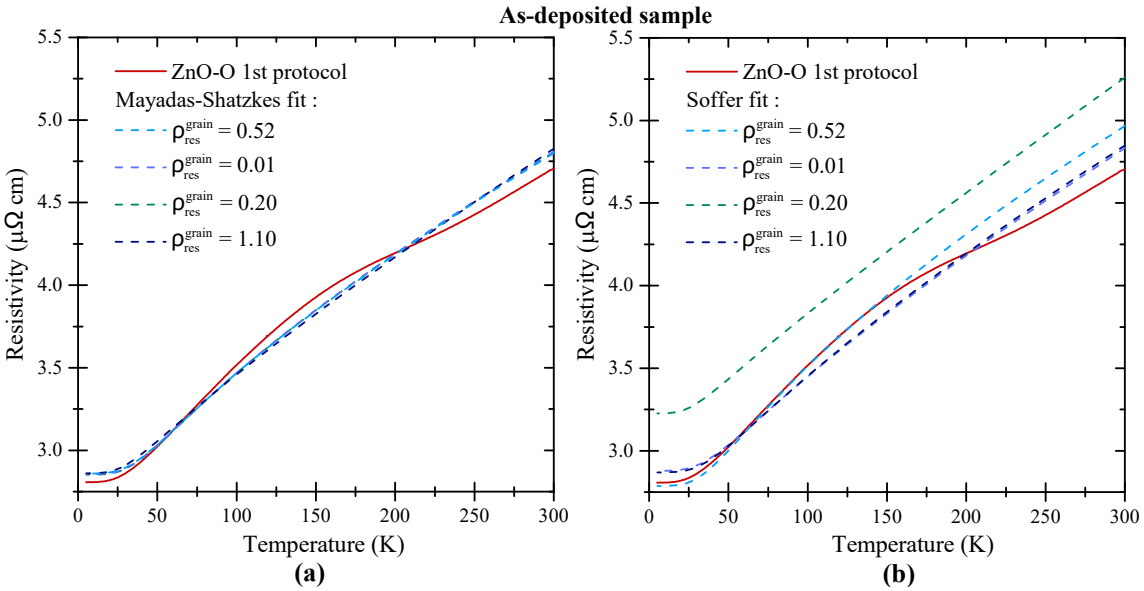

Figure 4.25 Mayadas-Shatzkes and Soffer simulations of the temperature dependent resistivity of the *ZnO-O* 1^{st} *protocol* sample. The fit was run at different ρ_{res}^{grain} values.

Diffraction analyses showed pretty similar in-plane grain size for all the single crystal based

samples (Tab. (4.5)). Therefore, their resistivity behaviours should not differ by the density of grain boundaries but much more by their distributions of grain boundary angles that reflect in the R-parameter. Putting aside the *ZnO-O* 1^{st} *protocol* sample, one can identify two types of behaviours in the fit results (Tab. (4.9)), that of the as-received and that of the treated single crystal samples.

The as-received samples (*ZnO-Zn-n* and *ZnO-O-n*) are characterized by p-coefficients close to one and R-parameters of the order of $\sim$0.30. This implies that only a very small fraction of electrons is scattered out of the specular direction at the interfaces and that the grain boundary scattering mechanism represents the main contribution to the silver resistivity. This behaviour reflects in the low interface roughnesses estimated through the Soffer model that are, however, in contrast with the previous topographical analysis of the single crystal surface (Sec. (4.2)). It should be noted that the more resistive samples are not associated with the rougher interfaces. According to the Sambles model, the *ZnO-Zn-n* sample presents also a slight asymmetry between the two silver interfaces. In fact, the coefficients p and R, obtained for the as-received single crystal based samples do not differ much from the AZO-based LINA and MISSTIC references, L2 and M2. In accordance with their raw temperature dependent resistivity curves (Fig. (4.22)), the scattering behaviour of the references is very similar to the more resistive as-received single crystal based samples, both being characterized by a resistivity governed by electron reflected at the grain boundaries.

Compared to the as-received substrates, the R and p coefficients of the 1^{st} *protocol* samples drop to values close to zero. This means that grain boundaries are nearly transparent to electrons and the resistivity is entirely driven by electron scattering at interfaces. This sizeable decrease of R is likely due to the strong improvement of the in-plane texture of the film that parallels the reduction of detrimental high angle grain boundaries. Note that the excessive roughness values obtained by the fit for *ZnO-O* 1^{st} *protocol* sample can be the result of an inaccurate fit (see Fig. (4.25)). At last, the 2^{nd} *protocol* samples, with topographical and structural characteristics in between the as-received and the 1^{st} *protocol* samples, present a R/p characteristics in between the two groups. Characterized by an interface scattering probability comparable to the 1^{st} *protocol* but a higher R-parameter denoting an higher concentration of large angle grain boundaries, its R/p values are comparable to the glass-based references L1 and M2.

Sample	ρ_{4P} [$\mu\Omega$**.cm**]	ρ_{300K} [$\mu\Omega$**.cm**]	ρ_{res}^{grain} [$\mu\Omega$**.cm**]	**R**	$\mathbf{p}_1$	$\mathbf{p}_2$	Θ_D [**K**]	$\mathbf{h}_1$ [**nm**]	$\mathbf{h}_2$ [**nm**]
As-deposited samples									
ZnO-Zn-n									
Mayadas-Shatzkes				0.30	1.00		161		
Sambles	4.90	5.96	0.52	0.29	0.96	1.00	161		
Soffer				0.30			161	0.00	0.00
ZnO-O-n									
Mayadas-Shatzkes				0.29	0.84		156		
Sambles	4.96	5.93	0.52	0.29	0.84	0.84	156		
Soffer				0.24			174	0.08	0.08
ZnO-Zn-1st pt									
Mayadas-Shatzkes				0.05	0.45		160		
Sambles	3.78	4.50	0.52	0.05	0.45	0.45	160		
Soffer				0.06			192	0.11	0.11
ZnO-O-1st pt									
Mayadas-Shatzkes				0.00	0.06		215		
Sambles	3.92	4.70	0.52	0.00	0.06	0.06	215		
Soffer				0.01			215	0.74	0.74
ZnO-O-2nd pt									
Mayadas-Shatzkes				0.21	0.54		149		
Sambles	4.39	6.19	0.52	0.21	0.54	0.54	149		
Soffer				0.19			169	0.11	0.11
AZO·L1									
Mayadas-Shatzkes				0.12	0.35		170		
Sambles	5.54	6.15	0.65	0.12	0.35	0.35	170		
Soffer				0.17			178	0.08	0.06
AZO·L2									
Mayadas-Shatzkes				0.23	0.89		138		
Sambles	5.12	7.08	0.65	0.23	0.89	0.89	138		
Soffer				0.18			153	0.09	0.09
AZO·M1									
Mayadas-Shatzkes				0.18	0.79		144		
Sambles	5.34	6.25	0.69	0.18	0.79	0.79	144		
Soffer				0.13			164	0.10	0.10
ZnO·M2									
Mayadas-Shatzkes				0.16	0.49		167		
Sambles	5.84	6.96	0.69	0.16	0.49	0.49	167		
Soffer				0.18			178	0.08	0.08
Ag		1.62					215		

Table 4.9 Parameters obtained by fitting the resistivity in temperature of the as-deposited single crystal based samples with three different models : Mayadas-Shatzkes, Sambles and Soffer. The estimated error bars are of the order of $\Delta p \simeq \pm 0.02$, $\Delta R \simeq \pm 0.05$, $\Delta\Theta_D \simeq \pm 5$ K and $\Delta h_1 = \Delta h_2 \simeq \pm 0.02$ nm. AZO·L1/AZO·L2/AZO·M1/ZnO·M2 correspond to LINA/MISSTIC prototype references previously introduced (Ch. (3)). Both room-temperature resistivities determined measured via *Napson* (ρ_{4P}) and via temperature dependent set ups (ρ_{300K}) are reported are reported.

4.10 The impact of annealing on single crystal based stacks

The topographic, structural and electrical studies performed on the single crystal based stacks proved that the first protocol of preparation was the most effective to obtain a high quality silver thin film with the lowest resistivity. This surface treatment was selected therefore for all the annealing studies. On the other hand, due to the contrasted results obtained with the second protocol, this preparation process was shelved.

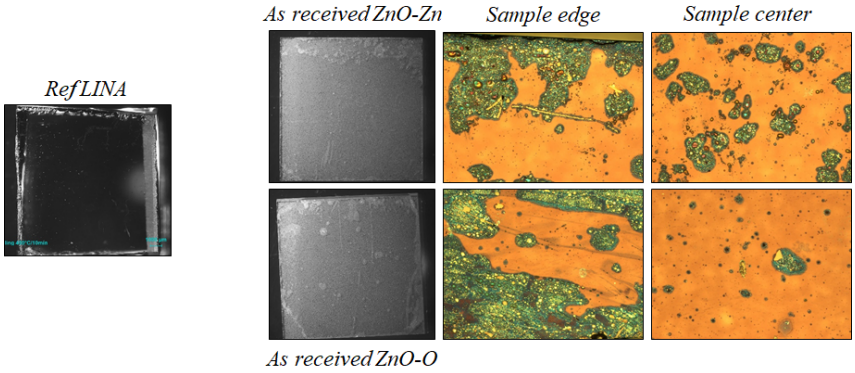

Figure 4.26 Optical image of the LINA reference and of the single crystal based stacks after annealing at 450°C for 10 min. The coatings on the single crystal samples show clear signs of corrosion/dewetting.

		Ref		As received		Treated	
ρ_{4P}		**L1**	**M2**	**ZnO-Zn**	**ZnO-O**	**ZnO-Zn**	**ZnO-O**
As-deposited	[$\mu\Omega$.**cm**]	5.54	5.84	4.90	4.96	3.78	3.92
After annealing *450°C – 10 min*	[$\mu\Omega$.**cm**]	4.32	-	3.95	4.17	-	-
Gain	[%]	22	-	19	16	-	-
After annealing *350°C – 10 min*	[$\mu\Omega$.**cm**]	4.75	5.58		-	3.08	3.07
Gain	[%]	14	5	-	-	18	22

Table 4.10 Resistivities of the single crystal samples before and after annealing compared to AZO·L1 (L1) and ZnO·M2 (M2) LINA/MISSTIC prototype references.

To enhance the structural and electrical properties of the coatings, a thermal treatment was applied. Despite all the benefits this process brings, an inadequate thermal treatment can also have a detrimental impact. Thermodynamically due to its poor adhesion energy on oxide, silver is prone to dewetting if excessively heated leading to grain coagulation, even discontinuous layer and therefore a drastic increase of resistivity (Fig. (4.26)). The role of diffusing species, in particular oxygen from the adjacent layer and/or the atmosphere [195], seems to be of paramount importance in this process. In the worst case, an abrupt increase of internal stress in the whole stack can lead to delamination. Typically, glass coatings are annealed in air at 650°C for 10 min. This temperature induces in large (at least (5×5) cm^2 in size) prototype industrial samples a resistivity gain between 20-30 %. Due to the specificity of our sample (size (1 × 1) cm^2 ; single crystals), the impact of annealing was tested gradually on a prototype reference stack (Tab. (4.10)). The sample was first heated at 300°C for 10 min before increasing the temperature up to 350°C while monitoring every 10 min its resistivity. The maximum gain of 14 % was achieved after 20 min of annealing at 350°C. Then the temperature was raised by step of 100°C

until 550°C where the first signs of dewetting were observed. Above 650°C, the resistivity gain decreased to 15 % and the dewetting became visible on the whole sample surface.

The annealing process was then tested on stacks on as-received single-crystals (Fig. (4.26)). The resistivity gain dropped between 19-16%, due to the appearance at 450°C of evident signs of dewetting. Therefore, the treatment of all other samples was limited to 10 min in air at 350°C. Despite this sizeable reduction of temperature compared to prototype samples, a similar gain in resistivity could be achieved (Tab. (4.10)).

		As received		**1stprotocol**				***Annealed*** **References**	
		ZnO-O	***Annealed***	**ZnO-Zn**	***Annealed***	**ZnO-O**	***Annealed***	**AZO·L1**	**ZnO·M2**
RC$_{Ag(111)}$	[°]	5.81	**2.31**	2.39	**2.04**	1.81	**1.42**	**15.25**	**14.60**
Mosaicity	[°]	-	**-**	2.29	**1.90**	1.15	**0.81**	**-**	**-**
ε_{OP}		0.001	**0.002**	0.002	**0.002**	0.004	**0.003**	**-**	**-**
ε_{33}	**(·10^3)**	1.57	**-3.21**	0.82	**-0.45**	1.07	**-0.45**	**-1.75**	**-1.46**
L$_{S,IP}$	**[nm]**	16	**16**	12	**13**	12	**15**	**12**	**9**
$\phi_{Ag(220)}$	**[nm]**	9.21	**8.72**	3.66	**3.11**	3.24	**2.60**	*non textured*	
TC$_{Ag(220)}$	**[%]**	80	**87**	99	**100**	99	**100**	**40**	**47**
ε_{11}=ε_{22}	**(·10^3)**	-1.28	**1.32**	-1.56	**1.62**	-1.01	**1.62**	**1.88**	**0.72**
ρ_{300K}	**[$\mu\Omega$.cm]**	5.93	**5.03**	4.50	**3.68**	4.70	**3.95**	**5.08**	**6.10**
ρ_{res}^{grain}	**[$\mu\Omega$.cm]**	0.52	**0.21**	0.52	**0.21**	0.52	**0.11**	**0.21**	**0.39**
R_{M-S}		0.29	**0.27**	0.05	**0.06**	0.00	**0.00**	**0.21**	**0.20**
$R_{Sambles}$		0.29	**0.27**	0.05	**0.06**	0.00	**0.00**	**0.21**	**0.20**
R_{Soffer}		0.24	**0.21**	0.06	**0.05**	0.01	**0.06**	**0.21**	**0.13**
p_{M-S}		0.84	**1.00**	0.45	**0.60**	0.06	**0.15**	**0.70**	**0.88**
p_1		0.84	**1.00**	0.45	**0.60**	0.06	**0.15**	**0.70**	**0.87**
p_2		0.84	**1.00**	0.45	**0.60**	0.06	**0.15**	**0.70**	**0.87**
h_1	**[nm]**	0.08	**0.07**	0.11	**0.14**	0.74	**0.17**	**0.06**	**0.09**
h_2	**[nm]**	0.08	**0.07**	0.11	**0.14**	0.74	**0.17**	**0.06**	**0.09**
Θ_{D-M-S}	**[K]**	156	**129**	160	**121**	215	**215**	**166**	**147**
$\Theta_{D-Sambles}$	**[K]**	156	**129**	160	**121**	215	**215**	**166**	**147**
$\Theta_{D-Soffer}$	**[K]**	174	**145**	192	**172**	215	**215**	**178**	**167**

Table 4.11 Structural properties and resistivity characteristics of single crystal based stacks and references before and after annealing. The data were collected through X-ray diffraction and through temperature-resistance measurements. Simulations of the resulting resistivity curves were based on Mayadas-Shatzkes, Sambles and Soffer theories.

After annealing, all single crystal based samples show very similar structural variations (Fig. (4.27) and Tab. (4.11)). A sizeable increase of the (111) silver peak intensity is observed and parallels the decrease of its rocking curve width. These features characterize an enhancement of the silver crystallinity and a decrease of its out-of-plane mosaicity. The intra-grain microstrain is not affected by the temperature treatment as observed from the constant ε_{OP} value. On the contrary, a small 2θ shift of the silver peaks to larger values highlights a small variation in the macros-

train (ε_{33}). The same structural improvements are observed also in the in-plane direction : (i) increase of the texture coefficient and of peak intensity and (ii) decrease of the ϕ-scan width. Along this direction, microstrain could not be determined due to the presence of only one clear diffraction peak [Ag (220)]. Nevertheless, the in-plane lattice constant evolves with a film stress changing from a compressive to a tensile state. This change, in line with the negative mismatch with the substrate, was also observed for the prototype reference samples. These evolutions of crystallinity are accompanied only by a small increase of the lateral domain size while the vertical domain size, close to the film thickness, remains in the same range. The decrease of defect concentration and the increase lateral domain size with respect to an as-deposited stack were also observed through TEM imaging on a *ZnO-O 1st protocol* single crystal sample (Fig. (4.28)). In parallel, the interface roughnesses do not show strong variation.

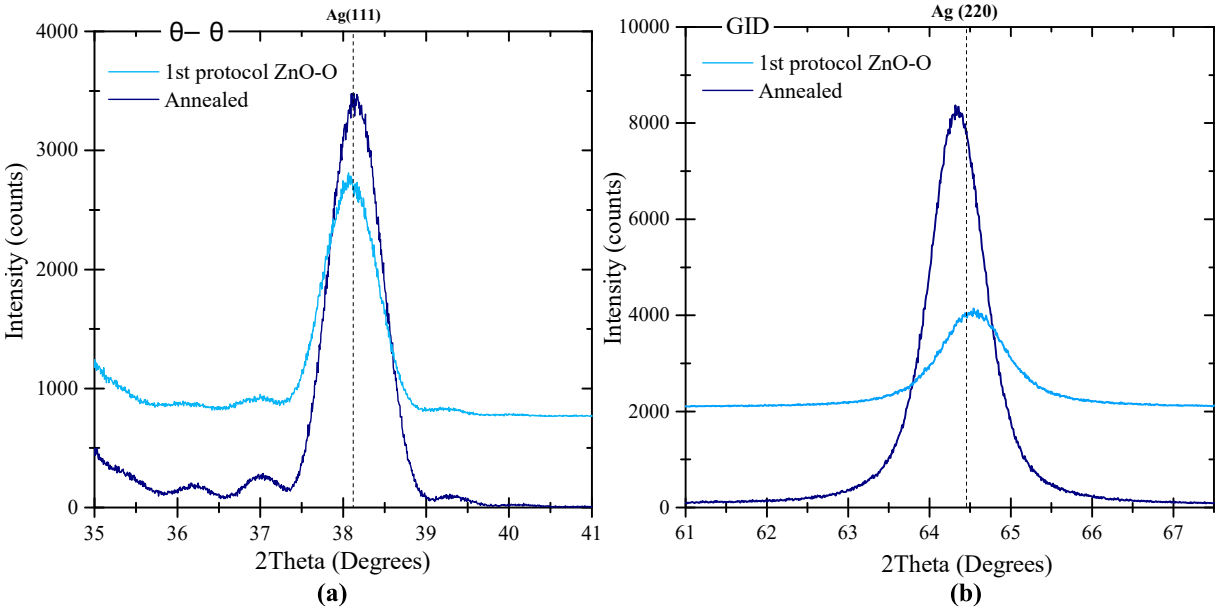

Figure 4.27 (a) $\theta - 2\theta$ and (b) grazing incidence diffractrograms of the O-terminated ZnO sample, treated with the first protocol, before and after annealing.

The temperature dependence of the resistivity of the annealed samples was then analysed with the previously described models : Mayadas-Shatzkes, Sambles and Soffer (Tab. (4.11)). The resistivity curves show similar shapes compared to pristine samples, characterized by a slight reduction of the profile concavity shape (see Fig. (4.29)-a *ZnO-O 1st protocol* sample) indicative of the reduction of the interface scattering contribution. Unfortunately, no study of room-temperature resistivity as function of film thickness could be performed to estimate ρ_{res}^{grain} after annealing. But, based on the sample resistivity gain comparable to a classical LINA prototype reference after a thermal treatment at 650°C for 10 min (Tab. (4.10)), it is reasonable to assume, after annealing, a similar concentration of intra-grain defects, mainly related to process parameters, and a similar ρ_{res}^{grain} of 0.21 $\mu\Omega$.cm value. Anyway, it was previously shown that small changes of this parameter do not strongly bias the conclusions on the other ones in the resistivity fit ; so ρ_{res}^{grain} was adapted to achieve the best agreement with experiments around this starting value (Fig. (4.29)).

The annealing induces a systematic increase of the interface scattering parameter p also supported by the decrease of the Soffer h_1 and h_2 roughness parameters. In the absence of XRR

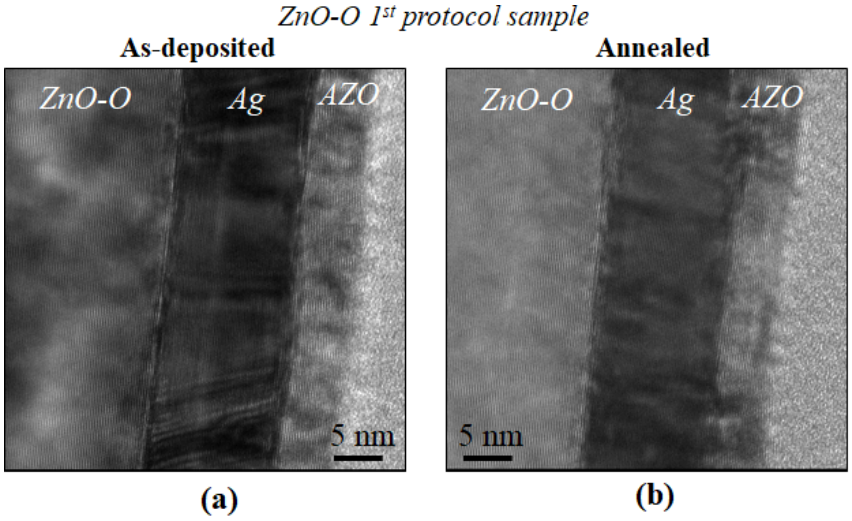

Figure 4.28 TEM cross section images before (a) and after (b) annealing of a *ZnO-O 1st protocol* sample. To be noted, the white areas observed in the single crystal bulk are TEM artefacts due to lamellar thickness variations.

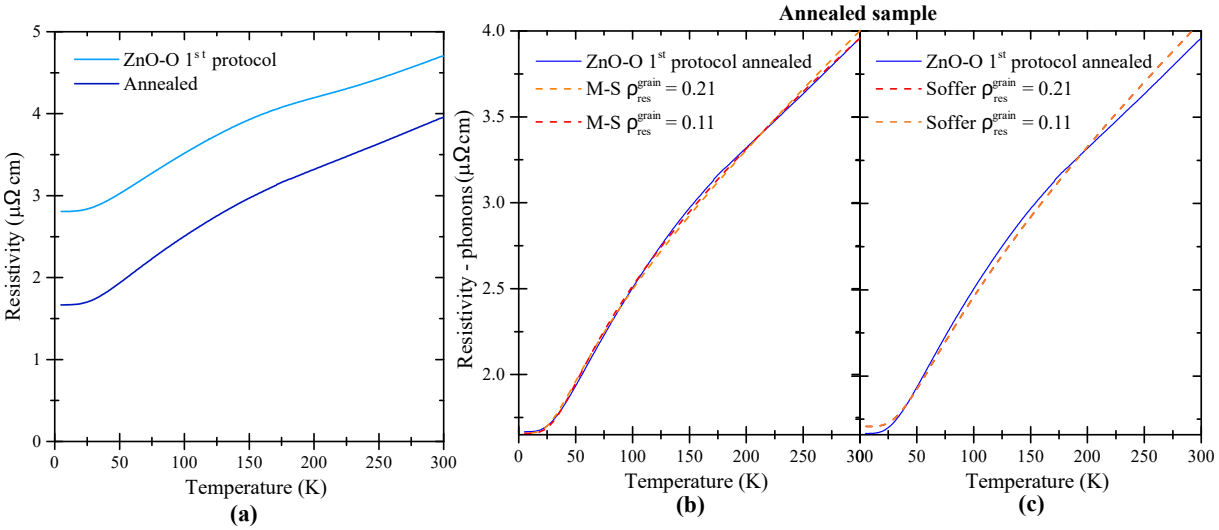

Figure 4.29 (a) Resistivity of the *ZnO-O 1st protocol* sample before and after annealing as a function of temperature. (b) Mayadas-Shatzkes and (c) Soffer model fits of the after annealing resistivity curve for different ρ_{res}^{grain} values.

data, this phenomenon suggests (i) either a smoothing of interfaces or (ii) a healing of specific interface defects. But the former mechanism was not evidenced in the case of glass-based reference samples (see Tab. (3.3)). In the as received single crystal sample, the p-coefficient even reaches one which implies a complete loss of out-of-specular interface scattering and a strong predominance of electron reflection mechanism at grain boundaries. In parallel, its R-parameter slightly reduces while the lateral domain size determined through the Scherrer equation compared to the pristine samples poorly evolves. This slight variation of R (which is already close to zero for the treated ZnO surface samples) is likely due to a better film texture and to a lower mosaicity due to the disappearance of large angle grain boundaries. This behaviour reminds the case of glass-based stacks resistivity, also governed by grain boundary scattering after annealing with the difference that no increase of the R parameter is observed after annealing for single

crystal samples. In the same way, for the best 1^{st} *protocol* samples, only an improvement on p is observed while R does not change staying close to zero. Already almost absent before annealing, the reflection of electron at grain boundaries does not vary. Finally, for all samples including references, the decrease of the Debye temperature (Tab. (4.11)) is at odd with the expected link of the phenomenon of phonon softening to the concentration of defects (Tab. (4.11)).

4.11 Reproducibility of the surface preparation protocol

The first protocol of surface preparation (Sec. (4.2.1)) turned out to be the best in terms of structure and resistivity. To check its reproducibility, two additional ZnO substrate (Zn- and O-terminated) were treated following the same recipe (Fig. (4.30)). No significant differences could be found compared to the first samples. The substrate surfaces showed a similar composition and a similar morphology with an even better roughness of 0.1 nm (against the 0.3 nm previously observed). In addition, to ensure that the surface preparation did not change the conductivity of the single crystal by introducing defects or impurities, the resistivity of the treated substrates were analysed. The treated ZnO-Zn substrate presented at room temperature a very high resistance value of about 20 MΩ, too important to be measured as a function of temperature and much higher than before treatment and than that of the silver film. At the opposite, for the O-terminated substrate, a decrease of its resistivity to $6 \cdot 10^6\,\mu\Omega$.cm with respect to the as-received substrate ($2 \cdot 10^7\,\mu\Omega$.cm) was observed.

A Ag-based stack was subsequently sputtered on the prepared substrates using the same conditions presented in Sec. (4.3). The good crystalline quality of silver was straightaway proved by the LEED image clearly showing the six diffraction peaks (Fig. (4.30)) with a signal/noise ratio of ~ 0.17 for Zn-terminated substrate and ~ 0.24 for the O-terminated single crystal. Also from a structural point of view (Tab. (4.12)), the replicas did not present strong variations. Only a slight improvement of the (111) texture was observed as well as a lowering of the ϕ-scan width, a sign of a better in-plane grain orientation.

The high quality of the silver thin film was reflected in their electrical properties, showing even lower resistivity values than with previous samples (Tab. (4.12)) of $2.96\,\mu\Omega$.cm, for the Zn-terminated, and of $3.02\,\mu\Omega$.cm, for the O-terminated sample. This significant resistivity variation, corresponding to a gain in the range of $\sim 22\%$ could probably be related to the improved in-plane texture exhibited by the replica samples. In respect to a prototype reference, as AZO·L1 ($5.54\,\mu\Omega$.cm) or ZnO·M1 ($5.84\,\mu\Omega$.cm), it corresponds to a conductivity gain of about 45%. The comparison remains remarkable even when considering a classic commercialised product, which generally shows more competitive conductivities than prototype samples ($\sim 4.20\,\mu\Omega$.cm before annealing). Here the gain is of the order of 30%, even lower than the annealed industrial value ($\sim 3.60\,\mu\Omega$.cm), a very promising result !
As the references, the main scattering mechanism occurring within the silver layer is the diffuse reflection of electron at the metal interfaces. The R-parameter in agreement with the high texturization of the film is on the contrary very small.

This findings shows that slight variations in the substrate preparation and in the deposition conditions can induce noticeable variation in the sample resistivity. At the same time, it should be mentioned that the samples were produced on single crystal substrates coming from a different batch, but same brand, than the rest of the analysed samples of this work.

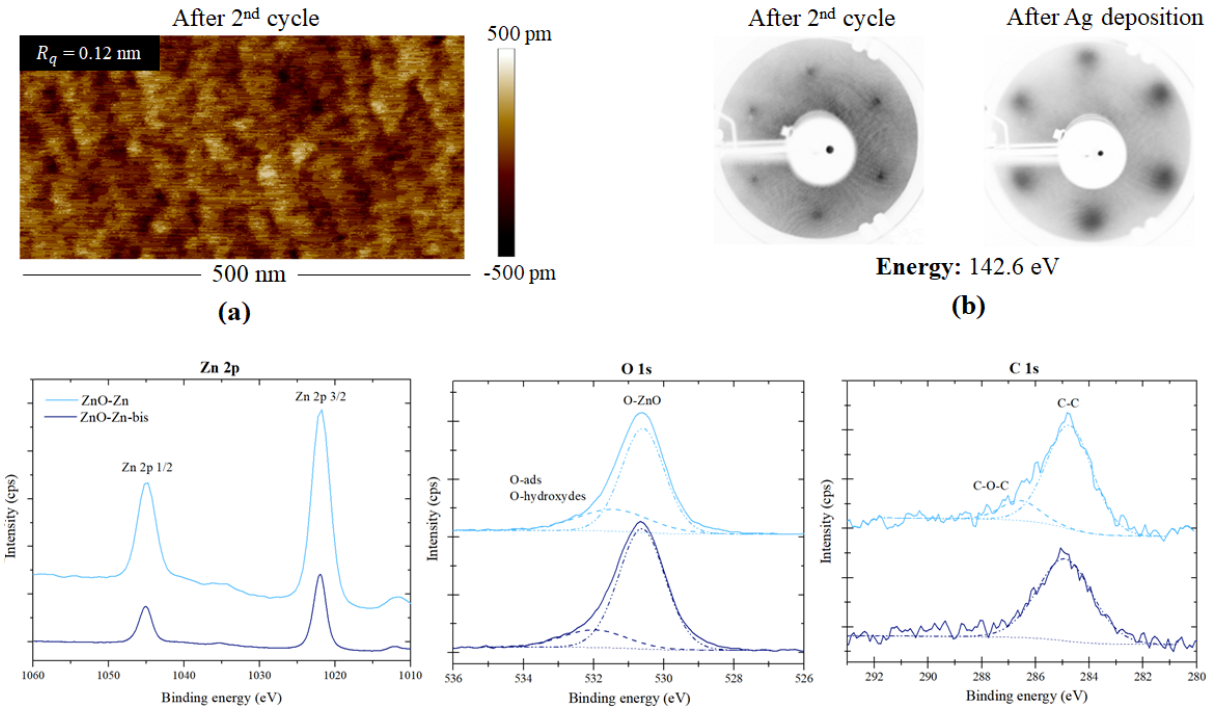

	Zn 2p	O 1s		C 1s	
		O-ZnO	O-H	C-C	C-O-C
ZnO-Zn	54%	29%	10%	4%	3%
ZnO-Zn-bis	57%	33%	5%	5%	0%
ZnO-O	50%	38%	9%	3%	0%
ZnO-O-bis	56%	36%	3%	3%	2%

(c)

Figure 4.30 (a) AFM, (b) LEED and (c) XPS composition of the second batch of ZnO-Zn sample at the end of the first protocol of surface treatment.

	As-deposited samples							
	ρ_{4P}	R		$p_1 = p_2$	$h_1 = h_2$	$L_{S,IP}$	$RC_{Ag(111)}$	$\phi_{Ag(220)}$
	[$\mu\Omega$.cm]	Sambles	Soffer		[nm]	[nm]	[°]	
ZnO-Zn	3.78	0.05	0.05	0.45	0.11	12	2.39	3.66
ZnO-Zn-bis	2.96	0.03	0.02	0.32	0.12	12	2.37	2.53
ZnO-O	3.92	0.00	0.01	0.06	0.74	12	1.81	3.24
ZnO-O-bis	3.02	0.02	0.04	0.35	0.15	10	1.82	2.68

Table 4.12 Summary of the single crystal based sample characteristics produced in different series to asses the repeatability of sample synthesis.

4.12 In summary

A model silver-based low-emissive stack, composed of $Ag_{12\ nm}$ - $AZO_{5\ nm}$- $SiN_{30\ nm}$, was sputtered on as-received and treated ZnO(0001) single crystal substrates of Zn- and O-terminations. The surface treatment protocol involving *in situ* Ar^+ sputtering/annealing cycles was optimized to achieve the best surface state for the metal epitaxial growth. The structural, morphological and electrical characteristics of the samples were then analysed and compared with prototype reference stacks grown on glass (Tab. (4.13)). Outstanding properties were observed for the silver layer on treated single crystal :

— structurally, showing the highest crystallinity degree and the best in-plane and out-of-plane texture ;
— topographically, exhibiting the lower interface roughness ;
— electrically, revealing the lower resistivity values.

Their conductivity was proven to be mainly governed by the electron scattering at the silver interfaces while the probability of been scattered at grain boundaries was astonishingly low. The comparison with reference prototype samples on glass clearly demonstrates that the grain boundary channel in resistivity is strongly influenced by the in-plane and out-of-plane texture of the silver grains *i.e.* the misorientation of the lattices of adjacent grains. This conclusion was allowed by the similarity of the lateral domain size (and therefore of grain boundary density) observed in sputtered layers, as if this characteristic was governed by the deposition process itself ; whatever the substrate, it was found close to the film thickness with only one grain in the perpendicular direction. Nevertheless surface roughness appeared to have a certain role on the stack conductivity that is difficult to rationalize maybe because of its small value in the present case and of a complex coupling with the grain boundary scattering channel. Conflicting roughness values for as-received and treated samples were obtained through AFM and Soffer estimations. Regarding the best ZnO termination to grow silver, it is not possible to draw a definitive conclusion. Indeed, silver deposited on O-terminated treated substrates showed the best structural quality but the Zn-terminated ones exhibited the best resistivity values. Annealing at a quite low temperature of 350°C leads to a gain of about 20% in resistivity that is assigned to a clear improvement of crystallinity due to a better texture and not to a really noticeable increase of grain size at variance with the glass-based references. This finding is explained by a decrease of the high-angle grain boundary density. In parallel, a sizeable healing of intra-grain defects as well as an improvement of the interface quality (marked by higher p values) is observed upon annealing.

Compared to industrialised Saint-Gobain products, exhibiting resistivity values of $\sim 4.20\,\mu\Omega$.cm before annealing, single crystal samples with a 30% lower resistivity could be obtained, reaching the value of $\sim 2.96\,\mu\Omega$ for a ZnO-Zn unannealed sample.

			Single Crystal		Glass References	
			ZnO-Zn	**ZnO-O**	**AZO·L2**	**ZnO·M2**
$\boldsymbol{\rho_{4P}}$	[$\mu\Omega$**.cm**]		2.96	3.02	5.54	5.84
R scattering		*Sambles*	0.03	0.02	0.21	0.19
		Soffer	0.02	0.04	0.14	0.13
p_1 ***scattering***			0.32	0.35	0.94	0.89
p_2			0.32	0.35	1.00	0.89
ZnO roughness	[**nm**]	*XRR*	0.28	0.26	0.50	0.44
		AFM	0.30	0.30	-	-
Ag roughness	[**nm**]	*XRR*	0.42	0.35	0.53	0.74
Roughness	[**nm**]	h_1	0.12	0.15	0.08	0.07
		h_2	0.12	0.15	0.08	0.07
Texture	[°]	$RC_{Ag(111)}$	2.37	1.82	13.78	16.92
	[°]	$\phi_{Ag(220)}$	2.53	2.68	*not textured*	
	[%]	$TC_{Ag(220)}$	100	100	31	21
d	[**nm**]	$D_{S,OP}$	12	13	10	9
		$D_{XRR,OP}$	13	12	12	11
L	[**nm**]	$L_{S,IP}$	12	10	7	8
		$L_{RC,IP}$	21	9	-	-

Table 4.13 Summary of the electrical, structural and topographical characteristics before annealing of the best single crystal based samples compared to prototype references. The results should also be compared to a commercialized industrial product exhibiting a resitvity of $\sim 4.20\,\mu\Omega$.cm.

Chapter 5

Homo-epitaxial ZnO-met buffer film as silver seed layer

In the previous chapter, the discussion focused on model system, in which a silver thin film has been grown directly on a ZnO(0001) single crystal substrate. To play with the nature of the interface, a thin buffer layer of ZnO-met of variable thickness (2-10 nm) has been inserted between the substrate and the metallic film. Outstanding results in terms of structural quality and of resistivity have been achieved leading, to our knowledge, to the smallest resistivity ever achieved for a 12 nm thick silver film. This chapter deals with the impact that this thin seed layer has on stacks, both on Zn- and O-terminated substrates, before and after annealing.

Chapter summary

5.1 Silver growth on homo-epitaxial ZnO-met buffer thin films

The previous chapter Ch. (4) demonstrated that the use of a ZnO single crystal induces the growth of a high-quality biaxial-textured Ag film with a very low resistivity. The fits of the temperature dependent resistivity showed a very low reflection coefficient of electrons at grain boundaries resulting in a dominating role of scattering at interfaces, that depends in turn substantially on the crystal surface treatment. To see if there is further room of improvement, a thin buffer layer of sputtered ZnO-met was introduced between the substrate and the silver film. The question at hand is to see if, in parallel, the positive impact of the Ag/ZnO epitaxial growth on the single crystal is kept after buffer layer sputtering. The oxide layer was grown in the experimental chamber MISSTIC right after the first protocol of surface preparation of ZnO(0001) using reactive deposition from a pure Zn-metallic target. The buffer thickness was varied between 2 and 10 nm on both O- and Zn-terminated single crystal substrates. Without exposing the sample to air, silver and AZO capping layers were subsequently deposited keeping the same thickness as for the industrial references (Fig. (5.1)) *i.e.* (ZnO(0001)-$ZnO_{x\ nm}$-$Ag_{12\ nm}$-$AZO_{5\ nm}$-$SiN_{30\ nm}$).

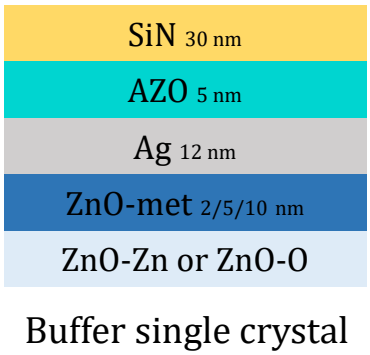

Figure 5.1 Schematic of the composition of stacks on single crystal based samples with a ZnO-met buffer layer.

5.1.1 Silver crystallinity improvement via a ZnO-met buffer

When looking at $\theta - 2\theta$ diffractograms of the whole stack (Fig. (5.2)-a,b), one can notice a shoulder on the low-angle side of the (002) and (004) ZnO peaks. It increases in intensity and shifts towards lower 2θ values with the film thickness. The effect is more pronounced for Zn-terminated substrates than for O-terminated ones. For homo-epitaxial growth on a single crystal substrate, this signal is generally associated to the sputtered layer itself [233–235]. This hypothesis is supported by the estimate of the vertical domain size, determined by the width of the shoulder, corresponding to the deposited buffer thickness, and by its absence in the single crystal references, thus excluding any role of the AZO capping. The shift towards low 2θ signs a tensile stress along the c-axis in the buffer layer. Since the material is deposited via a reactive sputtering in an oxygen environment, a likely explanation is the presence of excess oxygen atoms occupying interstitial positions and contributing to the expansion of inter-planar distances. As no side-peak is observed in the GIXRD diffractograms (not shown), it seems that the buffer ZnO-met layer has the same in-plane lattice constant as the single crystal substrate. It grows in homo-epitaxy on the single crystal substrate. Similar expansion along the $\vec{c}$ direction was also observed for ZnO seed layers in MISSTIC glass-based samples ; however, the reference film presents as well a reduced in-plane lattice constant following a Poisson elastic behaviour.

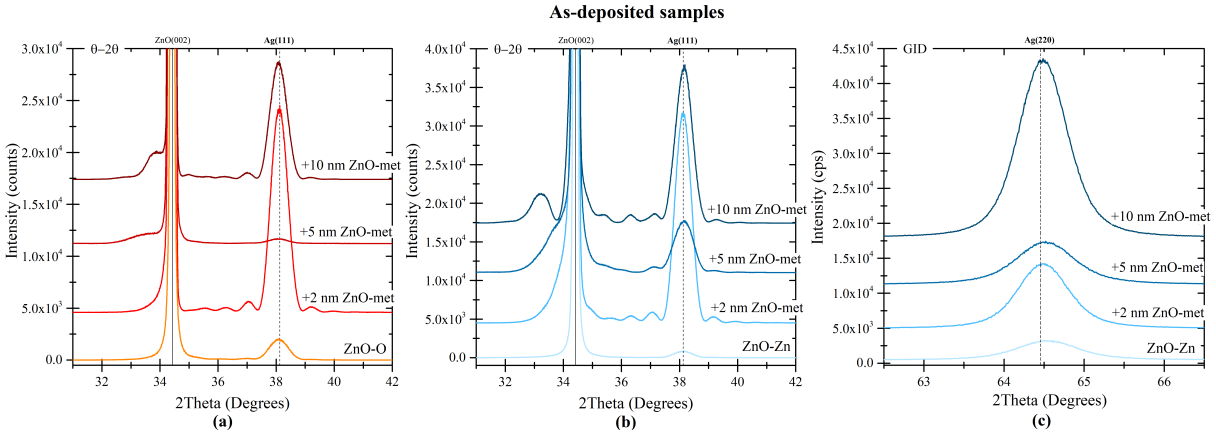

Figure 5.2 $\theta - 2\theta$ diffractograms corresponding to the (a) O- and (b) Zn-terminated single crystal based samples with ZnO-met buffer layers of increasing thicknesses. (c) Ag(220) peak of the Zn-terminated single crystal based substrates observed in GIXRD along the $[110]^*_{ZnO}$ direction.

As judged from diffraction (Fig. (5.2)), the insertion of a ZnO-met buffer has a tremendous influence on the metal crystalline quality. Compared to bare substrates, the samples with buffer layers show an out-of-plane (111) silver peak almost ten times more intense, particularly for the very thin buffer layers (2 nm thick), accompanied by clear Laue fringes. The increase in intensity is directly related to a clear improvement of the out-of-plane grain mosaicity and parallels a decrease of the substrate roughness as reported in Tab. (5.1). Along the perpendicular direction, the microstrain values (Tab. (5.2)) as well as the macrostrain values (ε_{33} ; Tab. (5.1)) remain small. Nevertheless, larger ε_{33} are observed for O-terminated samples.

For both terminations, the silver crystalline quality (peak intensity, out-of-plane orientation and visibility of Laue fringes) obtained for a 2 nm ZnO-met buffer layer worsens with thickness. The strongest degradation is observed for the 5 nm thick buffer for which the Laue fringes completely fade out. As summarized in Sec. (2.3.4.2), the two main factors that are detrimental to their contrast are : (i) the mean deviation δ from the average thickness d of the layer or (ii) the presence of dislocations. Based on the silver roughness determined by XRR (Tab. (5.1)), only the *ZnO-O + 5 nm ZnO-met buffer* sample shows a sizeable interface roughness increase ($RMS_{XRR}(Ag) = 1.46$ nm ; $RMS_{XRR}(ZnO) = 0.93$ nm), while the others do not deviate particularly from the average value ($RMS_{XRR} \simeq 0.5$ nm). At variance to the Zn-terminated series of samples, this specific O-terminated sample was made in a different sputtering batch than its companions, thus explaining its peculiar roughness behaviour. Beyond this peculiar case, the thickness deviation is thus excluded as the main cause of the Laue fringe fading. Indeed, according to Eq. (2.10), for a 12 nm film, Laue fringes should disappear for a mean deviation $\delta \geq 12 \times d_{Ag(111)} \approx 2.8$ nm, with $d_{Ag(111)} = 2.36$ Å [85], a value which is higher than the herein determined roughnesses. Accordingly, a more likely explanation is the presence of dislocations. Considering the observed scanned reciprocal space direction, the type of dislocation should have a Burger vector with an out-of-plane component as Frank partial dislocations. In the case of a cubic face-centred lattice, this corresponds to stacking faults due to the insertion (ABCACABC ...) or removal (ABCABACAB ...) of a layer as schematized in Fig. (5.3). This type of dislocations are known to form through the displacement cascades due to the irradiation with energetic atomic particles [27, 236] as it occurs during the sputtering process.

As-deposited samples						
				ZnO-Zn		**Ref**
		ZnO-Zn	+2 nm buffer	+5 nm buffer	+10 nm buffer	L1
$\mathbf{RC}_{Ag(111)}$	[°]	2.39	1.05	1.74	1.05	17.79
Mosaicity	[°]	2.29	0.18	0.99	0.41	-
$\boldsymbol{\varepsilon_{33}}$	$(\cdot\mathbf{10}^3)$	0.06	0.06	-0.20	-0.70	0.31
$\boldsymbol{a}_{OP-Ag}$	[Å]	4.09	4.09	4.08	4.08	4.09
$\mathbf{c}_{OP-ZnO}$	[Å]	0	5.3	5.3	5.4	5.2
$\mathbf{L}_{RC,IP}$	[nm]	21	13	9	14	-
$\boldsymbol{\phi}$ **scan**$_{Ag(220)}$	[°]	3.66	1.45	2.47	1.62	*no-texture*
$\mathbf{TC}_{Ag(220)}$	[%]	99	100	100	100	29
$\boldsymbol{\varepsilon_{11} = \varepsilon_{22}}$	$(\cdot\mathbf{10}^3)$	-1.01	-0.18	-0.59	-0.46	-1.28
$\boldsymbol{a}_{IP-Ag}$	[Å]	4.08	4.08	4.08	4.08	4.08
$\mathbf{RMS}_{XRR}$ **(Ag)**	[nm]	0.18	0.36	0.30	0.38	0.61
$\mathbf{RMS}_{XRR}$ **(sub)**	[nm]	0.44	0.17	0.21	0.26	0.57
				ZnO-O		**Ref**
		ZnO-O	+2 nm buffer	+5 nm buffer	+10 nm buffer	M2
$\mathbf{RC}_{Ag(111)}$	[°]	1.81	0.56	2.97	0.59	16.92
Mosaicity	[°]	1.15	0.26	3.03	-	-
$\boldsymbol{\varepsilon_{33}}$	$(\cdot\mathbf{10}^3)$	1.07	0.31	1.58	1.07	0.82
$\boldsymbol{a}_{OP-Ag}$	[Å]	4.09	4.09	4.09	4.09	4.09
$\mathbf{c}_{ZnO}$	[Å]	0	5.24	5.32	5.29	5.24
$\mathbf{L}_{RC,IP}$	[nm]	9	28	20	-	-
$\boldsymbol{\phi}$ **scan**$_{Ag(220)}$	[°]	3.24	1.34	4.28	1.45	*no-texture*
$\mathbf{TC}_{\boldsymbol{Ag(220)}}$	[%]	99	100	96	100	21
$\boldsymbol{\varepsilon_{11} = \varepsilon_{22}}$	$(\cdot\mathbf{10}^3)$	-1.01	-0.18	-0.87	-0.18	-0.69
$\boldsymbol{a}_{IP-Ag}$	[Å]	4.08	4.08	4.08	4.08	4.08
$\mathbf{RMS}_{XRR}$ **(Ag)**	[nm]	0.52	0.48	1.46	0.69	0.74
$\mathbf{RMS}_{XRR}$ **(sub)**	[nm]	0.52	0.31	0.93	0.37	0.44

Table 5.1 Silver structural characteristics in single crystal based samples with and without ZnO buffer layers along the out-of-plane (OP) and in-plane (IP) directions as obtained from X-ray analysis. The texture coefficient (TC) was determined from GIXRD analysis while the interface roughness of the upper surface of silver (RMS_{XRR} (Ag)) and the seed layer (ZnO single crystal or polycrystalline zinc oxide) roughness (RMS_{XRR} (sub)) by XRR. $L_{RC,IP}$ is the in-plane domain size deduced in parallel with the out-of-plane mosaic spread from (111)/(222) rocking curves. L1 and M1 correspond to the prototype LINA AZO·L1 and MISSTIC ZnO·M2 references.

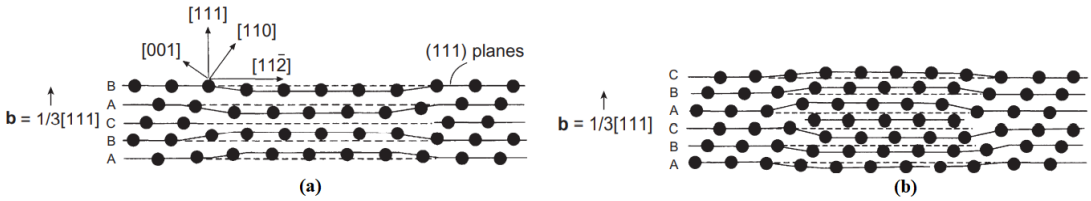

Figure 5.3 Stacking faults occurring along the ⟨111⟩ direction of a face-centred cubic metal associated to a Frank partial dislocation. Figure (a) illustrates an intrinsic stacking fault, while (b) an extrinsic one. Image credit [27].

As-deposited samples							
Out-of-plane							
	Vertical domain size				**Microstrain**		
	D -Scherrer	**SSP**	**H-W**	**W-H**	**SSP**	**H-W**	**W-H**
		nm				-	
ZnO-Zn	12	13	13	14	0.001	0.002	0.002
ZnO-Zn +2 nm ZnO-met	14	14	14	16	0.001	0.002	0.001
ZnO-Zn +5 nm ZnO-met	12	12	12	13	0.001	0.002	0.001
ZnO-Zn +10 nm ZnO-met	13	14	14	15	0.001	0.002	0.001
ZnO-O	12	14	14	18	0.002	0.004	0.003
ZnO-O +2 nm ZnO-met	13	14	14	15	0.001	0.002	0.001
ZnO-O +5 nm ZnO-met	11	12	12	14	0.002	0.004	0.002
ZnO-O +10 nm ZnO-met	13	14	14	16	0.001	0.002	0.001
AZO·L1	9						
ZnO·M2	9	9	10	7	0.002	0.002	0.003
In-plane							
	Lateral domain size				**Microstrain**		
	D -Scherrer	**SSP**	**H-W**	**W-H**	**SSP**	**H-W**	**W-H**
		nm				-	
ZnO-Zn	12	*12*	*12*	*12*	*0.001*	*0.001*	*0.000*
ZnO-Zn +2 nm ZnO-met	16		-			-	
ZnO-Zn +5 nm ZnO-met	13		-			-	
ZnO-Zn +10 nm ZnO-met	18		-			-	
ZnO-O	12	*9*	*9*	*8*	*0.002*	*0.003*	*0.002*
ZnO-O +2 nm ZnO-met	20		-			-	
ZnO-O +5 nm ZnO-met	13	*11*	*13*	*13*	*0.002*	*0.001*	*0.000*
ZnO-O +10 nm ZnO-met	18		-			-	
AZO·L1	9	9	8	37	0.003	0.002	0.007
ZnO·M2	8	8	5	6	0.002	0.005	0.006

Table 5.2 Vertical and lateral domain sizes as well as the out-of-plane microstrain of the single crystal based coating with ZnO-met buffer layers of increasing thickness. The values were estimated through the Scherrer equation, the Size-Strain, the Halder-Wagner and the Williamson-Hall plots. The out-of-plane structure properties were derived from the $\theta - 2\theta$ Ag(111) and Ag(222) diffraction peaks. In plane (in italic), the calculation was based on the GIXRD Ag(220) and Ag(111) peaks when visible and should be taken with caution.

Along the in-plane direction (Fig. (5.2)-c), a clear enhancement of intensity of the Ag (220) peak is observed for the samples with a ZnO-met buffer layer. It is accompanied by a reduced ϕ-scan width (Tab. (5.1)) that could be partly assigned to an increase of the lateral domain sizes (Tab. (5.1) and Tab. (5.2); values have to be taken with caution) and more likely to a better texture degree as testified by the texture coefficient that reaches its 100 % maximum value, thus confirming the growth of highly oriented biaxial films. Looking at macrostrain (Tab. (5.1)), despite the small values, it seems that a tensile strain in-plane compensates the out-of-plane compressive strain in agreement with the Poisson relation (see Fig. (5.4)).

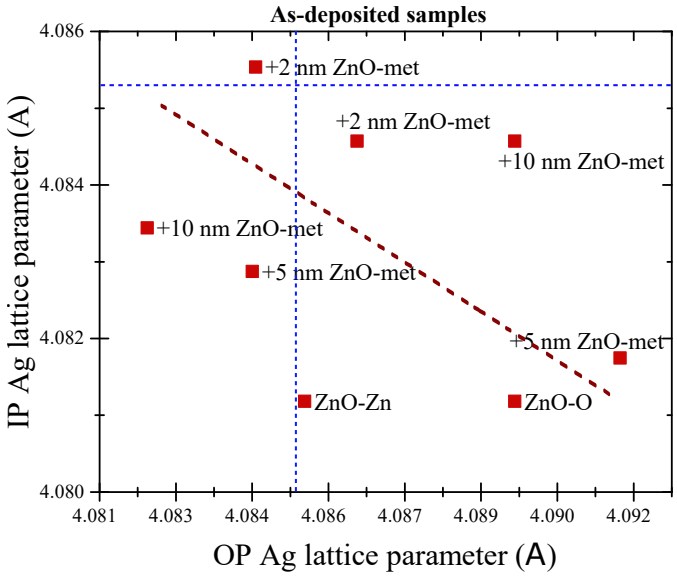

Figure 5.4 Relation between the in-plane and out-of-plane lattice parameters of the Ag thin film grown on a ZnO single crystal substrate with a ZnO-met buffer layer of increasing thickness (from 0 nm to 10 nm). The blue dash line correspond to the literature silver bulk lattice parameter value ($a_{bulk}Ag$=4.085Å).

As expected from the homo-epitaxial growth of the buffer layer, the presence of the ZnO-met film does not change the hexagon/hexagon epitaxial relationship with its -11 % mismatch already found on bare single crystal. This is attested by the presence of the Ag (220) GIXRD reflection, only visible along the $[110]^*_{ZnO}$ substrate direction, and by the position of the peaks in the pole figures (Fig. (5.5)). Compared to the bare crystals (Fig. (4.18)), the pole figures of the sample with a buffer layer show a reduced peak broadening, a sign of the increased texture and quality of the silver film. The presence of the buffer layer leads to the disappearance of the main ghost signals in the (111) and (200) pole figures, a fact which incidentally proves their link with the bare substrate. Comparing the pole figures of the *ZnO-O + 2 nm ZnO-met buffer* and *ZnO-O + 10 nm ZnO-met buffer* samples, slightly sharper features are found for the thinnest film in agreement with previous observations in $\theta - 2\theta$ and GIXRD scans (Fig. (5.2)).

To conclude, the reasons behind the outstanding Ag structural results observed for the samples with ZnO-met buffer layers are not obvious from the diffraction analysis. The present findings could be due to the burial of surface defects, remaining from the substrate preparation, by the homo-epitaxial growth of the ZnO-met layer. This illustrates the extreme sensitivity of the film structural quality to the nature of the seed substrate. Taking into account the XRR measurement incertitudes, any decrease of the interface roughnesses upon inserting the buffer layer is

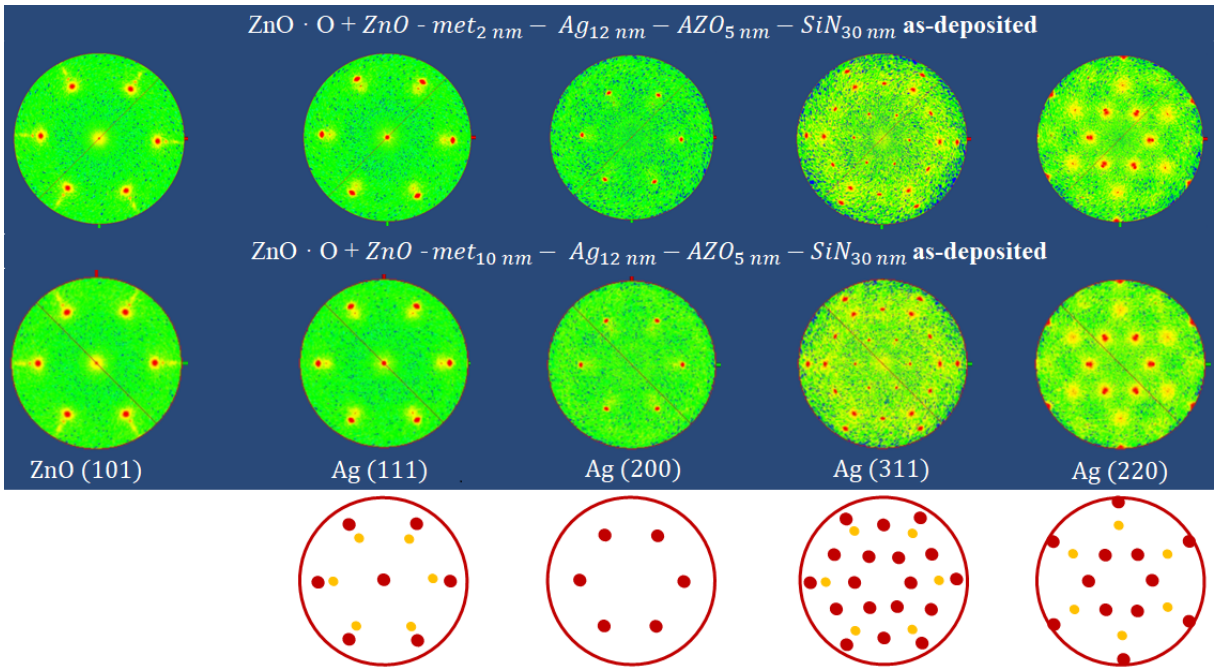

Figure 5.5 (Top) Pole figures of the *ZnO-O + 2 nm ZnO-met buffer* and *ZnO-O + 10 nm ZnO-met buffer* samples. The silver peaks attest for the biaxial texture of the film growing with an hexagonal/hexagonal epitaxy. (Bottom) Corresponding simulated pole figures for this epitaxial orientation. The Ag diffraction peaks are reported as red dots, while the peaks that are not included in the hexagon/hexagon epitaxy are represented by yellow dots. They correspond to ZnO-single crystal flanks peaks with close diffraction angles or a minor Ag orientation that has not been identified.

not obvious (Tab. (5.1)). Nevertheless, comparing the STEM images (Fig. (5.6)-a,b) of the lower silver interface in a *ZnO-O reference* sample and in a *ZnO-O + 2 nm ZnO-met buffer* sample, the thin ZnO-met buffer layer seems to give rise to a more defined interface. From the cross section TEM imaging, it is impossible to distinguish the ZnO-met buffer layer from the single crystal. This means that the seed layer grows in perfect epitaxy as concluded from GIXRD results with no visible extra defects.

5.1.2 Comparison with glass-based references and epitaxy

In Tab. (5.1) and Tab. (5.2), the characteristics of single crystal based samples, with and without a buffer layer, are compared with the *AZO·L1* and *ZnO·M2* glass-based references. Although all silver layers present similar vertical domain size close to the film thickness, the single crystal based samples firstly distinguish themselves by, on average, larger lateral domain size. An evident difference is also observed in the strong enhancement of the out-of-plane orientation with a higher textured film showing rocking curve widths ten times smaller than those of the glass-based references. Slight improvements in the interface surface roughnesses are also observed for single crystal samples, with the exception of *ZnO-O + 5 nm ZnO-met buffer*.
Comparable macrostrain values are observed between both types of samples, presenting similar silver parameter variations. The lattice deformations, that follow the Poisson effect in both directions (Fig. (3.19) and Fig. (5.4)), remain almost negligible as already pointed out for evaporated

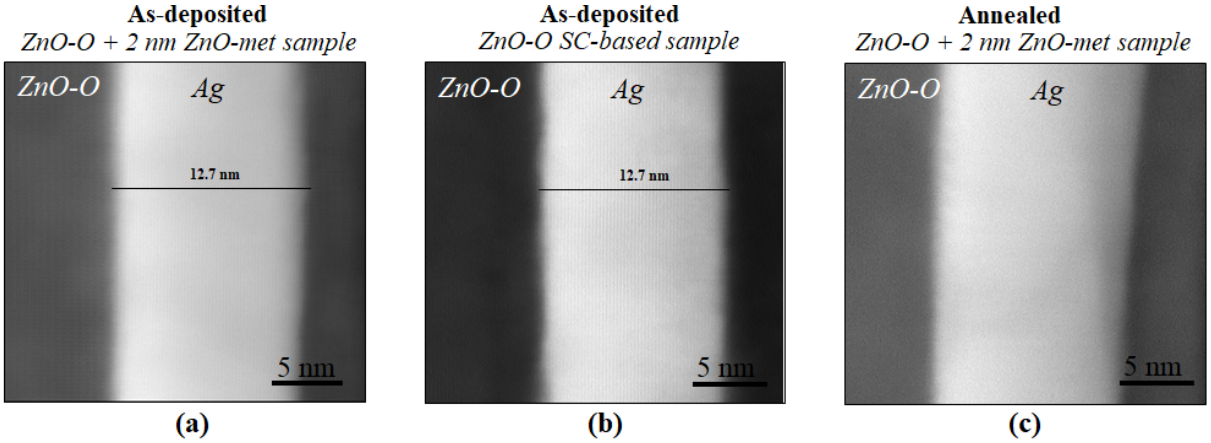

Figure 5.6 STEM cross section of the Ag-based stacks of (a) a *ZnO-O + 2 nm ZnO-met buffer* and (b) a ZnO-O reference sample. It is not possible to distinguish the buffer layer from the single crystal. In passing, the silver thickness agrees with XRR estimate. (c) STEM cross section of a *ZnO-O + 2 nm ZnO-met buffer* after annealing at 350°C for 10 min.

films [106]. If the hexagon/hexagon epitaxy is clearly demonstrated for single crystals, it was only suspected for the glass-based coatings from the correlation between the in-plane lattice parameters of the ZnO seed layer and of the silver film (but only after annealing Fig. (3.17)-e,f) in favour of a reduced lattice mismatch. Moreover, in those cases, stress induced by the growth process of the polycrystalline film and not by the epitaxy are not to be excluded even after annealing.

Nevertheless, for both epitaxies, simplified models predicts a critical thickness for the introduction of misfit interface dislocations in the range of the monolayer (see Sec. (1.4.1) and Sec. (1.4.2)), so well smaller than the film thickness. But probably owing to the fortuitous bulk lattice mismatch match value of -11 % that leads to a coincidence lattice of (9×9) Ag surface unit cell and (8×8) ZnO ones, the introduction of interface dislocations is not any more required to catch up the misfit. Only slight distortions between the coincidence sites are required leading to the very small deviations from the bulk lattice parameter (Fig. (5.4)). Moreover, if present and organized, an array of misfit dislocations has definite signatures in the in-plane diffraction line shape of the deposit peak [237, 238] that are not visible in the present data (Fig. (5.2)). Also, they have not been evidenced in TEM cross section (Fig. (4.28)).

5.2 The impact of the ZnO-met buffer on resistivity

5.2.1 Correlation between room-temperature resistivity and structural characteristics

In accordance with the previous diffraction analysis, the samples involving a ZnO-met buffer layer reveal a strong improvement in their electrical characteristics as reported in Tab. (5.3). With a resistivity gain of 15 % with respect to the bare single crystal samples and of ~ 40 % with respect to the glass-based references, the ZnO-O sample with a 2 nm ZnO-met buffer reaches the lowest record resistivity of 3.34 $\mu\Omega$.cm for an as-deposited stack. In parallel to the structural properties, the conductivity gain decreases with the buffer thickness, dropping to the lowest values for the 5 nm thick buffer samples.

As-deposited samples											
		References		ZnO-Zn				ZnO-O			
		AZO·L1	ZnO·M2	+0 nm ZnO-met	+2 nm ZnO-met	+5 nm ZnO-met	+10 nm ZnO-met	+0 nm ZnO-met	+2 nm ZnO-met	+5 nm ZnO-met	+10 nm ZnO-met
$R_{\square-4P}$	$[\Omega/sq]$	4.62	4.87	3.15	2.85	2.94	2.92	3.27	2.78	3.31	2.85
ρ_{4P}	$[\mu\Omega cm]$	5.54	5.84	3.78	3.41	3.53	3.50	3.92	3.34	3.97	3.42

Table 5.3 Sheet resistance and resistivity of the different single crystal based samples measured through a 4-points method at room temperature. LINA/MISSTIC glass-based references are included as matter of comparison.

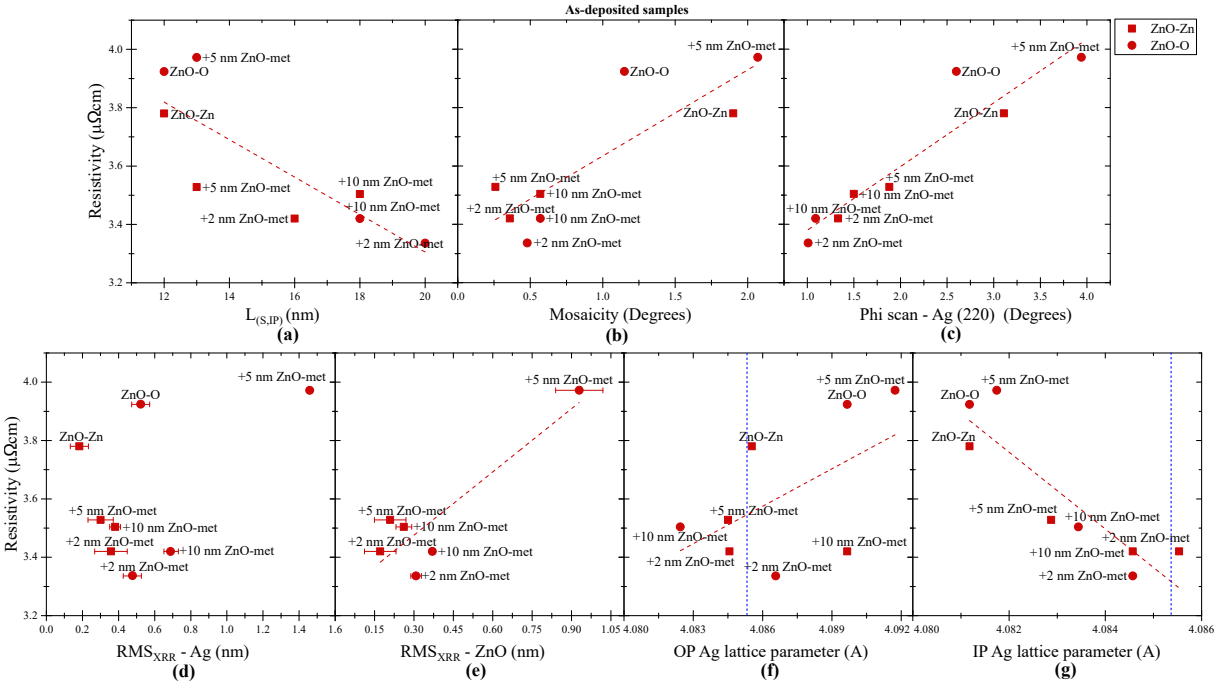

Figure 5.7 Room-temperature resistivity determined using the temperature-dependent set up as a function of (a) the lateral domain size, (b) the out-of-plane mosaicity, (c) the ϕ-peak broadening, the roughnesses estimated through reflectivity of (d) the silver layer and of (e) the ZnO-met buffer layer and (f) the out-of-plane and (g) the in-plane lattice parameters.

Contrary to previously analysed samples (Fig. (4.19)), the silver layers present here a larger lateral domain size variation, which allows to highlight the correlation between the resistivity and the density of grain boundaries (Fig. (5.7)-a). Within some fluctuations that could be related to the different used resistivity measurement set ups (Sec. (2.3.7) ; Fig. (2.17)), a clear correlation is also observed with the grain misorientation, determined through the mosaicity in the out-of-plane direction and by the ϕ-peak broadening in the in-plane direction (Fig. (5.7)-b,c.) Note that, along the in-plane direction, the correlation between resistivity and ϕ-peak width (Fig. (5.7)-c) still involves the interplay between in-plane mosaicity and lateral grain size broadening. Fur-

thermore, the impact of surface morphology was studied by plotting silver resistivity against the interface roughnesses determined by XRR. In both graphs (Fig. (5.7)-d,e), it is difficult to see a clear trend due to large uncertainties for roughness values below 1 nm. Nevertheless, thank to the *ZnO-O + 5 nm ZnO-met buffer*, a correlation seems to emerge with the ZnO-met buffer surface roughness, so that the layer with the greatest surface roughness induces a silver layer with the larger resistivity. The lattice parameters have also an influence on the silver resistivity. Samples with largest in-plane distances, and therefore smaller out-of-plane ones, present also the best conductivity values (Fig. (5.7)-f,g). This results is in line with the behaviour observed for annealed glass-based references discussed in Sec. (3.2) (Fig. (3.15)). Although in agreement with the misfit sign, this correlation may be fortuitous or indirect.

5.2.2 Temperature-dependent resistivity fit

The electrical properties of the ZnO-met buffer-based samples were also measured as a function of temperature (Fig. (5.8)) and fitted with the three previously detailed resistivity models, namely Mayadas-Shatzkes, Sambles and Soffer. Throughout the simulations, the distance between grain boundaries was fixed at the lateral domain size $L_{RC,IP}$ determined by X-ray diffraction from rocking scans while the other parameters were left free to vary. The value found for bare crystal samples, $\rho_{res}^{grain} = 0.52\,\mu\Omega$.cm, was used for the intra-grain resistivity of all other samples. This hypothesis was already shown not to strongly bias the conclusions (see Sec. (4.9)).

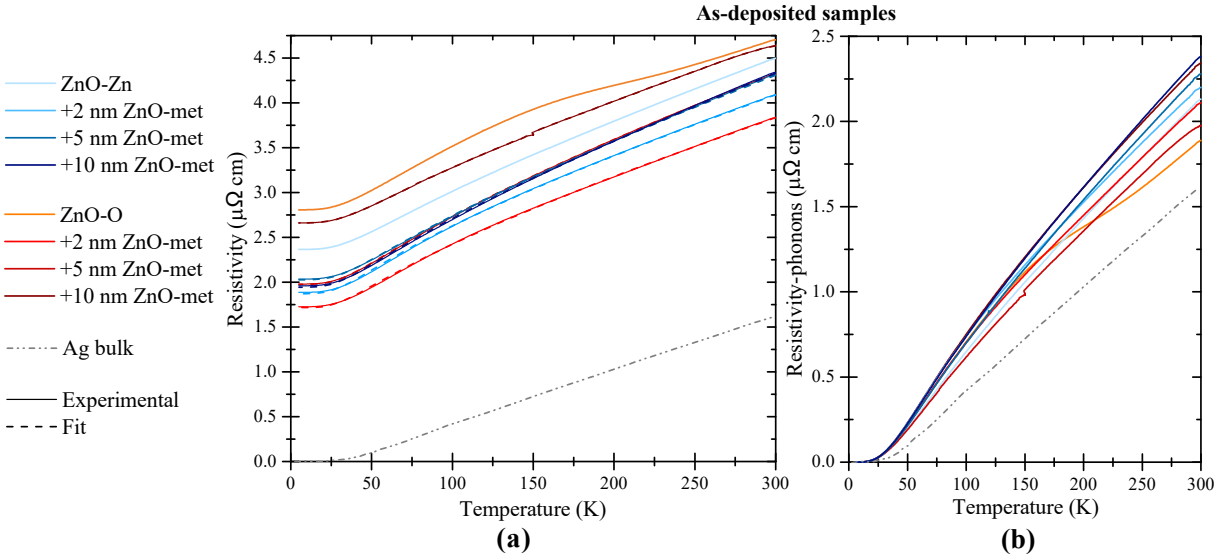

Figure 5.8 (a) Temperature dependent resistivity of Ag based stacks grown on a ZnO-met buffer layer (0 – 10 nm) on a single crystal substrate as compared to the bulk silver [93]. Full (respectively, dotted) lines correspond to data (respectively, fits). Fits parameters are reported in the Tab. (5.4). (b) Corresponding temperature dependent contribution $\rho_{ph}(T) = \rho(T) - \rho_{res}(T = 0K)$.

In all single crystal based samples (Tab. (5.4)), interface scattering remains the main mechanism hindering the metal electrical conductivity. At grain boundaries, the probability of electron reflection is very low for all models (*i.e.* $R = 0$). Therefore the gain in conductivity (Tab. (5.3)) is mainly assigned to the increase of lateral domain size (Tab. (5.1) and Fig. (5.7)-a). In parallel, on average, the p-parameter increases with the introduction of a ZnO-met buffer towards values

close to glass-based reference samples. If a good agreement is observed between the Mayadas-Shatzkes and the Sambles results, an asymmetry of roughness is, however, revealed by the Soffer model (*i.e.* $h_1 \neq h_2$), in the *ZnO-Zn + 2 nm ZnO-met buffer*, *ZnO-O + 2 nm ZnO-met buffer* and *ZnO-O + 5 nm ZnO-met buffer* samples. It could be related to the difference of zinc oxide nature between the seed layer and the capping layer, one deposited from a metallic target and the other from a ceramic target. As a matter of fact, even X-ray reflectivity measurements revealed a rougher Ag/AZO-capping interface than the buffer-ZnO/Ag one (Tab. (5.1)). Nevertheless, this asymmetry did not appear for bare single crystals. Since there is no clear-cut correlation between the resistivity and the roughness parameters h_1 and h_2 (Fig. (5.9)-a,b) and between resistivity and XRR roughnesses (Fig. (5.7)-d,e), the decrease of p with buffer introduction can not be assigned with certainty to a roughness change. Finally, as previously observed for prototype references, the improvement of silver film crystalline quality is not automatically accompanied by an increase in the Debye temperature (Fig. (5.9)-c). This suggests that there may be more complex reasons than structural imperfections to explain a lower value than in the bulk.

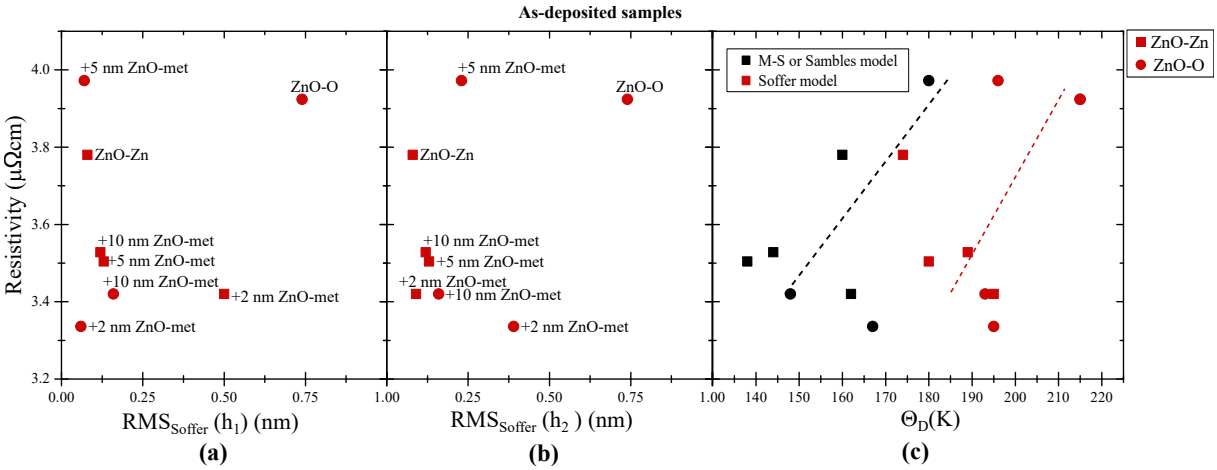

Figure 5.9 (a-b) Correlation between the interface roughnesses determined through the fit of the temperature-dependent resistivity fit with the Soffer model and the silver film resistivity. (c) The same but for the Debye temperature for the Mayadas-Shatzkes (black symbols) and Soffer (red symbols) models.

Sample	ρ_{4P} [$\mu\Omega$**cm**]	ρ_{300K} [$\mu\Omega$**cm**]	ρ_{res}^{grain} [$\mu\Omega$**cm**]	**R**	$\mathbf{p}_1$	$\mathbf{p}_2$	Θ_D [**K**]	$\mathbf{h}_1$ [**nm**]	$\mathbf{h}_2$ [**nm**]
As-deposited samples									
ZnO-Zn									
ZnO-Zn									
Mayadas-Shatzkes				0.05	0.45		160		
Sambles	3.78	4.50	0.52	0.05	0.45	0.45	160		
Soffer				0.06			174	0.08	0.08
+ 2nm ZnO-met									
Mayadas-Shatzkes				0.00	0.36		162		
Sambles	3.41	4.09	0.52	0.00	0.36	0.36	162		
Soffer				0.00			195	0.09	0.5
+ 5nm ZnO-met									
Mayadas-Shatzkes				0.04	0.56		144		
Sambles	3.53	4.31	0.52	0.04	0.56	0.56	144		
Soffer				0.04			189	0.12	0.12
+ 10nm ZnO-met									
Mayadas-Shatzkes				0.05	0.57		138		
Sambles	3.50	4.34	0.52	0.05	0.57	0.57	138		
Soffer				0.04			180	0.13	0.13
ZnO-O									
ZnO-O									
Mayadas-Shatzkes				0.00	0.06		215		
Sambles	3.92	4.70	0.52	0.00	0.06	0.06	215		
Soffer				0.01			215	0.74	0.74
+ 2nm ZnO-met									
Mayadas-Shatzkes				0.00	0.43		167		
Sambles	3.34	3.83	0.52	0.00	0.43	0.43	167		
Soffer				0.00			195	0.06	0.39
+ 5nm ZnO-met									
Mayadas-Shatzkes				0.05	0.29		180		
Sambles	3.97	4.66	0.52	0.05	0.29	0.29	180		
Soffer				0.10			196	0.07	0.23
+ 10nm ZnO-met									
Mayadas-Shatzkes				0.02	0.38		148		
Sambles	3.42	4.32	0.52	0.01	0.38	0.38	148		
Soffer				0.03			193	0.16	0.16
AZO·L1									
Mayadas-Shatzkes				0.12	0.35		170		
Sambles	5.54	6.15	0.65	0.12	0.35	0.35	170		
Soffer				0.17			178	0.08	0.06
ZnO·M2									
Mayadas-Shatzkes				0.16	0.49		167		
Sambles	5.84	6.96	0.69	0.16	0.49	0.49	167		
Soffer				0.18			178	0.08	0.08

Table 5.4 Resistivity parameters of the as-deposited single crystal based samples, without and with ZnO-met buffer layers, and of the prototype LINA and MISSTIC references, obtained by fitting the resistivity variation in temperature with three different models : Mayadas-Shatzkes, Sambles and Soffer. Both room-temreperature resistvities determined via the 4-points method (ρ_{4P}) and by tempertature-dependent resistivity set up (ρ_{300K}) are reported.

5.3 The impact of annealing for stacks with ZnO-met buffer layer

5.3.1 Resistivity and crystallinity gains upon annealing

Resistivity after annealing

To improve the performance of the stacks, the samples were annealed at 350°C for 10 min. The sheet resistance and resistivity measurements performed after heat treatment are presented in Tab. (5.5). After annealing, the samples show a nearly uniform gain in resistivity. The strongest change is observed for the *ZnO-O + 2 nm ZnO-met buffer* sample, with a resistivity gain of 24 %. Already showing the best conductivity value before annealing, this coating remains the best performing, revealing an extraordinary (and never achieved to our knowledge for a thin silver film !), value of ρ_{4P} of 2.54 $\mu\Omega$.cm. Regarding the samples with a 5 nm ZnO-met buffer, both show a significant decrease of their resistivity ρ_{4P} (18 % of resistivity gain), although before annealing their silver quality was very poor. The fluctuations among samples in the observed gain in resistivity upon annealing may be related to the fact that the synthesis and thermal treatments were not performed in a single batch. This is particularly evident when comparing the in-plane structural properties. Some specimens, such as *ZnO-O + 2 nm ZnO-met buffer* and *ZnO-O + 10 nm ZnO-met buffer*, despite having very similar structural properties, show different conductivities. This behaviour might be related to phenomena related to oxygen diffusion from the neighbouring AZO or ZnO-met layers or of an increase of surface roughness. A more detailed investigation of the structural and morphological properties of all samples was therefore undertaken.

		References		**ZnO-Zn**				**ZnO-O**			
		AZO·L1	**ZnO·M2**	**+0 nm ZnO-met**	**+2 nm ZnO-met**	**+5 nm ZnO-met**	**+10 nm ZnO-met**	**+0 nm ZnO-met**	**+2 nm ZnO-met**	**+5 nm ZnO-met**	**+10 nm ZnO-met**
As-deposited											
ρ_{4P}	[$\mu\Omega$**.cm**]	5.54	5.84	3.78	3.41	3.53	3.50	3.92	3.34	3.97	3.42
After annealing											
ρ_{4P}	[$\mu\Omega$**.cm**]	4.75	5.58	3.08	2.80	2.90	3.17	3.07	**2.54**	3.24	3.02
Gain	[%]	14	5	18	18	18	10	22	24	18	12

Table 5.5 Resistivity before and after annealing of the different single crystal samples and glass references measured through a 4-points method at room temperature. For each sample, the resistivity gain is specified. The record value ever achieved is 2.54 $\mu\Omega$.cm !

Structural and morphological characteristics after annealing

The microstructure characteristics after annealing were analysed via XRD techniques (Fig. (5.10) versus Fig. (5.2)). The results are reported in Tab. (5.6) (versus Tab. (5.1) before). Overall all samples show an improvement of their structural properties after the thermal treatment. However, few differences are observed compared to before annealing.

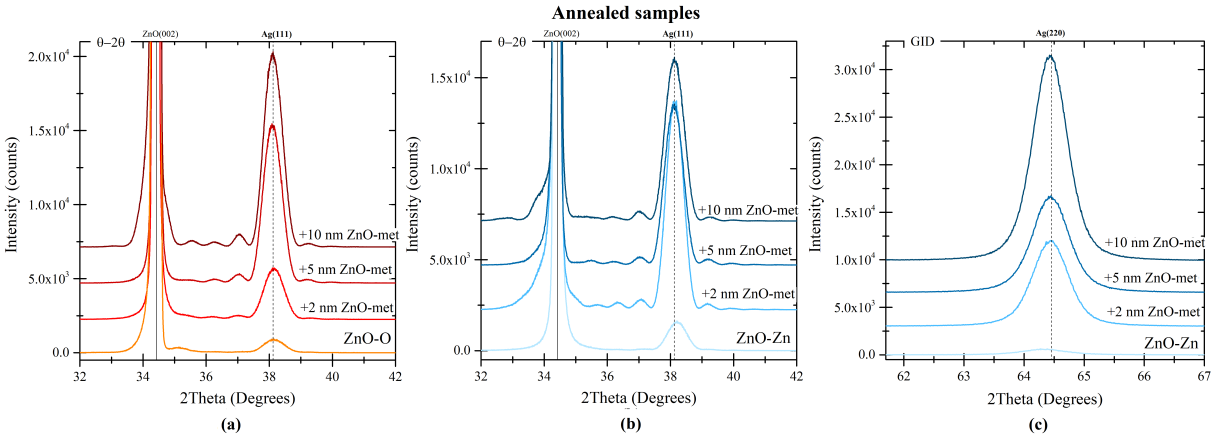

Figure 5.10 $\theta-2\theta$ diffractograms of the (a) ZnO-O and (b) ZnO-Zn single crystal based samples without and with ZnO-met buffer layers after annealing. (c) Ag(220) peak observed through GIXRD along the $[110]^*_{ZnO}$ direction for annealed stacks on Zn-terminated ZnO single crystal substrates.

In the out-of-plane direction, for all annealed samples, the Ag(111) peak intensity now increases with the buffer thickness. Differences between as-grown samples (Fig. (5.2)) are swept away upon annealing. In particular, the *ZnO-O + 2 nm ZnO-met buffer* sample suffers from a clear loss of crystallinity and to a lesser extent also the *ZnO-Zn + 2 nm ZnO-met buffer* and *ZnO-Zn + 10 nm ZnO-met buffer*. For these three samples, the worsening of crystallinity can be linked to an increase of the out-of-plane misorientation of the grains *i.e.* of the mosaicity value (Tab. (5.6) versus Tab. (5.1)). An explanation could be an oxygen diffusion from the ZnO-met buffer layer leading to the increase of internal dislocation and therefore a loss of the Laue fringes visibility, especially observed for *ZnO-O + 2 nm ZnO-met buffer*. Furthermore, all these samples are also characterized by an increase of interface roughnesses as seen by XRR. After annealing, for most samples, the strain state (ε_{33}) varies from tensile to compressive. The estimated values remains, however, very low (Tab. (5.6)).

Regarding the (002) ZnO peak, a shoulder linked to the ZnO-met buffer is still visible at 2θ values lower than the bulk peak (Fig. (5.10)-a) but the shift is reduced compared to as grown samples (Fig. (5.2)-a). This indicates a reduced tensile stress in the buffer layer. Having previously assigned it to an excess of oxygen atoms in the ZnO-met buffer lattice of the as-deposited layer, the stress reduction could be linked to their healing via diffusion upon annealing. For some samples, they could be at the origin of the previously discussed worsening of the crystalline quality of the nearby silver layer. For some samples on O-terminated crystals, *ZnO-O + 2 nm ZnO-met buffer* and *ZnO-O + 5 nm ZnO-met buffer* (Fig. (5.10)), this stress relaxation is even complete leading to a nearly symmetric ZnO (200) peak and a $c_{IP}-$lattice parameter close to that of the single crystal of 5.207 Å.

Annealed samples						
				ZnO-Zn		**Ref**
		ZnO	+2 nm buffer	+5 nm buffer	+10 nm buffer	L1
$\mathbf{D}_{\theta-2\theta,OP}$	**[nm]**	13	14	13	14	11
$\mathbf{RC}_{Ag(111)}$	[°]	2.04	1.01	1.23	0.98	15.25
Mosaicity	[°]	1.90	0.36	0.26	0.57	-
ε_{OP}		0.001	0.001	0.001	0.001	-
ε_{33}	$(\cdot\mathbf{10}^3)$	-0.45	-0.45	0.31	-0.20	-1.75
a_{OP-Ag}	[Å]	4.08	4.08	4.09	4.08	4.08
$\mathbf{c}_{OP-ZnO}$	[Å]	0	5.28	5.28	5.28	5.21
$\mathbf{L}_{\theta-2\theta,IP}$	nm	13	19	18	20	12
$\mathbf{L}_{RC,IP}$	nm	16	14	11	17	-
ϕ**-scan**$_{Ag(220)}$	[°]	3.11	1.33	1.88	1.50	*no-texture*
$\mathbf{TC}_{Ag(220)}$	[%]	100	100	100	100	40
$\boldsymbol{\varepsilon_{11} = \varepsilon_{22}}$	$(\cdot\mathbf{10}^3)$	1.62	0.24	0.37	0.51	1.88
a_{IP-Ag}	[Å]	4.09	4.09	4.09	4.09	4.09
RMS_{XRR}**(Ag)**	[Å]	0.28	0.57	0.33	0.18	0.53
RMS_{XRR}**(sub)**	[Å]	0.22	0.66	0.30	0.04	0.58
				ZnO-O		**Ref**
		ZnO	+2 nm buffer	+5 nm buffer	+10 nm buffer	M2
$\mathbf{D}_{\theta-2\theta,OP}$	**[nm]**	13	14	12	14	10
$\mathbf{RC}_{Ag(111)}$	[°]	1.42	0.75	2.44	0.52	14.60
Mosaicity	[°]	0.81	0.48	2.07	0.57	-
ε_{OP}		0.002	0.002	0.002	0.001	-
ε_{33}	$(\cdot\mathbf{10}^3)$	-0.45	0.56	-0.70	0.06	-1.46
a_{OP-Ag}	[Å]	4.08	4.09	4.08	4.09	4.08
$\mathbf{c}_{OP-ZnO}$	[Å]	0	5.21	5.21	5.21	5.22
$\mathbf{L}_{\theta-2\theta,OP}$	**[nm]**	15	28	13	24	9
$\mathbf{L}_{RC,IP}$	**[nm]**	12	24	11	44	-
ϕ**-scan**$_{Ag(220)}$	[°]	2.60	1.01	3.94	1.09	*no-texture*
$\mathbf{TC}_{Ag(220)}$	[%]	100	100	98	100	47
$\boldsymbol{\varepsilon_{11} = \varepsilon_{22}}$	$(\cdot\mathbf{10}^3)$	1.62	1.48	1.35	1.35	0.72
a_{IP-Ag}	[Å]	4.09	4.09	4.09	4.09	4.09
RMS_{XRR}**(Ag)**	[Å]	0.30	0.50	0.41	0.70	0.67
RMS_{XRR}**(sub)**	[Å]	0.34	0.28	0.19	0.45	0.57

Table 5.6 Same as Tab. (5.1) but after annealing the samples at 350°C during 10 min. L_D is the size deduced from the Scherrer equation on Ag (220) while $D_{\theta-2\theta,OP}$ and $L_{RC,IP}$ are deduced from the deconvolution of out-of-plane microstrain in $\theta - 2\theta$ scans and mosaicity in rocking scans.

Along the in-plane direction, the (220) Ag peak intensity slightly increases as a result of larger lateral domain sizes due to coarsening, and of the improvement of the grain orientation as seen in the Ag (220) ϕ-scan width sharpening (Fig. (5.10)-c and Tab. (5.6) versus Tab. (5.1)). For the *ZnO-O + 2 nm ZnO-met buffer*, *ZnO-Zn + 2 nm ZnO-met buffer* and *ZnO-Zn + 10 nm ZnO-met buffer*, that did not present a clear improvement in their out-of-plane structural properties, this in-plane structural enhancement could justify the outstanding conductivity gain observed after annealing. As with previous calculations, a discrepancy is observed between the lateral domain sizes $L_{S,IP}$ determined by applying Scherrer equation to the FWHM of the Ag(220) peak and

the value $L_{RC,IP}$ estimated through the FWHM of the Ag {111} rocking curves. This is related to the absence of several peaks of the same family in the in-plane direction that hinders the deconvolution of the microstrain contributions to the peak broadening, while in the out-of-plane direction, the value is the result of a linear regression with only two points. In both cases the estimated values are therefore associated to a certain uncertainty. Regarding the macrostrain, in agreement with the Poisson relation, the value is increased, shifting from a compressive to an expansive state (Tab. (5.6) vs Tab. (5.1)). The amplitude of the lattice distortion remains however very small. Thus, a clear linear trend is not established between the in-plane and out-of-plane lattice constants (Fig. (5.12)-f).

At last, the pole figures of the best conductive sample, *ZnO-O + 2 nm ZnO-met buffer*, after annealing (Fig. (5.11)) are pretty similar to those before (Fig. (5.5)) thus confirming the bi-axial texture of the silver film.

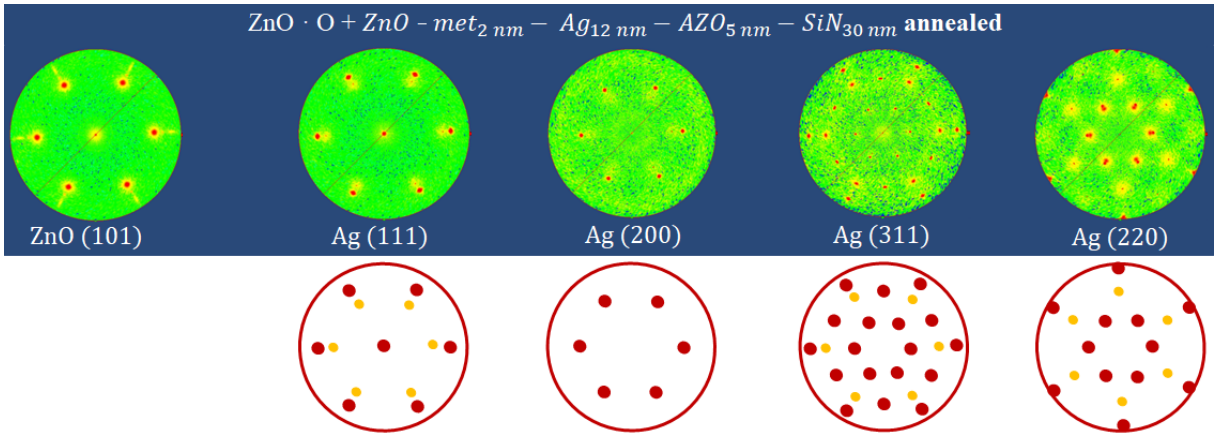

Figure 5.11 (Top) Pole figures of biaxial textured silver layer of the *ZnO-O + 2 nm ZnO-met buffer* sample after annealing. (Bottom) The corresponding simulated pole figures for an hexagon/hexagon epitaxy.

5.3.2 Comparison with annealed prototype references

After annealing, strong structural variations are still observed between the single crystal-based samples and the annealed glass-based references *AZO·L1* and *ZnO·M2* (Tab. (5.6)). Despite being annealed at the same temperature as the single crystal, the prototype samples do not show equal structural improvement. Their characteristics remain almost unchanged from the previous annealing. Thus, a wider discrepancy between the lateral domains and the out-of-plane grain orientation of the reference and of the single crystals is observed. Nonetheless, both type of samples present comparable roughness values, determined through XRR (RMS_{XRR}), for the silver interfaces. Regarding the macrostrain values, the prototype references present slightly larger absolute values, but still exhibiting the same lattice deformation in response to the thermal treatment (compressive state along the out-of-plane direction and expansive state in-plane).

5.3.3 Transport properties after annealing

Correlations between resistivity and structure

After annealing (350°C, 10 min), not all samples show a proportional decrease in resistivity. Nevertheless, in most cases (Fig. (5.12)), some linear dependencies with structural parameters are observed from which only a few values deviate. In agreement with the behaviour before annealing (Fig. (5.7)), the sample conductivity increases with the lateral domain size, corresponding to a decrease of the grain boundary density, as well as with the improvement of the grain orientation as judged by the correlation with the out-of-plane mosaicity (Fig. (5.12)-c) and with the Ag(220) ϕ-scan broadening (Fig. (5.12)-c). Despite a few samples (*ZnO-O + 2 nm ZnO-met buffer* and *ZnO-Zn + 10 nm ZnO-met buffer*) that differ from the general trend, a decrease of the resistivity is also observed as function of out-of-plane lattice constant (Fig. (5.12)-d,e). Owing to the hexagon/hexagon epitaxy, a less strained layer results in a higher conductivity. Finally, in Fig. (5.13)-a,b, the silver film resistivity has been plotted as a function of the interface roughnesses. It is hard to observe any trend, partly due to a small interval range of variations and to the uncertainty on the measurements.

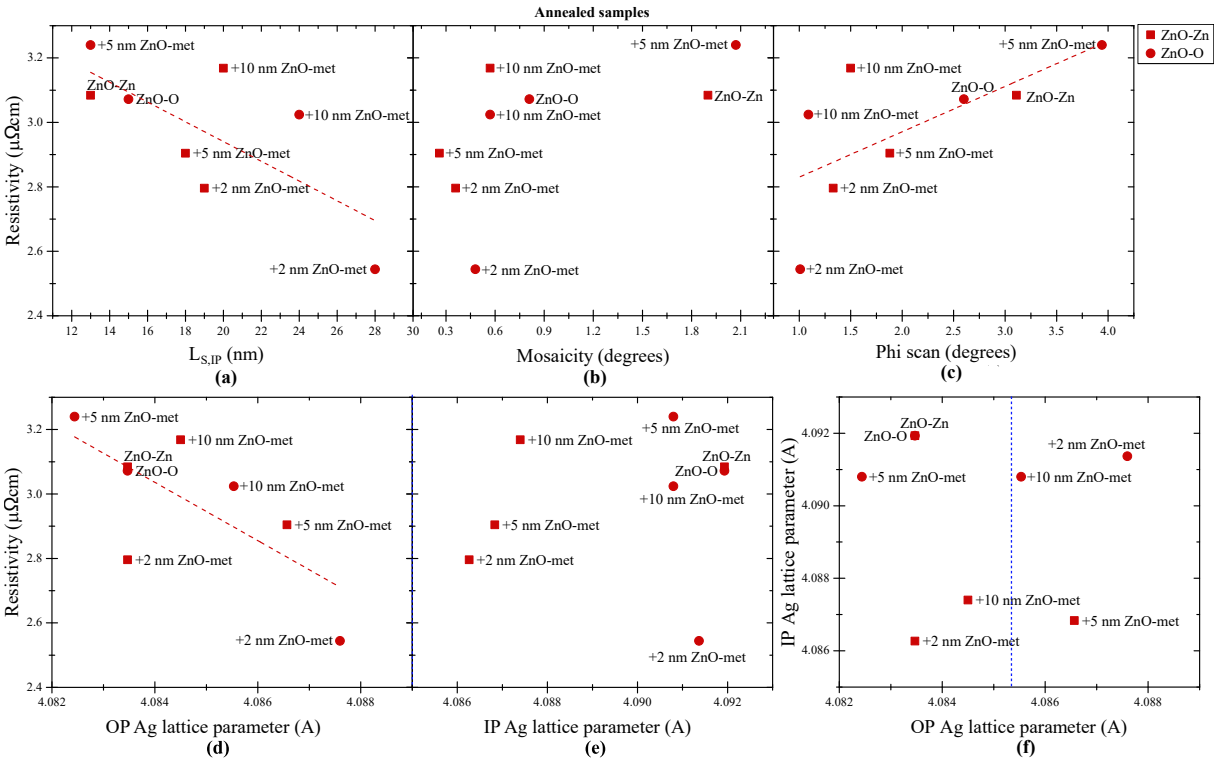

Figure 5.12 Correlations between the room-temperature resistivity and the Ag structural properties of single crystal based coatings with a ZnO-met buffer layer of variable thickness after annealing : (a) lateral domain size, (b) the out-of-plane mosaicity, (c) ϕ-scan broadening and (d) the out-of-plane and (e) in-plane lattice constants. In graph (f), the former is plotted as a function of the latter. The bulk silver lattice constant is $a_{Ag}^{bulk} = 4.085$ Å. Lines are only guides to the eyes to highlight the correlation between quantities.

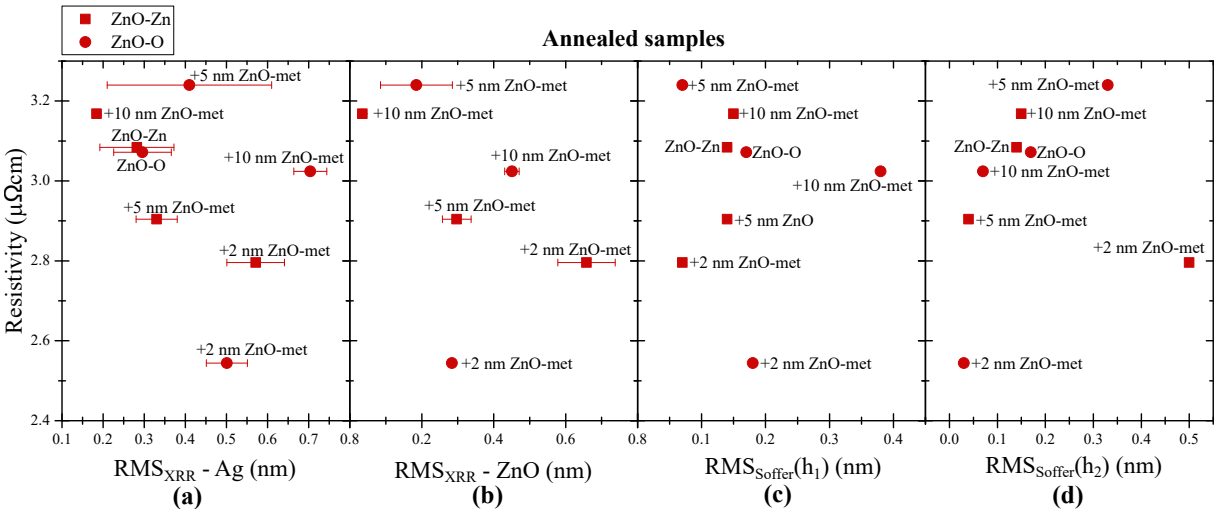

Figure 5.13 Silver resistivity as a function of interface roughnesses : (a-b) determined via XRR and (c-d) estimated via the Soffer model. h_1 and h_2 correspond to the two Ag external surfaces which, based on Soffer theory, can not be clearly assigned to a specific interface.

The R and p scattering parameters after annealing

Fig. (5.14)-a shows the resistivity of the samples with ZnO-met buffers as a function of temperature. After annealing, all the samples show a higher resistivity than the bulk silver that differs particularly in its phonon contribution (Fig. (5.14)-b). Observing Fig. (5.15), one can notice a variation in the temperature-dependent resistivity contributions of the samples on ZnO-O before and after annealing, leading to a gain up to 9% at room temperature. For the ZnO-Zn samples, the phonon contribution remains the same with the exception of *ZnO-Zn + 10 nm ZnO-met buffer*. Changes in the phonon contribution are not limited to a simple increase but involve also changes of curve concavity and thus of the nature of the electron scattering contribution (Fig. (5.14)-b,c). Although not directly obvious in Fig. (5.12)-d,e,f, this behaviour is in line with a more pronounced role of interfaces that could originate for example from the variation of the interface roughness induced by the healing of defects of the ZnO-met buffer as seen by diffraction.

Following the same procedure as before, the resistivity curves were fitted with the three temperature-dependent models : Mayadas-Shatzkes, Sambles and Soffer. The results are summarized in Tab. (5.7) and to be compared to those before annealing (Tab. (5.4)). Starting from the previously determined values $\rho_{res}^{grain} = 0.52\,\mu\Omega$.cm for bare crystals, ρ_{res}^{grain} had to be adjusted to obtain better fits leading to noticeable reduction of its values down to $0.1 - 0.2\,\mu\Omega$.cm. This healing of intra-grain defects is in line with a better visibility (Fig. 5.2-a) (except for the *ZnO-O + 2 nm ZnO-met buffer*) of the Laue fringes and a reduced stacking fault level.

As before annealing, since $R \simeq 0$, electron scattering mechanism at the silver interfaces remains the principal contribution to resistivity. All models agree with this weak contribution of grain boundary scattering. With a systematic decrease in the p-parameter values, the probability of phenomenon is intensified after annealing (Tab. (5.7) versus Tab. (5.4)). This agrees with the more pronounced concave shape of the curves (Fig. (5.15)). But this does not show up clearly through the correlations with roughnesses of Fig. (5.13). While fits with the Sambles model lead to symmetric interface, different h_1/h_2 values are found with the Soffer approach after annealing

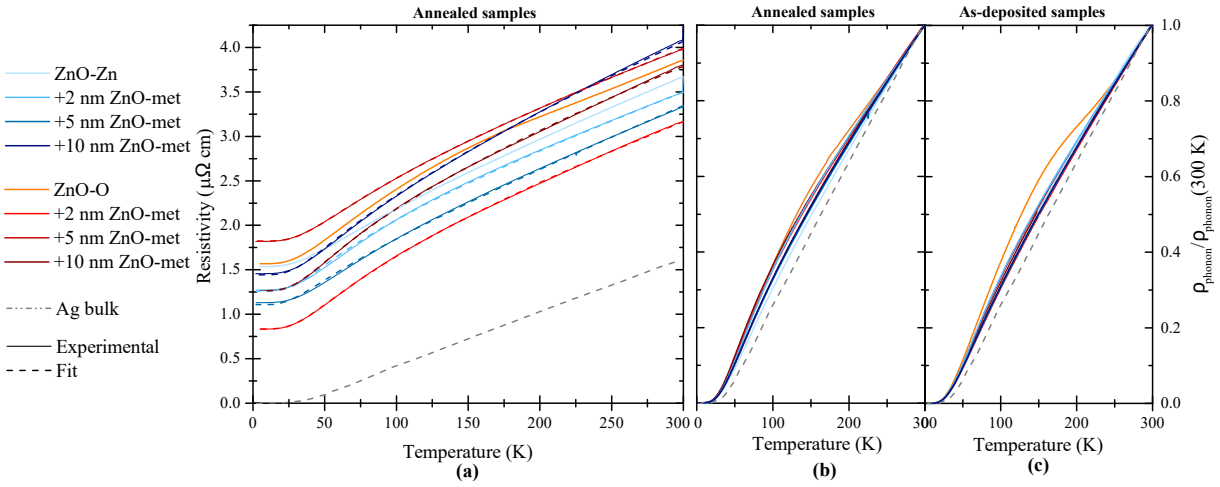

Figure 5.14 (a) Resistivity of the ZnO-met buffer-based samples after annealing as a function of temperature. Fit (dotted line) are overlapped on data (full line). (b-c) Overlap of their normalized phonon contributions $\rho_{ph}(T) = \rho(T) - \rho_{res}(T = 0K)$ after (b) and before (c) annealing. The behaviour of silver bulk [93] is plotted as a dashed grey line.

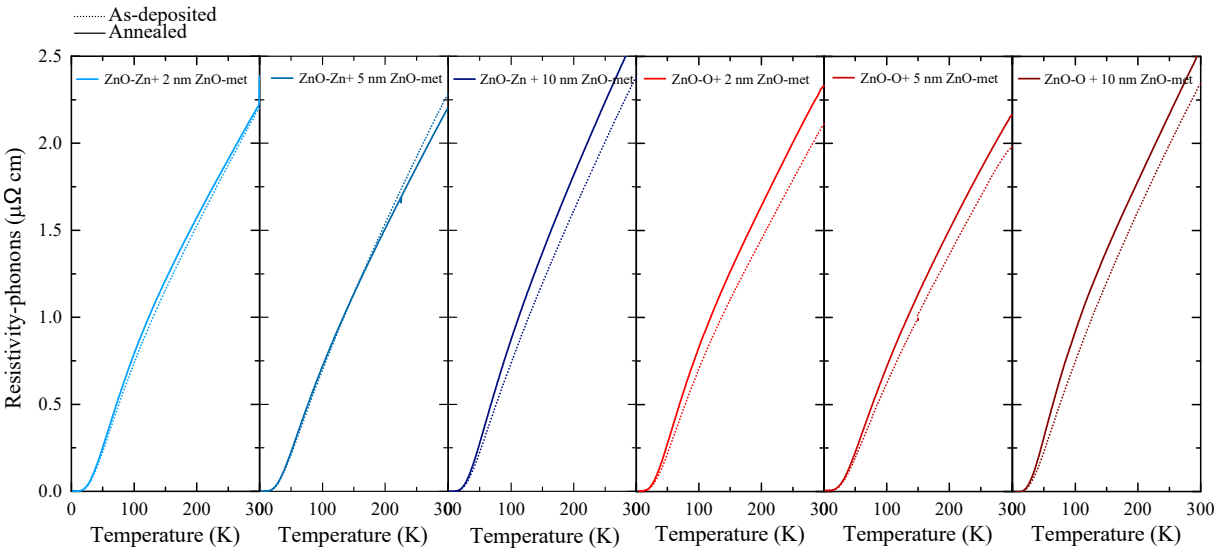

Figure 5.15 Comparison of the phonon contributions to the resistivity before (dotted line) and after annealing (full line) for samples with ZnO-met buffer layer.

for nearly all samples. The reason may lie in the difference of treatment of the probability of electron reflection with its incident angle on the interface between Sambles and Soffer models (Sec. (1.5)). This asymmetry was not so clear before annealing (Tab. (5.4)) and can be assigned to an interface evolution between the buffer ZnO-met layer and silver that parallels its structural relaxation to a less strained state. Defects in the ZnO-met buffer reactively sputtered from a metallic target could be at its origin. Somehow, the asymmetry of interfaces between the ZnO-met buffer and AZO capping is supported by STEM imaging (Fig. (5.6)).

If, for as-prepared ZnO substrates, the O-terminated samples have lower p-values than the Zn-terminated ones despite similar interface roughnesses with Ag, no clear-cut difference is found after buffer deposition (Tab. (5.4) and Tab. (5.7)). The role of the substrate polarity is wiped

off. After annealing, the main differences in terms of resistivity between glass-based and single crystal based samples becomes clearer. In the first case, where silver is characterized by low size grains, oriented only along the out-of-plane direction but random in-plane, conduction is mainly hindered by electron reflection at the grain boundaries. At the opposite, in single crystal based samples, where silver presents larger grain size and a highly biaxial orientation with very low grain boundary angles, interface scattering become the dominating mechanism, but with slightly poorer *p*-characteristics compared to the reference samples.

The correspondence between low R-value and good texture is also supported by the STEM plane view analysis of a Ag layer grown on a 2 nm ZnO-met buffer (Fig. (5.16)). Asides sharp defective dark area that delineate grain of hundred of nanometres in size, inner defective zones appear inside with a weaker dark contrast (Fig. (5.16)-a). Theses features are overlapped on an hexagonal array of dots, the periodicity of which corresponds to the coincidence of the hexagon/hexagon epitaxy. In fact, since atomic columns of the whole stack including the capping layer are imaged in STEM, their spacing does not correspond to the coincide site lattice at the interface (*i.e.* 2.5 nm) but to an hexagonal periodicity closer to 1.5 nm (see Fig. (5.17)). Imaging at a better resolution helps unravelling the nature of the inner defects (Fig. (5.16)-b). They correspond to anti-phase domain boundary of the coincidence between atomic columns; following a row from one domain to the other (line in Fig. (5.16)-b), one can notice a shift by half the periodicity. Such type of defects allows to catch up with the difference of registry between different grains and explain the reduced domain size (a few tens of nm) found by XRD. Intuitively, they should not impede much the electron transmission at variance to the sharper boundaries of Fig. (5.16). Looking at the difference between both types of domains in the STEM image (Fig. (5.16), one could wonder about the impact of distance D between reflective planes on R in the resistivity fit. From Eq. (1.33)-Eq. (1.34), it appears that these two parameters are strongly correlated in Mayadas-Shatzkes description of electron reflection at grain boundaries. To quantify this, calculations were performed by varying D in the case of *ZnO-O + 2 nm ZnO-met buffer* sample (Tab. (5.8)). To compensate the decrease of the density of grain boundaries, R increases but in a range of 0.04 that remains modest. Thus, the improved texture compared to industrial references is clearly the reason of such a low R-value beyond the nature of the grain boundaries.

Sample	ρ_{4P} [$\mu\Omega$**cm**]	ρ_{300K} [$\mu\Omega$**cm**]	ρ_{res}^{grain} [$\mu\Omega$**cm**]	**R**	$\mathbf{p}_1$	$\mathbf{p}_2$	Θ_D [**K**]	$\mathbf{h}_1$ [**nm**]	$\mathbf{h}_2$ [**nm**]
			ZnO-Zn						
ZnO-Zn									
Mayadas-Shatzkes				0.06	0.60		121		
Sambles	3.08	3.68	0.21	0.06	0.60	0.60	121		
Soffer				0.05			172	0.14	0.14
+ 2nm ZnO-met									
Mayadas-Shatzkes				0.00	0.34		188		
Sambles	2.80	3.49	0.11	0.00	0.34	0.34	188		
Soffer				0.02			212	0.07	0.50
+ 5nm ZnO-met									
Mayadas-Shatzkes				0.01	0.60		159		
Sambles	2.90	3.33	0.21	0.01	0.60	0.60	159		
Soffer				0.03			193	0.14	0.04
+ 10nm ZnO-met									
Mayadas-Shatzkes				0.05	0.59		127		
Sambles	3.17	4.08	0.21	0.05	0.58	0.58	127		
Soffer				0.06			182	0.15	0.15
			ZnO-O						
ZnO-O									
Mayadas-Shatzkes				0.00	0.15		215		
Sambles	3.07	3.95	0.11	0.00	0.15	0.15	215		
Soffer				0.06			215	0.17	0.17
+ 2nm ZnO-met									
Mayadas-Shatzkes				0.01	0.63		152		
Sambles	2.54	3.16	0.11	0.01	0.63	0.63	152		
Soffer				0.01			195	0.18	0.03
+ 5nm ZnO-met									
Mayadas-Shatzkes				0.02	0.33		180		
Sambles	3.24	3.97	0.21	0.02	0.33	0.33	180		
Soffer				0.04			202	0.07	0.33
+ 10nm ZnO-met									
Mayadas-Shatzkes				0.02	0.41		157		
Sambles	3.02	3.80	0.11	0.02	0.41	0.41	157		
Soffer				0.02			192	0.38	0.07
AZO·L1									
Mayadas-Shatzkes				0.21	0.70		166		
Sambles	4.75	5.08	0.21	0.21	0.70	0.70	166		
Soffer				0.21			178	0.06	0.06
ZnO·M2									
Mayadas-Shatzkes				0.20	0.88		147		
Sambles	5.58	6.10	0.39	0.20	0.87	0.87	147		
Soffer				0.13			167	0.09	0.09

Table 5.7 Results of the resistivity fit of the annealed single crystal based samples, without and with ZnO-met buffer layers, and of the prototype LINA and MISSTIC references, obtained by fitting the resistivity variation in temperature with three different models : Mayadas-Shatzkes, Sambles and Soffer. Both room-temperature resistivities determined via the 4-points method (ρ_{4P}) and by temperature dependent resistivity set up (ρ_{300K}) are reported.

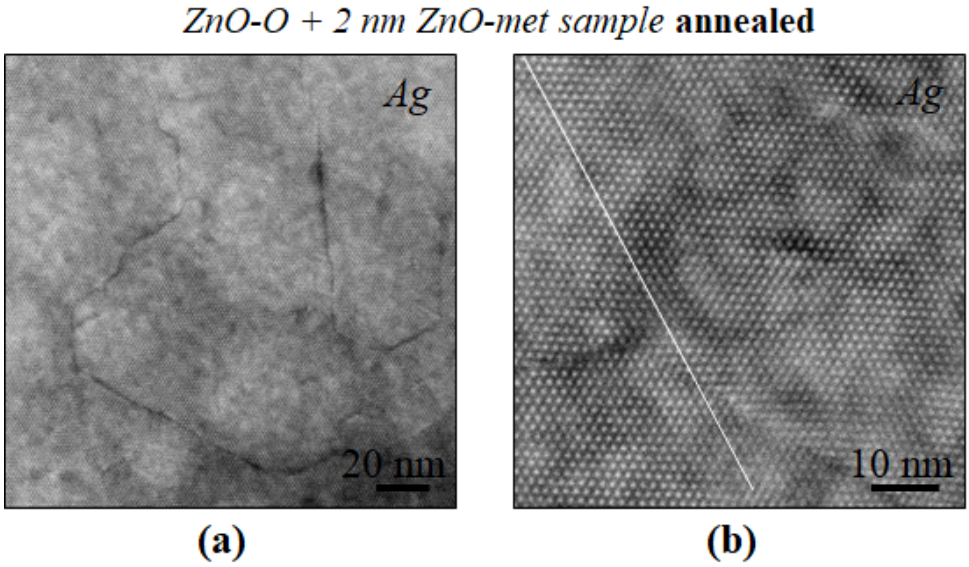

Figure 5.16 (a-b) STEM plane view of a annealed *ZnO-O + 2 nm ZnO-met buffer* sample. The clear Moiré pattern originates from the hexagon/hexagon epitaxy as sketched in Fig. (5.17)-b. The periodicity of $\sim$ 1.6 nm corresponds to the overlap of atomic columns of ZnO and Ag as shown in Fig. (5.17)-b. The line in figure (b) shows that darker areas correspond to anti-phase domain boundary delineating domains of a few tens of nanometres.

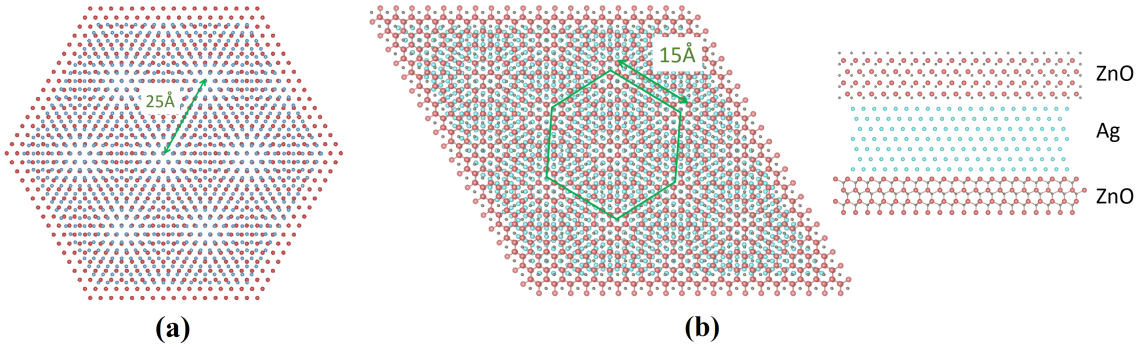

Figure 5.17 (a) Moiré pattern and coincidence site lattice of the -11 % misfit hexagon/hexagon epitaxy for the interface plane. The periodicity is 2.5 nm. Blue balls represents the unit cell in the Ag(111) plane of the interface and the red ones to that of ZnO(0001). (b) Moiré pattern of 1.5 nm induced by the atomic columns for ZnO/Ag/ZnO full stack in hexagon/hexagon orientation. The number of monolayers that does not represent the actual thicknesses have been selected just for visibility. Ag, Zn and O atoms are shown as blue, grey and red balls.

Annealed **ZnO-O + 2nm ZnO-met**								
	ρ_{res}^{grain} [$\mu\Omega$**cm**]	**R**	p_1	p_2	Θ_D [**K**]	h_1 [**nm**]	h_2 [**nm**]	D [**nm**]
Mayadas-Shatzkes		0.02	0.61		151			
Sambles	0.11	0.02	0.61	0.61	151			50
Soffer		0.06			196	0.19	0.04	
Mayadas-Shatzkes		0.04	0.61		151			
Sambles	0.11	0.04	0.61	0.61	151			100
Soffer		0.11			196	0.19	0.04	

Table 5.8 Electrical parameters obtained for the annealed *ZnO-O + 2 nm ZnO-met buffer* single crystal based stacks obtained by fitting the resistivity in temperature with three different models (Mayadas-Shatzkes, Sambles and Soffer) and varying the used lateral grain size value.

5.4 In summary

The chapter showed that the introduction of a thin ZnO-met buffer at the surface of the ZnO single crystal improves dramatically the structural and electrical properties of the silver film. The samples showed outstanding biaxial textured metallic film, with extremely low sheet resistance, reaching the record resistivity of 3.3 $\mu\Omega$cm before annealing dropping to 2.5 $\mu\Omega$cm after thermal treatment. These values set a lower bound for actual industrial low-emissive coatings which are today characterized by a resistivity 20% higher than single crystal sample before annealing (4.2 $\mu\Omega$cm) and 30% after annealing (3.6 $\mu\Omega$cm).

The gap in resistivity between crystal and glass-based samples was assigned, not only to larger grains, but also to lower grain boundary angles induced by the epitaxy at the interface. This translates into a reflection coefficient close zero and a resistivity only dominated by interface scattering before and after annealing. Whatever the sample is, glass or crystal-based, the thermal treatment reduces the intra-grain contribution to resistivity. But surprisingly, after annealing, the probability of out-of-specular interface scattering is worse for single crystals than for glass-based references at the opposite of their roughnesses.

Diffraction and electron microscopy pointed clearly at an hexagon/hexagon epitaxy with a weakly strained film. The epitaxial relationship and its effect on the Ag film texture is independent of the crystal termination. The ZnO-met buffer even smooths out their difference in terms of p-factor.

Conclusions and perspectives

General conclusions

This study falls within the industrial context of low-emissive silver-based coatings, grown by sputtering deposition at the surface of glass, and designed to improve the thermal insulation of windows. Since their far infra-red reflection scales with the electrical conductivity of the metallic film, this work aimed at identifying, through structural characterisations, the main mechanisms related to confinement that hinder the electron transport. More specifically, it focused on understanding the relative role, in the resistivity, of interface scattering and grain boundary reflectivity for electrons. In particular, the role of the in-plane texture induced by the ZnO seed layer was explored with simplified model stacks. For this purpose, R&D polycristalline sputtered coatings (*i.e.* glass/Si_xN_y/ZnO(seed)/[blocker]/Ag/[blocker]/ZnO(capping)/Si_xN_y where [...] stand for an optional layer) were compared to epitaxial films grown on ZnO(0001) single crystals Zn- or O-terminated (*i.e.* ZnO(0001)/[ZnO(buffer)]/Ag/ZnO(caping)/Si_xN_y), the orientation of which reproduces the out-of-plane texture of the formers. On crystals, the hetero-epitaxial growth of the metal was eased by applying an optimized sputtering/annealing preparation method of the surface to achieve biaxially textured silver films with outstanding structural and electrical properties. Thanks to the combinations of techniques (XRD, AFM and TEM), the structural characteristics of the coating, including interface roughnesses, were scrutinized and correlated to the room-temperature stack resistivity. Transport measurements in temperature turned to be relevant in unfolding the interfaces and grain boundaries in electron scattering. This could be achieved by analysing data with resistivity models of Mayadas-Shatzkes type that could reproduce soundly general trends.

On ZnO(0001) single crystals, whatever the termination Zn- or O-, all diffraction analysis as well as TEM imaging undoubtedly identified an hexagon/hexagon epitaxial relationship. Despite its large lattice mismatch of -11.5 % with the substrate, the film is poorly strained (Fig. (3)), maybe because of the existence of a long-range 2.5 nm interface coincidence lattice for $(9 \times 9)_{Ag}$ on $(8 \times 8)_{ZnO}$ surface unit cells. The reason of the domination of the hexagon/hexagon orientation over the 30°-rotated one with a lower misfit of $+2.5$ % escaped to the present study, but was previously assigned to the metal nucleation and growth along polar steps of the substrate surface. Deposited on a polycrystalline ZnO film showing intrinsically a $\vec{c}$-axis out-of-plane texture, silver is brought to grow with a preferential (111) out-of-plane orientation, although the texture is not as clear cut as on single crystal. Only some clues, such as the correlation between the in-plane ZnO and Ag lattice parameters after annealing, (Fig. (3)) and some traces of Moiré pattern in TEM images (Fig. (3.11)), pointed at a similar hexagon/hexagon epitaxy. Nevertheless, it should be reminded that the lattice distortion could also originate from extrinsic growth processes related to the polycrystalline state of the film.

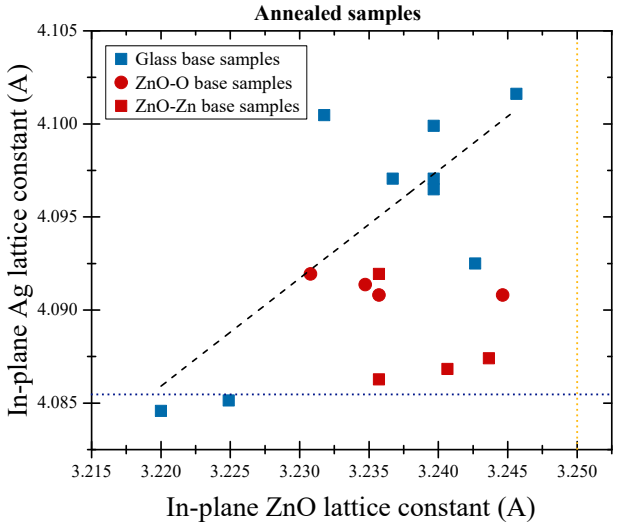

Figure 3 Relation between the in-plane lattice parameters of silver and zinc oxide of all analysed samples after annealing. The bulk silver lattice constant value of $a_{Ag}^{bulk} = 4.085$ Å, is represented with a blue dashline. The orange dashline correspond to the ZnO in-plane bulk parameter $a_{ZnO}^{bulk} = 3.250$ Å.

Owing to the fixed metal thickness of 12 nm, all Ag films involve, on average, one grain in their thickness. By comparing all the studied coatings, it appeared that the zinc oxide seed layer does not determine only the orientation of the metallic film, but depending on its nature (polycrystalline, single crystal, ZnO or AZO) and of its quality (surface roughness, crystallinity, texture, lateral grain size, etc...), it directly drives the structural and topographical properties of silver.

In classical glass-based coatings, the polycrystalline ZnO seed layer induces the growth of a polycrystalline Ag film characterized by small grains, of an average lateral size of ~ 7 nm before annealing (~ 14 nm after) only partially (111) textured along the out-of-plane direction but completely randomly oriented in-plane. The in-plane domain size and the out-of-plane orientation of the metal grains follow those of the seed layer, a finding assigned to epitaxy at the interface. The best silver quality, although also sensitive to the deposition machine, was obtained for films produced from a ceramic ZnO:Al target and not in reactive mode. On a ZnO(0001) single crystal, characterized by a smooth surface and the absence of grain boundaries, the silver film structural quality is tremendously improved. Compared to glass references, the metal presents out-standing crystallinity with way higher in-plane and out-of-plane textures and larger in-plane grain size (~ 15 nm before annealing and ~ 20 nm after). However, roughnesses at seed and capping interfaces do not drastically differ and are of the same order of magnitude (~ 0.5 nm).

In line with the variations of their structural and topographical characteristics, glass-based and single crystal-based samples present distinct transport properties. Thanks to the variety of samples and the numerous X-ray supporting data, the fit of resistivity in temperature provided consistent and clear explanations beyond error bars and the obvious scaling with the grain boundary density. With similar intra-grain defect concentration, the single crystal based samples distinguishes from glass-based samples by their extremely low R-parameter value, corresponding to a very low electron reflection coefficient at grain boundaries. This is a direct consequence of the correlation established between the grain boundary scattering channel and the in-plane tex-

ture of the silver grains *i.e.* the misorientation of the lattices of adjacent grains (the so-called grain boundary angle). This hypothesis is corroborated by the correlation observed between the texture parameters and resistivity. As a result, in single crystal based samples, interface scattering is the predominant scattering mechanism hindering conductivity. On the other hand, the loss of silver grain orientation in the in-plane direction results for glass-based samples in a strong increase of the R-coefficient. Hence, for these samples, resistivity is the result of the combined contribution of grain boundary and interface scattering channels. This latter can gain relevance if the interface is modified, either by removing the ZnO seed layer or by introducing a blocker film. Beyond these cases, for all samples, even when $R \simeq 0$, no clear-cut correlation between interface roughnesses and resistivity could be established whatever the analysis model. Of course, this could be due to uncertainty in the roughness determination and to the small range of explored values. Alternative explanations are (i) the extreme sensitivity of interface scattering to roughness or to its in-plane correlation length that is not taken into account in the models or (ii) the presence of interface states that lead to a loss of coherence of the electronic wave upon reflection or to local variation of the Schottky barrier height. This could explain why the p-parameter in crystal-based samples turned out to be worse than that of sputtered ZnO films. To sum up, larger grain boundary density and R-parameter explains larger resistivity in glass-based samples.

To improve further the sheet resistivity of model systems, a ZnO buffer layer of variable thickness ($2 - 10$ nm), was introduced between the single crystal substrate and the silver film. Probably, by smoothing the surface of the substrate and covering surface imperfections, the presence of a very thin buffer (2 nm) strongly enhances the already out-standing structural and resistivity properties of the silver film. Thus, better defined biaxial texture and larger domain sizes were observed. In terms of electrical transport, this resulted in a further decrease of the R-parameter and a predominance of interface scattering. Underlining the different nature of the silver interfaces, an asymmetry between the two scattering parameters p_1 and p_2 was found. Such a sample reached challenging record resistivity value of $\rho = 3.3\,\mu\Omega$.cm, 20% lower than a currently marketed industrial low-emissivity coating ($\rho = 4.2\,\mu\Omega$.cm).

Already used in the glazing industry, thermal treatment enhances the quality and the electrical performance of the coating by improving grain orientation, enlarging grain size through sintering and healing interface and intra-grain defects. As a result, a gain of resistivity of the order of ~ 20 % is usually achieved. In glass-based samples, the annealing induces a strong lowering of the interface scattering probability but a worsening of the electrons reflection at grain boundaries. If the average grain size increase is due to the sintering of adjacent grains with low-angle relative orientation, the increase of R is caused by the survival of the larger angle ones and, in the case of a blocker layer at the interface, to the favoured accumulation of a $Zn_xNi_yO_z$ compound at grain boundaries. For single crystal based samples, coarsening is still present leading to silver films with nearly no grain boundary reflection. Despite a lower annealing temperature (350°C instead of 650°C), a world record value of $\rho = 2.5\,\mu\Omega$.cm, 30 % lower than the annealed industrial reference ($\rho = 3.6\,\mu\Omega$.cm) was reached for the *ZnO-O + 2 nm buffer* sample.

At last, throughout all this study, no clear role of crystal termination could be evidenced ; differences in terms of interface scattering are even smoothed by the ZnO buffer.

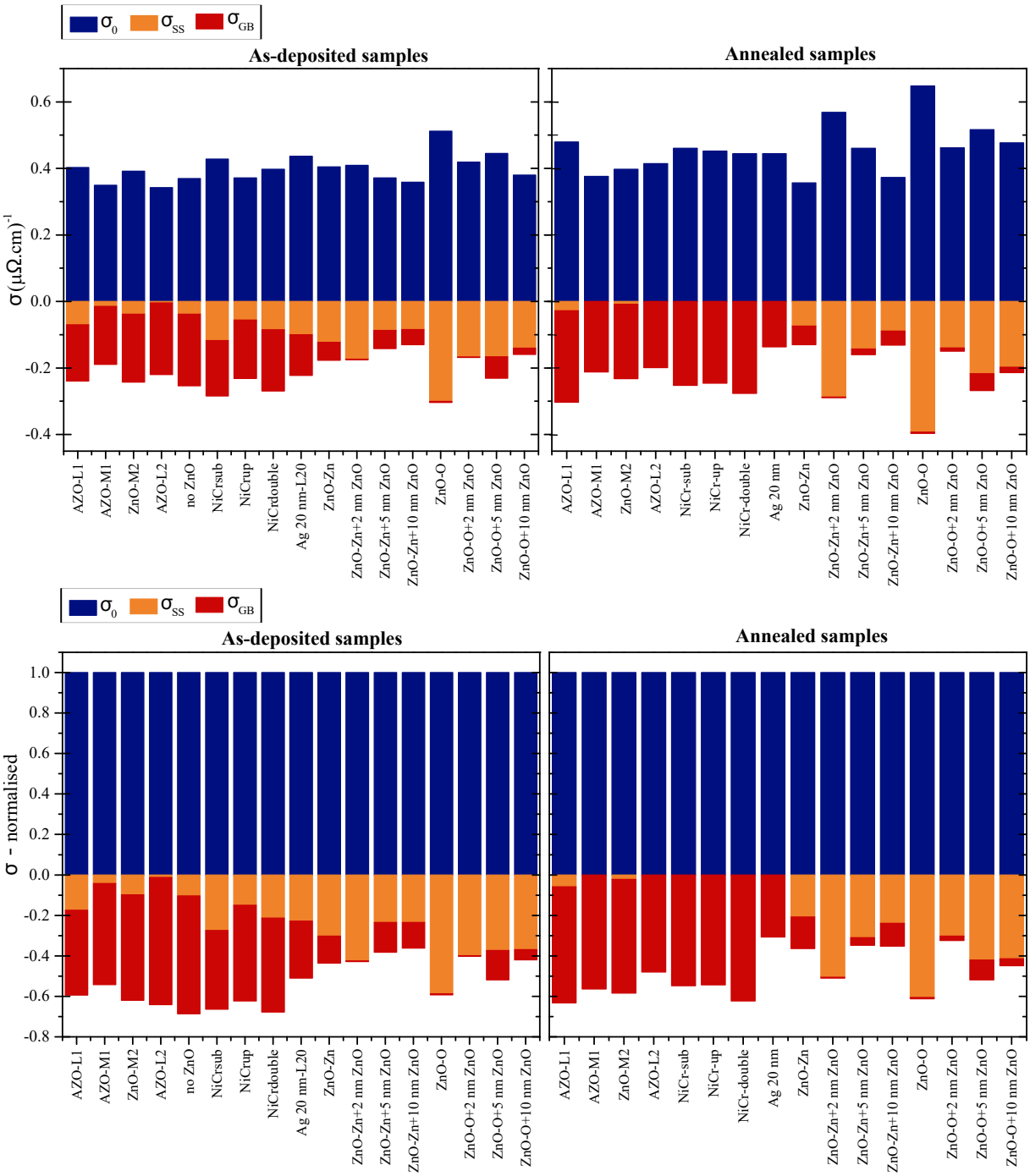

Figure 4 Reduction of bulk conductivity (σ_0; blue bar) from interface (σ_{SS}; orange bar) and from grain boundaries (σ_{GB}; red bar) for all the studied samples before (left) and after (right) annealing. Values correspond to the room-temperature contribution in the classical Mayadas-Shatkes model (see Eq. (5.1)). (Top) raw values, (Bottom) after normalisation to σ_0. It should be remained that the fit error associated to the *ZnO-O* single crytsal-based sample is larger than the other samples (see Sec. (4.9)).

To conclude, the relative role of the scattering channels at interfaces and at grain boundaries is globally summarized in Fig. (4) for all samples. These room-temperature conductivity values obtained from the fits of the resistivity curves with the classical Mayadas-Shatkes model encompass the effects of grain size, residual bulk resistivity and R, p-parameters. Counterintuitively, the figure is plotted in conductivity instead of resistivity, since according to Eq. (1.33) and Eq. (1.36), only the total film conductivity $\sigma_f = 1/\rho_f$ can be decomposed as :

$$\sigma_f = \sigma_0 - \sigma_{GB} - \sigma_{SS}, \tag{5.1}$$

where $\sigma_0 = 1/\rho_0$ is the bulk conductivity including intra-grain defects and phonons (Eq. (1.29)), $\sigma_{GB} = 1/(\rho_0 - \rho_{GB})$ is the term related to grains (term in α in Eq. (1.33)) and σ_{SS} is that due to interfaces (integral term in Eq. (1.36) that vanishes when $p = 1$). Physically, each channel of scattering induces a decrease of conductivity from the bulk value (minus sign in Eq. (5.1)). Fig. (4) illustrates clearly (i) the hierarchy of conductivity between glass-based references and single crystals (larger but negative σ_{GB}/σ_{SS}-terms) and (ii) the dominating role of interfaces for single crystal based samples (no σ_{GB}-term due to $R \simeq 0$) and of grain boundaries for reference samples.

Perspectives : in-plane texturization of the ZnO seed layer by the IBAS technique

All our results showed that there is still room for improvement of the resistivity of low-emissive coatings and that the in-plane texture is a key to achieve it ! Since the textures of ZnO and Ag are closely related, a solution would be to texture in-plane the seed layer using a modified sputtering process referred to as Ion Beam Assisted Sputtering (IBAS) (or more generally on Ion Beam Assisted Deposition, IBAD). During an IBAD growth, the film is bombarded in parallel with a high energy directional ion beam from an external ion source. This bombardment has a significant impact on the initial growth stage of the film through the preferred removal of atoms along given atomic planes, thus favouring a given crystallographic orientation compared to the ion beam direction. Its influence depends on the ion mass, energy and current density as well as on all the sputtering deposition parameters.

The process, more frequently combined with evaporation, or pulsed laser deposition, [239–242] was tested with sputtering growth by the group of Pr. M. Wuttig at RWTH Aachen University [3, 4] both for ZnO and MgO. A sketch of the IBAS set up available at the RWTH is shown in Fig. (5)-a. At an incidence angle of approximately 45°, the growing film can be *in situ* bombarded via Ar, N, Ne, O or Xe ions. In the PhD work of D. Kohl [3], it was demonstrated that highly out-of-plane crystallised ZnO films could be obtained on amorphous substrate but with some in-plane texture (Fig. (5)-b). Films were grown starting from a metallic-Zn target at a constant DC discharge current of 250 mA in a reactive Ar/O_2 atmosphere in oxide deposition mode. During sputtering, the pressure was maintained at 2 μbar, to minimize the collision between the auxiliary ions and the growing film. In addition, the target was covered with a ring-shaped metallic shield, with the aim of protecting the sample from the damage induced by negatively charged oxygen ions created at the target racetrack [91](Fig. (5)-a). The assisted bombardment was performed with Xe ions of an average energy of 180 eV and a current density of 11.5 $\mu A/cm^2$. With these conditions, the ion to atom arrival ratio at the substrate was estimated to be 2 % for a deposition rate of $0.1 - 0.15$ nm/s.

On the basis of D. Kohl results, we tried to reproduce the same IBAS ZnO films (Fig. (6)). Trying to achieve the perfect balance between atom deposition and removal due to ion bombardment, the

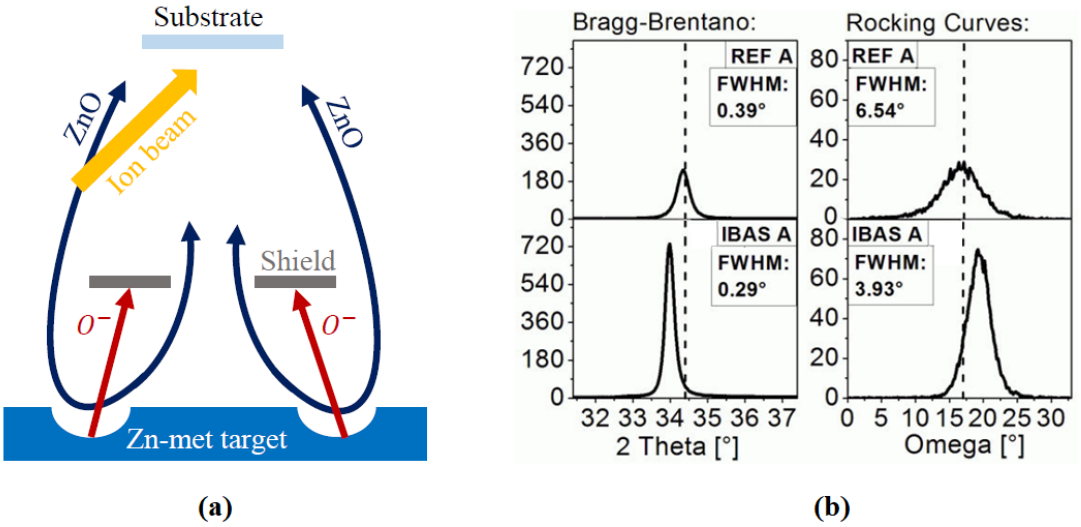

Figure 5 (a) Schematics of the IBAS sputtering machine showing the ion beam and the shield effect. (b) $\theta-2\theta$ XRD (002) peak of ZnO films grown without (bottom) and with (top) IBAS (film thickness 80 nm) [3].

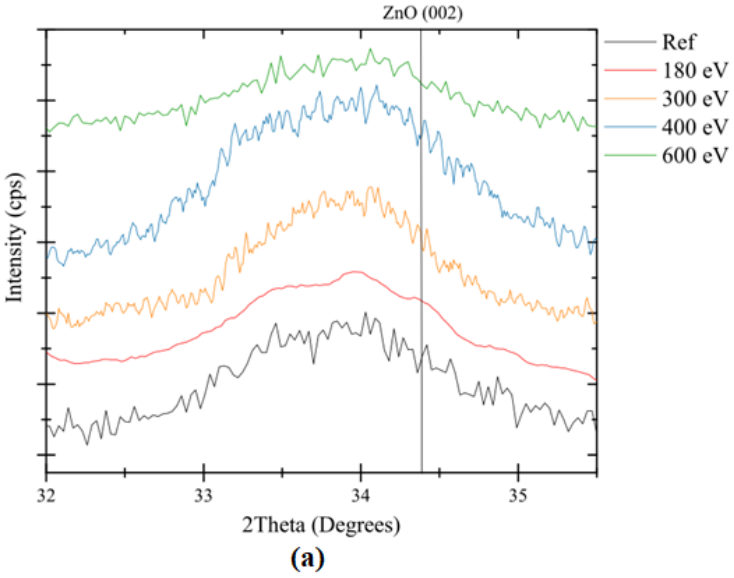

Sample	$RC_{ZnO(002)}$
Ref	18°
180 eV	14°
300 eV	17°
400 eV	18°
600 eV	17°

Figure 6 (a) $\theta - 2\theta$ ZnO(002) peaks of IBAS-ZnO layers deposited for different ion energy during this thesis (film thickness 50 nm) (b) Corresponding rocking curve width.

experimental parameter space was explored without however obtaining the perfect combo that could visibly enhance the out-of-plane texture of the oxide film as shown previously (Fig. (5)-b). One explanation of the failure could be related to the use of a suitable shielding device positioned on top of the target (Fig. (5)-a). Compared to a reference oxide layer of the same thickness and sputtered in the same conditions (only without the additional ion bombardment), our IBAS-ZnO present very similar density, surface roughness and $\theta - 2\theta$ peak shift. At the opposite of Kohl results where the IBAS-ZnO $\theta - 2\theta$ peak was characterized by a strong shift towards lower diffraction angle, in our case, the oxide layer grows under out-of-plane tensile strain probably resulting from a higher number of interstitial oxygen atoms. Since the oxygen flow was calibrated

based on the hysteresis curve of the sputtered material, it was not possible to further reduce it. Discrepancies were therefore assigned to a different shield device. Nevertheless, encouragingly, when an IBAS-ZnO was used as a buffer layer for an AZO film, an intensity increase was observed in the XRD resulting from an out-of-plane texture improvement. Further work is thus required to fully explore this promising direction.

Although, the academic studies concentrate on small samples of a few cm^2 in size, an industrial application of the IBAD process is in principle technically feasible. The company *Beam alloy Technology* uses IBAD to deposit hard coatings like TiN on surface areas up to (45×20) cm^2 [243]. By giving rise to biaxially textured MgO, IBAD was also employed by the company *SuperPower Inc.* to produce high temperature superconductors coated wires over areas larger (60×8) cm^2 [244].

List of abbreviations

OP : Out-of-plane direction
IP : In-plane direction

$\boldsymbol{d}$ (nm) : Film thickness in the models of Mayadas-Shatzkes type
$\mathbf{D}_{\boldsymbol{S,OP}}$ (nm) : Vertical coherent domain size determined by the Scherrer equation from a radial $\theta - 2\theta$ scan on Ag(111) or ZnO(002)
$\mathbf{D}_{\boldsymbol{\theta-2\theta,OP}}$ (°) : Vertical "grain" size obtained by deconvolution of the out-of-plane microstrain on the $\theta - 2\theta$ Ag (111) and (222) peaks

D (nm) : Distance between two grain boundaries in the Mayadas-Shatzkes model
$\mathbf{L}_{S,IP}$ (nm) : Lateral coherent domain size determined by Scherrer equation from radial GIXRD scan on Ag(220) or ZnO(100)

$\mathbf{RC}_{Ag(111)}$ (°) : Rocking curve width of the Ag(111) peak
$\mathbf{RC}_{ZnO(002)}$ (°) : Rocking curve width of the ZnO(002) peak
Mosaicity (°) : Out-of-plane disorientation of the grains obtained by deconvolution of the lateral "grain" size from rocking curves on Ag (111) and (222) peaks

$\boldsymbol{\Phi_{Ag(220)}}$ (°) : Width of the Ag(220) ϕ-scan peak

$\mathbf{TC}_{Ag(220)}$ (%) : Texture coefficient, or Lotgering factor, of the Ag(220) peak
$\mathbf{TC}_{ZnO(110)}$ (%) : Texture coefficient, or Lotgering factor, of the ZnO(110) peak
$\mathbf{TC}_{ZnO(100)}$ (%) : Texture coefficient, or Lotgering factor, of the ZnO(100) peak

$\boldsymbol{\varepsilon_{OP}}$: Out-of-plane microstrain in grains obtained by deconvolution of the vertical "grain" size on $\theta - 2\theta$ Ag (111) and (222) peaks
$\boldsymbol{\varepsilon_{IP}}$: In-plane microstrain in grains obtained by deconvolution of the lateral "grain" size on available peaks in GIXRD

$\boldsymbol{\varepsilon_{33}}$: Out-of-plane macrostrain determined via the shift of $\theta - 2\theta$ diffraction peak from the literature value
$\boldsymbol{\varepsilon_{11}} = \boldsymbol{\varepsilon_{22}}$: In-plane macrostrain determined via the shift of *GIXRD* diffraction peak shift from the literature value

$\boldsymbol{a_{Ag}^{bulk}}$ (Å or nm) : Silver bulk lattice parameter of 4.085 Å
$\boldsymbol{a_{OP-Ag}}$ (Å or nm) : Cubic lattice parameter of the sputtered silver film in the out-of-plane direction
$\boldsymbol{a_{IP-Ag}}$ (Å or nm) : Cubic lattice parameter of the sputtered silver film in the in-plane direction
$\boldsymbol{c_{ZnO}^{bulk}}$ (Å or nm) : Out-of-plane zinc oxide bulk lattice parameter of 5.206 Å

$\boldsymbol{a_{ZnO}^{bulk}}$ (Å or nm) : In-plane zinc oxide bulk lattice parameter of 3.250 Å
$\boldsymbol{c_{OP-ZnO}}$ (Å or nm) : Out-of-plane lattice parameter of the sputtered zinc oxide film
$\boldsymbol{a_{IP-ZnO}}$ (Å or nm) : In-plane lattice parameter of the sputtered zinc oxide film

$\mathbf{RMS}_{XRR}$ (nm) : Surface roughness determined through X-ray reflectivity
$\mathbf{RMS}_{AFM}$ (nm) : Surface roughness determined through AFM
$\mathbf{RMS}_{Soffer}$ (nm) : Surface roughness obtaining from the Soffer model fit of temperature dependent resistivities

$\mathbf{R}_{\square-4P}$ (Ω) : Room-temperature sheet resistance determined through 4-points method (via *Napson* apparatus)
$\boldsymbol{\rho_{4P}}$ ($\mu\Omega$.cm) : Room-temperature resistivity determined through the 4-points method (via *Napson* apparatus)
$\boldsymbol{\rho_{300\ K}}$ ($\mu\Omega$.cm) : Room-temperature resistivity determined through temperature dependent measurements

$\boldsymbol{\Theta_D}$ (K) : Debye temperature
$\boldsymbol{R}$: Grain boundary reflection coefficient in the Mayadas-Shatzkes model
$\boldsymbol{p}$: Interface specularity parameter in the Mayadas-Shatzkes model
$\boldsymbol{p_{1,2}}$: Specularity parameters that take into account the asymmetry of the upper and lower interfaces
$\boldsymbol{h_{1,2}}$ (nm) : Interface roughnesses resulting from Soffer fit that take into account the asymmetry of the upper and lower interfaces
$\boldsymbol{\rho_{res}^{grain}}$ ($\mu\Omega$.cm) : Intra-grain resistivity at $T = 0$ K
$\boldsymbol{l}$ (nm) : Mean free path of electrons at $T = 300$ K equal to 38 nm in bulk silver

Bibliography

[1] H. Arribart, *Couches conductrices transparentes. Applications aux vitrages isolants et aux vitrages actifs.* ESPCI ParisTech, 2011. iii

[2] E. Hagen et H. Rubens, « Über beziehungen des reflexions-und emissionsvermögens der metalle zu ihrem elektrischen leitvermögen », *Annalen der Physik*, vol. 316, no. 8, p. 873–901, 1903. iii

[3] D. Kohl, *The influence of energetic bombardment on the structure formation of sputtered zinc oxide films.* Thèse de doctorat, RWTH Aachen University, Germany, 2011. iv, v, 10, 18, 21, 86, 89, 119, 173, 174

[4] E.-R. Sittner, *Understanding and optimizing the electrical transport in silver thin films for the use as heat insulation glass coatings.* Thèse de doctorat, RWTH Aachen University, Germany, 2021. iv, 11, 21, 25, 56, 89, 90, 101, 173

[5] J. E. Greene, « Tracing the 5000-year recorded history of inorganic thin films from 3000 BC to the early 1900s AD », *Applied Physics Reviews*, vol. 1, no. 4, p. 041302, 2014. 2

[6] J. E. Greene, « Tracing the recorded history of thin-film sputter deposition : From the 1800s to 2017 », *Journal of Vacuum Science & Technology A : Vacuum, Surfaces, and Films*, vol. 35, no. 5, p. 05C204, 2017. 2

[7] M. Ohring, *Materials Science of Thin Films.* Elsevier, 2001. 2, 5, 7, 8, 13

[8] E. Bauer, « Phänomenologische theorie der kristallabscheidung an oberflächen. i », *Zeitschrift für Kristallographie-Crystalline Materials*, vol. 110, no. 1-6, p. 372–394, 1958. 3

[9] J. Venables, « Rate equation approaches to thin film nucleation kinetics », *Philosophical Magazine*, vol. 27, no. 3, p. 697–738, 1973. 3, 6

[10] E. Seebauer et C. Allen, « Estimating surface diffusion coefficients », *Progress in Surface Science*, vol. 49, no. 3, p. 265–330, 1995. 4

[11] T. Michely et J. Krug, *Islands, mounds and atoms*, vol. 42. Springer Science & Business Media, 2012. 5, 6

[12] D. Adamovic, E. Münger, V. Chirita, L. Hultman et J. Greene, « Low-energy ion irradiation during film growth : ticstic pathways leading to enhanced adatom migration rates », *Applied Physics Letters*, vol. 86, no. 21, p. 211915, 2005. 6

[13] M.-A. Hasan, S. Barnett, J.-E. Sundgren et J. Greene, « Nucleation and initial growth of In deposited on Si_3N_4 using low-energy ($\leq$ 300 eV) accelerated beams in ultrahigh vacuum », *Journal of Vacuum Science & Technology A : Vacuum, Surfaces, and Films*, vol. 5, no. 4, p. 1883–1887, 1987. 6

[14] J. A. Venables, G. D. T. Spiller et M. Hanbücken, « Nucleation and growth of thin films », *Reports on Progress in Physics*, vol. 47, p. 399–459, 1984. 6

[15] J. Venables et J. Harding, « Nucleation and growth of supported metal clusters at defect sites on oxide and halide (001) surfaces », *Journal of Crystal Growth*, vol. 211, p. 27–33, 2000. 7

[16] P. Meakin, « Droplet deposition, growth and coalescence », *Reports on Progress in Physics*, vol. 55, p. 157–240, 1992. 7

[17] G. Jeffers, M. A. Dubson et P. M. Duxbury, « Island to percolation transition during growth of metal films », *Journal of Applied Physics*, vol. 75, p. 5016–5020, 1994. 7

[18] M. Zinke-Allmang, « Phase separation on solid surfaces : nucleation, coarsening and coalescence kinetics », *Thin Solid Films*, vol. 346, p. 1–68, 1999. 7

[19] P. Ghekiere, *Structure evolution of biaxially aligned thin films deposited by sputtering*. Thèse de doctorat, Ghent University, 2007. 7, 8, 10

[20] S. Mahieu, P. Ghekiere, D. Depla et R. De Gryse, « Biaxial alignment in sputter deposited thin films », *Thin Solid Films*, vol. 515, no. 4, p. 1229–1249, 2006. 7, 8, 9, 10, 11, 14

[21] C. V. Thompson, « Structure evolution during processing of polycrystalline films », *Annual Review of Materials Science*, vol. 30, no. 1, p. 159–190, 2000. 7, 8

[22] S. Grachev, M. De Grazia, E. Barthel, E. Søndergård et R. Lazzari, « Real time monitoring of nanoparticle film growth at high deposition rate with optical spectroscopy of plasmon resonances », *Journal of Physics D : Applied Physics*, vol. 46, p. 375305–375315, 2013. 7

[23] J. A. Thornton, « The microstructure of sputter-deposited coatings », *Journal of Vacuum Science& Technology A : Vacuum, Surfaces, and Films*, vol. 4, no. 6, p. 3059–3065, 1986. 8

[24] M. Wuttig, *Strukturbildung beim reaktiven Sputtern dünner Filme*. EFDS WorkshopDresden, 2015. 8

[25] P. Ghekiere, S. Mahieu, G. De Winter, R. De Gryse et D. Depla, « Influence of the deposition parameters on the biaxial alignment of MgO grown by unbalanced magnetron sputtering », *Journal of Crystal Growth*, vol. 271, no. 3-4, p. 462–468, 2004. 10

[26] M. Saraiva et D. Depla, « Texture and microstructure in co-sputtered Mg-MO (M= Mg, Al, Cr, Ti, Zr, and Y) films », *Journal of Applied Physics*, vol. 111, no. 10, p. 104903, 2012. 10

[27] D. Hull et D. J. Bacon, *Introduction to dislocations*, vol. 37. Elsevier, 2011. 11, 147, 149

[28] P. Lejcek, *Grain boundary segregation in metals*, vol. 136. Springer Science & Business Media, 2010. 11, 12

[29] W. T. Read et W. Shockley, « Dislocation models of crystal grain boundaries », *Physical Review*, vol. 78, no. 3, p. 275, 1950. 12, 13

[30] C. M. Barr, L. Barnard, K. Hattar, K. Unocic, D. Morgan et M. Taheri, *Dependence of Grain Boundary Structure on Radiation Induced Segregation and Void Denuded Zones in a Model Ni-Cr Alloy*. Drexel University, 2010. 12

[31] I. Nakamichi, « Electrical resistivity and grain boundaries in metals », *in Materials Science Forum*, vol. 207, p. 47–58, Trans Tech Publ, 1996. 13

[32] T.-H. Kim, X.-G. Zhang, D. M. Nicholson, B. M. Evans, N. S. Kulkarni, B. Radhakrishnan, E. A. Kenik et A.-P. Li, « Large discrete resistance jump at grain boundary in copper nanowire », *Nano Letters*, vol. 10, no. 8, p. 3096–3100, 2010. 13

[33] T.-H. Kim, D. M. Nicholson, X.-G. Zhang, B. M. Evans, N. S. Kulkarni, E. A. Kenik, H. M. Meyer, B. Radhakrishnan et A.-P. Li, « Structural dependence of grain boundary

resistivity in copper nanowires », *Japanese Journal of Applied Physics*, vol. 50, no. 8S3, p. 08LB09, 2011. 13

[34] M. César, D. Liu, D. Gall et H. Guo, « Calculated resistances of single grain boundaries in copper », *Physical Review Applied*, vol. 2, no. 4, p. 044007, 2014. 13

[35] A. Karolik et A. Luhvich, « Calculation of electrical resistivity produced by dislocations and grain boundaries in metals », *Journal of Physics : Condensed Matter*, vol. 6, no. 4, p. 873, 1994. 13, 128, 129, 130

[36] A. Banerjee, C. Ghosh, K. Chattopadhyay, H. Minoura, A. K. Sarkar, A. Akiba, A. Kamiya et T. Endo, « Low-temperature deposition of ZnO thin films on PET and glass substrates by DC-sputtering technique », *Thin Solid Films*, vol. 496, no. 1, p. 112–116, 2006. 13

[37] Y. Xia, P. Wang, S. Shi, M. Zhang, G. He, J. Lv et Z. Sun, « Deposition and characterization of AZO thin films on flexible glass substrates using DC magnetron sputtering technique », *Ceramics International*, vol. 43, no. 5, p. 4536–4544, 2017. 13

[38] P. Sigmund et M. Szymonski, « Temperature-dependent sputtering of metals and insulators », *Applied Physics A*, vol. 33, no. 3, p. 141–152, 1984. 14

[39] J. Voronkoff, *Interactions dans les empilements de couches NiCr/ZnO déposées par pulvérisation : impact couplé des paramètres de dépôt et de recuit.* Thèse de doctorat, Sorbonne University, France, 2020. 14, 38, 56, 81, 82, 84, 86, 105

[40] D. Depla, S. Mahieu *et al.*, *Reactive sputter deposition*, vol. 109. Springer, 2008. 15, 16

[41] N. Laegreid et G. Wehner, « Sputtering yields of metals for Ar^+ and Ne^+ ions with energies from 50 to 600 eV », *Journal of Applied Physics*, vol. 32, no. 3, p. 365–369, 1961. 15

[42] Y. Tsuda, H. Omoto, K. Tanaka et H. Ohsaki, « The underlayer effects on the electrical resistivity of Ag thin film », *Thin Solid Films*, vol. 502, no. 1-2, p. 223–227, 2006. 15

[43] D. Depla, S. Mahieu et R. D. Gryse, « Depositing aluminium oxide : a case study of reactive magnetron sputtering », *in Reactive sputter deposition*, p. 153–197, Springer, 2008. 15

[44] J. Sarkar, *Sputtering materials for VLSI and thin film devices.* William Andrew, 2010. 16

[45] O. Tuna, Y. Selamet, G. Aygun et L. Ozyuzer, « High quality ITO thin films grown by DC and RF sputtering without oxygen », *Journal of Physics D : Applied Physics*, vol. 43, no. 5, p. 055402, 2010. 16

[46] K. Fukuda, S. H. N. Lim et A. Anders, « Coalescence of magnetron-sputtered silver islands affected by transition metal seeding (Ni, Cr, Nb, Zr, Mo, W, Ta) and other parameters », *Thin Solid Films*, vol. 516, no. 14, p. 4546–4552, 2008. 17, 39, 84

[47] A. Bingel, O. Stenzel, P. Naujok, R. Müller, S. Shestaeva, M. Steglich, U. Schulz, N. Kaiser et A. Tünnermann, « AZO/Ag/AZO transparent conductive films : correlation between the structural, electrical, and optical properties and development of an optical model », *Optical Materials Express*, vol. 6, no. 10, p. 3217–3232, 2016. 17

[48] R. Hong, X. Jiang, B. Szyszka, V. Sittinger, S. Xu, W. Werner et G. Heide, « Comparison of the ZnO : Al films deposited in static and dynamic modes by reactive mid-frequency magnetron sputtering », *Journal of Crystal Growth*, vol. 253, no. 1-4, p. 117–128, 2003. 17

[49] W. a. a. Hirschwald, vol. 7*in Current Topics in Material Science*, chapitre Zinc Oxide : properties and behaviour of the bulk, the solid/vacuum and solid/gas interfaces. Amsterdam, North Holland Publishing, 1981. 17, 18, 20

[50] R. M. Hewlett et M. A. McLachlan, « Surface structure modification of ZnO and the impact on electronic properties », *Advanced Materials*, vol. 28, no. 20, p. 3893–3921, 2016. 17

[51] H. Morkoç et Ü. Özgür, *Zinc oxide : fundamentals, materials and device technology*. John Wiley & Sons, 2008. 17

[52] O. Garcia-Martinez, R. Rojas, E. Vila et J. M. De Vidales, « Microstructural characterization of nanocrystals of ZnO and CuO obtained from basic salts », *Solid State Ionics*, vol. 63, p. 442–449, 1993. 18, 74, 75

[53] T. Nagata, T. Nakamura, R. Hayakawa, T. Yoshimura, S. Oh, N. Hiroshiba, T. Chikyow, N. Fujimura et Y. Wakayama, « Photoelectron spectroscopic study on monolayer pentacene thin-film/polar ZnO single-crystal hybrid interface », *Applied Physics Express*, vol. 10, no. 2, 2017. 18

[54] Ü. Özgür, Y. I. Alivov, C. Liu, A. Teke, M. Reshchikov, S. Doğan, V. Avrutin, S.-J. Cho et Morkoç, « A comprehensive review of ZnO materials and devices », *Journal of Applied Physics*, vol. 98, no. 4, p. 11, 2005. 18, 20

[55] C. Tang, M. J. Spencer et A. S. Barnard, « Activity of ZnO polar surfaces : an insight from surface energies », *Physical Chemistry Chemical Physics*, vol. 16, no. 40, p. 22139–22144, 2014. 18, 110

[56] S. J. Pearton, D. P. Norton, K. Ip, Y. W. Heo et T. Steiner, « Recent progress in processing and properties of ZnO », *Progress in Materials Science*, vol. 50, p. 293–340, 2005. 18, 20

[57] G. P. Mohanty et L. V. Azároff, « Electron density distributions in ZnO crystals », *The Journal of Chemical Physics*, vol. 35, no. 4, p. 1268–1270, 1961. 18

[58] A. Janotti et C. G. Van de Walle, « Oxygen vacancies in ZnO », *Applied Physics Letters*, vol. 87, no. 12, p. 122102, 2005. 18

[59] A. Janotti et C. G. Van de Walle, « Native point defects in ZnO », *Physical Review B*, vol. 76, no. 16, p. 165202, 2007. 18

[60] M. McCluskey et S. Jokela, « Sources of n-type conductivity in ZnO », *Physica B : Condensed Matter*, vol. 401, p. 355–357, 2007. 18

[61] K. Ellmer, « Transparent conductive zinc oxide and its derivatives », *in Handbook of transparent conductors*, p. 193–263, Springer, 2011. 18

[62] D. C. Look, D. Reynolds, C. Litton, R. Jones, D. Eason et G. Cantwell, « Characterization of homoepitaxial p-type ZnO grown by molecular beam epitaxy », *Applied Physics Letters*, vol. 81, no. 10, p. 1830–1832, 2002. 18

[63] J. Robertson, R. Gillen et S. Clark, « Advances in understanding of transparent conducting oxides », *Thin Solid Films*, vol. 520, no. 10, p. 3714–3720, 2012. 18

[64] P. Tasker, « The stability of ionic crystal surfaces », *Journal of Physics C : Solid State Physics*, vol. 12, no. 22, p. 4977, 1979. 19

[65] J. Goniakowski, F. Finocchi et C. Noguera, « Polarity of oxide surfaces and nanostructures », *Reports on Progress in Physics*, vol. 71, no. 1, p. 016501, 2007. 19, 38

[66] C. Noguera et J. Goniakowski, « Polarity in oxide nano-objects », *Chemical Reviews*, vol. 113, no. 6, p. 4073–4105, 2013. 19

[67] E. Chernysheva, *Zinc oxide growth and its interfaces with metals observed by photoemission*. Thèse de doctorat, University Pierre and Marie Curie, France, 2017. 19, 38, 102

[68] U. Diebold, L. V. Koplitz et O. Dulub, « Atomic-scale properties of low-index ZnO surfaces », *Applied Surface Science*, vol. 237, no. 1-4, p. 336–342, 2004. 19, 20

[69] M.-H. Du, S. Zhang, J. Northrup et S. C. Erwin, « Stabilization mechanisms of polar surfaces : ZnO surfaces », *Physical Review B*, vol. 78, no. 15, p. 155424, 2008. 19, 122

[70] S. Benedetti, I. Valenti, S. Valeri, S. Castilla, E. Touzé, Y. Bronstein, A. Toumar, F. Finocchi et R. Lazzari, « Polar-step driven metal nucleation and growth : the Ag/ZnO($10\bar{1}0$) case », *Journal of Physical Chemistry C*, vol. 124, p. 6130–6140, 2020. 19, 26, 122, 123

[71] F. Ostendorf, S. Torbrügge et M. Reichling, « Atomic scale evidence for faceting stabilization of a polar oxide surface », *Physical Review B*, vol. 77, no. 4, p. 041405, 2008. 19

[72] M. Valtiner, S. Borodin et G. Grundmeier, « Preparation and characterisation of hydroxide stabilised ZnO (0001)-Zn-OH surfaces », *Physical Chemistry Chemical Physics*, vol. 9, no. 19, p. 2406–2412, 2007. 19

[73] M. Valtiner, S. Borodin et G. Grundmeier, « Stabilization and acidic dissolution mechanism of single-crystalline ZnO(0001) surfaces in electrolytes studied by in-situ AFM imaging and ex-situ LEED », *Langmuir*, vol. 24, no. 10, p. 5350–5358, 2008. 19

[74] C. Wöll, « The chemistry and physics of zinc oxide surfaces », *Progress in Surface Science*, vol. 82, no. 2-3, p. 55–120, 2007. 19

[75] T. Becker, M. Kunat, C. Boas, U. Burghaus, C. Wöll *et al.*, « Interaction of hydrogen with metal oxides : the case of the polar ZnO(0001) surface », *Surface Science*, vol. 486, no. 3, p. L502–L506, 2001. 19

[76] R. Lindsay, C. A. Muryn, E. Michelangeli et G. Thornton, « Zno (0001^{-})–o surface structure : hydrogen-free (1×1) termination », *Surface science*, vol. 565, no. 2-3, p. L283–L287, 2004. 19

[77] J. V. Lauritsen, S. Porsgaard, M. K. Rasmussen, M. C. Jensen, R. Bechstein, K. Meinander, B. S. Clausen, S. Helveg, R. Wahl, G. Kresse *et al.*, « Stabilization principles for polar surfaces of ZnO », *ACS nano*, vol. 5, no. 7, p. 5987–5994, 2011. 19, 20

[78] T. Yanagitani et M. Kiuchi, « Control of in-plane and out-of-plane texture in shear mode piezoelectric ZnO films by ion-beam irradiation », *Journal of Applied Physics*, vol. 102, no. 4, p. 044115, 2007. 21

[79] K. Sundaram et A. Khan, « Characterization and optimization of zinc oxide films by rf magnetron sputtering », *Thin Solid Films*, vol. 295, no. 1-2, p. 87–91, 1997. 21

[80] I. Petrov, V. Orlinov et A. Misiuk, « Highly oriented ZnO films obtained by dc reactive sputtering of a zinc target », *Thin Solid Films*, vol. 120, no. 1, p. 55–67, 1984. 21

[81] Y. E. Lee, J. B. Lee, Y. J. Kim, H. K. Yang, J. C. Park et H. J. Kim, « Microstructural evolution and preferred orientation change of radio-frequency-magnetron sputtered ZnO thin films », *Journal of Vacuum Science & Technology A : Vacuum, Surfaces, and Films*, vol. 14, no. 3, p. 1943–1948, 1996. 21

[82] N. Ohashi, Y. Adachi, T. Ohsawa, K. Matsumoto, I. Sakaguchi, H. Haneda, S. Ueda, H. Yoshikawa et K. Kobayashi, « Polarity-dependent photoemission spectra of wurtzite-type zinc oxide », *Applied Physics Letters*, vol. 94, p. 122102, 2009. 21

[83] M. Allen, D. Y. Zemlyanov, G. I. N. Waterhouse, J. B. Metson, T. D. Veal, C. F. McConville et S. M. Durbin, « Polarity effects in the X-ray photoemission of ZnO and other wurtzite semiconductors », *Applied Physics Letters*, vol. 98, no. 10, p. 101906, 2011. 21

[84] A. Bikowski, T. Welzel et K. Ellmer, « The correlation between the radial distribution of high-energetic ions and the structural as well as electrical properties of magnetron sputtered ZnO : Al films », *Journal of Applied Physics*, vol. 114, no. 22, p. 223716, 2013. 21, 74

[85] P. Ries, *Silver thin films. Improving the efficiency of low-E coatings by employing different seed layers.* Thèse de doctorat, RWTH Aachen University, Germany, 2015. 21, 89, 147

[86] O. Kappertz, *Atomistic effects in reactive direct current sputter deposition.* Thèse de doctorat, RWTH Aachen University, Germany, 2003. 21, 43, 74

[87] O. Knotek, R. Elsing, G. Krämer et F. Jungblut, « On the origin of compressive stress in PVD coatings—an explicative model », *Surface and Coatings Technology*, vol. 46, no. 3, p. 265–274, 1991. 21

[88] C. Davis, « A simple model for the formation of compressive stress in thin films by ion bombardment », *Thin Solid Films*, vol. 226, no. 1, p. 30–34, 1993. 21

[89] O. Kappertz, R. Drese et M. Wuttig, « Correlation between structure, stress and deposition parameters in direct current sputtered zinc oxide films », *Journal of Vacuum Science & Technology A : Vacuum, Surfaces, and Films*, vol. 20, no. 6, p. 2084–2095, 2002. 21, 43, 74

[90] J. Hinze et K. Ellmer, « In-situ measurement of mechanical stress in polycrystalline zinc-oxide thin films prepared by magnetron sputtering », *Journal of Applied Physics*, vol. 88, no. 5, p. 2443–2450, 2000. 21, 43, 74

[91] D. Severin, O. Kappertz, T. Nyberg, S. Berg et M. Wuttig, « The effect of target aging on the structure formation of zinc oxide during reactive sputtering », *Thin Solid Films*, vol. 515, no. 7-8, p. 3554–3558, 2007. 21, 22, 173

[92] H. L. Skriver et N. Rosengaard, « Surface energy and work function of elemental metals », *Physical Review B*, vol. 46, no. 11, p. 7157, 1992. 22, 25

[93] R. A. Matula, « Electrical resistivity of copper, gold, palladium, and silver », *Journal of Physical and Chemical Reference Data*, vol. 8, no. 4, p. 1147–1298, 1979. 22, 23, 95, 96, 101, 104, 131, 132, 154, 163

[94] C. Kittel, *Introduction to Solid State Physcis.* Global edition, 1968. 23, 28, 102

[95] Z. Lin et P. D. Bristowe, « Microscopic characteristics of the Ag(111)/ZnO(0001) interface present in optical coatings », *Physical Review B*, vol. 75, no. 20, 2007. 23, 25, 26, 122

[96] T. A. Dankovich et D. G. Gray, « Bactericidal paper impregnated with silver nanoparticles for point-of-use water treatment », *Environmental Science & Technology*, vol. 45, no. 5, p. 1992–1998, 2011. 23

[97] J. L. Ferracane, *Materials in dentistry : principles and applications.* Lippincott Williams & Wilkins, 2001. 23

[98] J. Schierholz, L. Lucas, A. Rump et G. Pulverer, « Efficacy of silver-coated medical devices », *Journal of Hospital infection*, vol. 40, no. 4, p. 257–262, 1998. 23

[99] D. Dowling, K. Donnelly, M. McConnell, R. Eloy et M. Arnaud, « Deposition of anti-bacterial silver coatings on polymeric substrates », *Thin Solid Films*, vol. 398, p. 602–606, 2001. 23

[100] E. D. Palik, *Handbook of Optical Constants of Solids*, vol. 1-3. Academic Press, 1985. 23

[101] P. Johnson et R. Christy, « Optical constant of noble metals », *Physical Review B*, vol. 6, p. 4370–4379, 1972. 23

[102] M. Wuttig et X. Liu, *Ultrathin metal films : magnetic and structural properties*, vol. 206. Springer Science & Business Media, 2004. 23, 24, 26

[103] J. Matthews, « Defects associated with the accommodation of misfit between crystals », *Journal of Vacuum Science and Technology*, vol. 12, no. 1, p. 126–133, 1975. 24

[104] S.-Q. Yang, J. Du et Y.-J. Zhao, « First-principles study of ZnO/Mg heterogeneous nucleation interfaces », *Materials Research Express*, vol. 5, no. 3, p. 036519, 2018. 25

[105] N. Jedrecy, G. Renaud, R. Lazzari et J. Jupille, « Flat-top silver nanocrystals on the two polar faces of ZnO : an all angle X-ray scattering investigation », *Physical Review B*, vol. 72, no. 4, 2005. 25, 26, 122, 123

[106] N. Jedrecy, G. Renaud, R. Lazzari et J. Jupille, « Unstrained islands with interface coincidence sites versus strained islands : X-ray measurements on Ag/ZnO », *Physical Review B*, vol. 72, no. 19, 2005. 25, 26, 87, 122, 152

[107] W. Gaebler, K. Jacobi et W. Ranke, « The structure and electronic properties of thin palladium films on zinc oxide studied by AES and UPS », *Surface Science*, vol. 75, no. 2, p. 355–367, 1978. 25

[108] Q. Hérault, *Vers la compréhension de la croissance des couches minces d'argent par pulvérisation, à la lumière de mesures operando*. Thèse de doctorat, Sorbonne University, France, 2019. 25, 38, 87, 124

[109] M. Arbab, « The base layer effect on the DC conductivity and structure of direct current magnetron sputtered thin films of silver », *Thin Solid Films*, vol. 381, no. 1, p. 15–21, 2001. 25, 38, 68

[110] K. H. Ernst, A. Ludviksoson, R. Zhang, J. Yoshihara et C. T. Campbell, « Growth model for metal films on oxide surfaces : Cu on ZnO(000$\bar{1}$)-O », *Physical Review B*, vol. 47, no. 20, p. 13782–13796, 1993. 26

[111] N. Jedrecy, S. Gallini, M. Sauvage-Simkin et R. Pinchaux, « Copper growth on the O-terminated ZnO(0001) surface : Structure and morphology », *Physical Review B*, vol. 64, p. 085424, 2001. 26

[112] H. Jacobs, W. Mokwa, D. Kohl et G. Heiland, « Preparation of Pd/ZnO(000$\bar{1}$) model catalyst and its characterization by AES, LEED and UHV reaction studies », *Surface Science*, vol. 160, p. 217–234, 1985. 26

[113] W. T. Petrie et J. M. Vohs, « Interaction of platinum films with the (000$\bar{1}$) and (0001) surfaces of ZnO », *Journal of Chemical Physics*, vol. 101, no. 9, p. 8098–8107, 1994. 26

[114] N. W. Ashcroft, N. D. Mermin *et al.*, « Solid state physics », 1976. 26

[115] D. Beaglehole, « The optical properties of the noble metals », *Proceedings of the Physical Society (1958-1967)*, vol. 87, no. 2, p. 461, 1966. 29

[116] F. Schwabl, *Advanced quantum mechanics [electronic resource]*. Springer. 29

[117] J.-F. Wang, C.-J. Zhang et J.-F. Hu, « Correlativity and the origin of the T2 difference between the Bloch Grüneisen law and the Debye law », *Canadian journal of physics*, vol. 82, no. 8, p. 585–592, 2004. 29

[118] D. Cvijović, « The Bloch-Gruneisen function of arbitrary order and its series representations », *Theoretical and Mathematical Physics*, vol. 166, no. 1, p. 37–42, 2011. 29

[119] A. Bid, A. Bora et A. Raychaudhuri, « Temperature dependence of the resistance of metallic nanowires of diameter ≤ 15 nm : Applicability of Bloch-Grüneisen theorem », *Physical Review B*, vol. 74, no. 3, p. 035426, 2006. 29, 102

[120] M. Philipp, *Electrical transport and scattering mechanisms in thin silver films for thermally insulating glazing*. Thèse de doctorat, Sorbonne University, France, and Technische Dresden University, Germany, 2011. 29, 33, 96, 101, 102

[121] J. M. Ziman, *Electrons and phonons : the theory of transport phenomena in solids*. Oxford university press, 2001. 30, 35

[122] D. Ferry, *Semiconductor transport*. CRC Press, 2000. 30

[123] A. Bulusu et D. Walker, « Review of electronic transport models for thermoelectric materials », *Superlattices and Microstructures*, vol. 44, no. 1, p. 1–36, 2008. 30

[124] R. C. Munoz et C. Arenas, « Size effects and charge transport in metals : Quantum theory of the resistivity of nanometric metallic structures arising from electron scattering by grain boundaries and by rough surfaces », *Applied Physics Reviews*, vol. 4, p. 011102, 2017. 30, 33

[125] K. Fuchs, « The conductivity of thin metallic films according to the electron theory of metals », *in Mathematical Proceedings of the Cambridge Philosophical Society*, vol. 34, p. 100–108, Cambridge University Press, 1938. 30, 96, 131

[126] E. H. Sondheimer, « The mean free path of electrons in metals », *Advances in Physics*, vol. 50, no. 6, p. 499–537, 2001. 30

[127] A. Mayadas, M. Shatzkes et J. Janak, « Electrical resistivity model for polycrystalline films : the case of specular reflection at external surfaces », *Applied Physics Letters*, vol. 14, no. 11, p. 345–347, 1969. 30, 31, 64, 96, 99, 130

[128] A. Mayadas et M. Shatzkes, « Electrical-resistivity model for polycrystalline films : the case of arbitrary reflection at external surfaces », *Physical Review B*, vol. 1, no. 4, p. 1382, 1970. 30, 31, 32

[129] P. Wißmann, « The electrical resistivity of pure and gas covered metal films », *in Surface physics*, p. 1–96, Springer, 1975. 30

[130] Y. F. Zhu, X. Y. Lang, W. T. Zheng et Q. Jiang, « Electron scattering and electrical conductance in polycrystalline metallic films and wires : Impact of grain boundary scattering related to melting point », *ACS Nano*, vol. 4, p. 3781–3788, 2010. 31, 101

[131] C. Pichard, C. Tellier et A. Tosser, « Thickness dependence of the temperature coefficient of resistivity of polycrystalline films in a three-dimensional conduction model », *Physica Status Solidi (a)*, vol. 65, no. 1, p. 327–334, 1981. 31

[132] C. R. Tellier et A. J. Tosser, *Size effects in thin films*, vol. 2. Elsevier, 2016. 31

[133] G. Reiss, J. Vancea et H. Hoffmann, « Grain-boundary resistance in polycrystalline metals », *Physical Review Letters*, vol. 56, no. 19, p. 2100, 1986. 32

[134] H. Hoffmann, *Festkorperprobleme*. J. Treusche, 1982. 32

[135] T. Sun, B. Yao, A. P. Warren, K. Barmak, M. F. Toney, R. E. Peale et K. R. Coffey, « Surface and grain-boundary scattering in nanometric cu films », *Physical Review B*, vol. 81, p. 155454, 2010. 32

[136] R. Cornely et T. Ali, « Resistivity and microstructure of polycrystalline au films deposited by rf bias-diode and triode sputtering », *Journal of Applied Physics*, vol. 49, no. 7, p. 4094–4097, 1978. 32

[137] W. Steinhögl, G. Schindler, G. Steinlesberger et M. Engelhardt, « Size-dependent resistivity of metallic wires in the mesoscopic range », *Physical Review B*, vol. 66, no. 7, p. 075414, 2002. 32

[138] H. Marom, M. Ritterband et M. Eizenberg, « The contribution of grain boundary scattering versus surface scattering to the resistivity of thin polycrystalline films », *Thin Solid Films*, vol. 510, no. 1-2, p. 62–67, 2006. 32, 101

[139] P. M. T. M. van Attekum, P. H. Woerlee, G. C. Verkade et A. A. M. Hoeben, « Influence of grain boundaries and surface Debye temperature on the electrical resistance of thin gold films », *Physical Review B*, vol. 29, no. 2, p. 645–650, 1984. 33, 36, 102

[140] K. Elsom et J. Sambles, « Macroscopic surface roughness and the resistivity of thin metal films », *Journal of Physics F : Metal Physics*, vol. 11, no. 3, p. 647, 1981. 33

[141] J. R. Sambles, K. C. Elsom et D. J. Jarvis, « The electrical resistivity of gold films », *Philosophical Transactions of the Royal Society of London. Series A, mathematical and physical sciences*, vol. 304, no. 1486, p. 365–396, 1982. 33, 35

[142] J. Sambles, « The resistivity of thin metal films—some critical remarks », *Thin Solid Films*, vol. 106, no. 4, p. 321–331, 1983. 33, 35, 64, 96, 99, 130

[143] H. J. Juretschke, « Electrical conductivity of thin metallic films with unlike surfaces », *Journal of Applied Physics*, vol. 37, no. 1, p. 435–435, 1966. 33

[144] M. Lucas, « Electrical conductivity of thin metallic films with unlike surfaces », *Journal of Applied Physics*, vol. 36, no. 5, p. 1632–1635, 1965. 33

[145] A. Cottey, « The electrical conductivity of thin metal films with very smooth surfaces », *Thin Solid Films*, vol. 1, no. 4, p. 297–307, 1968. 33

[146] P. J. Price, « Anisotropic conduction in solids near surfaces », *IBM Journal of Research and Development*, vol. 4, no. 2, p. 152–157, 1960. 34

[147] R. Englman et E. Sondheimer, « The electrical conductivity of anisotropic thin films », *Proceedings of the Physical Society. Section B*, vol. 69, no. 4, p. 449, 1956. 34

[148] K. E. Saeger et R. Lück, « Evidence of anisotropic mean free path as furnished by galvanomagnetic measurements », *Physik der kondensierten Materie*, vol. 9, no. 1-2, p. 91–97, 1969. 35

[149] S. B. Soffer, « Statistical model for the size effect in electrical conduction », *Journal of Applied Physics*, vol. 38, no. 4, p. 1710–1715, 1967. 35, 64, 96, 99, 130

[150] J. Parrott, « A new theory of the size effect in electrical conduction », *Proceedings of the Physical Society (1958-1967)*, vol. 85, no. 6, p. 1143, 1965. 35

[151] U. Jacob, J. Vancea et H. Hoffmann, « Surface-roughness contributions to the electrical resistivity of polycrystalline metal films », *Physical Review B*, vol. 41, no. 17, p. 11852, 1990. 35

[152] F. Warkusz, « Size effects in metallic films », *Electrocomponent Science and Technology*, vol. 5, no. 2, p. 99–105, 1978. 35

[153] C. Tellier, C. Pichard et A. Tosser, « Statistical model of electrical conduction in polycrystalline metals », *Thin Solid Films*, vol. 61, no. 3, p. 349–354, 1979. 35

[154] C. Pichard, C. Tellier et A. Tosser, « A three-dimensional model for grain boundary resistivity in metal films », *Thin Solid Films*, vol. 62, no. 2, p. 189–194, 1979. 35

[155] C. Pichard, C. Tellier et A. Tosser, « Linear variations in conductivity with thickness of thin polycrystalline films », *Journal of Materials Science*, vol. 15, no. 9, p. 2236–2240, 1980. 35

[156] J. Sambles, K. Elsom et G. Sharp-Dent, « The effect of sample thickness on the resistivity of aluminium », *Journal of Physics F : Metal Physics*, vol. 11, no. 5, p. 1075, 1981. 35

[157] J. Sambles, I. Coulson et D. Jarvis, « Radiation annealing of epitaxial silver films », *Vacuum*, vol. 33, no. 10-12, p. 737–739, 1983. 35

[158] J. Goniakowski, C. Noguera et L. Giordano, « Using polarity for engineering oxide nanostructures : structural phase diagram in free and supported mgo (111) ultrathin films », *Physical review letters*, vol. 93, no. 21, p. 215702, 2004. 38

[159] L. A. B. Pilkington, « Review lecture : the float glass process », *Proceedings of the Royal Society of London. A. Mathematical and Physical Sciences*, vol. 314, no. 1516, p. 1–25, 1969. 38, 39

[160] N. S. G. Co., « Pilkington ». https://www.pilkington.com/fr-fr/fr/nsg-group/education/le-procede-float/overview, 11 2021. 39

[161] S. Ben Khemis, *Couche mince de silice amorphe dopée alumine comme barrière de diffusion dans les verres fonctionnalisés*. Thèse de doctorat, Sorbonne University, France, 2021. 39

[162] H. Ibach, *Physics of Surfaces and Interfaces*. Springer-Verlag Berlin Heidelberg, 2006. 46

[163] J. Chastain et R. C. King Jr, « Handbook of X-ray photoelectron spectroscopy », *Perkin-Elmer, USA*, p. 261, 1992. 47

[164] S. Tanuma, C. J. Powell et D. R. Penn, « Calculations of electron inelastic mean free paths (IMFPS). iv. evaluation of calculated IMFPs and of the predictive IMFP formula TPP-2 for electron energies between 50 and 2000 ev », *Surface and Interface Analysis*, vol. 20, no. 1, p. 77–89, 1993. 48

[165] D. A. Shirley, « High-resolution X-ray photoemission spectrum of the valence bands of gold », *Physical Review B*, vol. 5, no. 12, p. 4709, 1972. 49

[166] S. Jeong, S. Kho, D. Jung, S. Lee et J.-H. Boo, « Deposition of aluminum-doped zinc oxide films by RF magnetron sputtering and study of their surface characteristics », *Surface and Coatings technology*, vol. 174, p. 187–192, 2003. 49

[167] M. Chen, X. Wang, Y. Yu, Z. Pei, X. Bai, C. Sun, R. Huang et L. Wen, « X-ray photoelectron spectroscopy and Auger electron spectroscopy studies of Al-doped ZnO films », *Applied Surface Science*, vol. 158, no. 1-2, p. 134–140, 2000. 49

[168] R. Al-Gaashani, S. Radiman, A. Daud, N. Tabet et Y. Al-Douri, « XPS and optical studies of different morphologies of ZnO nanostructures prepared by microwave methods », *Ceramics International*, vol. 39, no. 3, p. 2283–2292, 2013. 49, 110

[169] G. Greczynski et L. Hultman, « X-ray photoelectron spectroscopy : Towards reliable binding energy referencing », *Progress in Materials Science*, vol. 107, p. 100591, 2020. 49

[170] A. R. West, *Basic Solid State Chemistry*. John Wiley & Sons Incorporated, 1999. 50

[171] B. Cullity, « Elements of X-ray diffraction, addison-wesley, reading, ma 1978. ». 51, 55

[172] D. Schumacher, *Surface scattering experiments with conduction electrons*, vol. 128. Springer, 2007. 53

[173] C. Ern, W. Donner, H. Dosch, B. Adams et D. Nowikow, « Temperature-dependent interfacial stiffness of the disorder layer in a thin Cu_3Au alloy film », *Physical Review Letters*, vol. 85, no. 9, p. 1926, 2000. 53

[174] V. Klosek, « Crystallographic textures », *in EPJ Web of Conferences*, vol. 155, p. 00005, EDP Sciences, 2017. 54

[175] M. Moram et M. Vickers, « X-ray diffraction of III-nitrides », *Reports on Progress in Physics*, vol. 72, no. 3, p. 036502, 2009. 55, 57

[176] T. H. De Keijser, J. Langford, E. J. Mittemeijer et A. Vogels, « Use of the Voigt function in a single-line method for the analysis of X-ray diffraction line broadening », *Journal of Applied Crystallography*, vol. 15, no. 3, p. 308–314, 1982. 56

[177] C. Charpentier, P. Prod'Homme, I. Maurin, M. Chaigneau et P. R. i Cabarrocas, « X-ray diffraction and raman spectroscopy for a better understanding of ZnO :Al growth process », *EPJ Photovoltaics*, vol. 2, p. 25002, 2011. 57

[178] G. Williamson et W. Hall, « X-ray line broadening from filed aluminium and wolfram », *Acta Metallurgica*, vol. 1, no. 1, p. 22–31, 1953. 58

[179] V. Mote, Y. Purushotham et B. Dole, « Williamson-Hall analysis in estimation of lattice strain in nanometer-sized ZnO particles », *Journal of Theoretical and Applied Physics*, vol. 6, no. 1, p. 1–8, 2012. 58

[180] A. Monshi, M. R. Foroughi et M. R. Monshi, « Modified Scherrer equation to estimate more accurately nano-crystallite size using XRD », *World Journal of Nano Science and Engineering*, vol. 02, no. 03, p. 154–160, 2012. 58

[181] D. Nath, F. Singh et R. Das, « X-ray diffraction analysis by Williamson-Hall, Halder-Wagner and size-strain plot methods of CdSe nanoparticles-a comparative study », *Materials Chemistry and Physics*, vol. 239, p. 122021, 2020. 58

[182] F. Izumi, T. Ikeda *et al.*, « Implementation of the Williamson-Hall and Halder-Wagner methods into RIETAN-FP », 2015. 58

[183] R. Chierchia, T. Böttcher, H. Heinke, S. Einfeldt, S. Figge et D. Hommel, « Microstructure of heteroepitaxial GaN revealed by X-ray diffraction », *Journal of Applied physics*, vol. 93, no. 11, p. 8918–8925, 2003. 59

[184] R. Furushima, S. Tanaka, Z. Kato et K. Uematsu, « Orientation distribution-lotgering factor relationship in a polycrystalline material—as an example of bismuth titanate prepared by a magnetic field », *Journal of the Ceramic Society of Japan*, vol. 118, no. 1382, p. 921–926, 2010. 59

[185] T. Uchikoshi, C. Matsunaga, T. S. Suzuki, Y. Sakka et M. Matsuda, « Electrophoretic deposition of orientation-controlled zeolite L layer on porous ceramic substrate », *Journal of the Ceramic Society of Japan*, vol. 121, no. 1412, p. 370–372, 2013. 59

[186] J. A. Horn, S. Zhang, U. Selvaraj, G. L. Messing et S. Trolier-McKinstry, « Templated grain growth of textured bismuth titanate », *Journal of the American Ceramic Society*, vol. 82, no. 4, p. 921–926, 1999. 59

[187] T. Kimura, « Microstructure development and texture formation in lead-free piezoelectric ceramics prepared by templated grain growth process », *Journal of the Ceramic Society of Japan*, vol. 124, no. 4, p. 268–282, 2016. 59

[188] S. Tanaka, A. Makiya, Z. Kato, N. Uchida, T. Kimura et K. Uematsu, « Fabrication of c-axis oriented polycrystalline ZnO by using a rotating magnetic field and following sintering », *Journal of Materials Research*, vol. 21, no. 3, p. 703–707, 2006. 59

[189] J. Daillant et A. Gibaud, *X-ray and neutron reflectivity : principle and applications vol. 770 in Lectures notes in physics*. Springer, 2009. 60

[190] C. Li, G. Habler, L. C. Baldwin et R. Abart, « An improved FIB sample preparation technique for site-specific plan-view specimens : A new cutting geometry », *Ultramicroscopy*, vol. 184, p. 310–317, 2018. 62

[191] A. Valery, *Caractérisation de microtextures par la technique ACOM-TEM dans le cadre du développement des technologies avancées en microélectronique*. Thèse de doctorat, Université Grenoble Alpes (ComUE), 2017. 63

[192] I. Miccoli, F. Edler, H. Pfnur et C. Tegenkamp, « The 100th anniversary of the four-point probe technique : the role of probe geometries in isotropic and anisotropic systems », *Journal of Physics : Condensed Matter*, vol. 27, no. 22, p. 223201, 2015. 63, 111

[193] K. Kato, H. Omoto et A. Takamatsu, « Optimum structure of metal oxide under-layer used in Ag-based multilayer », *Vacuum*, vol. 83, no. 3, p. 606–609, 2008. 68

[194] J. Pierson, D. Wiederkehr et A. Billard, « Reactive magnetron sputtering of copper, silver, and gold », *Thin Solid Films*, vol. 478, no. 1-2, p. 196–205, 2005. 84

[195] P. Jacquet, *Vers la compréhension et le contrôle du démouillage des couches d'argent.* Thèse de doctorat, University Pierre and Marie Curie, 2017. 84, 136

[196] R. Martin-Palma et J. Martinez-Duart, « Ni-Cr passivation of very thin Ag films for low-emissivity multilayer coatings », *Journal of Vacuum Science & Technology A : Vacuum, Surfaces, and Films*, vol. 17, no. 6, p. 3449–3451, 1999. 84

[197] X. Caillet, *Understanding the role and influence of blocker layers in silver-based stacks - bibliographic study.* Tecnhical Report SGR SGR/CM – XC – n. 7506/11, 2011. 84

[198] E. Chason et P. R. Guduru, « Tutorial : understanding residual stress in polycristalline thin films through real-time measurements and physical models », *Journal of Applied Physics*, vol. 119, p. 191101, 2016. 87, 124

[199] G. Abadias, E. Chason, J. Keckes, M. Sebastiani, G. B. Thompson, E. Barthel, G. L. Doll, C. E. Murray, C. H. Stoessel et L. Martinu, « Review article : Stress in thin films and coatings : Current status, challenges, and prospects », *Journal of Vacuum Science and Technology*, vol. 36, no. 2, p. 020801, 2018. 87, 124

[200] Q. Hérault, I. Gozhyk, M. Balestrieri, H. Montigaud, S. Grachev et R. Lazzari, « Kinetics and mechanisms of stress relaxation in sputtered silver thin films », *Acta Materialia*, vol. 221, p. 117385, 2021. 87, 124

[201] G. T. Meaden, *Electrical resistance of metals.* Springer, 2013. 97

[202] J. De Vries, « Temperature and thickness dependence of the resistivity of thin polycrystalline aluminium, cobalt, nickel, palladium, silver and gold films », *Thin Solid Films*, vol. 167, no. 1-2, p. 25–32, 1988. 97

[203] N. Artunç, M. Bilge et G. Utlu, « The effects of grain boundary scattering on the electrical resistivity of single-layered silver and double-layered silver/chromium thin films », *Surface and Coatings Technology*, vol. 201, no. 19-20, p. 8377–8381, 2007. 101

[204] V. Duggal et V. Nagpal, « Size effect in thin single-crystal silver films », *Applied Physics Letters*, vol. 13, no. 6, p. 206–207, 1968. 101

[205] M. Hubin et J. Gouault, « Resistivity and thermoelectric power between-100° C and+ 100° C of gold and silver thin films formed and studied in ultrahigh vacuum », *Thin Solid Films*, vol. 24, no. 2, p. 311–331, 1974. 101

[206] V. N. Rao, S. Mohan et P. J. Reddy, « The size effect in the thermoelectric power of silver films », *Thin Solid Films*, vol. 42, no. 3, p. 283–289, 1977. 101

[207] J. Greiser, P. Müllner et E. Arzt, « Abnormal growth of "giant" grains in silver thin films », *Acta Materialia*, vol. 49, no. 6, p. 1041–1050, 2001. 102

[208] C. Li et Z. Wang, « Computational modelling and ab initio calculations in MAX phases–i », *Advances in Science and Technology of Mn+ 1AXn Phases*, p. 197–222, 2012. 102

[209] J. Spreadborough et J. Christian, « The measurement of the lattice expansions and Debye temperatures of titanium and silver by X-ray methods », *Proceedings of the Physical Society (1958-1967)*, vol. 74, no. 5, p. 609, 1959. 102

[210] W. Ma, X. Zhang et K. Takahashi, « Electrical properties and reduced Debye temperature of polycrystalline thin gold films », *Journal of Physics D : Applied Physics*, vol. 43, no. 46, p. 465301, 2010. 102

[211] Z. Cheng, L. Liu, S. Xu, M. Lu et X. Wang, « Temperature dependence of electrical and thermal conduction in single silver nanowire », *Scientific Reports*, vol. 5, no. 1, p. 1–12, 2015. 102

[212] D. Jackson, « Approximate calculation of surface Debye temperatures », *Surface Science*, vol. 43, no. 2, p. 431–440, 1974. 102

[213] M. Kostelitz et J. Domange, « Effective surface Debye-Waller temperatures and mean-square displacements for gold from LEED measurements », *Solid State Communications*, vol. 13, no. 3, p. 241–244, 1973. 102

[214] U. Stuhr, H. Wipf, K. Andersen et H. Hahn, « Low-frequency modes in nanocrystalline Pd », *Physical Review Letters*, vol. 81, no. 7, p. 1449, 1998. 102

[215] P. Derlet, R. Meyer, L. Lewis, U. Stuhr et H. Van Swygenhoven, « Low-frequency vibrational properties of nanocrystalline materials », *Physical Review Letters*, vol. 87, no. 20, p. 205501, 2001. 102

[216] G. Kästle, T. Müller, H.-G. Boyen, A. Klimmer et P. Ziemann, « Resistivity and phonon softening in ion-irradiated epitaxial gold films », *Journal of Applied Physics*, vol. 96, no. 12, p. 7272–7277, 2004. 102

[217] J. Williams, H. Yoshikawa, S. Ueda, Y. Yamashita, K. Kobayashi, Y. Adachi, H. Haneda, T. Ohgaki, H. Miyazaki, T. Ishigaki *et al.*, « Polarity-dependent photoemission spectra of wurtzite-type zinc oxide », *Applied Physics Letters*, vol. 100, no. 5, p. 051902, 2012. 110

[218] A. Shchukarev et D. Korolkov, « XPS study of group IA carbonates », *Central European Journal of Chemistry*, vol. 2, no. 2, p. 347–362, 2004. 110

[219] A. Mang, K. Reimann *et al.*, « Band gaps, crystal-field splitting, spin-orbit coupling, and exciton binding energies in ZnO under hydrostatic pressure », *Solid State Communications*, vol. 94, no. 4, p. 251–254, 1995. 110

[220] B. E. Sernelius, K.-F. Berggren, Z.-C. Jin, I. Hamberg et C. G. Granqvist, « Band-gap tailoring of ZnO by means of heavy Al doping », *Physical Review B*, vol. 37, no. 17, p. 10244, 1988. 110

[221] F. K. Shan et Y. S. Yu, « Band gap energy of pure and Al-doped ZnO thin films », *Journal of the European Ceramic Society*, vol. 24, no. 6, p. 1869–1872, 2004. 110

[222] M. Guzzi, *Principi di fisica dei semiconduttori*. HOEPLI EDITORE, 2013. 111

[223] K. Kumarappan, *Photoemission studies of ex-situ and in-situ surface cleaning and electronic properties of ZnO surfaces*. Thèse de doctorat, Dublin City University, Ireland, 2015. 111

[224] D. Mora-Fonz, T. Lazauskas, M. R. Farrow, C. R. A. Catlow, S. M. Woodley et A. A. Sokol, « Why are polar surfaces of ZnO stable ? », *Chemistry of Materials*, vol. 29, no. 12, p. 5306–5320, 2017. 113

[225] P. Sokolov, A. Baranov, Z. V. Dobrokhotov et V. Solozhenko, « Synthesis and thermal stability of cubic ZnO in the salt nanocomposites », *Russian Chemical Bulletin*, vol. 59, no. 2, p. 325–328, 2010. 113

[226] X. Gu, S. Sabuktagin, A. Teke, D. Johnstone, H. Morkoç, B. Nemeth et J. Nause, « Effect of thermal treatment on ZnO substrate for epitaxial growth », *Journal of Materials Science : Materials in Electronics*, vol. 15, no. 6, p. 373–378, 2004. 113

[227] O. Dulub, U. Diebold et G. Kresse, « Novel stabilization mechanism on polar surfaces : ZnO(0001)-Zn », *Physical Review Letters*, vol. 90, no. 1, p. 016102, 2003. 123

[228] M. Valtiner, M. Todorova, G. Grundmeier et J. Neugebauer, « Temperature stabilized surface reconstructions at polar ZnO(0001) », *Physical Review Letters*, vol. 103, no. 6, p. 065502, 2009. 123

[229] S. Torbrugge, F. Ostendorf et M. Reichling, « Stabilization of zinc-terminated ZnO(0001) by a modified surface stoichiometry », *The Journal of Physical Chemistry C*, vol. 113, no. 12, p. 4909–4914, 2009. 123

[230] T. Tan, S. Zhang, J. Wang, Y. Zheng, H. Lai, J. Liu, F. Qin et C. Wang, « Resolving the stacking fault structure of silver nanoplates », *Nanoscale*, vol. 13, no. 1, p. 195–205, 2021. 125

[231] R. Brown, « A dislocation model of grain boundary electrical resistivity », *Journal of Physics F : Metal Physics*, vol. 7, no. 8, p. 1477, 1977. 128, 129, 130

[232] D. Tanner et D. Larson, « Electrical resistivity of silver films », *Physical Review*, vol. 166, no. 3, p. 652, 1968. 131

[233] H. Kim, I. W. Yeu, G. Han, G. Ju, Y. J. Lee, Y.-h. Shin, J.-H. Choi, H. C. Koo et H.-j. Kim, « Surface morphology evolution and underlying defects in homoepitaxial growth of GaAs(110) », *Journal of Alloys and Compounds*, vol. 874, p. 159848, 2021. 146

[234] F. Gunkel, S. Wicklein, S. Hoffmann-Eifert, P. Meuffels, P. Brinks, M. Huijben, G. Rijnders, R. Waser et R. Dittmann, « Transport limits in defect-engineered $LaAlO_3/SrTiO_3$ bilayers », *Nanoscale*, vol. 7, no. 3, p. 1013–1022, 2015. 146

[235] S. Bin Anooz, A. Popp, R. Grüneberg, C. Wouters, R. Schewski, M. Schmidbauer, M. Albrecht, A. Fiedler, M. Ramsteiner, D. Klimm *et al.*, « Indium incorporation in homoepitaxial β-Ga_2O_3 thin films grown by metal organic vapor phase epitaxy », *Journal of Applied Physics*, vol. 125, no. 19, p. 195702, 2019. 146

[236] S. Song, J. Cole et S. Bruemmer, « Formation of partial dislocations during intersection of glide dislocations with Frank loops in fcc lattices », *Acta Materialia*, vol. 45, no. 2, p. 501–511, 1997. 147

[237] G. Renaud, P. Guénard et A. Barbier, « Misfit dislocation network at the Ag/MgO(001) interface : A grazing-incidence X-ray-scattering study », *Phys. Rev. B*, vol. 58, p. 7310, 1998. 152

[238] J. Olander, R. Lazzari, J. Jupille, B. Mangili, J. Goniakowski et G. Renaud, « Size- and temperature-dependent epitaxy for a strong film-substrate mismatch : The case of Pt/MgO(001) », *Physical Review B*, vol. 76, no. 7, 2007. 152

[239] P. N. Arendt et S. R. Foltyn, « Biaxially textured ibad-mgo templates for ybco-coated conductors », *MRS bulletin*, vol. 29, no. 8, p. 543–550, 2004. 173

[240] D. Zhang, R. Gao et H. Ma, « Burstein shift and uv photoresponse in ibad-deposited transparent conducting zno films », *Thin Solid Films*, vol. 295, no. 1-2, p. 83–86, 1997. 173

[241] D. Zhang et D. Brodie, « Effects of annealing zno films prepared by ion-beam-assisted reactive deposition », *Thin Solid Films*, vol. 238, no. 1, p. 95–100, 1994. 173

[242] K. Wang, Y. Vygranenko et A. Nathan, « Fabrication and characterization of nio/zno/ito p–i–n heterostructure », *Thin Solid Films*, vol. 516, no. 7, p. 1640–1643, 2008. 173

[243] A. H. Deutchman et R. J. Partyka, « Dual ion beam ballistic alloying process », fév. 12 1991. US Patent 4,992,298. 175

[244] D. P. Norton et V. Selvamanickam, « Method of producing biaxially textured buffer layers and related articles, devices and systems », fév. 1 2005. US Patent 6,849,580. 175

Impact of texture on resistivity of silver-based model low-emissive coatings

Abstract In the industrial context of sputtered low-emissive silver-based coatings, this work aimed at identifying, through structural and topographical characterizations, the contributions of interface scattering and grain boundary reflectivity in the electron transport and film resistivity. In particular, the impact of the in-plane texture induced by the ZnO seed layer was explored with simplified model stacks. For this purpose, R&D polycrystalline coatings, characterized by a silver film only preferentially oriented along the (111) out-of-plane direction, were compared, before and after annealing, to films in hexagon/hexagon epitaxy (lattice mismatch -11.5%) on ZnO(0001) single crystals (Zn- or O-terminated) presenting a clear biaxial-texture with outstanding structural and electrical properties. Resistivity characterizations were carried out in temperature and analysed via models of Mayadas-Shatzkes type. In line with the variations of their structural and topographical characteristics, determined through XRD, AFM and TEM, glass-based and single crystal-based samples presented distinct transport properties. Improvements in the in-plane grain orientation and decrease of grain density proved to help reducing the electron-grain boundary scattering, while no clear-cut correlation between interface roughnesses and resistivity could be established whatever the analysis model. Nonetheless, interface contribution could be lowered through post-deposition thermal treatment. World record resistivity values, up to 30% lower than the industrial products, were reached for single crystal-based samples.

Keywords : silver, zinc oxide, resistivity, thin films, texture, low-emissive coating.

Impact de la texture sur la résistivité des revêtements modèles à faible émissivité à base d'argent

Résumé Dans le contexte industriel des revêtements à faible émissivité à base d'argent déposés par pulvérisation cathodique, ce travail visait à identifier, au travers de caractérisations structurales et topographiques, les contributions de la diffusion à l'interface et de la réflectivité aux joints de grain dans le transport électronique et la résistivité du film. En particulier, le rôle de la texture dans le plan, induite par la couche de nucléation de ZnO a été exploré dans des d'empilements modèles. Dans ce but, des revêtements polycristallins RD caractérisés par un film d'argent seulement orienté préférentiellement le long de la direction hors plan (111) ont été comparés, avant et après recuit, à des films déposés sur des monocristaux de ZnO(0001) terminés Zn ou O (épitaxie hexagone/hexagone avec désaccord paramétrique de -11.5%), présentant une texture biaxiale claire avec des propriétés structurales et électriques exceptionnelles. Les caractérisations électriques ont été effectuées en température et analysées via des modèles de type Mayadas-Shatzkes. En accord avec les variations de leurs caractéristiques structurales et topographiques obtenues par XRD, AFM et TEM, les échantillons sur substrat de verre et monocristallins ont montré des propriétés de transport distinctes. L'amélioration de l'orientation des grains dans le plan et la diminution de leur densité ont permis de réduire la diffusion des électrons aux

joints des grains, alors qu'aucune relation claire entre résistivité et rugosités d'interface n'a pu être établie. Cependant la contribution de résistivité de l'interface a pu être réduite par traitement thermique. Ainsi, des valeurs de résistivité record, jusqu'à 30% inférieures aux références industrielles, ont été atteintes.

Mots-clés : argent, oxyde de zinc, résistivité, couches minces, texture, revêtement à faible émissivité.